NEUTRINO SOURCES
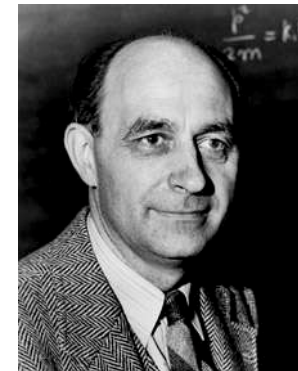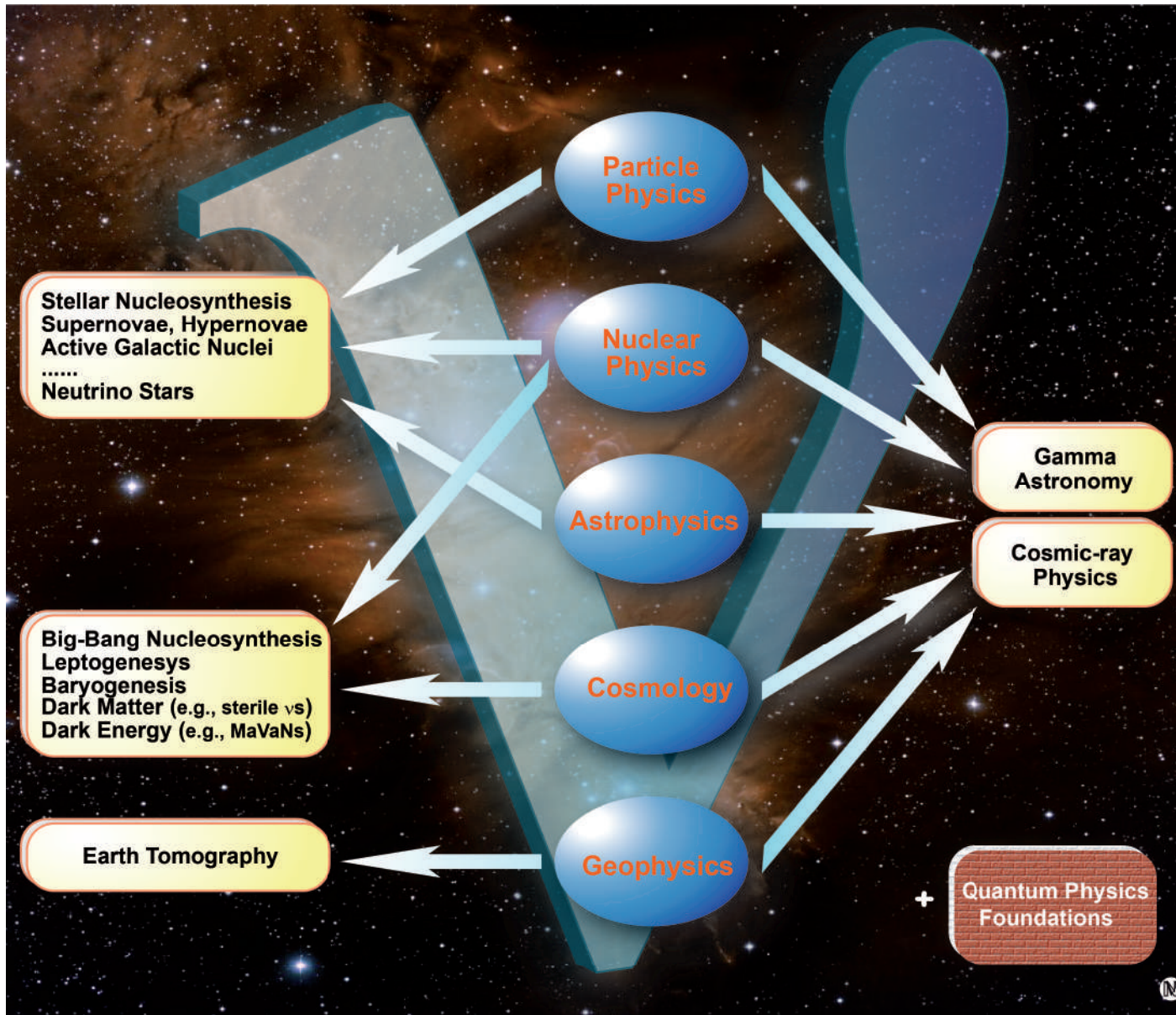
V.A. Naumov
JINR, Dubna
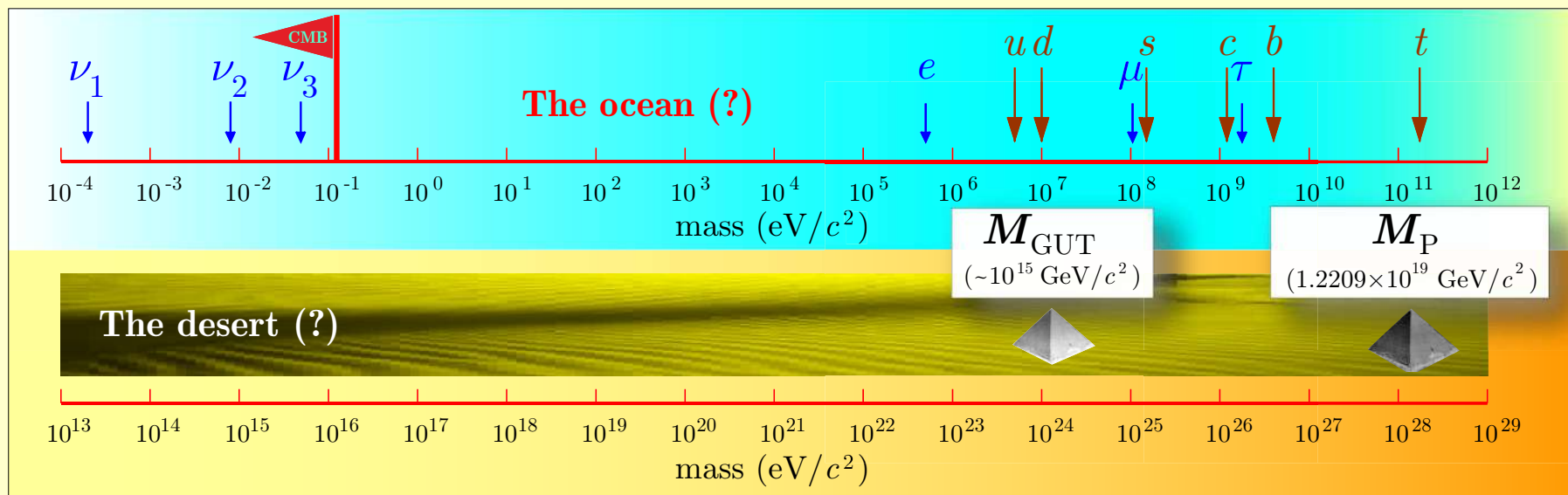
22nd Baikal Summer School on Physics of Elementary Particles & Astrophysics
Bolshie Koty, July 12−19, 2022

Particle linking physics, astrophysics, and more...

What do we know and don't know about neutrinos?

Angels vs. hippos.

According to the current theoretical understanding, the neutrino fields/states of definite flavor are superpositions of the fields/states with definite, generally different masses [and vice versa]:

$$\nu_\alpha = \sum_i V_{\alpha i} \nu_i \qquad \text{for neutrino fields,}$$

$$|\nu_\alpha\rangle = \sum_i V_{\alpha i}^* |\nu_i\rangle \qquad \text{for neutrino states;}$$

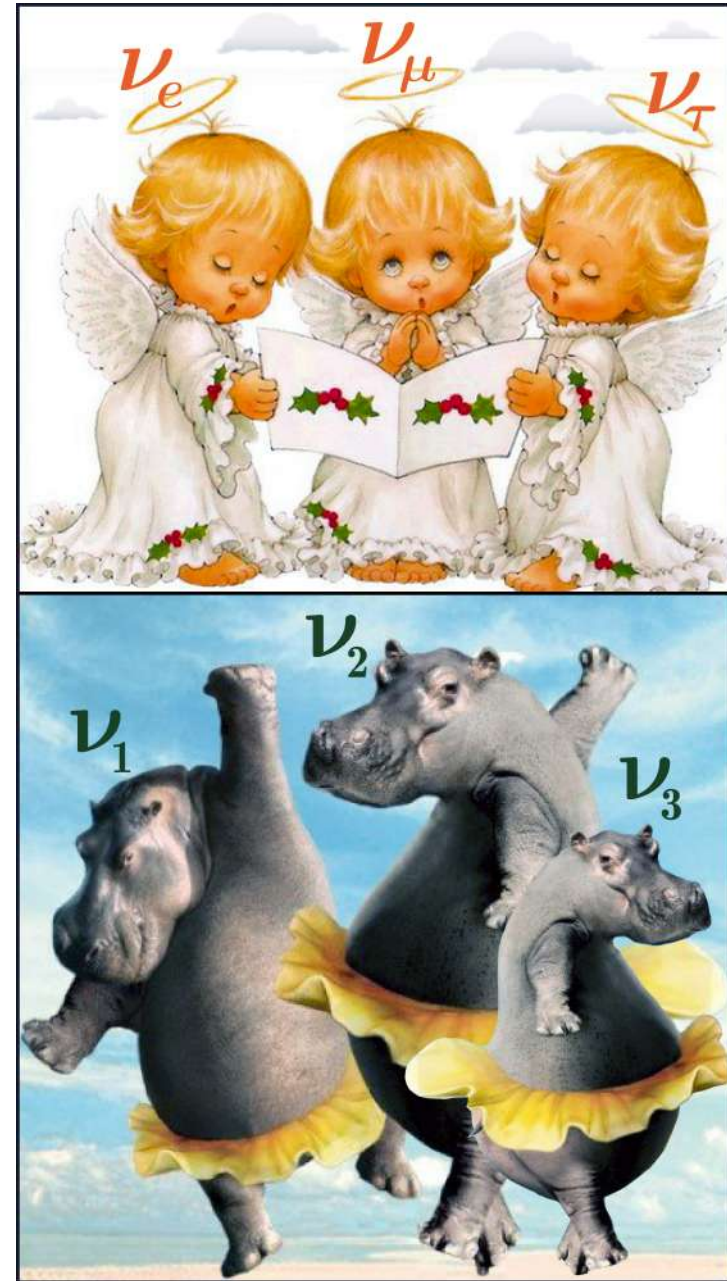$$\alpha = e, \mu, \tau, \quad i = 1, 2, 3, \dots$$

Here $V_{\alpha i}$ are the elements of the Pontecorvo-Maki-Nakagawa-Sakata neutrino vacuum mixing matrix $\mathbf{V}$,

ν_α / ν_i	–	flavor/mass eigenfield
$|\nu_\alpha\rangle / |\nu_i\rangle$	–	flavor/mass eigenstate

This concept leads to the possibility of transitions between the neutrinos of different flavors

$$\nu_\alpha \longleftrightarrow \nu_\beta,$$

phenomenon known as **neutrino flavor oscillations**.

Interaction Lagrangian and weak currents.

In the Standard Model (SM), the charged and neutral current neutrino interactions with leptons are described by the following parts of the full Lagrangian:

$$\mathcal{L}_I^{\mathsf{CC}}(x) = -\frac{g}{2\sqrt{2}} j_\ell^{\mathsf{CC}}(x) W^\ell(x) + \mathsf{H.c.} \quad \text{and} \quad \mathcal{L}_I^{\mathsf{NC}}(x) = -\frac{g}{2\cos\theta_{\mathsf{W}}} j_\ell^{\mathsf{NC}}(x) Z^\ell(x).$$

Here g is the $SU(2)$ (electro-weak) gauge coupling ($g^2 = 4\sqrt{2} m_W^2 G_F$, $g\sin\theta_{\mathsf{W}} = |e|$), and θ_{W} is the weak mixing (Weinberg) angle ($\sin^2\theta_{\mathsf{W}} \approx 0.23$).

The leptonic charged current and neutrino neutral current are given by the expressions:

$$j_\ell^{\mathsf{CC}}(x) = 2 \sum_{\ell=e,\mu,\tau,\dots} \overline{\nu}_{\ell,L}(x) \gamma_\ell \ell_L(x) \quad \text{and} \quad j_\ell^{\mathsf{NC}}(x) = \sum_{\ell=e,\mu,\tau,\dots} \overline{\nu}_{\ell,L}(x) \gamma_\ell \nu_{\ell,L}(x).$$

Phenomenologically, the charged and neutral currents may include (yet unknown) heavy neutrinos and corresponding heavy charged leptons. The left- and right-handed fermion fields are defined as usually:

$$\nu_{\ell,L/R}(x) = P_{L/R}\nu_\ell(x), \quad \ell_{L/R}(x) = P_{L/R}\ell(x), \quad P_{L/R} \equiv (1 \mp \gamma_5)/2,$$

The full SM Lagrangian with **massless** νs is invariant with respect to the global transformations

$$\nu_\ell(x) \to e^{i\Lambda_\ell}\nu_\ell(x) \text{ and } \ell(x) \to e^{i\Lambda_\ell}\ell(x) \text{ with } \Lambda_\ell = \mathsf{const.}$$

By Noether's theorem this leads to conservation of the individual lepton flavor numbers (more rarely called lepton flavor charges) L_ℓ. It is agreed that

$$\boxed{L_\ell(\ell^-, \nu_\ell) = +1, \quad L_\ell(\ell^+, \overline{\nu}_\ell) = -1, \quad \ell^\pm = e^\pm, \mu^\pm, \tau^\pm, \mathsf{etc.}}$$

Mass matrix and PMNS matrix − synopsis.

The most general mass term for 3-generation neutrinos can have two forms, depending on transformation properties of the neutrino field $\nu(x)$ with respect to charge conjugation

$$\nu \longmapsto \nu^c = C\,\overline{\nu}^T, \quad \overline{\nu} \longmapsto \overline{\nu^c} = -\nu^T C,$$

Dirac mass term $\quad \boxed{\nu^c(x) \neq \nu(x)}$

$$\mathcal{L}_{\mathsf{D}}(x) = -\overline{\boldsymbol{\nu}}_R(x)\,\mathbf{M}_{\mathsf{D}}\,\boldsymbol{\nu}_L(x) + \text{H.c.}$$
$$\uparrow$$
complex $3{\times}3$ matrix

Violates CP (T) and L_ℓ, but saves $\displaystyle\sum_\ell L_\ell$

$$\mathbf{V}_{\mathsf{D}} = \mathbf{V}$$

Majorana mass term $\quad \boxed{\nu^c(x) = \nu(x)}$

$$\mathcal{L}_{\mathsf{M}}(x) = -\frac{1}{2}\overline{\boldsymbol{\nu}}^c_L(x)\,\mathbf{M}_{\mathsf{M}}\,\boldsymbol{\nu}_L(x) + \text{H.c.}$$
$$\uparrow$$
complex symmetric $3{\times}3$ matrix

Violates CP (T), L_ℓ, and $\displaystyle\sum_\ell L_\ell$

$$\mathbf{V}_{\mathsf{M}} = \mathbf{V}\,\text{diag}\left(e^{i\alpha_1/2}, e^{i\alpha_2/2}, 1\right)$$

$$\mathbf{V} = \mathbf{O}_{23}\boldsymbol{\Gamma}_{\mathsf{D}}\mathbf{O}_{13}\boldsymbol{\Gamma}_{\mathsf{D}}^\dagger\mathbf{O}_{12} = \begin{pmatrix} c_{12}c_{13} & s_{12}c_{13} & s_{13}e^{-i\delta} \\ -s_{12}c_{23} - c_{12}s_{23}s_{13}e^{i\delta} & c_{12}c_{23} - s_{12}s_{23}s_{13}e^{i\delta} & s_{23}c_{13} \\ s_{12}s_{23} - c_{12}c_{23}s_{13}e^{i\delta} & -c_{12}s_{23} - s_{12}c_{23}s_{13}e^{i\delta} & c_{23}c_{13} \end{pmatrix},$$

where $c_{ij} \equiv \cos\theta_{ij}$, $s_{ij} \equiv \sin\theta_{ij}$, θ_{ij} are the mixing angles, δ and $\ell_{1,2}$ are, respectively, the Dirac and Majorana CP-violating phases.

So here is what we know today:

V_{fit}	Normal Ordering (best fit)		Inverted Ordering ($\Delta\chi^2 = 7.0$)	
	bfp $\pm 1\sigma$	3σ range	bfp $\pm 1\sigma$	3σ range
$\sin^2\theta_{12}$	$0.304^{+0.012}_{-0.012}$	$0.269 \to 0.343$	$0.304^{+0.013}_{-0.012}$	$0.269 \to 0.343$
$\theta_{12}/°$	$33.45^{+0.77}_{-0.75}$	$31.27 \to 35.87$	$33.45^{+0.78}_{-0.75}$	$31.27 \to 35.87$
$\sin^2\theta_{23}$	$0.450^{+0.019}_{-0.016}$	$0.408 \to 0.603$	$0.570^{+0.016}_{-0.022}$	$0.410 \to 0.613$
$\theta_{23}/°$	$42.1^{+1.1}_{-0.9}$	$39.7 \to 50.9$	$49.0^{+0.9}_{-1.3}$	$39.8 \to 51.6$
$\sin^2\theta_{13}$	$0.02246^{+0.00062}_{-0.00062}$	$0.02060 \to 0.02435$	$0.02241^{+0.00074}_{-0.00062}$	$0.02055 \to 0.02457$
$\theta_{13}/°$	$8.62^{+0.12}_{-0.12}$	$8.25 \to 8.98$	$8.61^{+0.14}_{-0.12}$	$8.24 \to 9.02$
$\delta_{\mathrm{CP}}/°$	230^{+36}_{-25}	$144 \to 350$	278^{+22}_{-30}	$194 \to 345$
$\dfrac{\Delta m_{21}^2}{10^{-5}\ \mathrm{eV}^2}$	$7.42^{+0.21}_{-0.20}$	$6.82 \to 8.04$	$7.42^{+0.21}_{-0.20}$	$6.82 \to 8.04$
$\dfrac{\Delta m_{3\ell}^2}{10^{-3}\ \mathrm{eV}^2}$	$+2.510^{+0.027}_{-0.027}$	$+2.430 \to +2.593$	$-2.490^{+0.026}_{-0.028}$	$-2.574 \to -2.410$

(left margin label: With SK atmospheric data)

Three-flavor oscillation parameters from a recent fit to global data ("NuFIT 5.1") performed by the NuFIT team. Note that $\Delta m_{3\ell}^2 \equiv \Delta m_{31}^2 > 0$ for NO and $\Delta m_{3\ell}^2 \equiv \Delta m_{32}^2 < 0$ for IO.

[See I. Esteban *et al.* (The NuFIT team), "The fate of hints: updated global analysis of three-flavor neutrino oscillations," JHEP09(2020)178, arXiv:2007.14792 [hep-ph]. Present update (October 2021) is from ⟨ http://www.nu-fit.org/ ⟩.]

List of data used in the NuFIT 5.1 analysis (October 2021)

Solar experiments:

Homestake chlorine total rate (1 dp), Gallex & GNO total rates (2 dp), SAGE total rate (1 dp), SK-I full energy and zenith spectrum (44 dp), SK-II full energy and day/night spectrum (33 dp), SK-III full energy and day/night spectrum (42 dp), SK-IV 2970-day day-night asymmetry and energy spectrum (24 dp), SNO combined analysis (7 dp), Borexino Phase-I 741-day low-energy data (33 dp), Borexino Phase-I 246-day high-energy data (6 dp), Borexino Phase-II 408-day low-energy data (42 dp).

Atmospheric experiments:

IceCube/DeepCore 3-year data (64 dp), SK-I–IV 364.8 kiloton years + χ^2 map.

Reactor experiments:

KamLAND separate DS1, DS2, DS3 spectra with Daya-Bay reactor $\overline{\nu}_e$ fluxes (69 dp), Double-Chooz FD/ND spectral ratio, with 1276-day (FD), 587-day (ND) exposures (26 dp), Daya-Bay 1958-day EH2/EH1 and EH3/EH1 spectral ratios (52 dp), RENO 2908-day FD/ND spectral ratio (45 dp).

Accelerator experiments:

MINOS 10.71 PoT$_{20}$ ν_μ-disappearance data (39 dp), MINOS 3.36 PoT$_{20}$ $\overline{\nu}_\mu$-disappearance data (14 dp), MINOS 10.60 PoT$_{20}$ ν_e-appearance data (5 dp), MINOS 3.30 PoT$_{20}$ $\overline{\nu}_e$-appearance (5 dp), T2K 19.7 PoT$_{20}$ ν_μ-disappearance data (35 dp), T2K 19.7 PoT$_{20}$ ν_e-appearance data (23 dp for the CCQE and 16 dp for CC1π samples), T2K 16.3 PoT$_{20}$ $\overline{\nu}_\mu$-disappearance data (35 dp), T2K 16.3 PoT$_{20}$ $\overline{\nu}_e$-appearance data (23 dp), NOvA 13.6 PoT$_{20}$ ν_μ-disappearance data (76 dp), NOvA 13.6 PoT$_{20}$ ν_e-appearance data (13 dp), NOvA 12.5 PoT$_{20}$ $\overline{\nu}_\mu$-disappearance data (76 dp), NOvA 12.5 PoT$_{20}$ $\overline{\nu}_e$-appearance data (13 dp).

Here dp = data point(s), PoT$_{20}$ = 10^{20} PoT (Protons on Target), and EH = Experiment Hall.

Neutrino oscillation parameter plot.

The regions of neutrino squared-mass splitting

$$\Delta m^2 = \left|\Delta m_{ij}^2\right| = \left|m_j^2 - m_i^2\right|$$

and $\tan^2\theta$ (where θ is one of the mixing angles θ_{ij} corresponding to a particular experiment) favored or excluded by various experiments. Contributed to RPP-2018[a] by Hitoshi Murayama (University of California, Berkeley).
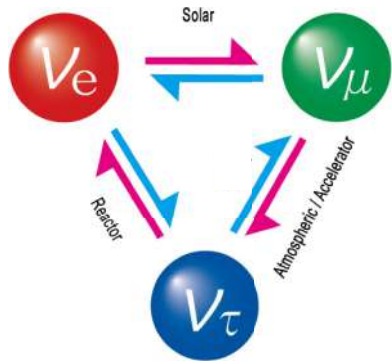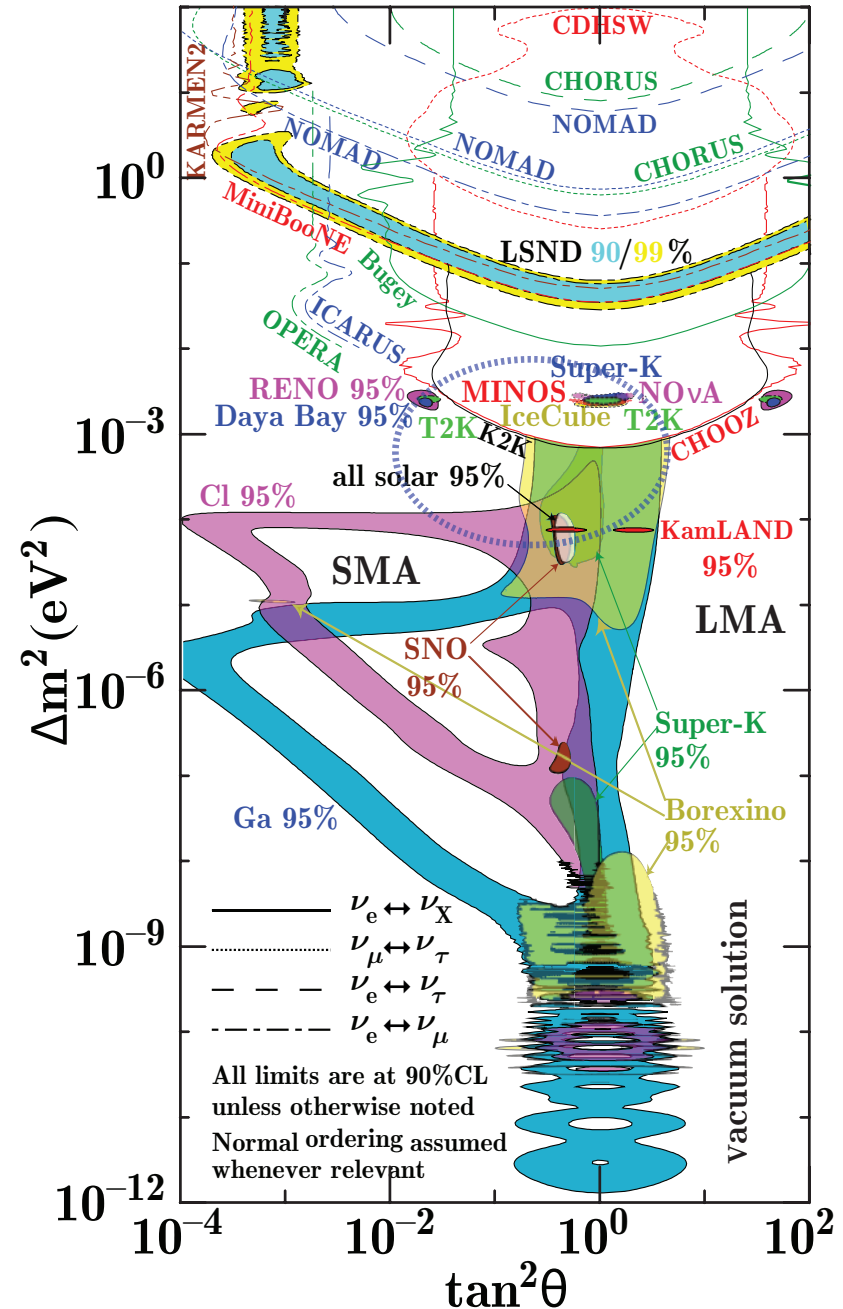

Figure includes the most rigorous results from before 2018, but data from many earlier experiments (e.g., BUST, NUSEX, Fréjus, IMB, Kamiokande, MACRO, SOUDAN 2) are ignored.

[a]M. Tanabashi *et al.* (Particle Data Group), "Review of Particle Physics", Phys. Rev. D **98** (2018) 030001.

In the absence of CP violation, the mixing angles may be represented as Euler angles relating the flavor eigenstates to the mass eigenstates. ▷

According to the NuFIT analysis (p. 7), the best-fit mixing angles and δ for the normal mass ordering (a bit preferred) are:

	PNMS	CKM
$\theta_{12}/°$	$33.45^{+0.77}_{-0.75}$	13.04 ± 0.05
$\theta_{23}/°$	$42.1^{+1.1}_{-0.9}$	2.38 ± 0.06
$\theta_{13}/°$	$8.62^{+0.12}_{-0.12}$	0.201 ± 0.011
$\delta°$	230^{+36}_{-25}	68.8 ± 4.5

The CKM angles and CP phase are also shown for comparison.

It should be stressed that the neutrino mass spectrum is still undetermined. ▷

Flavor content of mass states and mass content of flavor states is the same for Dirac ν and $\overline{\nu}$ (CP phase δ only changes the sign for $\overline{\nu}$) and for Majorana left/right νs ($\left|V^{\mathsf{D}}_{\alpha i}\right| = \left|V^{\mathsf{M}}_{\alpha i}\right|$).
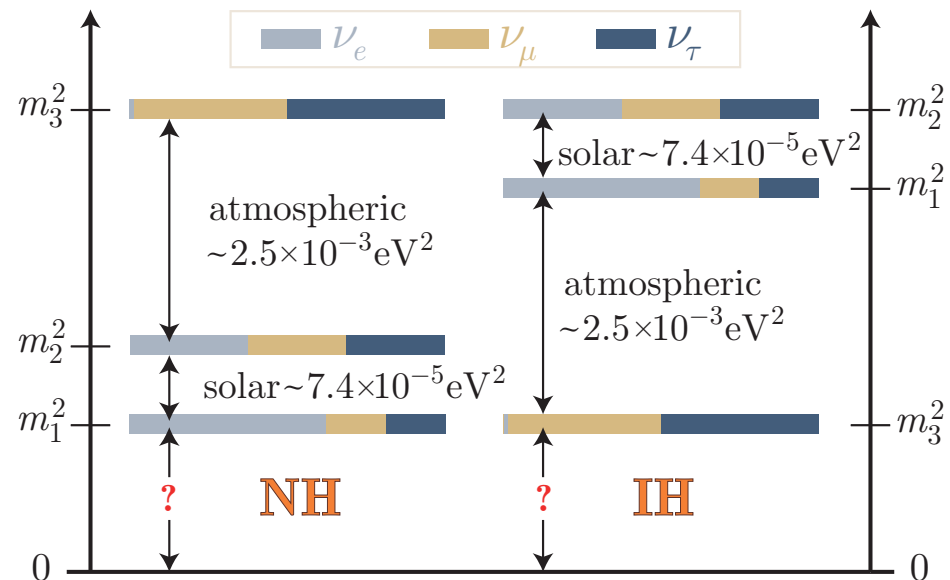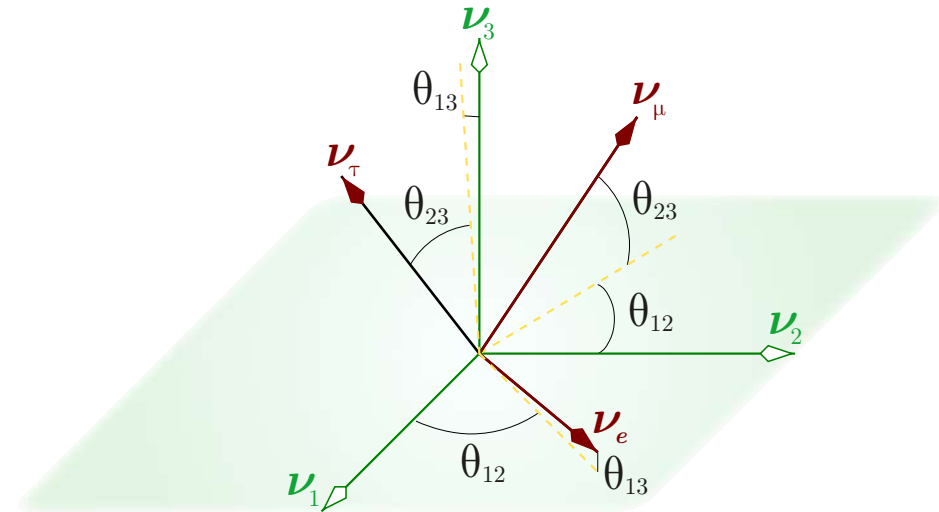
Flavor content of mass states and mass content of flavor states.

$$\left(\,|V_{\alpha i}|^2\,\right)_{\mathsf{NH}} = \begin{pmatrix} 0.681 & 0.297 & 0.0225 \\ 0.130 & 0.430 & 0.439 \\ 0.189 & 0.273 & 0.538 \end{pmatrix}, \quad \left(\,|V_{\alpha i}|^2\,\right)_{\mathsf{IH}} = \begin{pmatrix} 0.681 & 0.297 & 0.0224 \\ 0.149 & 0.294 & 0.557 \\ 0.170 & 0.409 & 0.421 \end{pmatrix}.$$
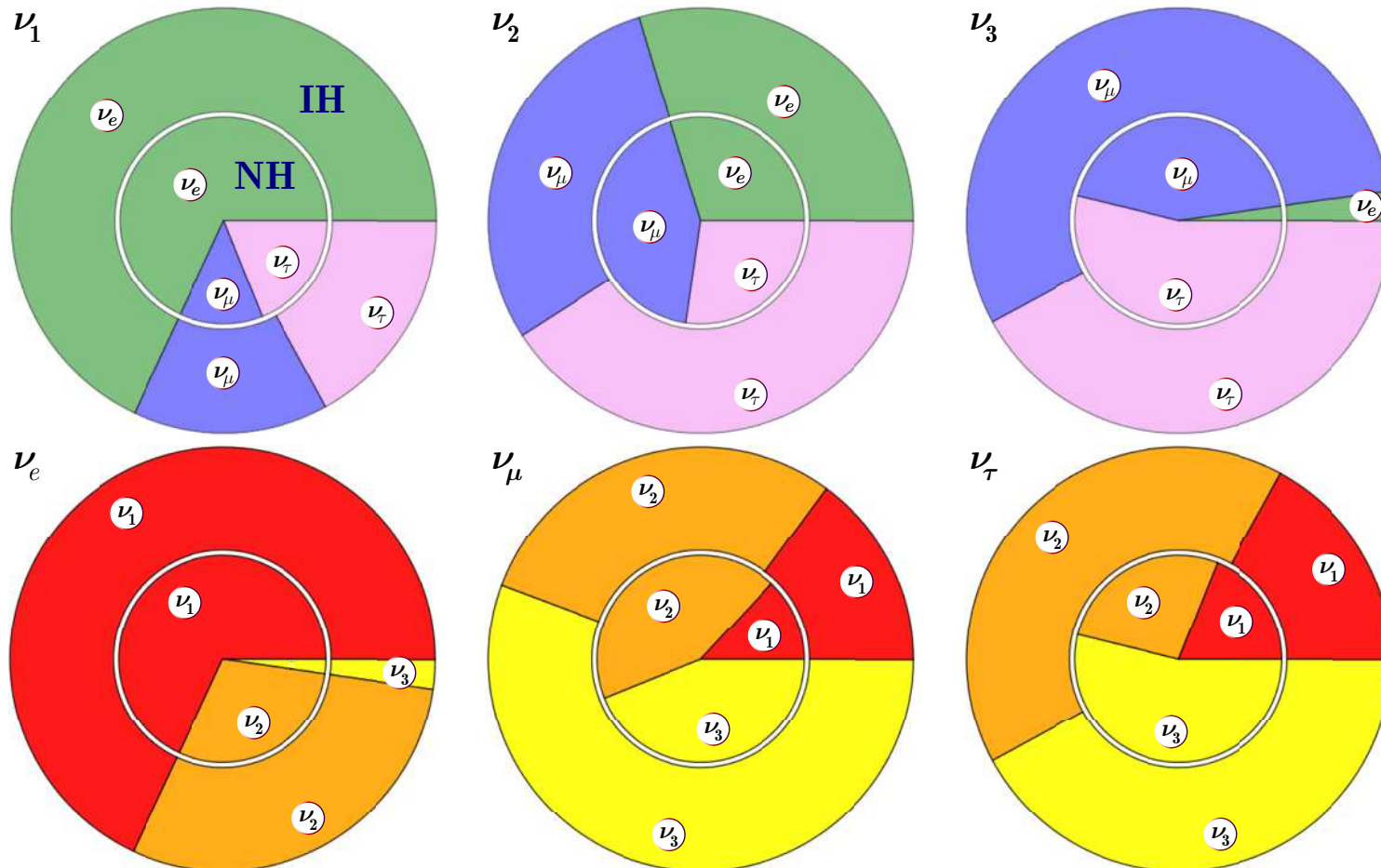
Current status of the neutrino masses from oscillation experiments.

So, NuFIT 5.1 provides the following constraints for the mass squared splittings:

$$m_2^2 - m_1^2 = 7.42^{+0.21}_{-0.20} \times 10^{-5} \text{ eV}^2 \quad \text{("solar" for NH and IH)}$$
$$m_3^2 - m_1^2 = 2.51^{+0.027}_{-0.027} \times 10^{-3} \text{ eV}^2 \quad \text{("atmospheric" for NH)} \tag{1}$$
$$m_2^2 - m_3^2 = 2.49^{+0.026}_{-0.028} \times 10^{-3} \text{ eV}^2 \quad \text{("atmospheric" for IH)}$$

These result imply that at least two of the neutrino eigenfields have nonzero masses

$$\Downarrow$$

there are (at least) two very different possible scenarios related to the mass ordering:
$$m_1 \ll m_2 < m_3 \quad \text{(normal hierarchy)} \quad \text{or} \quad m_3 \ll m_1 < m_2 \quad \text{(inverted hierarchy)}.$$

The data on mass squared splittings (1) give the following estimates (henceforth $\sum m_\nu \equiv \sum_{i=1}^{3} m_i$):
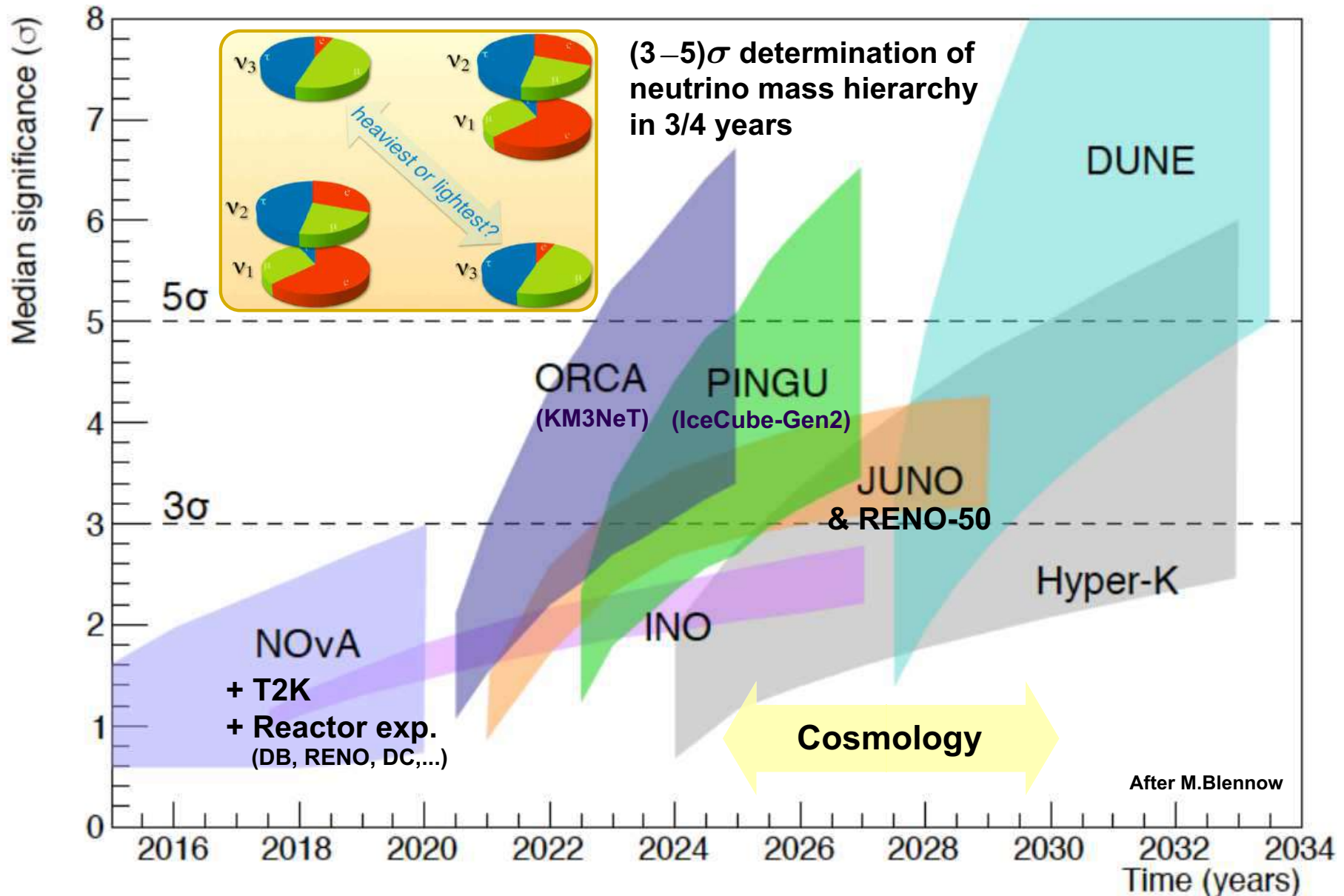
$$\begin{cases} m_2 = (8.61 \pm 0.122) \times 10^{-3} \text{ eV}, \\ m_3 = (5.01 \pm 0.027) \times 10^{-2} \text{ eV}, \end{cases} \implies \sum m_\nu \geq m_2 + m_3 = 0.0587 \pm 0.0003 \text{ eV (for NH)} \tag{2}$$

$$\begin{cases} m_2 = (4.99 \pm 0.028) \times 10^{-2} \text{ eV}, \\ m_1 = (4.92 \pm 0.029) \times 10^{-2} \text{ eV}, \end{cases} \implies \sum m_\nu \geq m_1 + m_1 = 0.0983 \pm 0.0006 \text{ eV (for IH)} \tag{3}$$

Therefore, the lower bounds on $\sum m_\nu$ at 1σ C.L. are:

$$\sum m_\nu^{\text{NH}} > 0.0584 \text{ eV} \quad \text{and} \quad \sum m_\nu^{\text{IH}} > 0.0977 \text{ eV}.$$

Note: Current accelerator and reactor data favor the NH scenario, but the question is not yet closed.

A summary of sensitivities to the neutrino mass hierarchy for various experimental approaches, with timescales, as claimed by the proponents in each case. Widths indicate main expected uncertainty.

Open problems in neutrino physics.

- Are neutrinos Dirac or Majorana fermions?
- What is the absolute mass scale of (known) neutrinos?
  Why neutrino masses are so small? [Does any version of see-saw work?]
  What is the neutrino mass spectrum? [$\text{sign}(\Delta m_{32}^2) \iff$ NH or IH.]
  Can the lightest neutrinos be massless fermions? [Not quasiparticles in Weyl semimetals!]
- Why neutrino mixing is so different from quark mixing?
  ~~What physics is responsible for the octant degeneracy? [sign(θ_{23} − 45°).]~~
- What are the source and scale of CP/T violation in the neutrino sector?
  How many CP violating phases are there?
- Is CPT conserved in the neutrino sector?
- How many neutrino flavors are there?

$$\left[\mathbf{V}_{\text{PMNS}} \approx \begin{pmatrix} 1/\sqrt{2} & -1/\sqrt{2} & e^{i\delta}/7 \\ 1/2 & 1/2 & -1/\sqrt{2} \\ 1/2 & 1/2 & 1/\sqrt{2} \end{pmatrix} \right]$$

- Whether the number of neutrinos with definite masses is equal to or greater than the number of flavor neutrinos? In other words, do sterile neutrinos exist? [a] If so,
  - What is their mass spectrum?
  - Do they mix with active neutrinos?
  - Do light (heavy) sterile neutrinos constitute hot (cold) dark matter?
- Are (all) neutrinos stable particles?

---

[a] Hints from LSND+MiniBooNE, Neutrino-4, SAGE+GALLEX+BEST are in tension with many other data.

Neutrinos on Earth and in the Heavens

radio/microwave | infrared/optical | x-rays | gamma-rays | neutrinos | cosmic-rays

By IceCube Collaboration

https://astronomy.com/sitefiles/resources/image.aspx?item={8FF61E76-1A93-4E02-A2BD-C990F1ED4FF8}

Distance [Mpc]

10^4

10^3 — cosmological max of star formation

10^2 — nearest blazar

10^1

10^0 — nearest galaxy

10^{-1}

10^{-2} — galactic centre

10^{-3}

10^{-6} 10^{-4} 10^{-2} 10^0 10^2 10^4 10^6 10^8 10^{10} 10^{12} 10^{14} 10^{16} 10^{18} 10^{20}

Energy [eV]

opaque to photons; transparent to neutrinos and gravitational waves
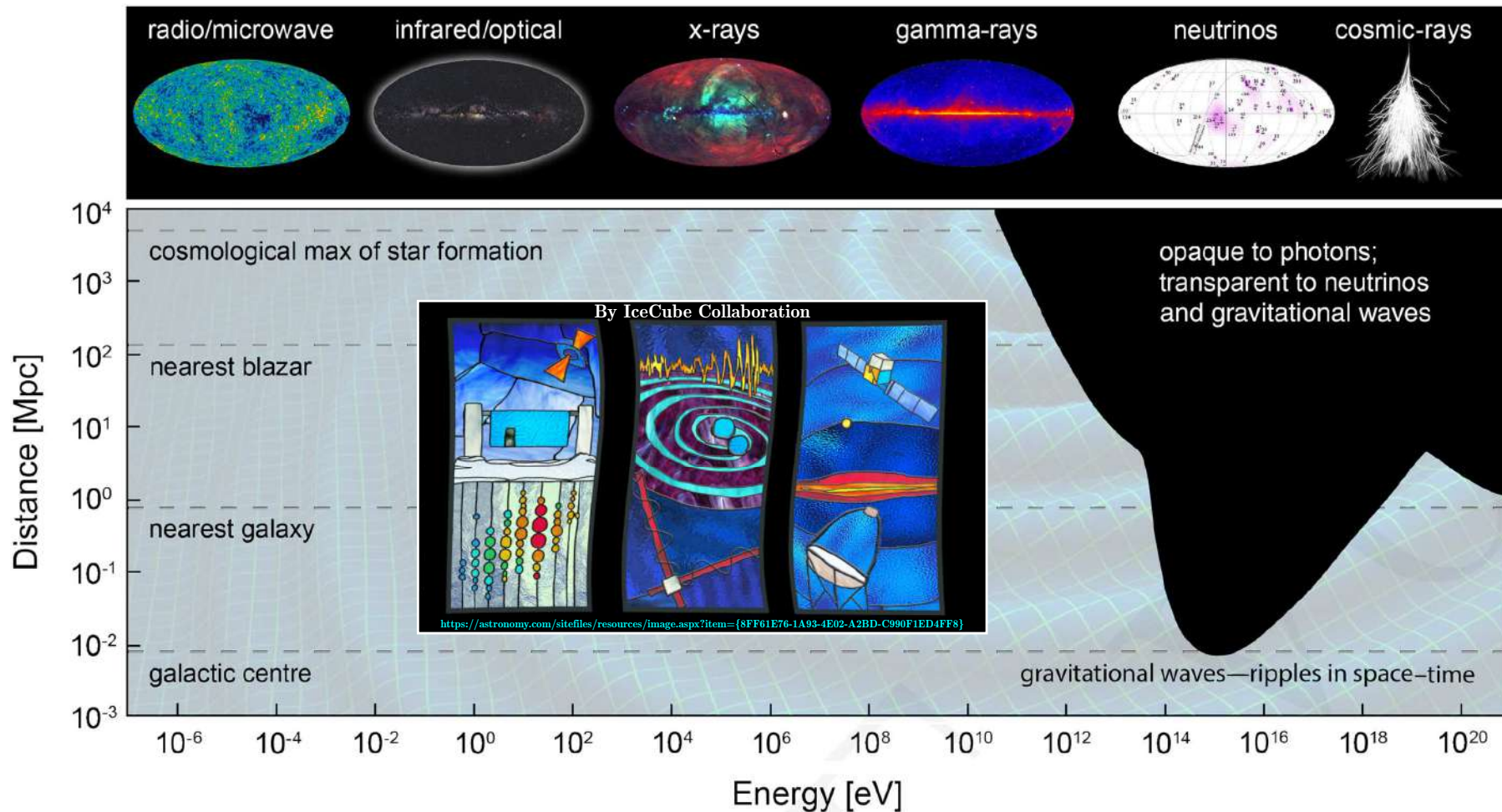
gravitational waves—ripples in space–time

Figure shows the distance horizon at which the Universe becomes optically thick to electromagnetic radiation. While lower-energy photons can travel to us from the farthest corners of the Universe, the highest energy photons and cosmic rays are attenuated after short distances, obscuring our view of the most energetic cosmic events. In contrast, the Universe is transparent to gravitational waves and neutrinos, making them suitable probes of the high-energy sky.

[From I. Bartos & M. Kowalski, "Multimessenger Astronomy" (Physics World Discovery, IoP Publishing, Bristol, 2017).]

Preview of local $\nu/\overline{\nu}$ flows in crude curves
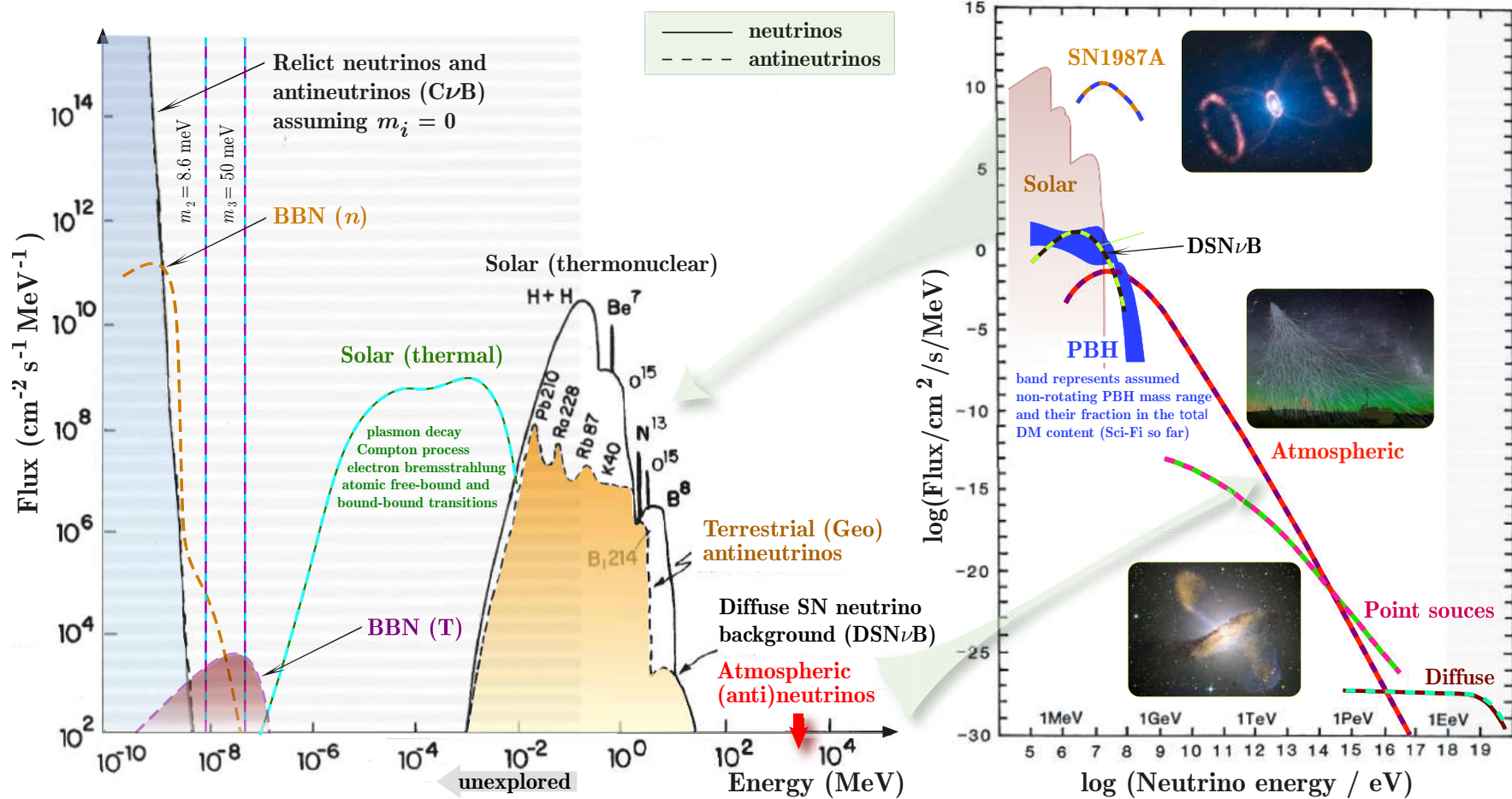
[Constructed from the data of L. M. Krauss *et al.*, "Antineutrino astronomy and geophysics", Nature **310** (1984) 191–198 and E. Vitagliano *et al.*, "Grand unified neutrino spectrum at Earth: Sources and spectral components," Rev. Mod. Phys. **92** (2020) 45006, arXiv:1910.11878 [astro-ph.HE] (*left panel*) and A. M. Bakich, "Aspects of neutrino astronomy", Space Sci. Rev. **49** (1989) 259–310 and R. Calabrese *et al.*, "Primordial black hole dark matter evaporating on the neutrino floor," Phys. Lett. B **829** (2022) 137050, arXiv:2106.02492 [hep-ph] (*right panel*).]

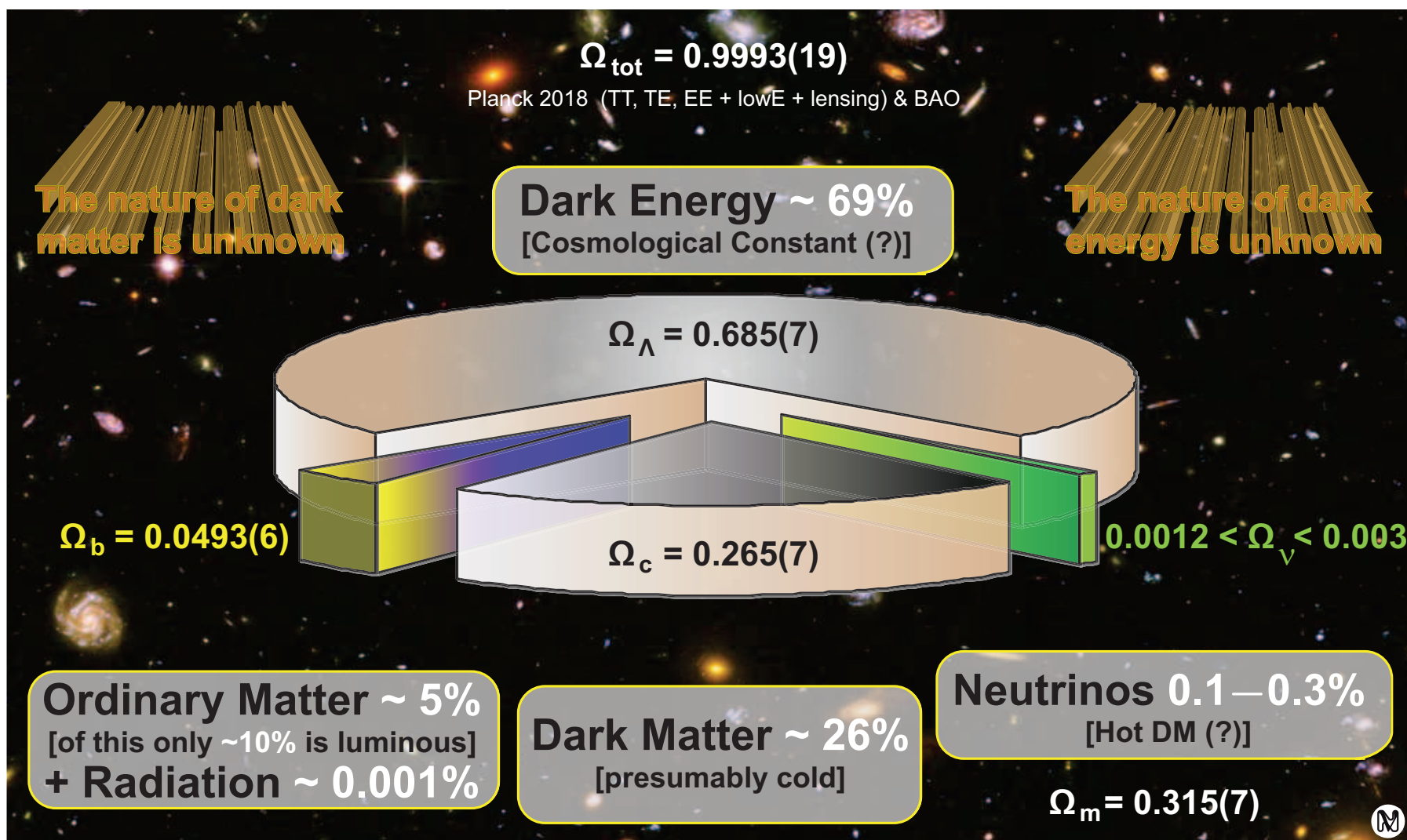**Modern collection of the dominant $\nu/\overline{\nu}$ fluxes ("Grand unified neutrino spectrum") on Earth.**
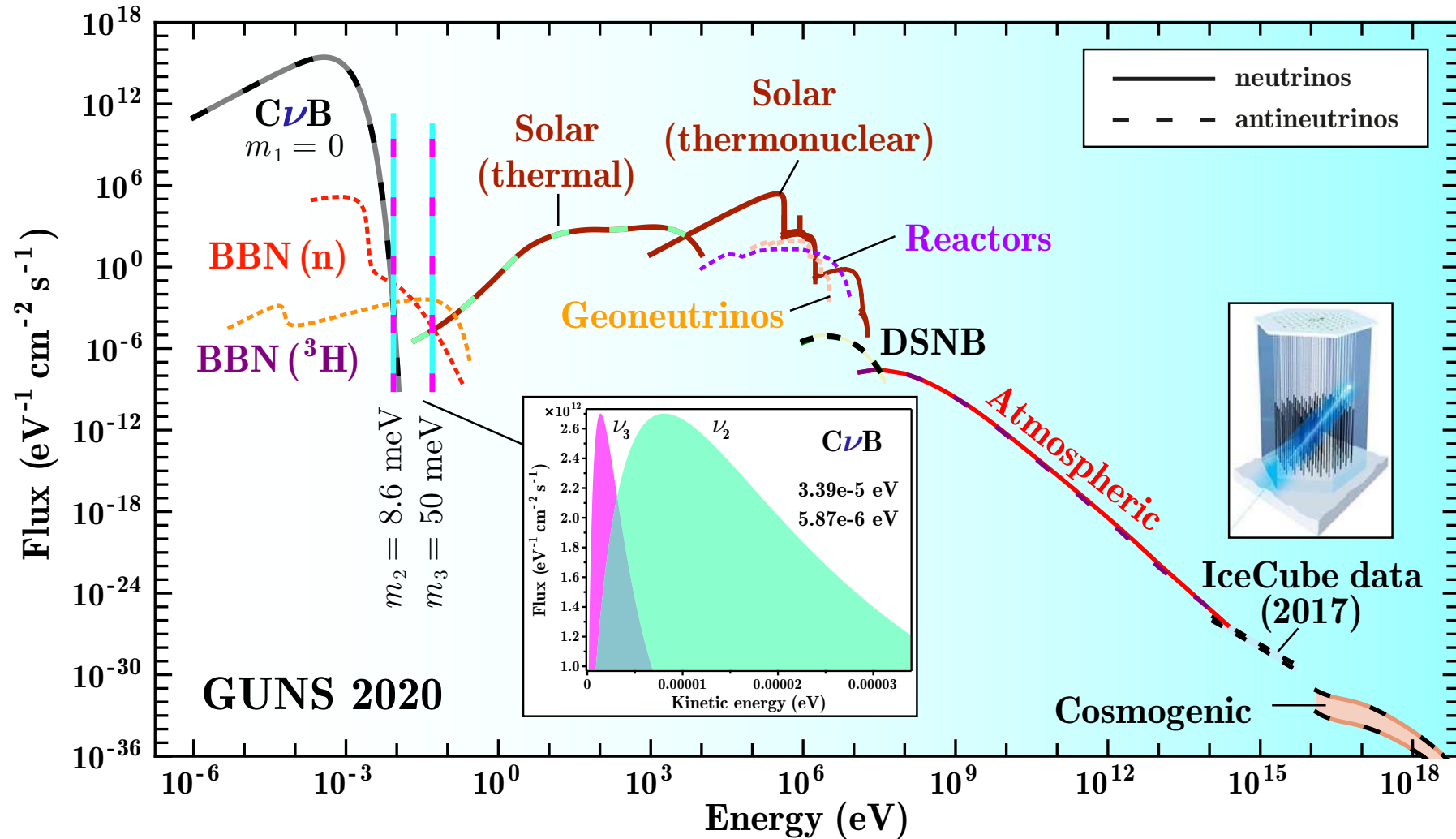
The continuous spectra are integrated over directions and summed over flavors $\Longrightarrow$ flavor conversion between source and detector does not affect the plot. "Monoenergetic" spectra are in cm^{-2}s^{-1}.

[Figure is adopted from E. Vitagliano *et al.*, (2020), see Ref. in p. 17.]

CνB.

Relict neutrinos (or Cosmic Neutrino Background, or CNB, or CνB) produce the largest neutrino flux on Earth, but compose only a very small fraction of invisible (non-luminous) matter in the Universe.

Ω_{tot} = 0.9993(19)

Planck 2018 (TT, TE, EE + lowE + lensing) & BAO

The nature of dark matter is unknown

Dark Energy ~ 69%
[Cosmological Constant (?)]

The nature of dark energy is unknown

Ω_{Λ} = 0.685(7)

Ω_b = 0.0493(6)

Ω_c = 0.265(7)

0.0012 < Ω_{ν} < 0.003

Ordinary Matter ~ 5%
[of this only ~10% is luminous]
+ Radiation ~ 0.001%

Dark Matter ~ 26%
[presumably cold]

Neutrinos 0.1−0.3%
[Hot DM (?)]

Ω_m = 0.315(7)

CMB as a probe of CνB.

It is not yet realistic to directly detect the νs created within the first second after the Big Bang, and which have too little energy now. However, for the first time, *Planck*, ESA's mission has unambiguously detected the effect CνB has on relic radiation maps. The quality of these maps is now such that the imprints left by dark matter and relic νs are clearly visible.[a]

---
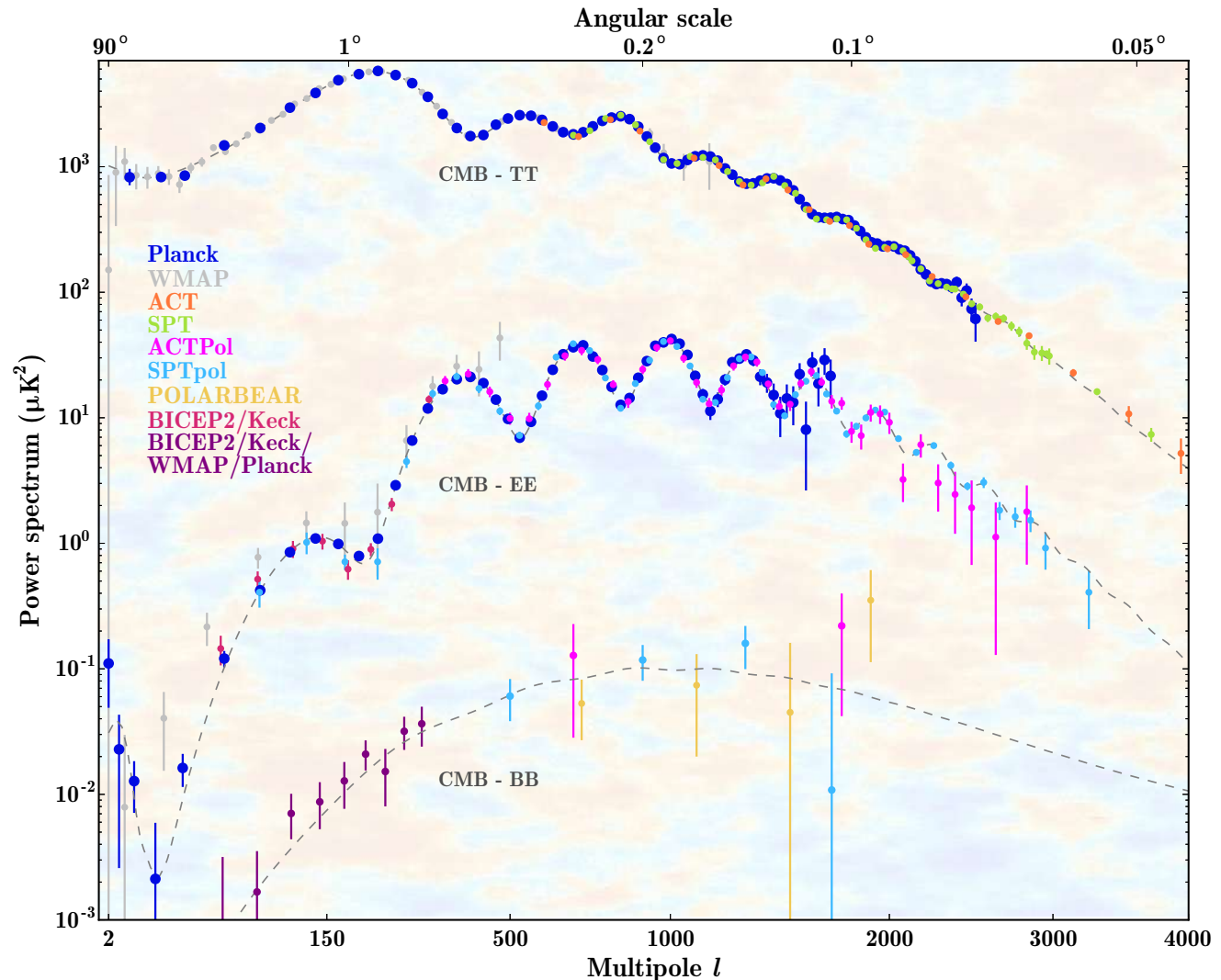
[a] See N. Aghanim *et al.* (*Planck* Collaboration), "Planck 2018 results. I. Overview and the cosmological legacy of Planck", Astron. Astrophys. **641** (2020) A1, arXiv:1807.06205 [astro-ph.CO]; "Planck 2018 results. VI. Cosmological parameters", Astron. Astrophys. **641** (2020) A6, arXiv:1807.06209 [astro-ph.CO].

The relic photon spectrum almost exactly follows the blackbody spectrum with temperature

$$T_0 = 2.7255 \pm 0.0006 \text{ K}.$$

After many decades of experimental and theoretical efforts, the CMB is known to be almost isotropic but having small temperature fluctuations (called CMB anisotropy) with amplitude
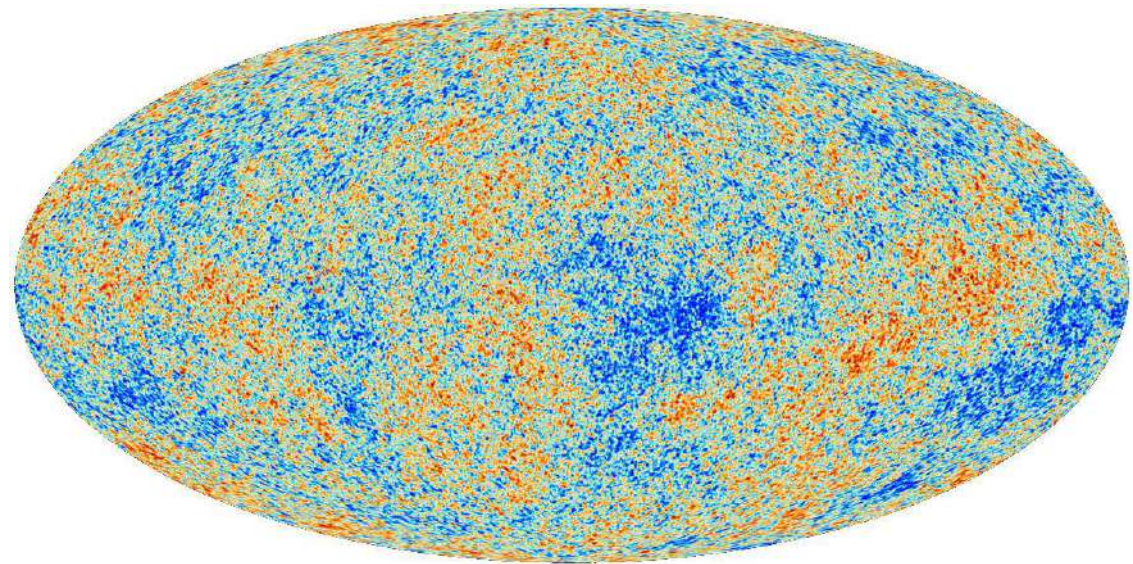
$$\delta T \sim \left(10^{-5} - 10^{-3}\right).$$

These fluctuations can be decomposed in a sum of spherical harmonics $Y_{lm}(\theta, \phi)$
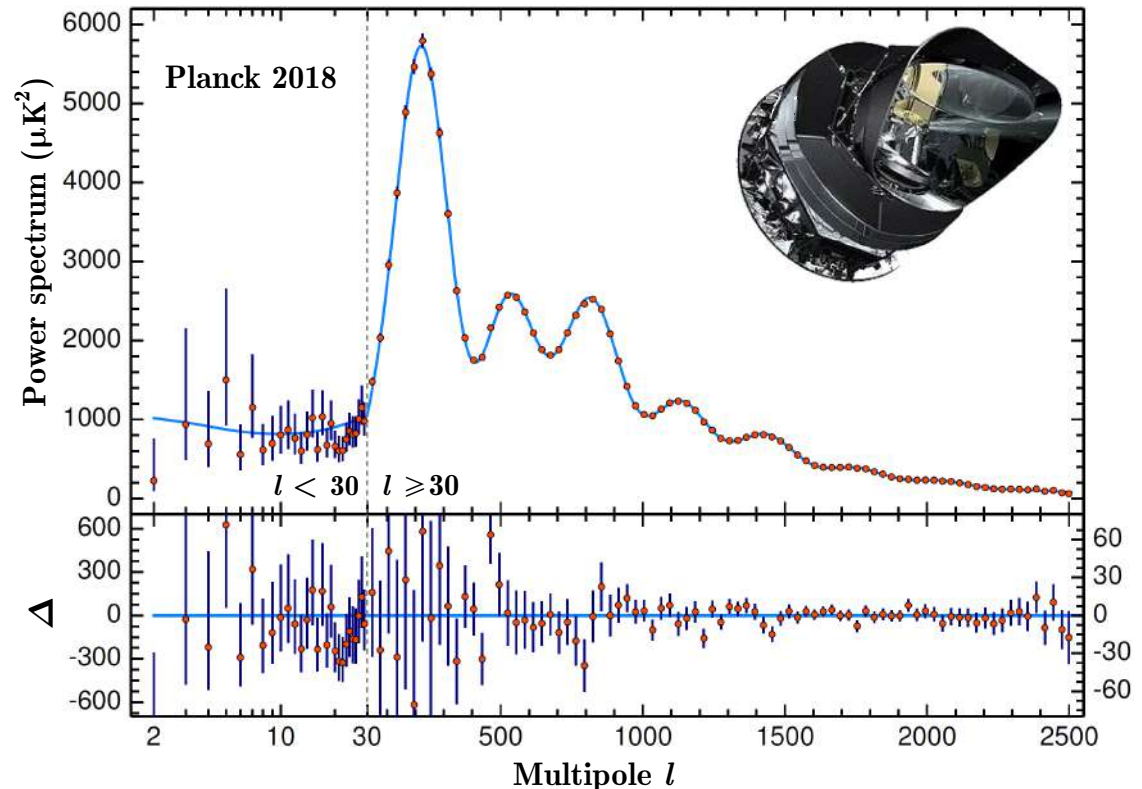
$$\delta T(\theta, \phi) = \sum_{l=1}^{\infty} \sum_{m=-l}^{l} a_{lm} Y_{lm}(\theta, \phi).$$

The averaged squared coefficients a_{lm} give the variance

$$C_l = \langle |a_{lm}|^2 \rangle = \frac{1}{2l+1} \sum_{m=-l}^{l} |a_{lm}|^2.$$

CMB maps can be compressed into the power spectrum

CνB temperature, number density, etc. (rough estimate).

1. Entropy density. In thermal equilibrium, the total entropy density, s, of a multicomponent ideal gas mixture of elementary particles is

$$s = \sum_i \frac{\rho_i + p_i}{k_B T_i},$$

$t \approx 10^{-12} - 10^{-6}$ s $\qquad\qquad\qquad\qquad\qquad\qquad\qquad\qquad t \gtrsim 10^{-6}$ s

$i \in \left\{ q,\, \overline{q},\, \ell^\pm,\, \nu_\ell,\, \overline{\nu}_\ell,\, \gamma,\, W^\pm,\, Z,\, H,\, g,\, \text{God knows what else} \right\}$ or $i \in \left\{ p,\, n,\, e^\pm,\, \nu_\ell,\, \overline{\nu}_\ell,\, \gamma \ldots \right\}$,

where ρ_i, p_i, and T_i are, respectively, the equilibrium energy density, pressure, and temperature of particles of type i, and k_B is the Boltzmann constant (hereafter we simply denote $k_B T_i = T_i$). The energy density for bosons (sign $-$) and fermions (sign $+$) is given by

$$\rho_i = \frac{g_i}{(2\pi)^3} \int_0^\infty \frac{E_i d\mathbf{k}}{\exp\left[(E_i - \mu_i)/T_i\right] \mp 1} = \frac{g_i}{2\pi^2} \int_0^\infty \frac{E_i k^2 dk}{\exp\left[(E_i - \mu_i)/T_i\right] \mp 1},$$

where g_i, $E_i = \sqrt{k^2 + m_i}$, m_i, and μ_i are, respectively, the number of the internal degrees of freedom, energy, mass, and chemical potential of the ith gas component; $k = |\mathbf{k}|$, $d\mathbf{k} = d^3 k$.

$\bullet$ We'll consider a very early and hot Universe, when all particles are ultrarelativistic ($T_i \gg m_i$).
$\bullet$ Since the L and B asymmetries are $\sim 10^{-9}$, the chemical potentials are negligibly small. Then

$$\rho_i = \frac{g_i T_i^4}{2\pi^2} \int_0^\infty \frac{x^3 dx}{e^x \mp 1} = \frac{\pi^2}{30} \hat{g}_i T_i^4, \quad \hat{g}_i = \begin{cases} g_i & \text{for bosons,} \\ \dfrac{7}{8} g_i & \text{for fermions.} \end{cases}$$

The well-known formulas are used here:

$$\int_0^\infty \frac{x^n dx}{e^x - 1} = \Gamma(n+1)\zeta(n+1), \quad \int_0^\infty \frac{x^n dx}{e^x + 1} = \Gamma(n+1)\zeta(n+1)\left(1 - \frac{1}{2^n}\right).$$

Now, by using the equations of state $3p_i = \rho_i$ valid for ultrarelativistic particles, we obtain

$$s = \frac{4}{3} \sum_i \frac{\rho_i}{T_i} = \frac{2}{45} \pi^2 g_* T^3, \quad \text{where} \quad g_* = g_*^{\text{th}} + g_*^{\text{dec}}, \quad T = T_\gamma,$$

where we introduced the effective numbers of degrees of freedom (NDF) of particles which are in thermal equilibrium with γs (g_*^{th}) and those that are decoupled from equilibrium with γs (g_*^{dec}):

$$g_*^{\text{th}} = \sum_i \hat{g}_i \quad \text{and} \quad g_*^{\text{dec}} = \sum_i \hat{g}_i \left(\frac{T_i}{T} \right)^4.$$

i	$q\,\overline{q}, p, n, \ell^\pm$	$\nu_\ell, \overline{\nu}_\ell$	γ, g	$W^\pm, Z$	H
g_i	2	1	2	3	1

2. Homework: Calculate g_* for $T \gg m_t \approx 173$ GeV and for $T = 1 - 100$ MeV.

3. Freeze-out temperature. At energies $E_\nu \sim T \sim 2 - 3$ MeV, ν and $\overline{\nu}$ cannot produce particles heavier than $e^\pm$, but can scatter on each other or on $e^\pm$ and participate in the reactions $e^+ e^- \leftrightarrow \nu\overline{\nu}$. The cross sections of all these processes are of the same order:

$$\sigma_\nu \sim G_F^2 E_\nu^2 \sim G_F^2 T^2$$

($G_F \simeq 1.17 \times 10^{-5}$ GeV^{-2} is the Fermi constant). The mean free path ($=$ time between collisions) is

$$\tau_\nu = \langle n \sigma_\nu v_{\text{rel}} \rangle^{-1},$$

where n is the equilibrium number density of the initial particle,

$$n = \frac{g}{2\pi^2} \int_0^\infty \frac{k^2 dk}{\exp\left(k/T\right) + 1} = \frac{3}{4} g \frac{\zeta(3)}{\pi^2} T^3,$$

and $v_{\text{rel}} \simeq 1$ is the relative velocity of the colliding particle. Therefore, $\tau_\nu \sim 1/\left(G_F^2 T^5\right)$ and the number of collisions that occurred after the time t can (very approximately) be estimated as follows

$$N_{\text{coll}} = \int_t^\infty \frac{dt'}{\tau_\nu(t')} \sim \frac{t}{\tau_\nu(t)} \sim \frac{1}{H(t)\tau_\nu(t)},$$

where $H(t) = T^2/M_P$ is the Hubble "constant" ($M_P = \sqrt{\hbar c/G} \simeq 2.18 \times 10^{-5}$ g $\simeq 1.22 \times 10^{19}$ GeV is the Planck mass and $G \simeq 6.674 \times 10^{-11}$ kg^{-1}m^{3}s^{-2} is the gravitational constant).
● Neutrinos are in thermal equilibrium at $N_{\text{coll}} \gg 1$ and are free streaming at $N_{\text{coll}} \ll 1$. Therefore, they decouple from matter ("freeze out") at $N_{\text{coll}} \sim 1$. Thus, the freeze-out temperature is determined solely by the fundamental constants:

$$T_\nu^{\text{freeze-out}} \sim \left(M_P G_F^2\right)^{-1/3} \sim 2 - 3 \text{ MeV}.$$

4. CνB temperature. Since the total entropies of γ, $e^\pm$, and $\nu/\overline{\nu}$ are separately conserved with good precision during the period of photons' decoupling from the matter and their heating due to $e^+ e^-$ annihilation,

$$g_*(aT)^3\big|_{\text{before}} = g_*(aT)^3\big|_{\text{after}}, \quad a = a(t) = (1+z)^{-1}$$

(a is the scale factor and z is the redshift). The effective NDF of γ and $e^\pm$ before and after the $e^+ e^-$ annihilation are $2 + (7/8)4 = 11$ and 2, respectively. Thus, neglecting a small residual reheating of neutrinos, non-equilibrium corrections, and so on, we have

$$T_\nu = \left(\frac{4}{11}\right)^{1/3} T_\gamma \approx 0.714\, T_\gamma$$

This relation remains the same today. Based on the present-day value from *Planck* 2018 one finds

$$T_{\text{CMB}} = 2.7255 \text{ K} \quad \Longrightarrow \quad T_\nu^0 \approx 1.945 \text{ K} \approx 0.168 \text{ meV}.$$

5. CνB particle density. For each neutrino mass eigenstate we get

$$n_\nu + n_{\overline{\nu}} = \frac{3}{2}\frac{\zeta(3)}{\pi^2}T_\nu^3 = \frac{6}{11}\frac{\zeta(3)}{\pi^2}T_\gamma^3 = \frac{3}{11}\,n_\gamma.$$

This relation remains the same today. Based on the present-day value from *Planck* 2018 one finds

$$n_{\mathsf{CMB}} \simeq 410.5 \text{ cm}^{-3} \implies n_{\nu+\overline{\nu}}^0 \simeq 112 \text{ cm}^{-3}.$$

For a more advanced approach (relativistic Boltzmann equations), see Appendix, pp. 90–97.

6. Number of effective neutrino species.

The radiation after $e^\pm$ disappears consists of γs and νs. Before some of νs become nonrelativistic, the radiation density is expressed as

$$\rho_{\mathsf{rad}} = \left[1 + N_{\mathsf{eff}}\frac{7}{8}\left(\frac{4}{11}\right)^{4/3}\right]\rho_\gamma, \tag{4}$$

where N_{eff}, the effective number of thermally excited NDFs, is just a way to parameterize ρ_{rad}.

The "canonical" number of effective neutrino species is slightly larger than 3:

$$N_{\mathsf{eff}} = \mathbf{3.045(1)} = \mathbf{3} + \mathbf{0.010} + \mathbf{0.035}$$

0.010 comes from plasma effects, reducing ρ_γ, and 0.035 comes from non-instant neutrino decoupling from hotter e^+e^- (providing the residual neutrino heating). Additional adjustments ($\sim 0.04 - 0.05$) come from QED radiative corrections and neutrino oscillation effects (with MSW and damping).

- ○ More generally, the number of effective neutrino species in cosmological plasma, N_{eff}, is defined as the ratio of the energy density of **all** relativistic particles, excluding CMB γs, normalized to the energy density of one type of massless equilibrium $\nu + \overline{\nu}$.
- ○ Recall the LEP+SLC result $N_\nu = 2.984 \pm 0.008$ obtained from $\sigma_{e^+e^-\to\mathsf{hadrons}}$ at $E_{\mathsf{cm}} \sim m_Z$.

Planck 2018: neutrino summary.
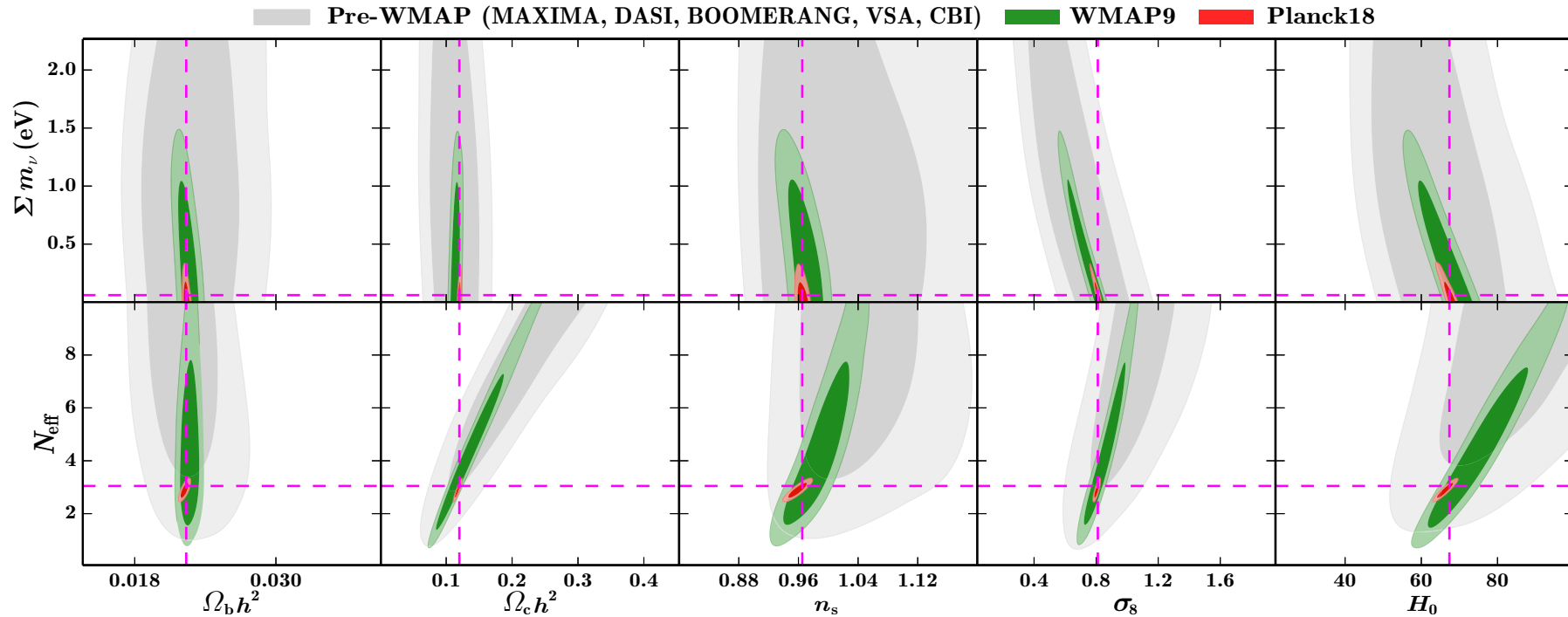
Successive reductions in the allowed parameter space for various one-parameter extensions to ΛCDM, from pre-WMAP to *Planck*. The contours display the 68 % and 95 % C.L. for the extra parameter vs. five other base-ΛCDM parameters. The dashed lines indicate the ΛCDM best-fit parameters or fixed default values of the extended parameters.

Fitted parameters:

$\Omega_b h^2$ – baryon density, $\Omega_c h^2$ – CDM density, H_0 – today's Hubble parameter,
n_s – spectral index of a power-law spectrum of adiabatic perturbations,
σ_8 – normalization of the (linear theory) matter power spectrum.

Finally *Planck* 2018 (+BAO) sets:

$$\sum m_\nu < 0.12 \text{ eV}, \quad N_{\text{eff}} = 2.99 \pm 0.17, \quad \Delta N_{\text{eff}} < 0.3.$$

Roughly speaking, this means that sterile neutrinos are not supported.

But(!) this constraint implies degenerate mass hierarchy (DH), $m_i = \sum m_\nu / 3$, and many other model assumptions. Results for other ν mass spectra have been obtained recently ($m_0 \equiv m_{\text{min}}$):[a]

		Base			Base+SNe		
		DH	NH	IH	DH	NH	IH
ΛCDM $+ \sum m_\nu$							
	ω_c	0.1194 ± 0.0009	0.1192 ± 0.0009	0.1191 ± 0.0009	0.1193 ± 0.0009	0.1191 ± 0.0009	0.1189 ± 0.0009
	ω_b	0.02242 ± 0.00013	$0.02242^{+0.00013}_{-0.00014}$	0.02243 ± 0.00013	0.02243 ± 0.00013	0.02244 ± 0.00013	0.02244 ± 0.00013
	Θ_s	1.04100 ± 0.00029	1.04100 ± 0.00029	1.04100 ± 0.00029	1.04102 ± 0.00029	1.04103 ± 0.00029	1.04103 ± 0.00029
	τ	$0.0554^{+0.0068}_{-0.0076}$	$0.0569^{+0.0066}_{-0.0076}$	$0.0585^{+0.0069}_{-0.0076}$	0.0556 ± 0.0071	$0.0573^{+0.0069}_{-0.0076}$	$0.0588^{+0.0068}_{-0.0077}$
	n_s	0.9666 ± 0.0036	0.9668 ± 0.0037	0.9671 ± 0.0037	0.9669 ± 0.0036	0.9673 ± 0.0036	0.9675 ± 0.0037
$\ln[10^{10} A_s]$		$3.048^{+0.014}_{-0.015}$	$3.051^{+0.014}_{-0.015}$	3.053 ± 0.015	3.046 ± 0.014	3.049 ± 0.014	$3.052^{+0.014}_{-0.015}$
	m_0 (eV)	< 0.040	< 0.040	< 0.042	< 0.038	< 0.038	< 0.039
	$\sum m_\nu$ (eV)	< 0.12	< 0.15	< 0.17	< 0.11	< 0.14	< 0.16
H_0 (km/s/Mpc)		$67.81^{+0.54}_{-0.46}$	$67.50^{+0.49}_{-0.44}$	67.22 ± 0.45	$67.89^{+0.52}_{-0.45}$	67.59 ± 0.44	67.33 ± 0.43
	σ_8	$0.814^{+0.010}_{-0.007}$	$0.806^{+0.009}_{-0.006}$	$0.799^{+0.008}_{-0.006}$	$0.815^{+0.010}_{-0.007}$	$0.806^{+0.008}_{-0.006}$	$0.799^{+0.008}_{-0.006}$
	S_8	0.827 ± 0.011	0.823 ± 0.011	0.820 ± 0.011	0.826 ± 0.011	0.822 ± 0.011	0.818 ± 0.011
$\Delta\chi^2 = \chi^2 - \chi^2_{IH}$		-2.89	-0.95	0	-2.73	-1.27	0

Let's recall the latest oscillation lower limits: $\sum m_\nu^{\text{NH}} \gtrsim 0.058$ eV and $\sum m_\nu^{\text{IH}} \gtrsim 0.098$ eV.

---

[a] Sh. R. Choudhury & S. Hannestad, "Updated results on neutrino mass and mass hierarchy from cosmology with Planck 2018 likelihoods," JCAP07(2020)037, arXiv:1907.12598 [astro-ph.CO].

Redshift z

Energy Density [eV/cm³] vs Scale Factor a

Photons (CMB)

Decoupling

CDM+Baryons

Neutrinos 10 %
Dark Matter 63%
Photons 15 %
Atoms 12 %
13.7 BILLION YEARS AGO
(Universe 380,000 years old)

Atoms 4.6%
Dark Energy 72%
Dark Matter 23%
TODAY

Λ **(Dark Energy)**

Neutrinos (CνB)
- - - - - - $\Sigma m_\nu = 0.50$ eV
- - - - $\Sigma m_\nu = 0.05$ eV
—— $\Sigma m_\nu = 0$ eV
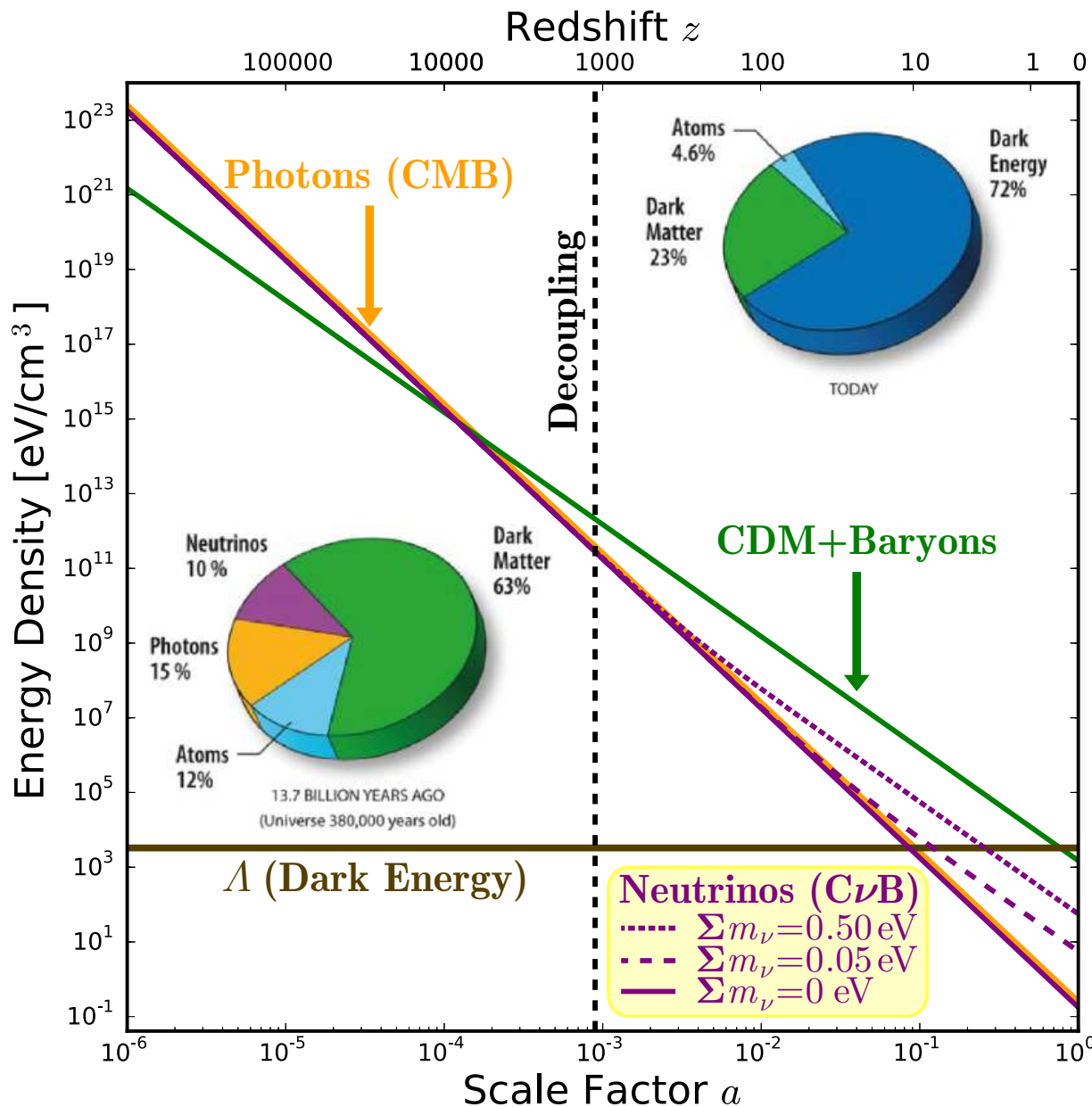
◁   Neutrinos were ultrarelativistic at the γ decoupling epoch ($z \sim 10^3$) and are a part of matter budget today ($z = 0$).

Reminder: The scale factor $a(t)$ is defined by

$$d(t) = a(t)d(t_0), \quad a(t_0) = 1,$$

where $d(t)$ is the proper distance at epoch t and $t_0 = 13.799 \pm 0.021$ Gyr is the present age of the Universe. From the geodesic equation for a light wave

$$ds^2 = \frac{a^2 dr^2}{1 - k^2 r^2} - dt^2 = 0$$

($c = 1$) it follows that

$$1 + z = \frac{\lambda_{\mathrm{obsv}}}{\lambda_{\mathrm{emit}}} = \frac{a(t_0)}{a(t)}.$$

[Figure is taken from J. Carlstrom (for the CMB-S4 collaboration), "CMB Stage 4 Update," AAAC January 28, 2016.]

~10^{-43} s

Gravitation Waves

~1 s

Massless Neutrinos

~10^5 yr

CMB photons
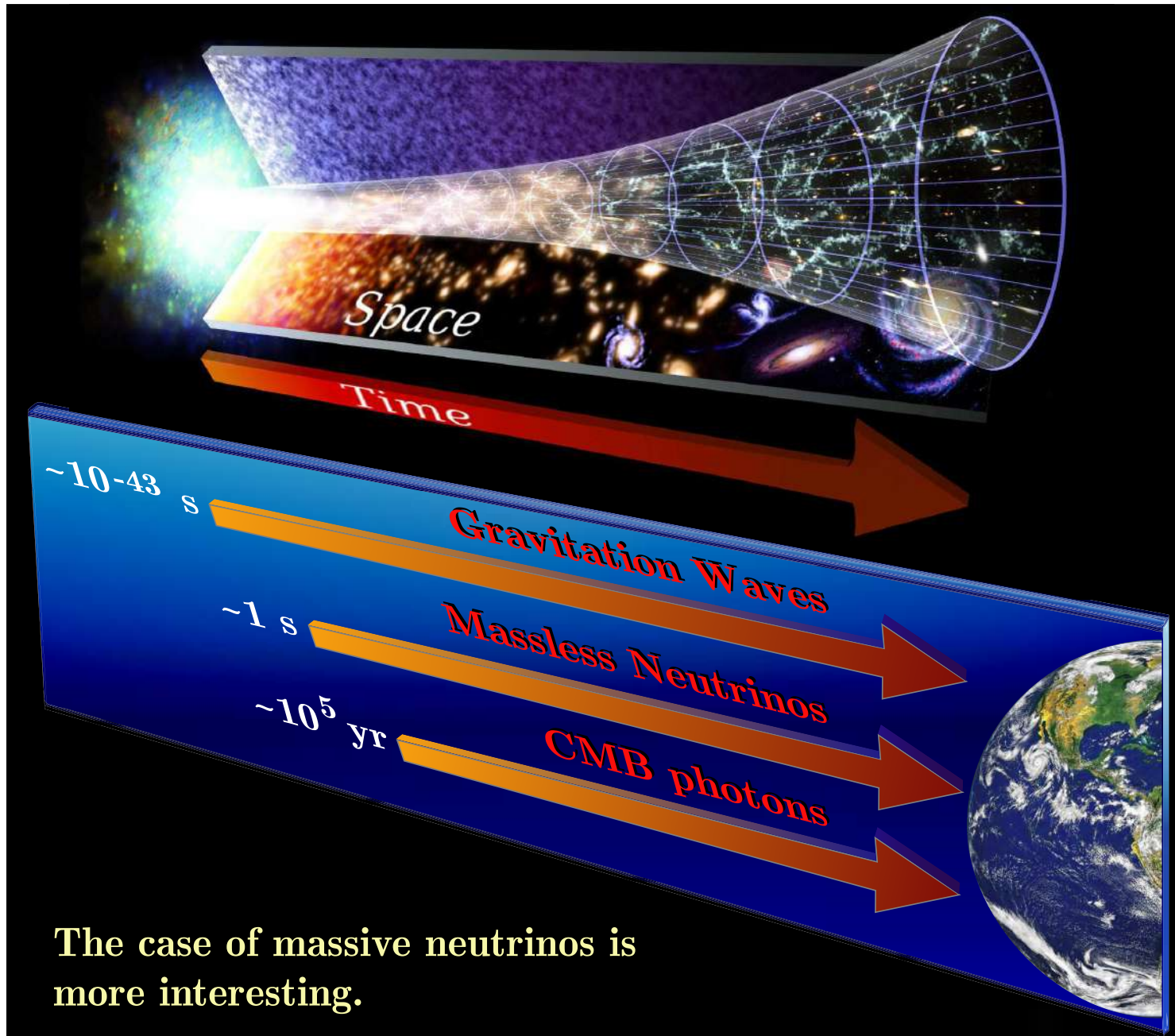
The case of massive neutrinos is more interesting.

Last scattering surface of neutrinos.

The geodesic equation for neutrinos with definite mass m_ν can be written as

$$v_\nu(t)dt = \pm \frac{adr}{\sqrt{1 - kr^2}},$$

where $v_\nu(t) = p_\nu(t)/E_\nu(t) = p_\nu(t)/\sqrt{p_\nu^2(t) + m_\nu^2}$ is the redshifted neutrino velocity. Massive neutrinos slow down once they become nonrelativistic, so the integral determining the distance to the last scattering surface (LSS) generalizes to[a]

$$\chi = \int_{t_i}^{t_0} \frac{v(t)dt}{a(t)} = \int_{t_i}^{t_0} \frac{dt}{a(t)} \frac{p_0/a(t)}{\sqrt{[p_0/a(t)]^2 + m_\nu^2}},$$

where p_0 is the current neutrino momentum. Massive neutrinos travel more slowly than massless ones so arrive here from much closer distances. The CνB temperature today is $T_\nu = 1.95 \times 10^{-4}$ eV, so there will be a range of p_0's drawn from a Fermi-Dirac distribution, each of which will be associated with a different distance to the LSS.

Figures in pp. 31 and 32 show, respectively, the comoving distance traveled by a massive neutrino since decoupling as a function of m_ν for two different values of p_0 and the probability that a neutrino with mass m_ν last scatters at a given comoving distance from us (the so-called visibility function; the definition is given in the legend to the Figure).

---

[a] For details, see G. S. Bisnovatyi-Kogan and Z. F. Seidov, Astron. Zh. **60** (1983) 220–222 [Sov. Astron. **27** (1983) 125-126]; G. S. Bisnovatyi-Kogan and Z. F. Seidov, Astrophys. Space Sci. **102** (1984) 131–154; S. Dodelson and M. Vesterinen, "Cosmic neutrino last scattering surface", Phys. Rev. Lett. **103** (2009) 171301, arXiv:0907.2887 [astro-ph.CO]; Erratum: *ibid.* **103** (2009) 249901.

$T_\nu = 1.95 \times 10^{-4}\,\mathrm{eV}$

CMB

$p_0 = 3\,T_\nu$

$p_0 = 0.5\,T_\nu$

Neutrino LSS for
$m_\nu \sim 0.001$ eV
$p_0 \sim 0.5\,T_\nu$

PRL **103** (2009) 171301

Distance to LSS (Mpc/h)

m_ν (eV)

$m_\nu = 1$ eV
$m_\nu = 0.05$ eV
$m_\nu = 0.0001$ eV
CMB

$$\frac{dP}{d\chi} = \frac{dP}{dp_0}\left(\frac{d\chi}{dp_0}\right)^{-1}$$

$$\frac{dP}{dp_0} = \frac{2}{3\zeta(3)\,T_\nu^3}\frac{p_0^2}{e^{p_0/T_\nu}+1}$$

$dP/d\ln\chi$ [Visibility Function]

100

10

1

0.1

1 eV

0.05 eV

Excluded

100   1000   10000

Distance to LSS (Mpc/h)
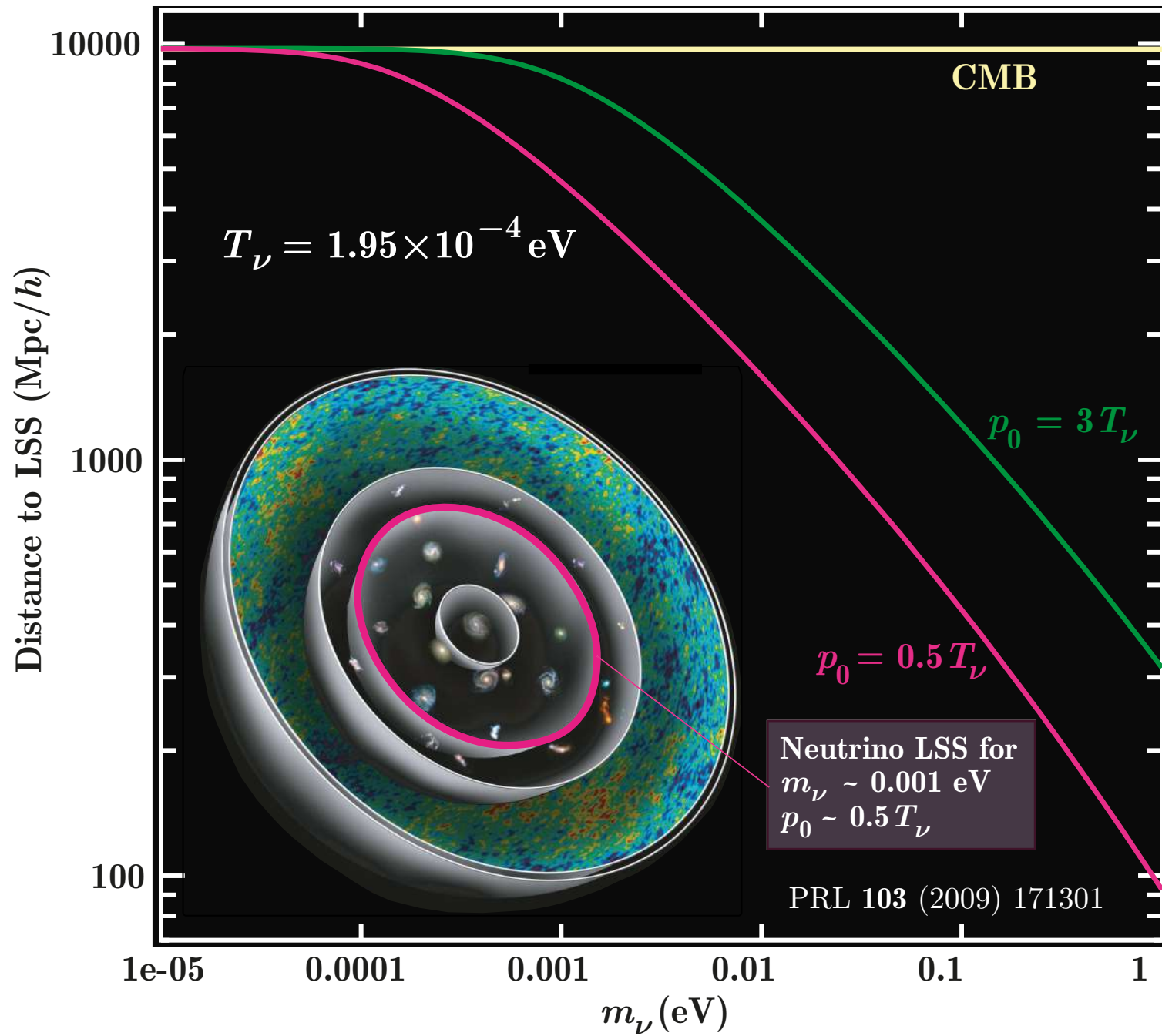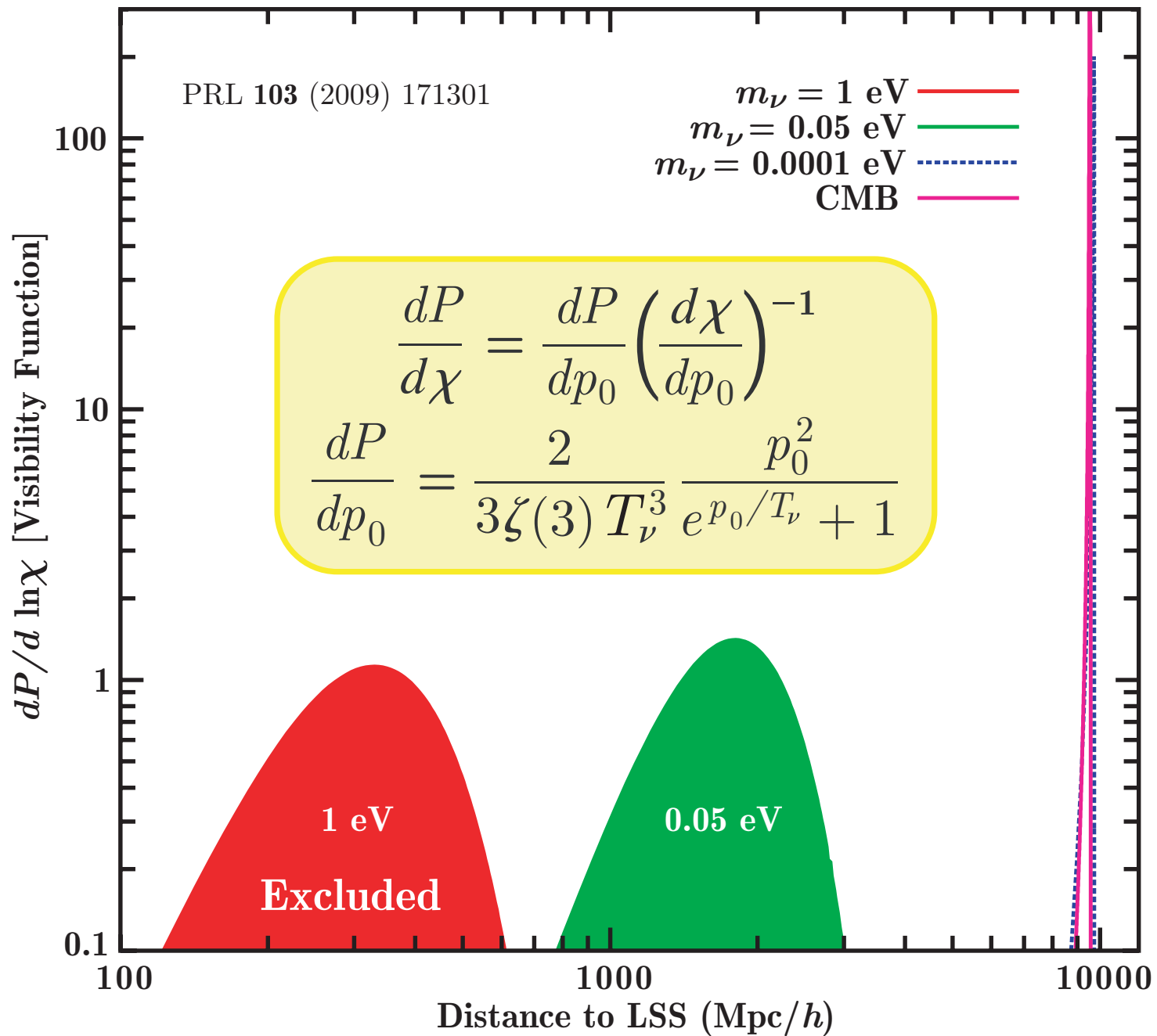
Neutrino & cosmological structure formation.

Neutrinos with mass on the sub-eV scale behave as a hot component of dark matter. Neutrinos stream out of high-density regions into low-density regions, thereby damping out small-scale density perturbations.

Figure shows the slices of baryon density distribution. All slices are $200\,h^{-1}\mathrm{Mpc}$ wide and show the baryonic mass averaged over the volume of a grid cell. Each grid cell is $\sim 391\,h^{-1}\mathrm{kpc}$. The *top panel* shows a simulation without neutrinos ($\Omega_\nu = 0$). The middle and the *bottom panels* are taken from simulations with $\Omega_\nu = 0.02$ ($\Sigma m_\nu = 0.95$ eV) and $\Omega_\nu = 0.04$ ($\Sigma m_\nu = 1.90$ eV). The baryon density fields in the middle and the *bottom panels* are less evolved relative to the no-neutrino (*top panel*) case.

(The unrealistically large neutrino masses were chosen so as to make the comparison clear.)

The simulations were run with the number of CDM particles $N_{\mathsf{CDM}} = 256^3$ and number of gas particles $N_{\mathsf{gas}} = 512^3$. The density projections were made using the analysis and visualization tool YT (python-based package for analysing ENZO[a]).

[S. Agarwal & H. A. Feldman, "The effect of massive neutrinos on the matter power spectrum," Mon. Not. Roy. Astron. Soc. **410** (2011) 1647–1654.]

---

[a] $\mathrm{ENZO}\,1.5$ code is a publicly available adaptive mesh refinement, grid-based hybrid code (hydro + N-body) designed to simulate cosmological structure formation; see URL: ⟨http://lca.ucsd.edu/projects/enzo⟩.
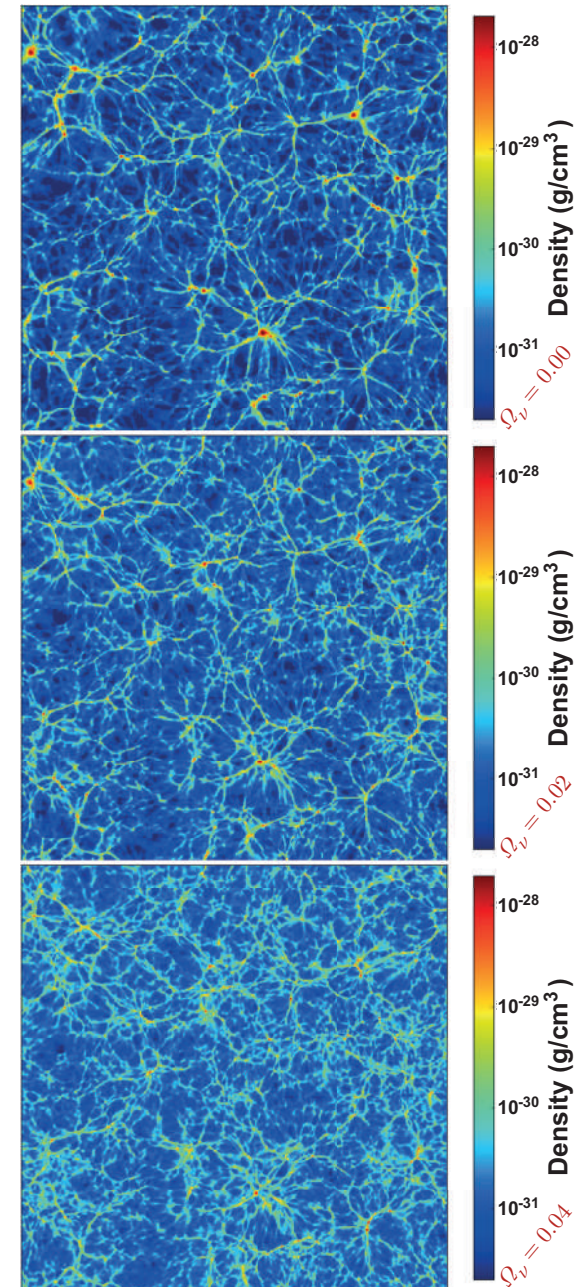
Big Bang nucleosynthesis.

Big Bang nucleosynthesis (BBN) is the creation of the light elements and isotopes thereof of primordial cosmic composition (which to a large degree is the cosmic composition) of the observable Universe. BBN produced overwhelmingly most of the modern cosmic abundances of Hydrogen, Deuterium, and Helium-3 and 4, and some significant part or maybe almost all of the cosmic abundance of Lithium-6 and 7.

BBN (cosmic time $\sim 10 - 1200$ s) occurred ~ 13.8 Gyr ago.

Figure shows a fragment of the full nuclear network of the BBN reactions that produce the lightest (and most abundant) isotopes. A more detailed network is shown on p. 36.
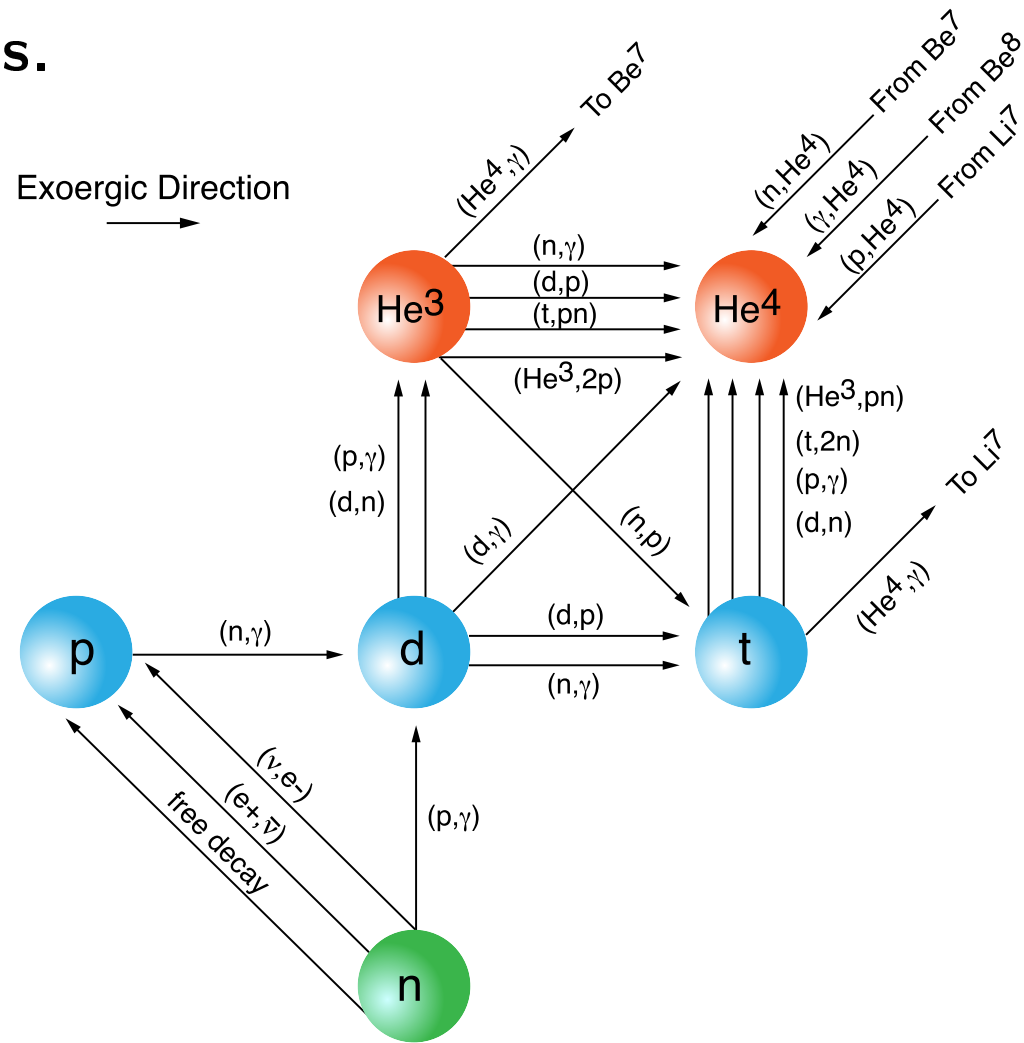
[Figure is borrowed from the Cococubed website http://cococubed.asu.edu/code_pages/net_bigbang.shtml.]

34
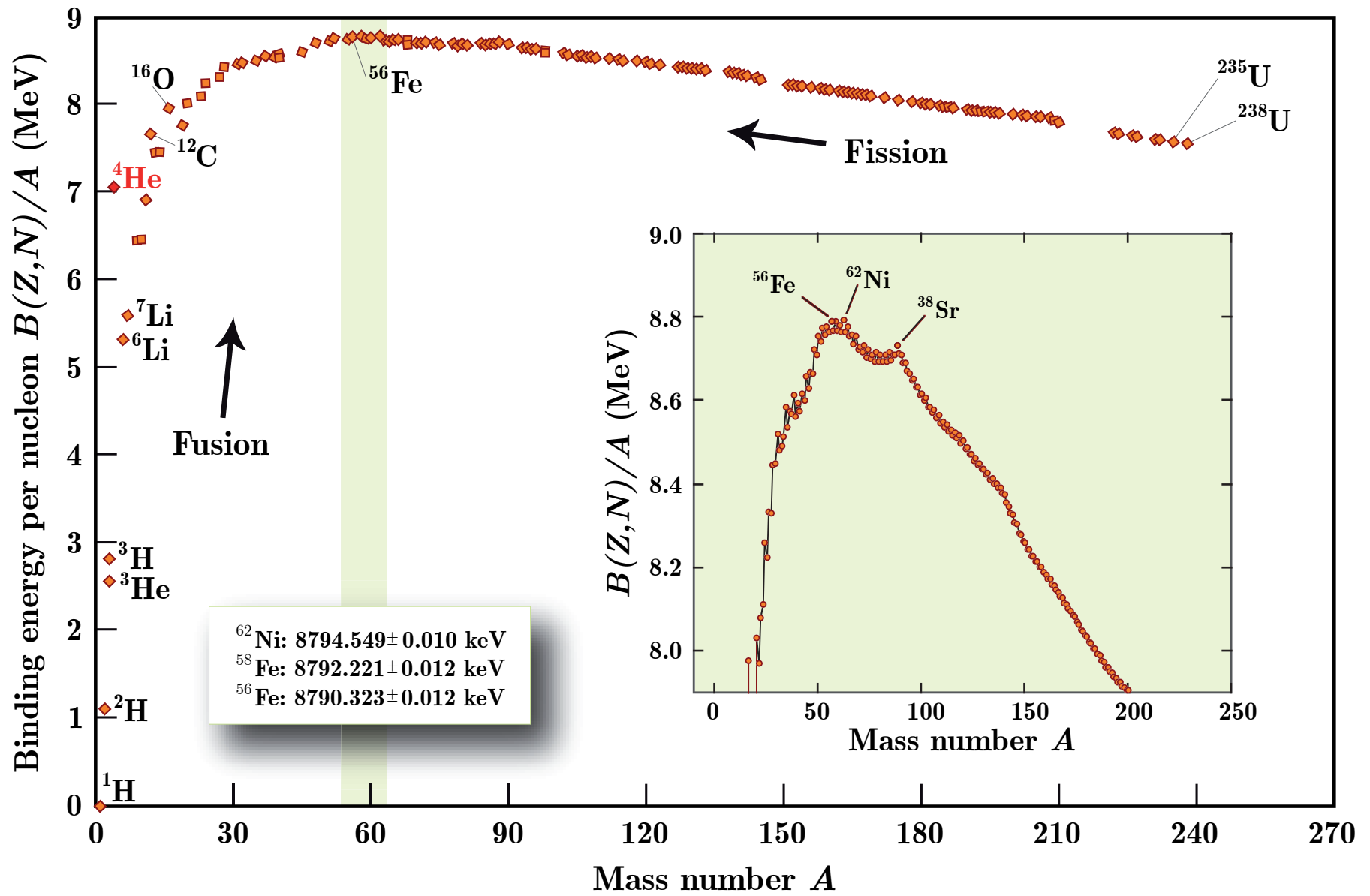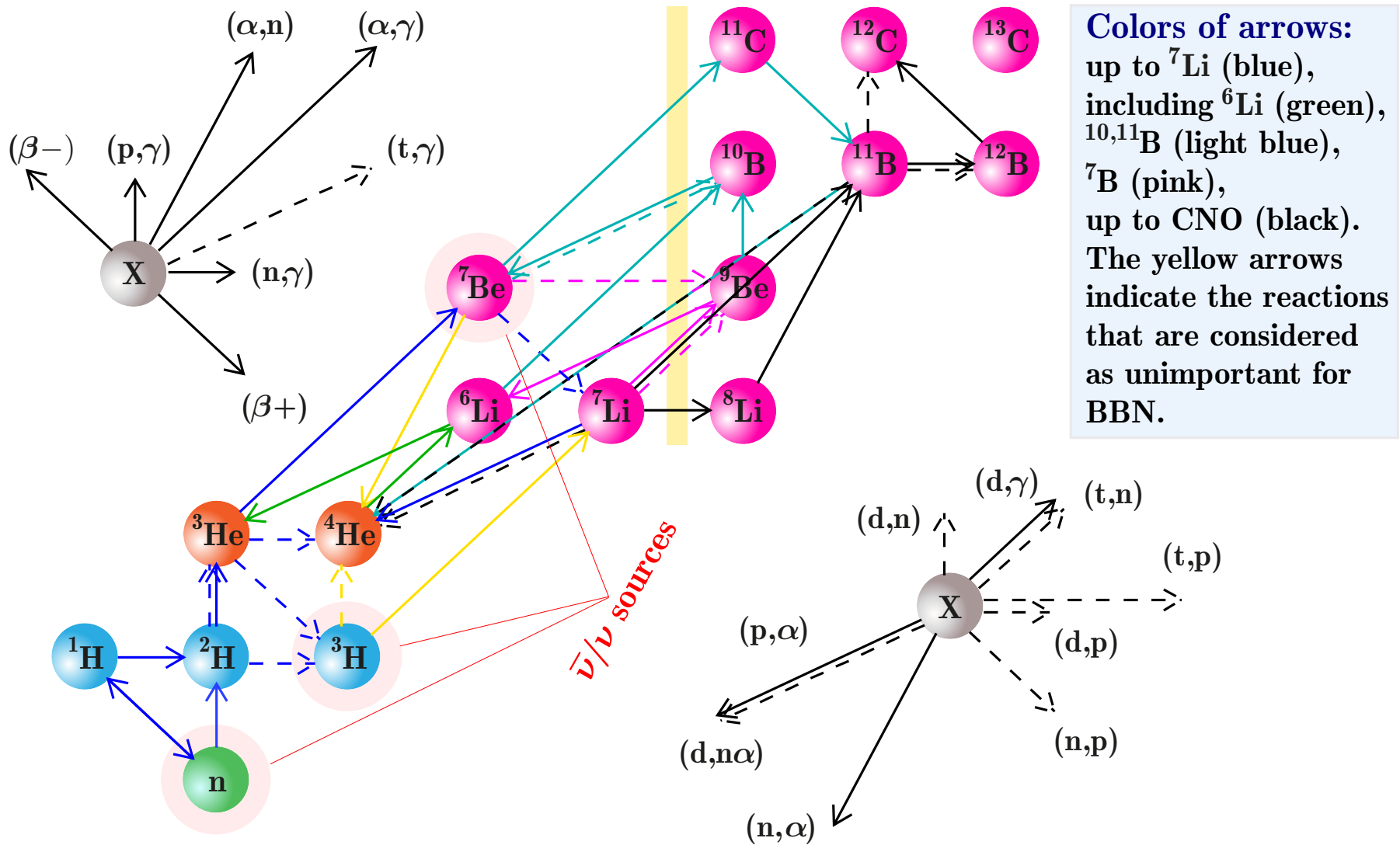
Nuclear network of the most important reactions in BBN (out of the 424) producing or destructing light isotopes up to CNO. The symbols for the arrows include their length and direction.

[Adopted from C. Pitrou *et al.*, "Precision big bang nucleosynthesis with improved Helium-4 predictions," Phys. Rept. **754** (2018) 1–66, arXiv:1801.08023 [astro-ph.CO].]

BBN – another presentation.

The reaction network:

$$n^0 \longrightarrow p^+ + e^- + \bar{\nu}_e \qquad\qquad p^+ + n^0 \longrightarrow {}^2_1D + \gamma$$

$${}^2_1D + p^+ \longrightarrow {}^3_2He + \gamma \qquad\qquad {}^2_1D + {}^2_1D \longrightarrow {}^3_2He + n^0$$

$${}^2_1D + {}^2_1D \longrightarrow {}^3_1T + p^+ \qquad\qquad {}^3_1T + {}^2_1D \longrightarrow {}^4_2He + n^0$$

$${}^3_2He + {}^4_2He \longrightarrow {}^7_3Li + \gamma \qquad\qquad {}^3_2He + n^0 \longrightarrow {}^3_1T + p^+$$

$${}^3_2He + {}^2_1D \longrightarrow {}^4_2He + p^+ \qquad\qquad {}^3_2He + {}^4_2He \longrightarrow {}^7_4Be + \gamma$$

$${}^7_3Li + p^+ \longrightarrow {}^4_2He + {}^4_2He \qquad\qquad {}^7_4Be + n^0 \longrightarrow {}^7_3Li + p^+$$

37
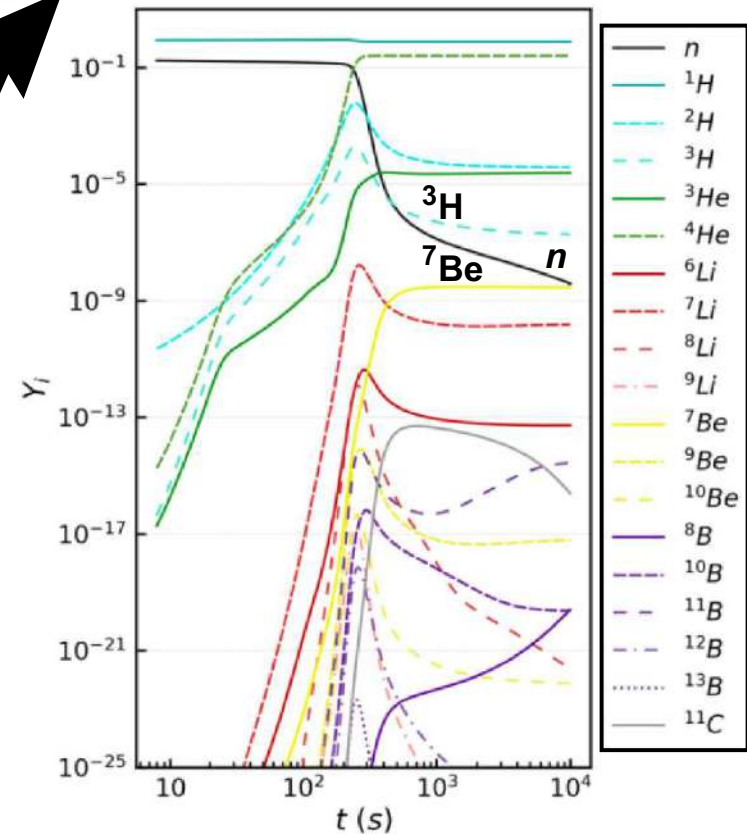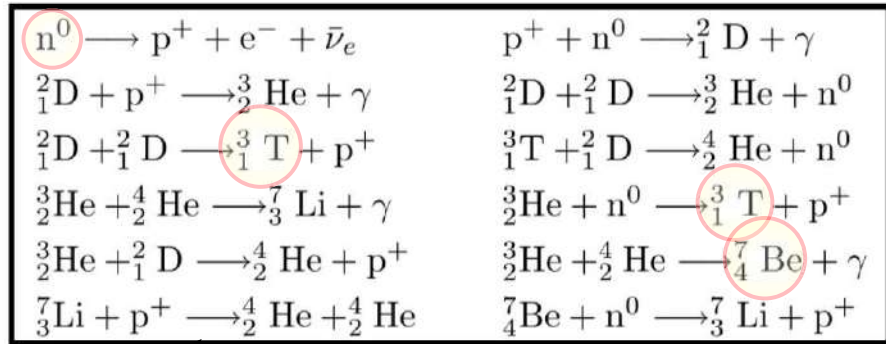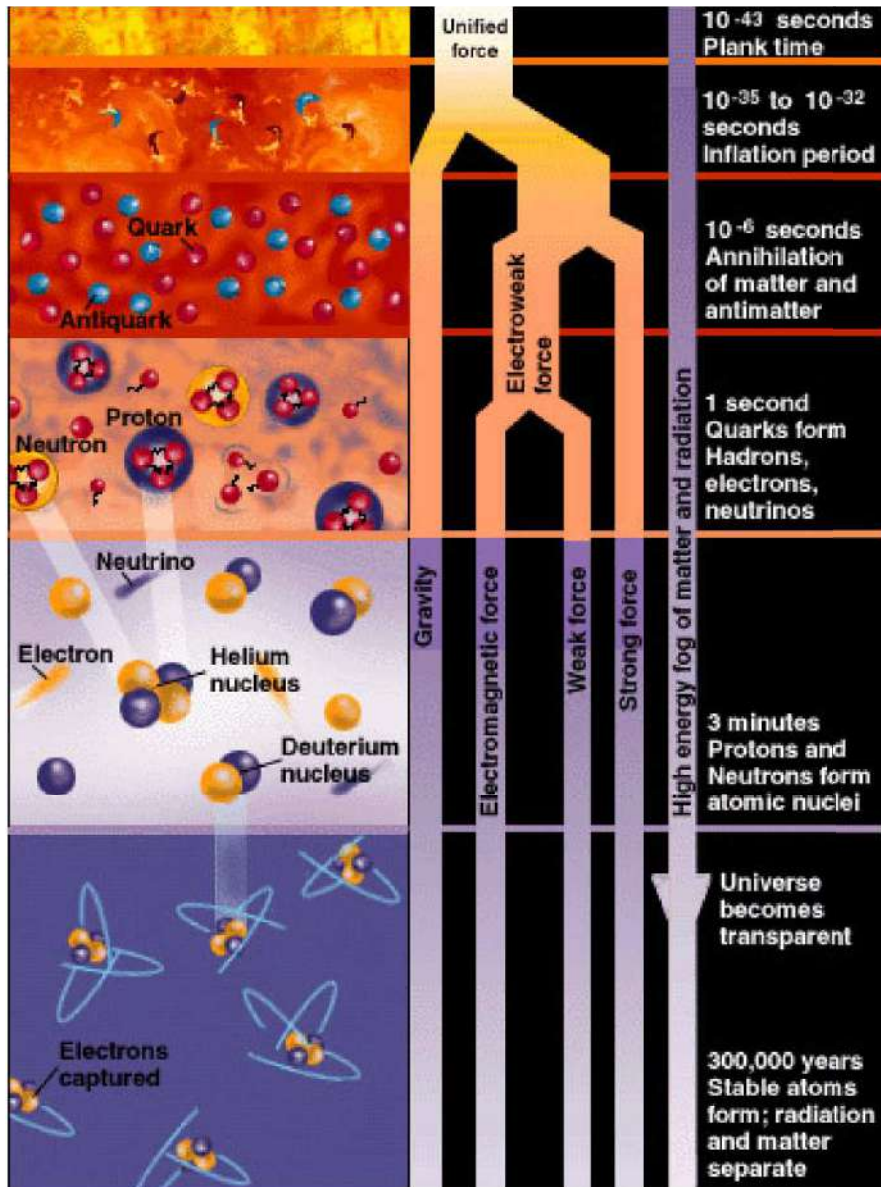
Digression: The primordial Lithium problem.

Precise knowledge of the baryon-to-photon ratio $\eta = n_b/n_\gamma$ of the Universe from observations of the CMB anisotropies has made the Standard BBN a parameter-free theory. Although, there is a good agreement over a range of nine orders of magnitude between abundances of light elements deduced from observations and calculated in BBN, there remains a yet-unexplained discrepancy of ^{7}Li abundance higher by a factor of $3 - 4$ when calculated theoretically. The primordial abundances depend on

- astrophysical nuclear reaction rates,
- number of light neutrino flavors (N_ν),
- neutron lifetime (τ_n), and
- baryon-to-photon ratio (η).

The discrepancy is not yet explained.

[Figure is adopted from P. A. Zyla *et al.* (Particle Data Group), "Review of Particle Physics," PTEP **2020** (2020) 083C01. Exp. limit for ^{3}He/H is added.]
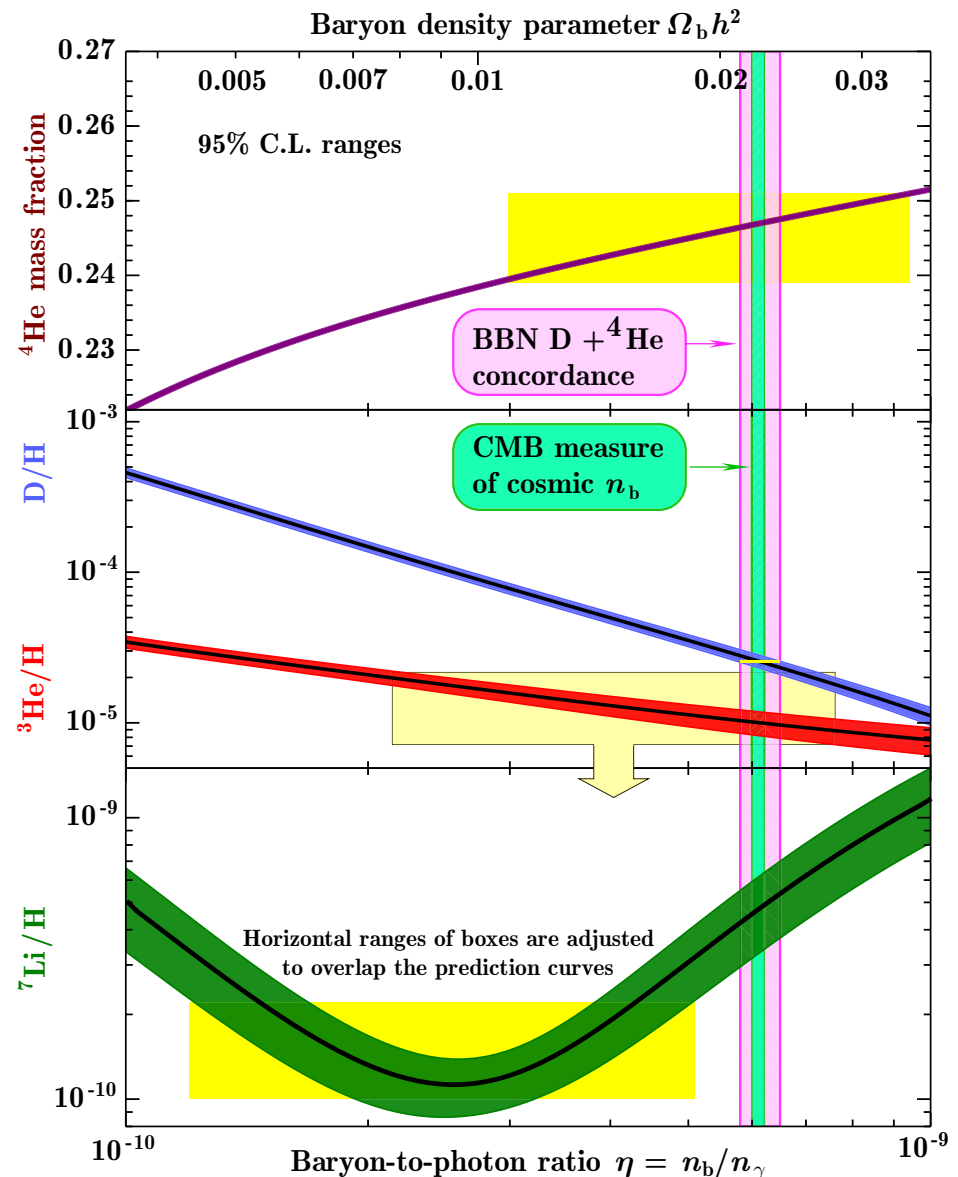
So, during the first few minutes, the Universe produces observed light elements. Subsequent decays of neutrons and tritons,

$$n \to p + e + \overline{\nu}_e$$

$$(\text{half-life} = 611 \pm 1 \text{ s}),$$

$$^3\text{H} \to {}^3\text{He} + e^- + \overline{\nu}_e$$

$$(\text{half-life} = 12.32 \pm 0.02 \text{ yr}),$$

produce a very small $\overline{\nu}_e$ flux. Later ^7Be produce (even smaller) flux of ν_e of 861.8 keV (89.6%) or 384.2 keV (10.4%) through bound-electron capture,

$$^7\text{Be} + e^- \to {}^7\text{Li} + \nu_e$$
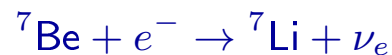
$$(\text{half-life} = 53.3 \text{ d}).$$

Figure shows evolution of light-element abundances as indicated at the lines. Colored solid lines are neutrons (n) and the unstable but longlived isotopes tritium (T) and beryllium (^7Be), which produced $\overline{\nu}_e$ and ν_e but have not themselves survived to this day.
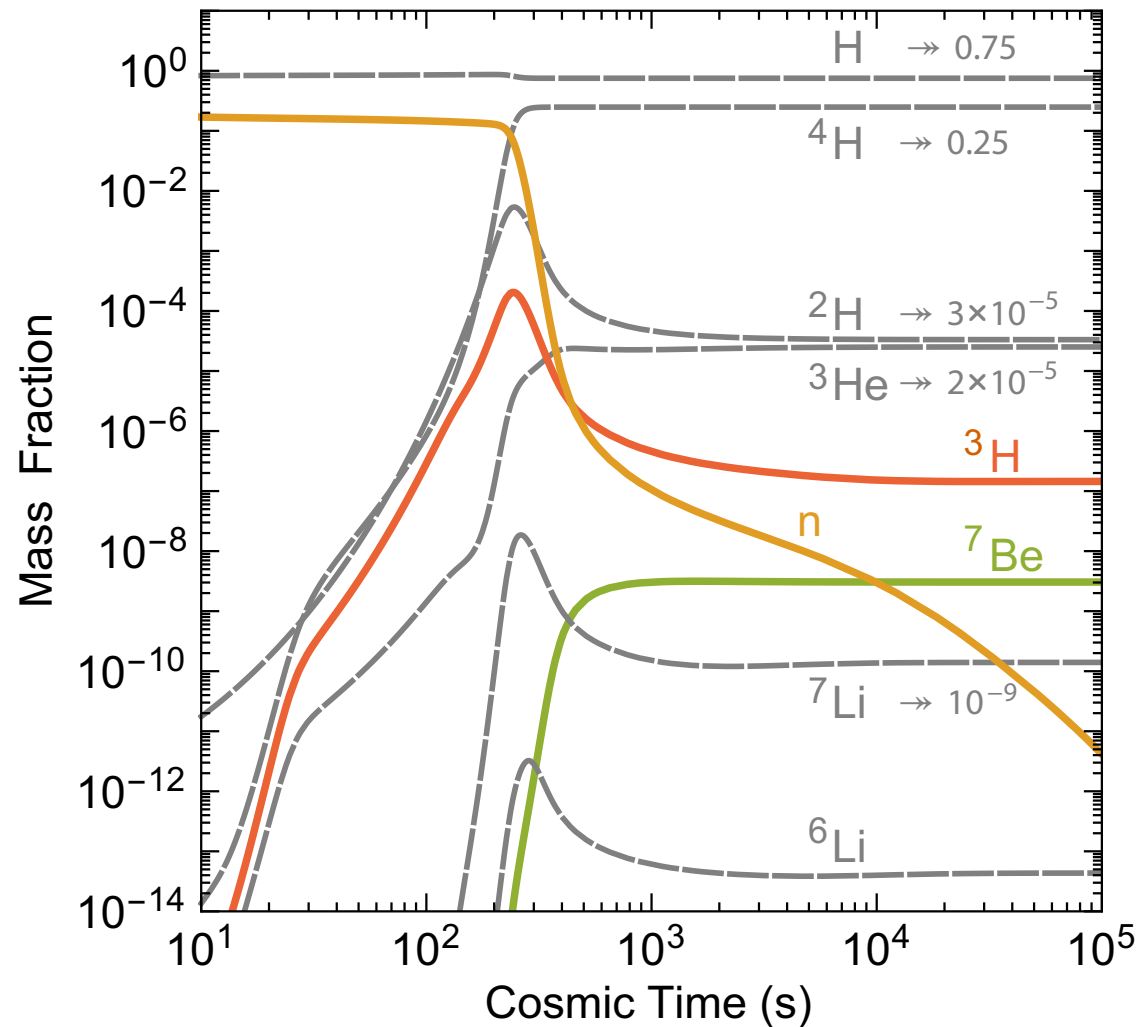
[Figure is adopted from E. Vitagliano *et al.*, (2020), see Ref. in p. 17.]
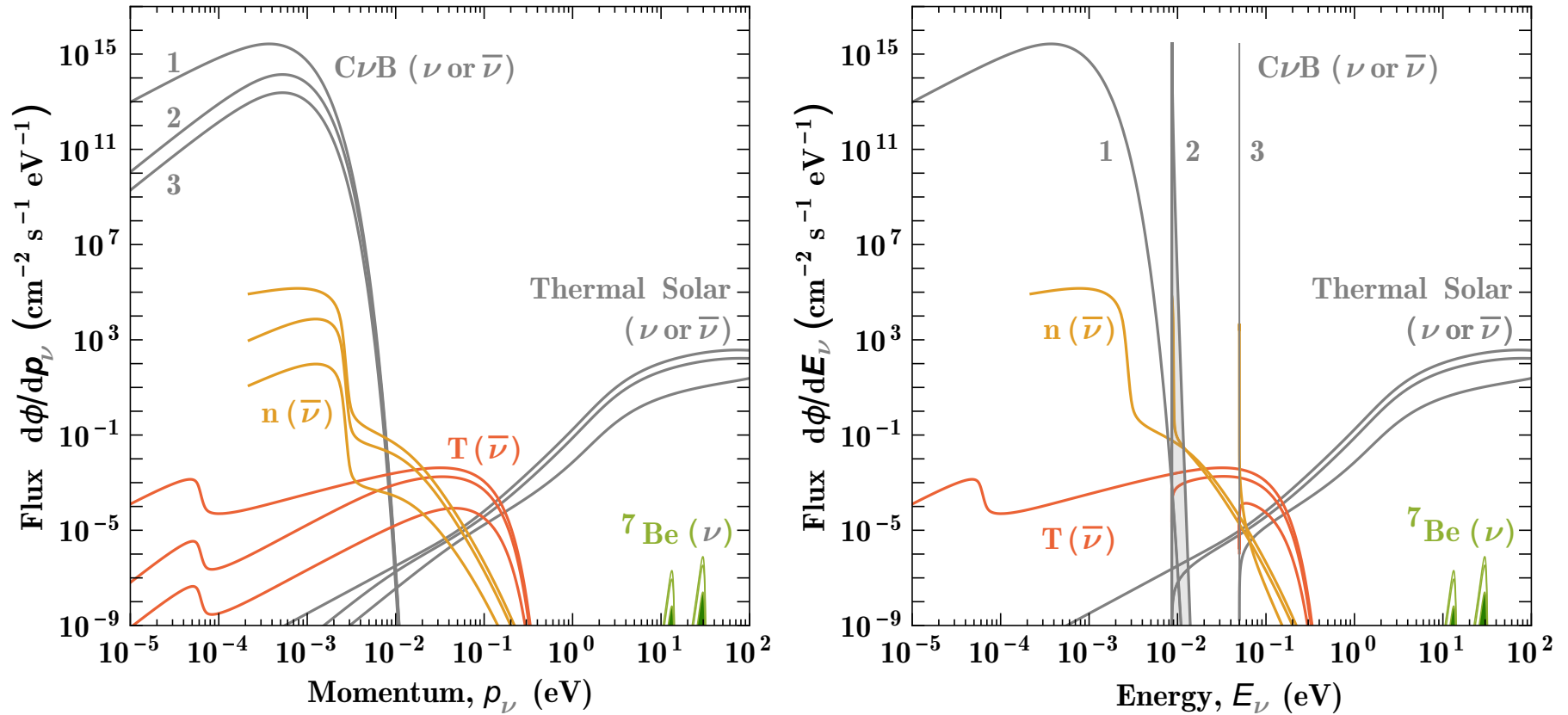
Flux densities of the lowest-energy mass eigenstates ν_i and $\overline{\nu}_i$ with $m_i = 0, 8.6, 50$ meV from several sources (CνB, BBN, Sun), calculated using the probabilities (mass-eigenstate content) listed in Table:

CνB			BBN			Sun (bremsstrahlung)		
1	2	3	1	2	3	1	2	3
1/3	1/3	1/3	0.681	0.297	0.022	0.432	0.323	0.245

[Figures are borrowed from E. Vitagliano *et al.*, (2020), see Ref. in p. 17.]

Explanation of the above table.

- CνB: The relic νs and $\overline{\nu}$s consist essentially of an equal mixture of all flavors
  $\Longrightarrow$ the probability for finding a random flavor in any of the mass eigenstates is $1/3$.
  The flavor density matrix is essentially proportional to the unit matrix from the beginning
  $\Longrightarrow$ The flavor conversion (including MSW) don't seem to have any effect.
- BBN: The BBN neutrinos are produced in the electron flavor, so their flavor content will change with time. Flavor evolution in the early Universe can involve many complications. e.g., neutrinos themselves are an important background medium, leading to collective flavor evolution, However, the BBN neutrinos are largely produced after BBN is complete at $T \gtrsim 60$ MeV.
  The matter density in the post-BBN era is $\sim 10^{-5}$ g/cm^3.
  $\Longrightarrow$ matter effects and collective neutrino oscillations are not important.
  $\Longrightarrow$ Flavor evolution of MeV-range neutrinos occurs in the vacuum, and the mass content of the initial flavor states does not evolve.
  $\Longrightarrow$ One can use the best-fit probabilities of finding $\nu_e/\overline{\nu}_e$ in $\nu_i/\overline{\nu}_i$ states given in p. 11.
- Sun: The main processes of thermal ν and $\overline{\nu}$ production in the solar plasma, are
  - plasmon decay, $\gamma \to \overline{\nu}\nu$,
  - Compton process (photoproduction), $\gamma + e \to e + \overline{\nu}\nu$,
  - bremsstrahlung, $e + (Ze) \to (Ze) + e + \overline{\nu}\nu$ (dominates at low energies), and
  - atomic free-bound and bound-bound transitions, $(Ze)^* \to (Ze) + \overline{\nu}\nu$.
  The thermal neutrinos have energies $\lesssim$ keV, corresponding to the temperature in the solar core. Bremsstrahlung produces almost pure $\nu_e\overline{\nu}_e$ fluxes due to vector-current interaction and fluxes of any flavor equally due to axial-vector interaction. Adding the vector (28.4%) and axial-vector (71.6%) contributions gives the above numbers. Higher-energies range is more complicated.
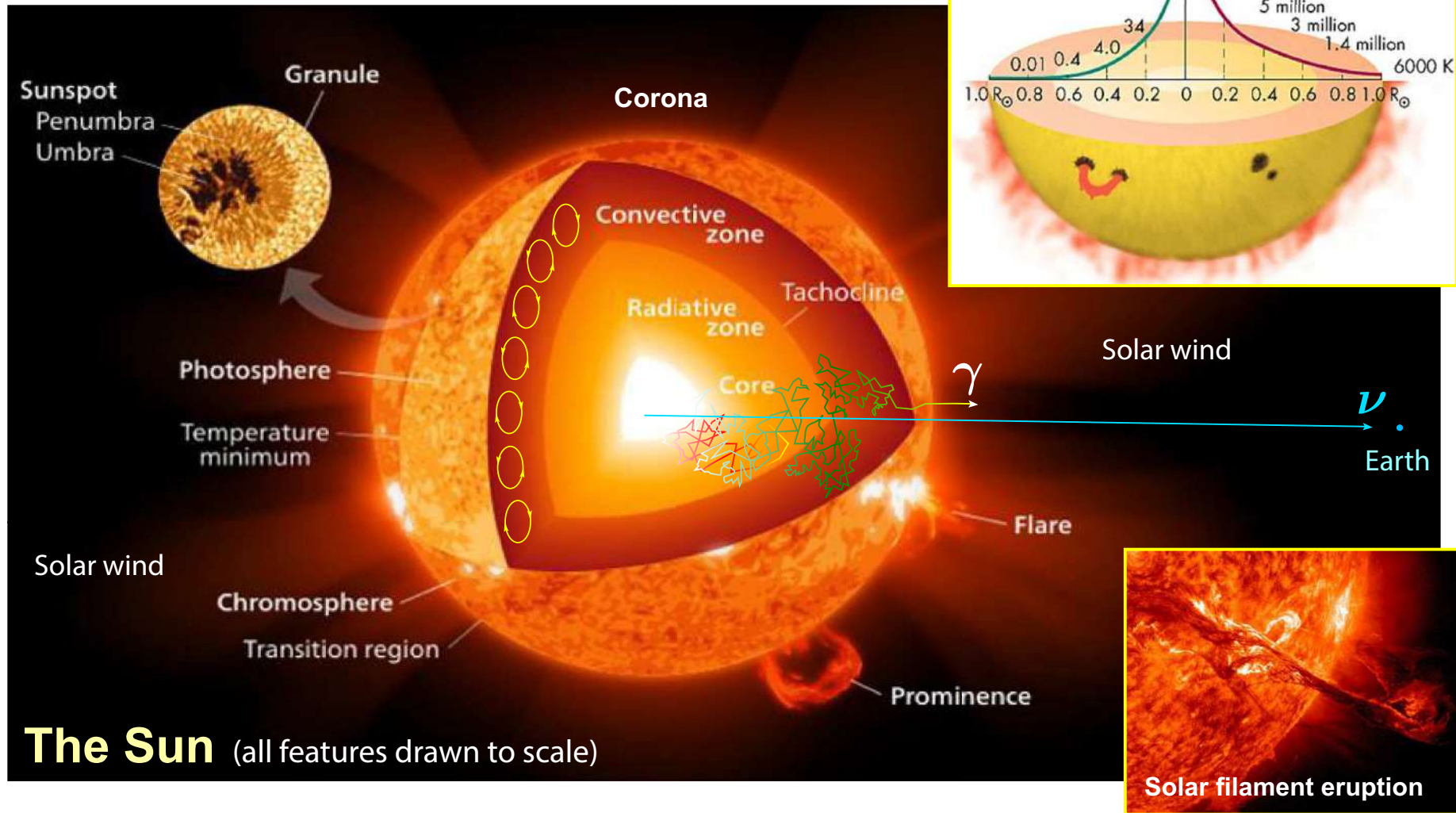
N_{eff} from BBN
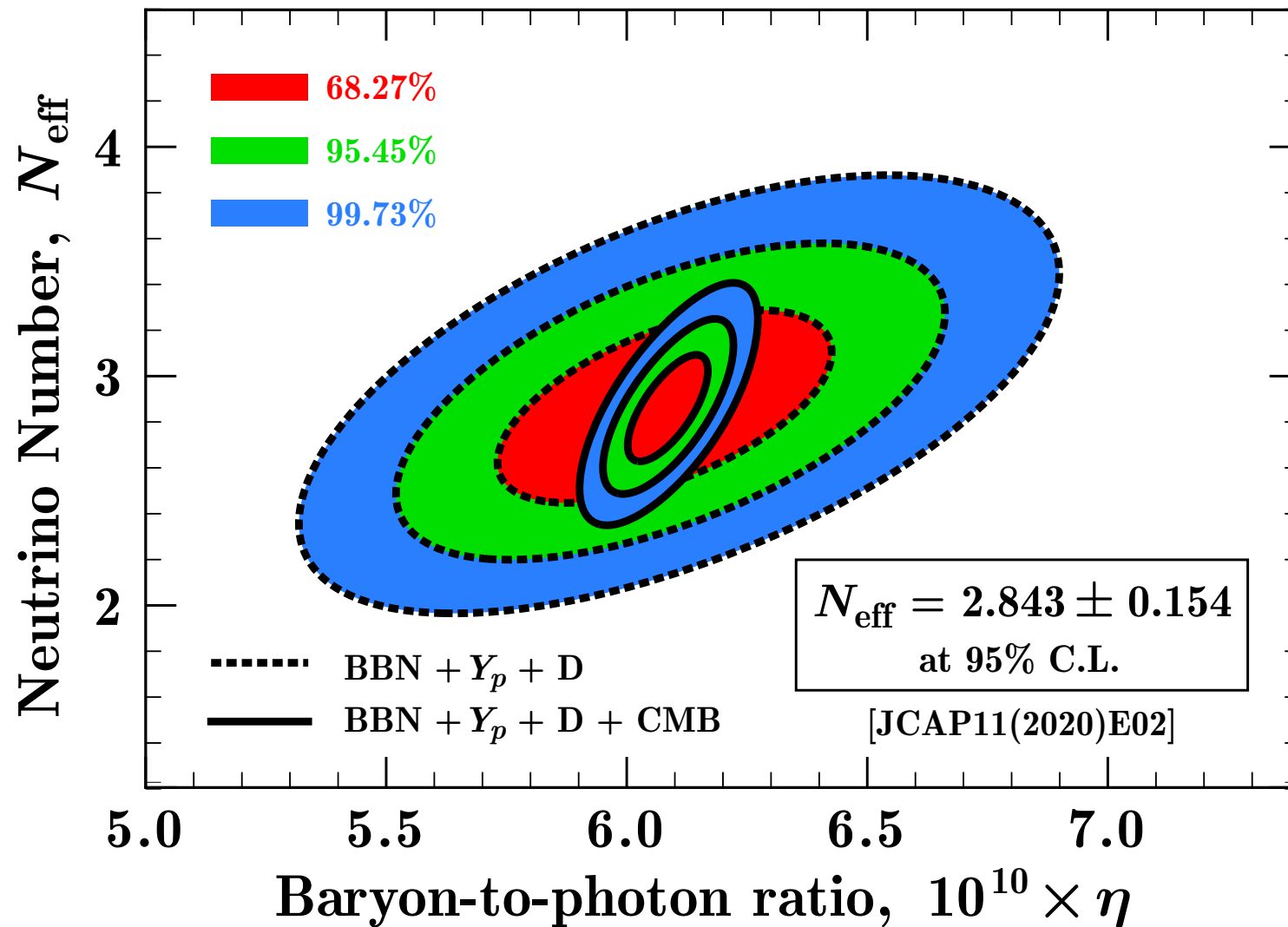
Likelihood distributions in (N_{eff}, η) space (here Y_p and D are the ^{4}He and D mass fractions).

[From B. D. Fields *et al.*, "Big-Bang Nucleosynthesis after Planck," JCAP03(2020)010, arXiv:1912.01132 [astro-ph.CO].]

Solar (thermonuclear) neutrinos.

Various regions of the surface and interior of the Sun. [From ⟨ https://medium.com/starts-with-a-bang/ 11-scientific-advances-of-the-last-100-years-gave-us-our-entire-universe-b9e17f1adcd6⟩.]

The life of any star is an unceasing struggle between gravity and pressure. Both act in all directions, but gravity tries to compress everything to the star's core and pressure decreases with increasing distance from the core, by that pushing stellar layers outward. When gravity dominates, the star contracts causing the pressure to rise and thus resisting further contraction. When the outward pressure gradient dominates, stellar layers expand, thus decreasing the pressure and terminating further expansion of the star.
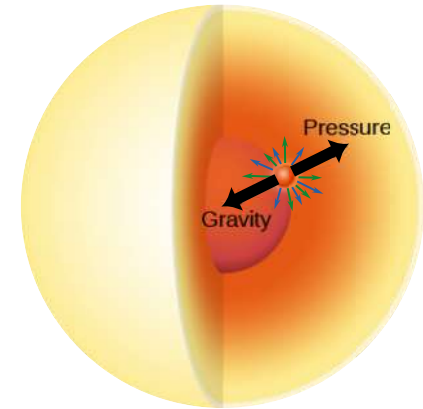
Since a star shines, it loses energy from its interior. This reduces the pressure and leads to contraction of the star. Without a mechanism of restoring the energy lost, a typical star cannot live more than some tens of millions of years. It has long been known that such a mechanism is provided by the reactions of thermonuclear fusion (the formation of light nuclei from lighter ones) within the star.[a]

If the daughter nucleus is more bound than the fusing ones, the reaction releases nuclear binding energy. The latter rises steeply from zero for ^{1}H to 7.074 MeV ($\sim 10^{-12}$ J) per proton for ^{4}He and reaches a peak at about 8.79 MeV per nucleon for the iron-nickel group before decreasing for heavier isotopes (see Figure at p. 35). If a star initially consisted of pure hydrogen, it could gain a maximum of about 8.79 MeV per nucleon by fusion to iron[b]. This is an extremely complicated and multistage process occurring at very high temperatures and densities. But most of the available nuclear binding energy ($\sim 80\%$) is already released when ^{4}He is built up in the first stage. The transmutation of four protons into one α particle is the fully dominant energy source for the present-day Sun.

---

[a] This source of stellar energy was independently suggested by Jean Baptiste Perrin (1919) and Arthur Stanley Eddington (1920). But the first to propose the principle of nuclear fusion was William Draper Harkins (1915).

[b] The binding energy per nucleon for the three most tightly bound isotopes are 8790.323 ± 0.012 keV (^{56}Fe), 8792.221 ± 0.012 keV (^{58}Fe), and 8794.549 ± 0.010 keV (^{62}Ni); the isotope ^{56}Fe is the end product of normal stellar fusion because it is in very close but unbridgeable proximity to the most stable isotope ^{62}Ni.

The energy production rate averaged over the solar core does not catch our fancy: it is as low as $10 - 15$ W/m^3 that is compatible with the power of a pocket torch. However the luminosity of the Sun is about 4×10^{26} W, equivalent to $\sim 10^{17}$ typical nuclear power plants.
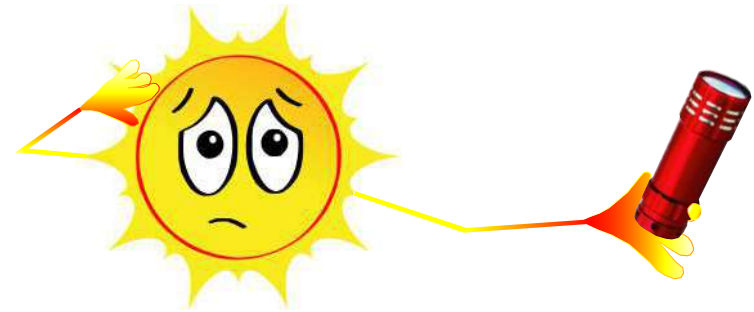
The net luminosity is so huge because the Sun converts $\sim 7 \times 10^8$ metric tons of hydrogen (or about 4×10^{38} protons) to helium per second. The hydrogen is consumed at a lower rate than in any other evolutionary phase of the Sun and thus the central hydrogen-burning lifetime of the Sun is much longer than that for other phases of its evolution. The Sun contains $\sim 10^{57}$ atoms (mostly hydrogen, with a little helium and traces of the other elements like Carbon, Nitrogen, Oxygen, Magnesium, and so on); so it has enough fuel to shine actively for more than 10^{10} years.

A conversion of a proton into a bound neutron is only possible with production of an electron neutrino through β^+ decay or electron capture. The hydrogen-to-helium fusion is also a rather multistage process which occurs in two key simultaneously running reaction sequences, the pp (or proton-proton) chains and the CNO (Carbon-Nitrogen-Oxygen) cycle[a] and the neutrinos are necessarily emitted as a result of some of the pp and CNO reactions.

Since the low-energy neutrinos are extremely penetrating ultrarelativistic particles, they escape the Sun in two seconds without being scattered or absorbed[b] and reach the Earth in about eight minutes from the time they were produced. By detecting these neutrinos, we may learn a lot about the "instantaneous" conditions inside the Sun and, as a surprising bonus, about the neutrinos themselves.

---

[a] Both sequences were worked out at the end of 1930s by Carl Friedrich von Weizsäcker and Hans Albrecht Bethe, though *without mentioning the neutrinos* (note that Bethe knew the theory of Fermi).

[b] The ν-N interaction cross section, σ_ν, at $E_\nu = 1$ MeV is about 10^{-44} cm^2. So the mean free pass $\lambda_\nu = 1/(\sigma_\nu n) \sim m_p/(\sigma_\nu \rho)$ of the 1 MeV neutrinos in the matter of density $\rho = 100$ g/cm^3 is $\sim 10^{15}$ km ~ 0.1 pc.

pp chain.
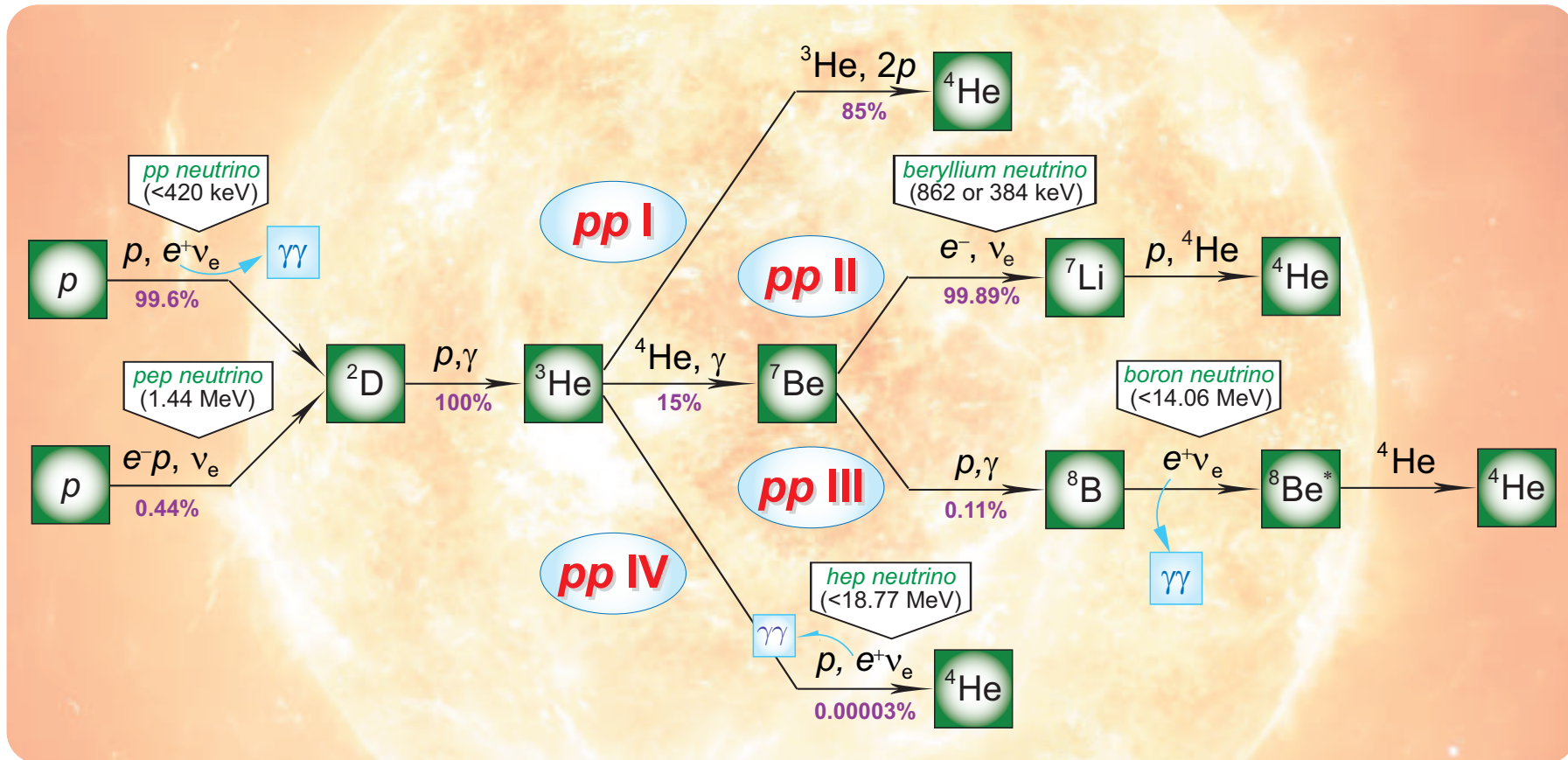
The diagram shows the full pp chain responsible for production of about 98.4% of the solar energy.
The neutrinos export 3%, 4%, and 28% of the energy in pp I, pp II, pp III, respectively.
All four pp chains are active simultaneously in a H-burning star containing significant ^{4}He.
The details depend on density, temperature and composition but in Sun the pp I dominates.
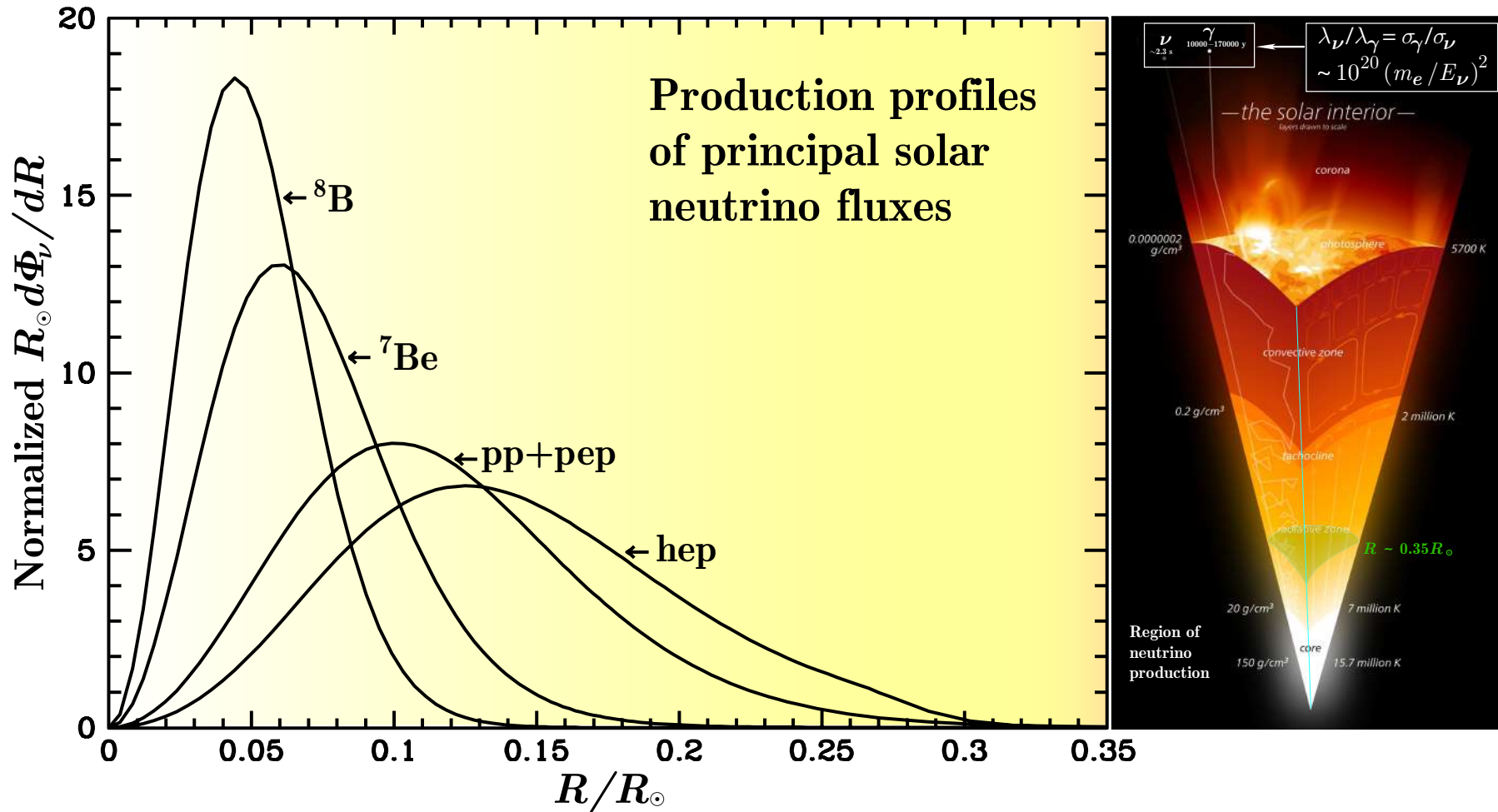
CNO bi-cycle.
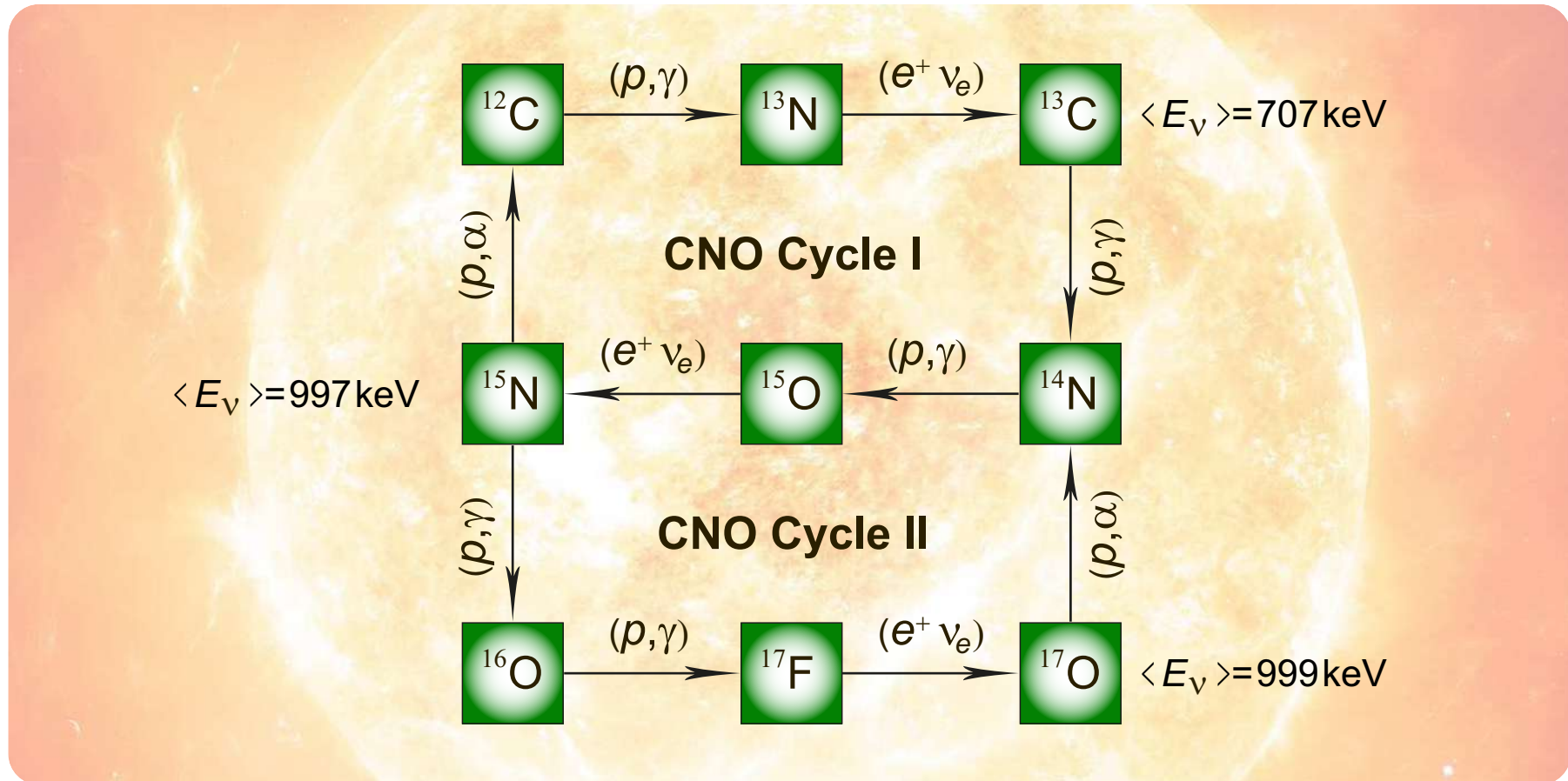
The diagram of the full CNO bi-cycle responsible for production of about 1.5–1.6% of the solar energy. The cycle I dominates in Sun. The CNO cycles III and IV (will be discussed in Sect. 147, p. 147) are essential for the hydrogen burning in massive stars. The full reaction net includes ^{18}F, ^{18}O, and ^{19}F.

Solar neutrino fluxes.

Figure shows the pp and CNO neutrino fluxes (versus energy) on Earth, calculated in the comprehensive solar model "BS05(OP)" by J. N. Bahcall *et al.*
Line and spectral fluxes are, respectively, in $cm^{-2}s^{-1}$ and in $cm^{-2}s^{-1}MeV^{-1}$. Some minor neutrino contributions are not included. Also shown are the uncertainties of the neutrino flux calculation (on the $1\,\sigma$ level) and the threshold neutrino energies for the gallium, chlorine, and water-Cherenkov detectors.
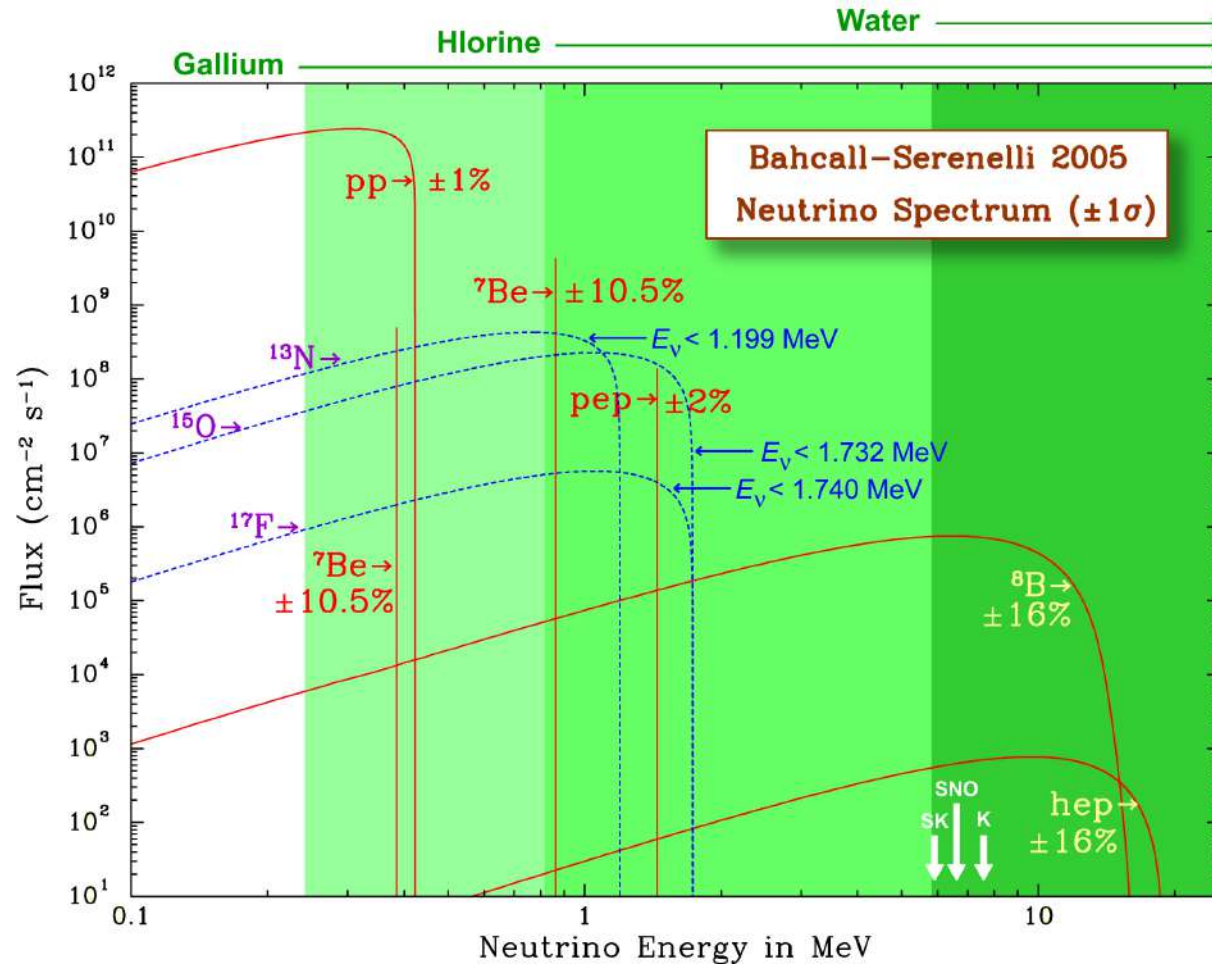
[Figure is taken from J. N. Bahcall, A. M. Serenelli, and S. Basu, "New solar opacities, abundances, helioseismology, and neutrino fluxes," ApJ **621** (2005) L85–L88, astro-ph/0412440.]

Production profiles of principal solar neutrino fluxes

$\lambda_{\nu}/\lambda_{\gamma} = \sigma_{\gamma}/\sigma_{\nu} \sim 10^{20} (m_e/E_{\nu})^2$

—the solar interior—

The left figure shows the normalized flows (production profiles)[a] of the pp-chain neutrinos produced within the solar core, calculated within the so-called "BS05(OP)" SSM as functions of the relative solar radius $R/R_{\odot}$ (see also p. 136). The right figure schematically illustrates the solar interior.

[Data for the left figure were taken from John Bahcall's homepage, URL: ⟨http://www.sns.ias.edu/~jnb/⟩.]

[a] The production profiles are normalized to unity when integrated over $R/R_{\odot}$.

49

The future of the Sun.
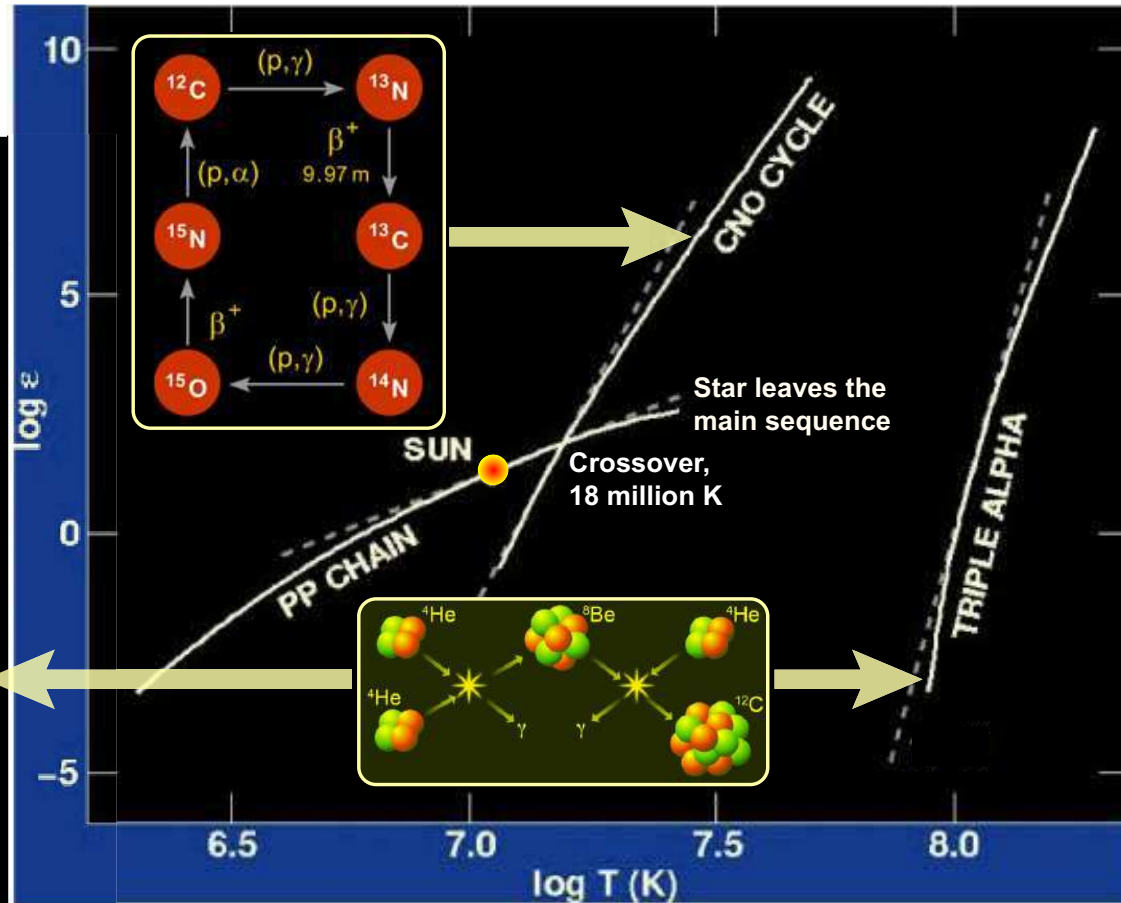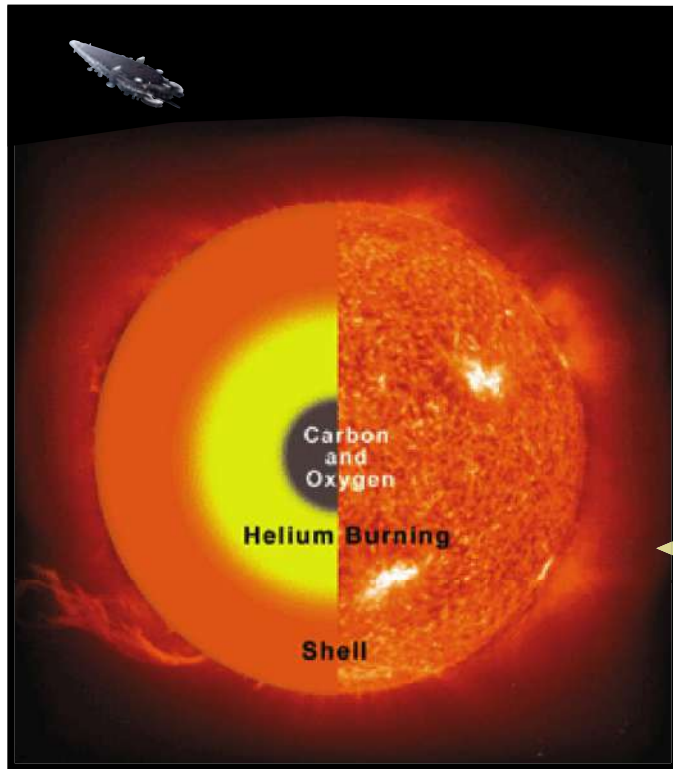
When there is no longer any hydrogen left to burn in the central regions of a star, gravity compresses the core until the temperature reaches the point where helium burning reactions become possible. In such reactions, two ^{4}He nuclei fuse to form a ^{8}Be nucleus, but this is very unstable to fission and rapidly decays to two ^{4}He nuclei again. Very rarely, however, a third helium nucleus can be added to ^{8}Be before it decays, forming ^{12}C by the so-called triple-alpha reaction:

$$^4\text{He} + ^4\text{He} \rightarrow ^8\text{Be}, \quad ^8\text{Be} + ^4\text{He} \rightarrow ^{12}\text{C} + \gamma.$$
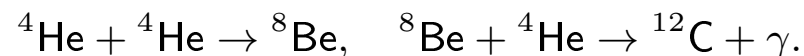
Today

Sun

Mercury
0.38 AU

Venus
0.72 AU

Earth
1 AU

Mars
1.52 AU

not to scale

7.588 billion
years from now

Sun as red giant
0.9 solar mass

Earth
1.1 AU

7.59 billion
years from now

Sun as red giant
0.8 solar mass

Mars
1.9 AU

Atmospheric neutrinos.

Why are atmospheric neutrinos important for astroparticle physics?

The mechanism of neutrino production in the atmosphere is well understood: Electron and muon neutrinos and antineutrinos come into being from decay of unstable particles, generated in the collisions of primary and secondary cosmic rays with air nuclei. Fraction of tau neutrinos and antineutrinos in the atmospheric neutrino (AN) flux is very small because ν_τ and $\overline{\nu}_\tau$ arise only from the decay of heavy particles (like D_s or B mesons) whose production cross sections are small.

However the chain of processes which lead to lepton generation is rather intricate seeing that the primaries and secondaries (both stable and unstable) can repeatedly interact in the atmosphere with absorption, regeneration or overcharging, and dissipation of energy through electromagnetic interactions.
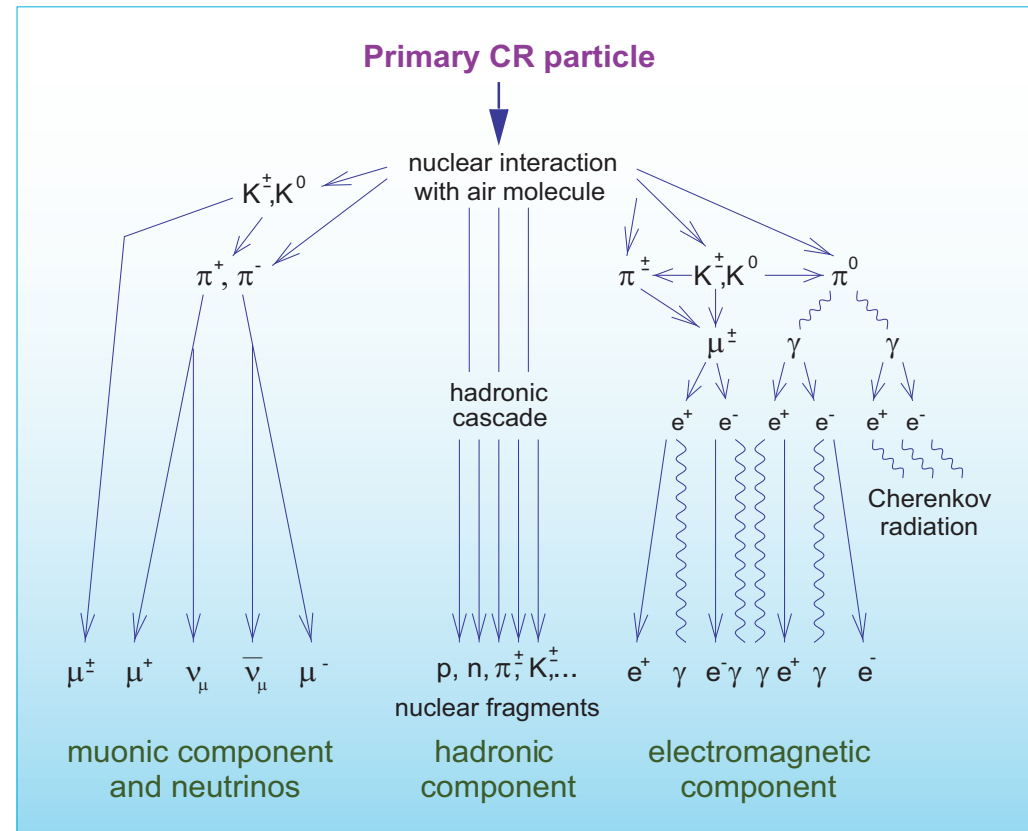
A schematic view of atmospheric cascade initiated by a primary cosmic-ray particle.

52
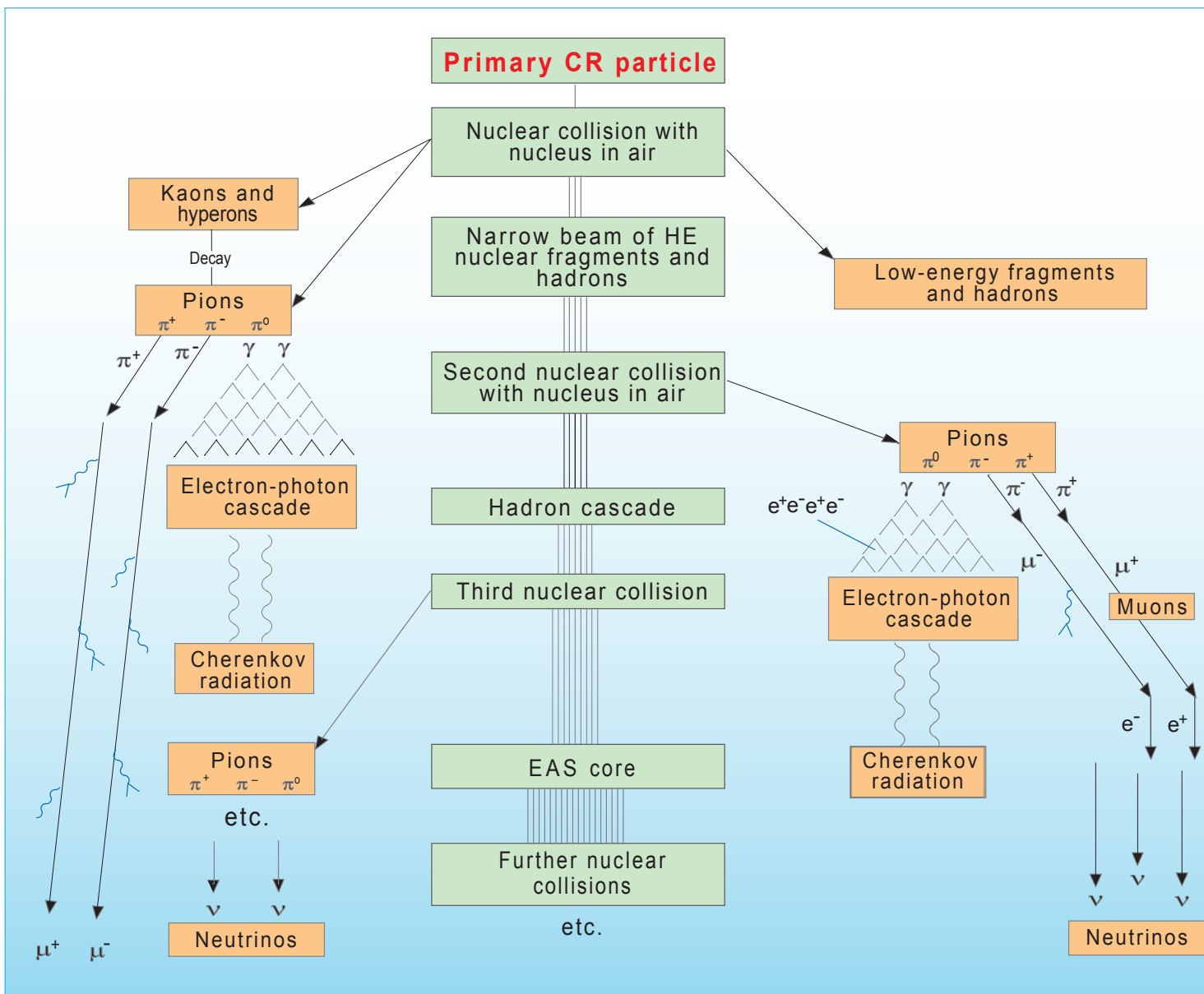
Another schematic view of the cosmic-ray initiated cascade process in the atmosphere.

Some complicating factors.

✦ **Geomagnetic effects.** At low energies, the Earth's magnetic field gives rise to the spatial (longitudinal and latitudinal) and angular (zenithal and azimuthal) asymmetries in the lepton fluxes. Complicated structure of the real geomagnetic field, the Earth's penumbra, and re-entrant albedo embarrass the analysis of the geomagnetic effects.

✦ **Solar activity.** Quasi-periodical variations of solar activity modify the low-energy part of the primary cosmic-ray spectrum and therefore affect the muon and neutrino intensities (below some hundreds of MeV), making them time-dependent.

✦ **3D effects.** At very low energies ($E_{\mu,\nu} \lesssim 500$ MeV), the 3-dimensionality of nuclear reactions and decays is important.

✦ **Meteorological effects.** These are essential at all energies of interest.

✦ **Muon polarization and depolarization effects.** Muons whose decay is an important source of neutrinos up to the multi-TeV energy range, change their polarization due to energy loss and multiply scattering, affecting the neutrino spectra.

✦ **Branchy chains.** With increasing energy, life-times of light mesons grow and the production and decay chains become branchy: "anything produce everything".

Consequently, an accurate calculation of the muon and neutrino fluxes presents a hard multi-factor problem complicated by uncertainties in the primary cosmic-ray spectrum and composition, inclusive and total inelastic cross sections for particle interactions and by pure computational difficulties.

Ergo...

Solution to the atmospheric neutrino problem is of prime necessity for the study of many fundamental issues of particle physics, astrophysics, and cosmology.

✦ **AN as annoying background.** The AN flux represents an unavoidable background for some key low-energy experiments with underground detectors, e. g.:

- Search for proton decay and $n \to \overline{n}$ transitions in nuclei.
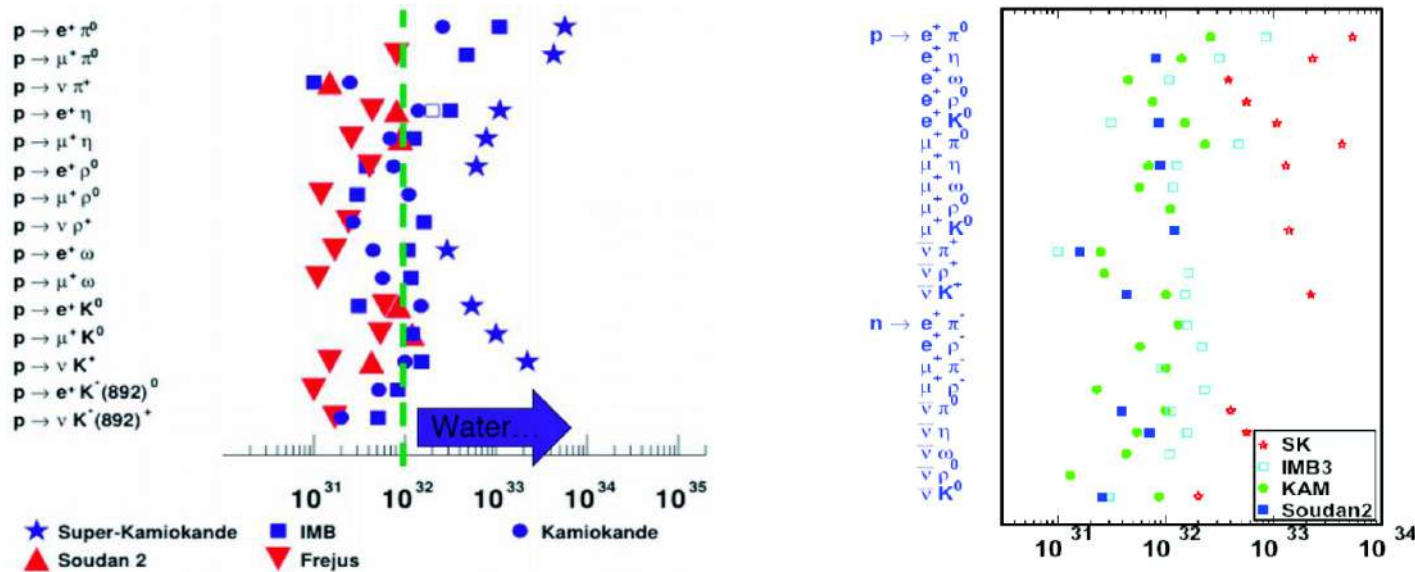
The best current lower limit on $T_{n \to \overline{n}}$ for neutrons bound in ^{16}O is 1.9×10^{32} yrs. The corresponding limit for the free neutron oscillation time ($\tau_{n \to \overline{n}}$) is 2.7×10^8 s (compared to $\tau_{n \to \overline{n}} > 0.86 \times 10^8$ s as was measured by the ILL/Grenoble experiment).
[K. Abe *et al.* (Super-Kamiokande Collaboration), Phys. Rev. D **91** (2015) 072006, arXiv:1109.4227 [hep-ex].]

- Most of experiments on high-energy neutrino astrophysics with large underground and underwater/ice neutrino telescopes:
  - detection of neutrinos from diffuse neutrino backgrounds,
  - indirect detection of *non-relativistic* dark matter through νs produced in the annihilation of the DM particles captured in Earth and Sun, or
  - direct detection of *relativistic* WIMPs (weakly-interacting massive particles) of astrophysical or cosmological origin.

  These experiments will be an effect of the AN flux at energies from ~ 1 TeV to some tens of PeV. However, in the absence of a generally recognized and tried model for charm hadroproduction (see below), the current estimates of the ν_μ and (most notably) ν_e backgrounds have unacceptably wide scatter even at multi-TeV neutrino energies, which shoots up with energy. At $E_\nu \sim 100$ TeV, different estimates of the ν_μ and ν_e spectra vary within a few orders of magnitude.
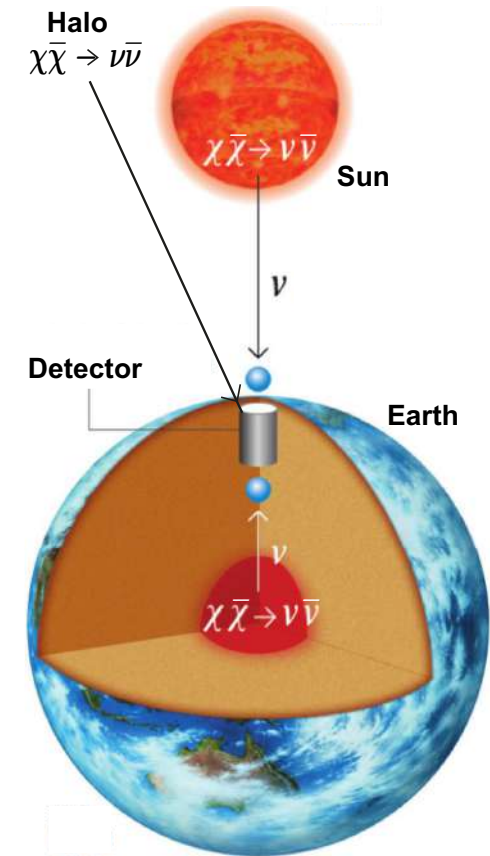
- **Study of HE and UHE neutrino interactions.** Measurements of the cross sections for $\nu_\ell N$ and $\overline{\nu}_\ell N$ charged-current interactions at $\sqrt{s} \sim m_W$ ($E_\nu \sim 3.4$ TeV) provide an important test for the Standard Model. With modern accelerators, the interactions of neutrinos are studied at energies up to several hundreds of GeV whereas deep underwater experiments with AN will enable to enlarge the region of neutrino energies up to a few tens of TeV.

- **Study of Neutrino oscillations and all that.** At the same time, the AN flux is a natural instrument for studying neutrino oscillations, neutrino decay and neutrino interactions with matter at energies beyond the reach of accelerator experiments.

AN fluxes at low and intermediate energies: Geomagnetic effects.

Due to geomagnetic effects, the low-energy AN spectra and angular distributions are quite different for different sites of the globe. Figures in p. 61 display the predictions of CORT package for ten underground neutrino laboratories listed in Table at p. 60. The *left panel* shows the ν_e, $\overline{\nu}_e$, ν_μ and $\overline{\nu}_\mu$ energy spectra averaged over all zenith and azimuth angles. The ratios of the AN fluxes averaged over the lower and upper semispheres ("up-to-down" ratios) are shown in *right panel*. As a result of geomagnetic effects, the spectra and up-to-down ratios at energies below a few GeV are quite distinct for five groups of underground labs: 1) SOUDAN + SNO/SNOLAB + IMB, 2) HPW, NUSEX + Fréjus, 3) Gran Sasso + Baksan, 4) Kamioka and 5) KGF.

Technical note:

The exact definition of the fluxes of upward- and downward-going neutrinos is given by the following formulas:

$$F_\nu^{\text{down}}(E) = \int_0^1 \langle F_\nu(E, \vartheta) \rangle_\varphi \, d\cos\vartheta, \tag{5a}$$

$$F_\nu^{\text{up}}(E) = \int_{-1}^0 \langle F_\nu(E, \vartheta) \rangle_\varphi \, d\cos\vartheta, \tag{5b}$$

where

$$\langle F_\nu(E,\vartheta)\rangle_\varphi = \frac{1}{2\pi}\int_0^{2\pi} F_\nu\left(E,\vartheta, R_c\left(\Theta, \Phi, \vartheta, \varphi\right)\right) d\varphi, \qquad \text{for} \quad 0 \leq \vartheta \leq \frac{\pi}{2}, \qquad \text{(6a)}$$

$$= \frac{1}{2\pi}\int_0^{2\pi} F_\nu\left(E,\vartheta^*, R_c\left(\Theta^*, \Phi^*, \vartheta^*, \varphi^*\right)\right) d\varphi, \qquad \text{for} \quad \frac{\pi}{2} \leq \vartheta \leq \pi, \qquad \text{(6b)}$$

$F_\nu(E,\vartheta, R_c)$ is the neutrino differential energy spectrum on the Earth surface with the oblique geomagnetic cutoff rigidity R_c which is a function of the geomagnetic latitude and longitude, Θ and Φ, and zenith and azimuthal angles, ϑ and φ (all are defined in the frame of the detector, K, see Figure).

The starred variables in Eq. (6b) are the corresponding angles defined in the local frame K^* associated with the neutrino entry point.

Clearly, the azimuthal dependence of the neutrino flux is only due to the geomagnetic effects. Therefore, within the framework of the 1D cascade theory, it is a function of three variables E, ϑ and R_c.

Рис. 1: "Neutrinos — antipodes" (how to connect geomagnetic coordinates in two points of the globe).

It is a useful (and not too trivial) exercise in spherical geometry to prove that

$$\sin \Theta^* = \sin 2\vartheta \sin \varphi \cos \Theta - \cos \vartheta \sin \Theta, \quad |\Theta^*| < \pi/2,$$

$$\sin (\Phi^* - \Phi) = \sin 2\vartheta \cos \varphi / \cos \Theta^*,$$

$$\cos (\Phi^* - \Phi) = -\left(\sin 2\vartheta \sin \varphi \sin \Theta + \cos 2\vartheta \cos \Theta\right) / \cos \Theta^*,$$

$$\vartheta^* = \pi - \vartheta,$$

$$\sin \varphi^* = \left(\sin 2\vartheta \sin \Theta + \cos 2\vartheta \sin \varphi \cos \Theta\right) / \cos \Theta^*,$$

$$\cos \varphi^* = \cos \varphi \cos \Theta / \cos \Theta^*.$$

For near horizontal directions ($|\vartheta - \pi/2| \ll 1$) the above formulas yield

$$\Theta^* \simeq \Theta + (\pi - 2\vartheta) \sin \Phi,$$

$$\Phi^* \simeq \Phi - (\pi - 2\vartheta) \cos \Phi \tan \Theta,$$

$$\varphi^* \simeq \varphi + (\pi - 2\vartheta) \cos \Phi \sec \Theta.$$

Finally, the 4π averaged flux is

$$\langle F_\nu(E) \rangle_{4\pi} = \int_{-1}^{1} \langle F_\nu(E, \vartheta) \rangle_\varphi \, d\cos\vartheta = \frac{1}{2} \left[F_\nu^{\text{down}}(E) + F_\nu^{\text{up}}(E) \right].$$
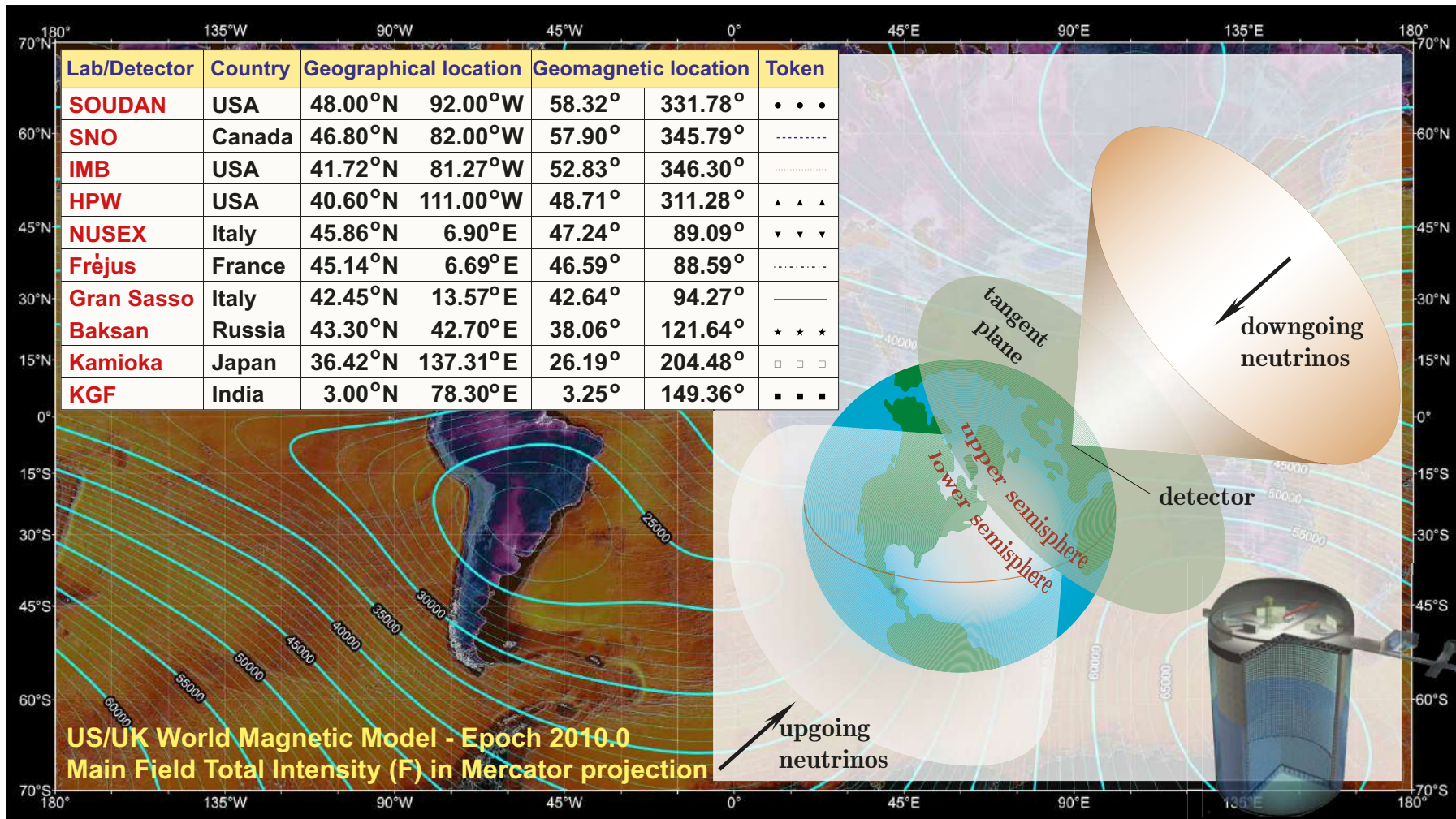
Lab/Detector	Country	Geographical location		Geomagnetic location		Token
SOUDAN	USA	48.00°N	92.00°W	58.32°	331.78°	• • •
SNO	Canada	46.80°N	82.00°W	57.90°	345.79°	--------
IMB	USA	41.72°N	81.27°W	52.83°	346.30°	·········
HPW	USA	40.60°N	111.00°W	48.71°	311.28°	▲ ▲ ▲
NUSEX	Italy	45.86°N	6.90°E	47.24°	89.09°	▼ ▼ ▼
Fréjus	France	45.14°N	6.69°E	46.59°	88.59°	-·-·-·-·
Gran Sasso	Italy	42.45°N	13.57°E	42.64°	94.27°	———
Baksan	Russia	43.30°N	42.70°E	38.06°	121.64°	⋆ ⋆ ⋆
Kamioka	Japan	36.42°N	137.31°E	26.19°	204.48°	□ □ □
KGF	India	3.00°N	78.30°E	3.25°	149.36°	■ ■ ■

US/UK World Magnetic Model - Epoch 2010.0
Main Field Total Intensity (F) in Mercator projection

Table shows a list of ten past and present underground laboratories. The "tokens" in the last column are used in next slide. The figure on the right schematically illustrates averaging over the upper and lower hemispheres. The background represents a map with isolines of the geomagnetic field intensity.

60
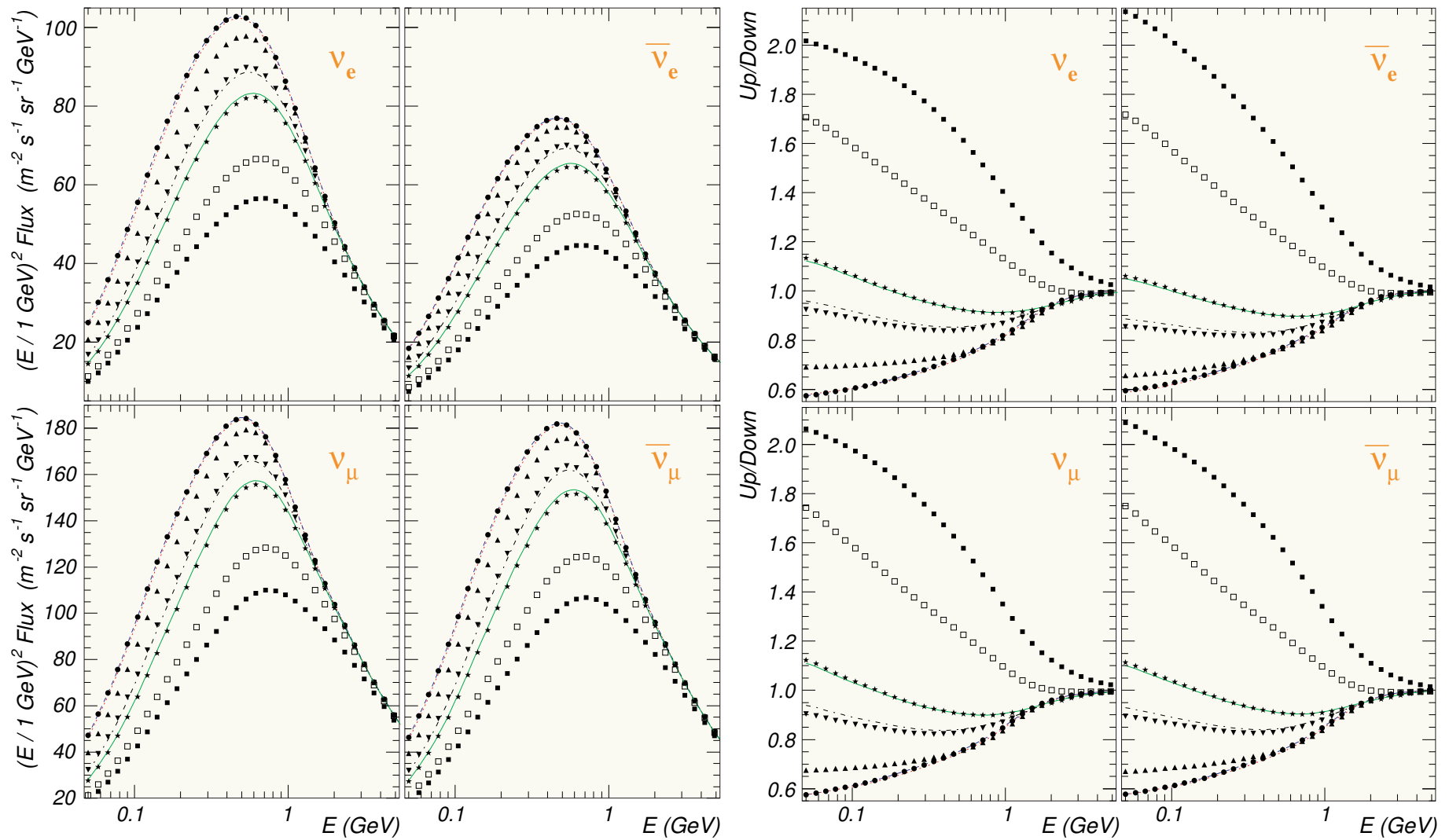
The 4π-averaged fluxes (*left panel*) and up-to-down ratios (*right panel*) of the ν_e, $\overline{\nu}_e$, ν_μ, and $\overline{\nu}_\mu$ fluxes for ten underground laboratories (see Table in p. 60 for the notation).

[From VN, "Atmospheric muons and neutrinos", in: *Proc. of the 2nd Workshop on Methodical Aspects of Underwater/Ice Neutrino Telescopes*, Hamburg, August 15–16, 2001, ed. by R. Wischnewski, pp.31–46, arXiv:hep-ph/0201310.]

AN fluxes at low and intermediate energies: Evidence for oscillations.
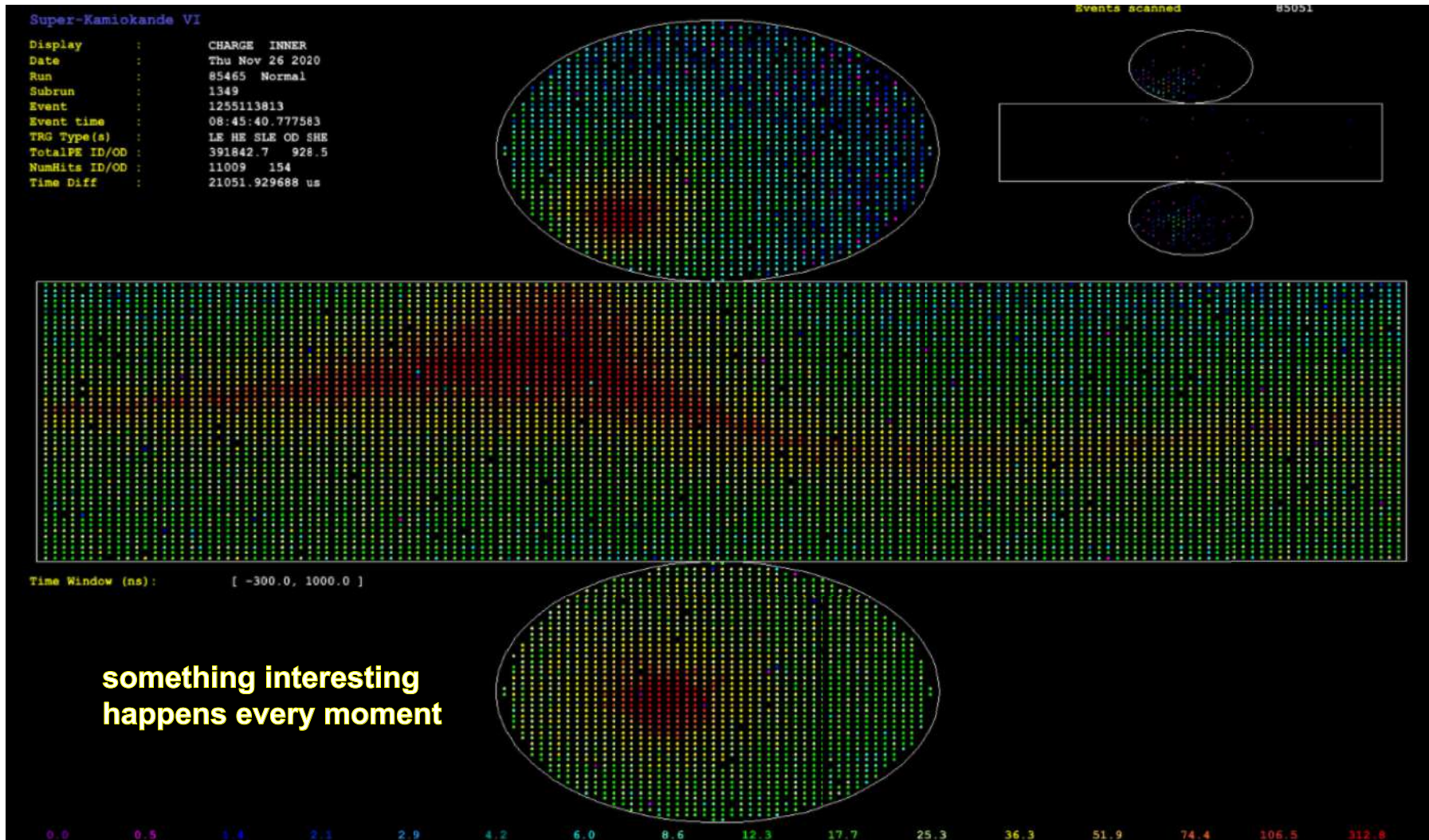
An event in the Super-Kamiokande Realtime Monitor which looks like a down-going through-going atmospheric muon. [From ⟨ http://www-sk.icrr.u-tokyo.ac.jp/realtimemonitor/ ⟩. Provided by Kamioka Observatory, ICRR, University of Tokyo]

The high effective granularity of the Super Kamiokande detector allows the accurate measurement of the energy, position, and direction of charged particles in the few MeV – few GeV energy range, and the pattern of hit phototubes also allows electrons to be distinguished from heavier particles like muons or pions. Figure shows the hit patterns from typical muon, electron, and neutral pion events in Super-Kamiokande.
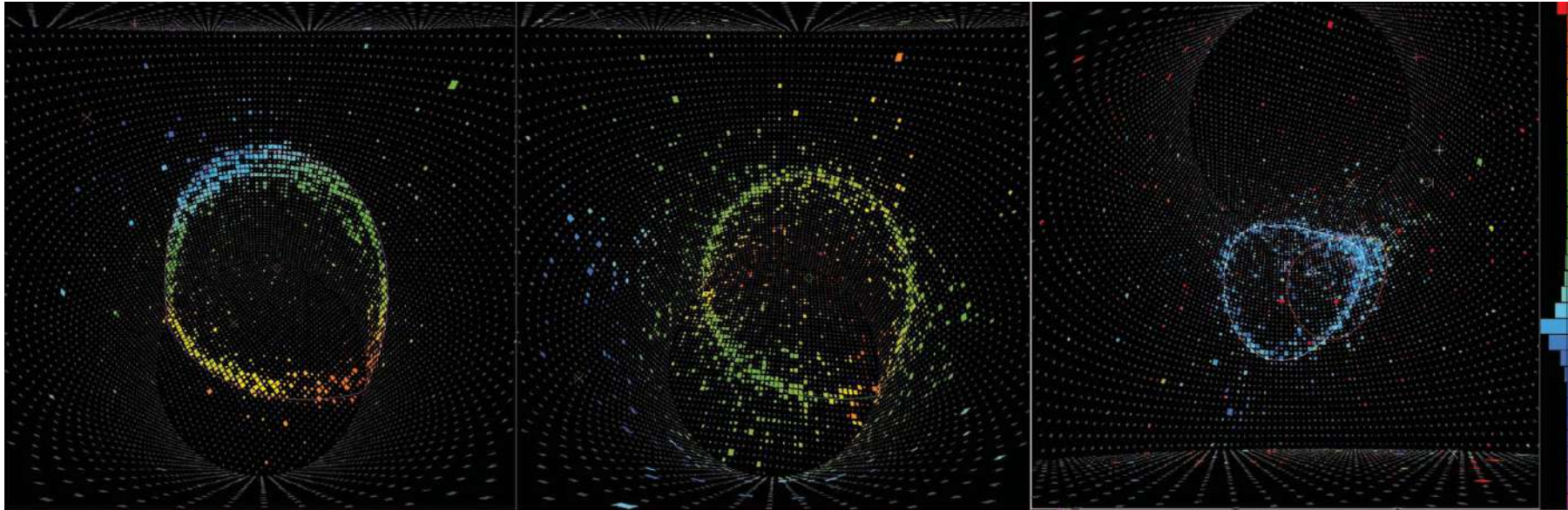
Left panel: a muon induced event, showing the clearly defined ring structure.

Middle panel: an electron induced event, showing the fuzzier ring caused by showering.

Right panel: an event from a π^0, and a 2nd ring can be seen on the right edge of the main ring.

Each colored square indicates a hit photomultiplier, with the size of the square showing the amount of charge in the phototube and the color the relative timing. The event discrimination is good enough to remove all but a handful of background events from the electron neutrino appearance sample.

[Borrowed from D. Wark, "The T2K experiment" (feature article), Nucl. Phys. News **19** (2009) 26–33.]
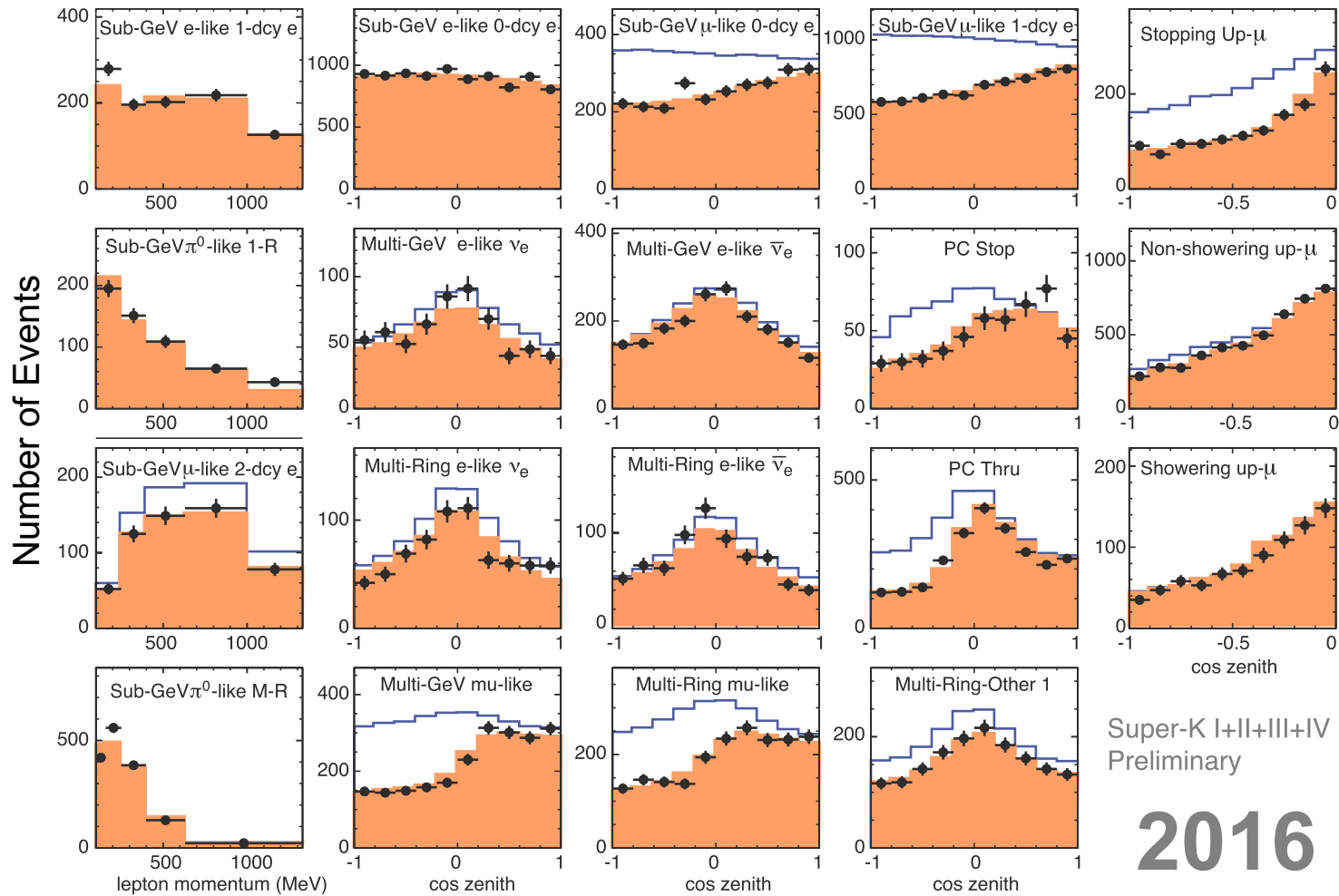
Zenith angle and momentum distributions for atmospheric neutrino subsamples used for recent analyses by Super-Kamiokande to study subleading effects, preferences for mass hierarchy and δ_{CP}, as well as searches for astrophysical neutrino sources such as dark matter annihilation.

[From T. Kajita *et al.* (for the Super-Kamiokande Collaboration), "Establishing atmospheric neutrino oscillations with Super-Kamiokande, "Nucl. Phys. B **908** (2016) 14–29.]
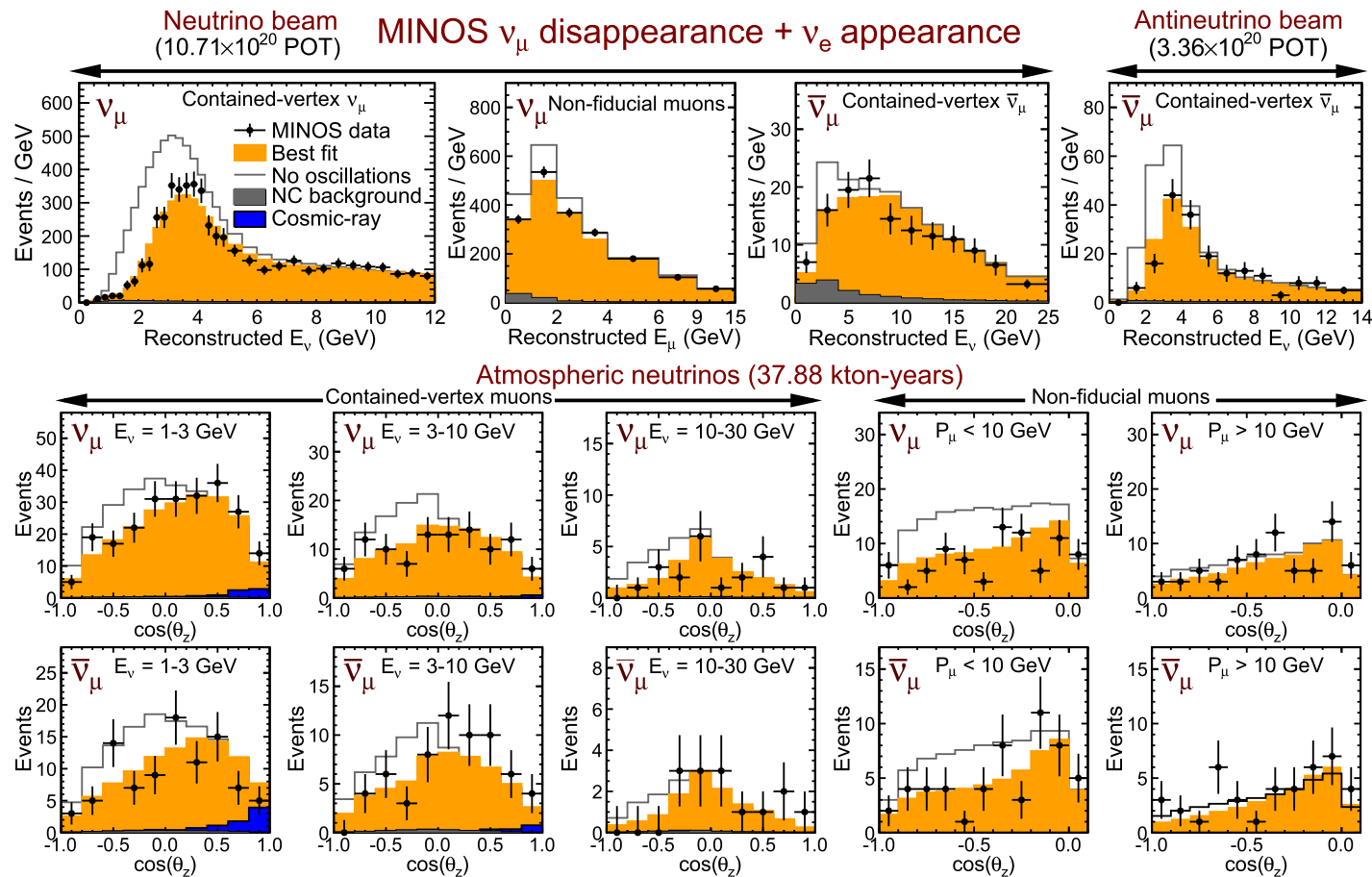
The event spectra at MINOS from 10.71×10^{20} POT FHC (ν_μ-dominated) mode, 3.36×10^{20} POT RHC ($\overline{\nu}_\mu$-dominated) mode and 37.88 kt·yrs of atmospheric data. The data are shown compared to the prediction in absence of oscillations (grey lines) and to the best-fit prediction (red). The beam histograms (top) also include the NC background component (filled grey) and the atmospheric histograms (bottom) include the cosmic-ray background contribution filled blue).

[From L. H. Whitehead (for the MINOS Collaboration), "Neutrino oscillations with MINOS and MINOS+," Nucl. Phys. B **908** (2016) 130–150. (POT = Protons-on-Target, FHC = Forward Horn Current, RHC = Reverse Horn Current.)]
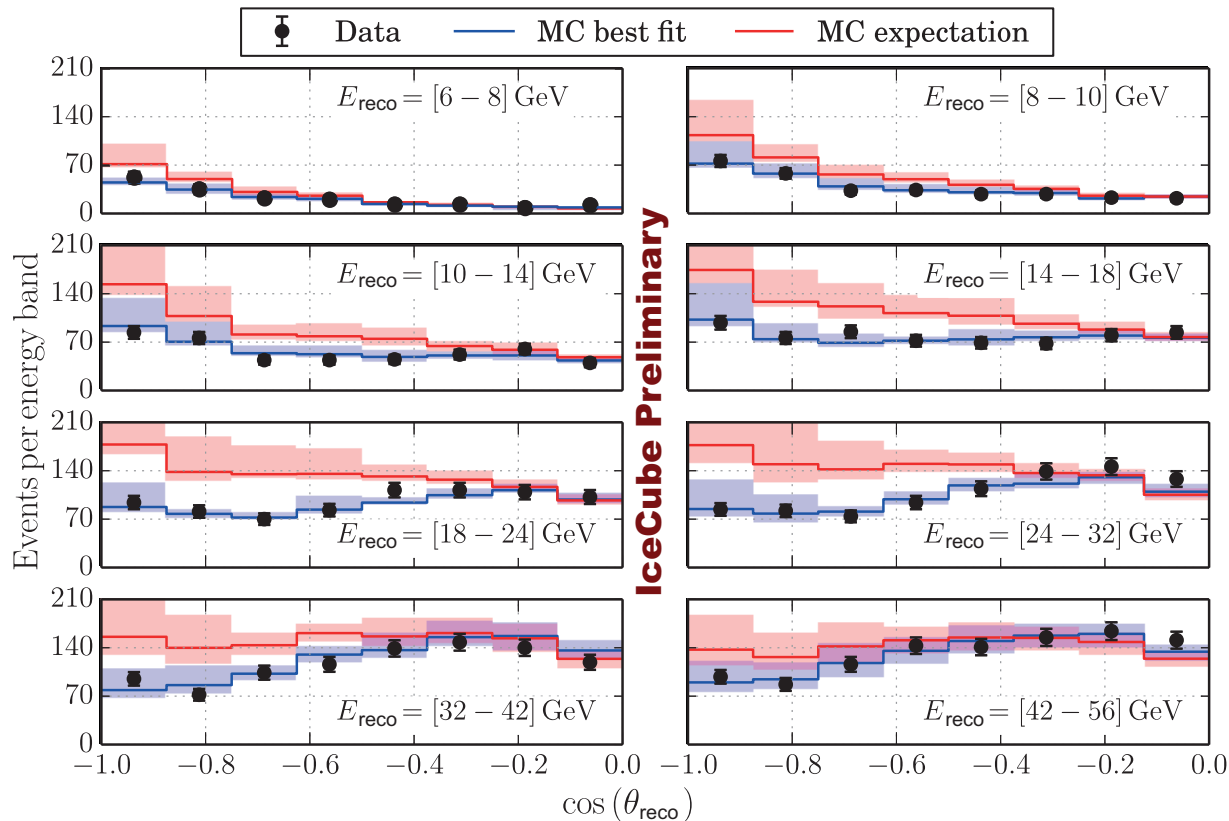
The **DeepCore** sub-array consists of 8 strings irregularly placed in the center of the IceCube detector. The string-to-string distances in this region range from 40 to 70 m. The strings are instrumented starting at a depth of 1760 m, and house PMTs with 35% higher efficiency than the standard IceCube PMTs. The separation between Digital Optical Modules (DOMs) in a string is of 7 m, with a *dusty* gap of 250 m between the DOMs 10 and 11.

⚠ Distribution of events in IceCube as a function of reconstructed direction and energy. Data are compared to the best fit and expectation without oscillations. Bands indicate assumed systematic uncertainties. The events of interest for the measurement are ν_μ and $\overline{\nu}_\mu$ charged current interactions in the DeepCore fiducial volume. Between May 2011 and April 2014, 953 days of good detector live-time are used. The analysis selects 5174 events with an expectation from simulation of 6980 without oscillations.

[From J. P. Yanez (for the IceCube Collaboration), "Results from atmospheric neutrino oscillations with IceCube DeepCore," AIP Conf. Proc. **1666** (2015) 100002.]
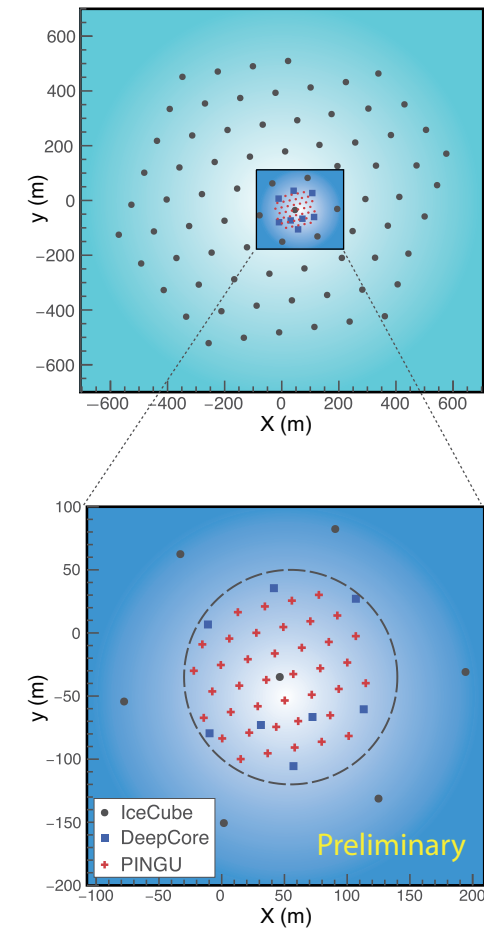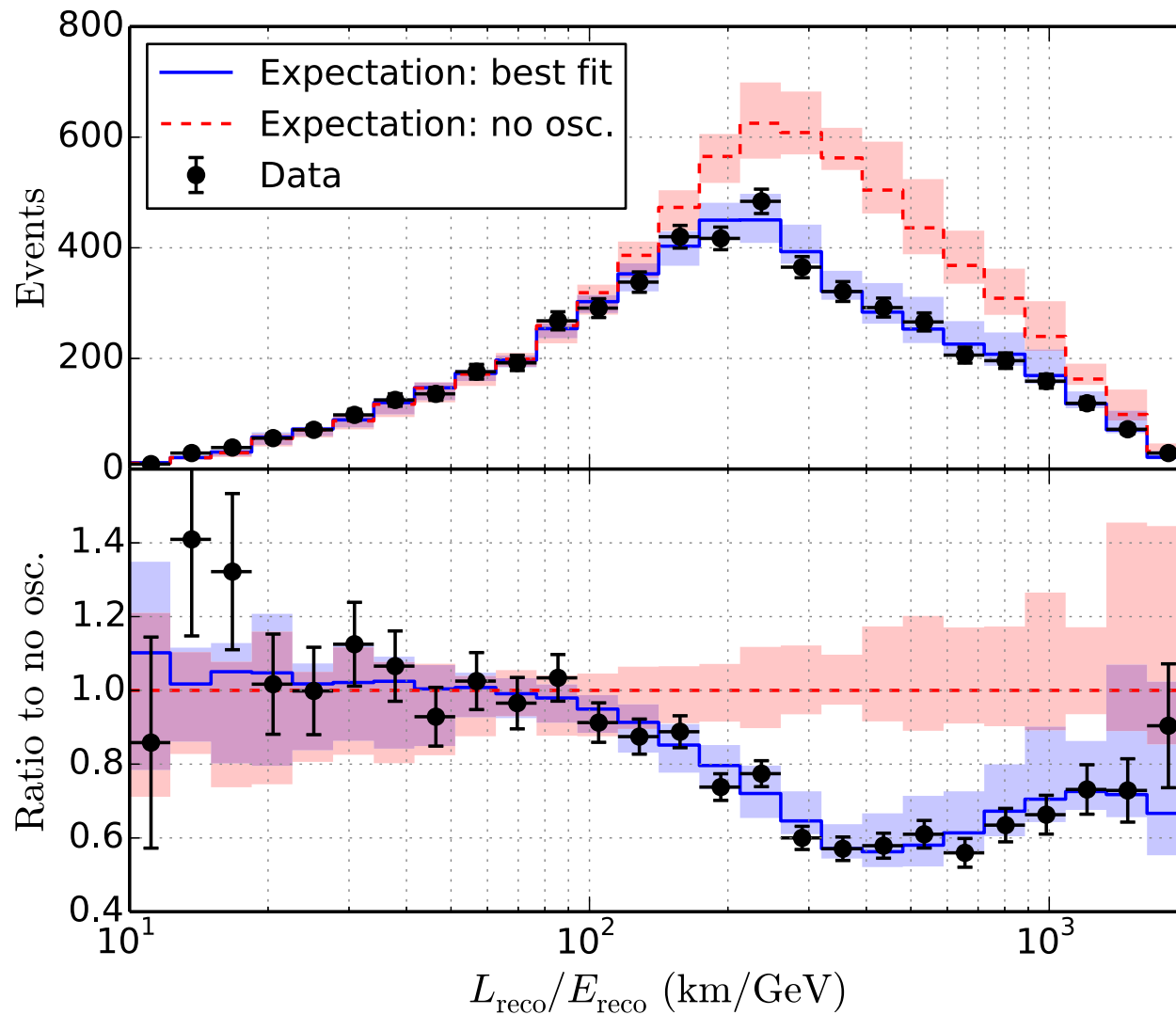
The events from 953 days of the IceCube-DeepCore data used in the analysis, plotted against L/E so that deviations arising from the oscillation can be seen. The solid line shows the best fit to the data while the dashed line illustrates the "no oscillation" scenario.
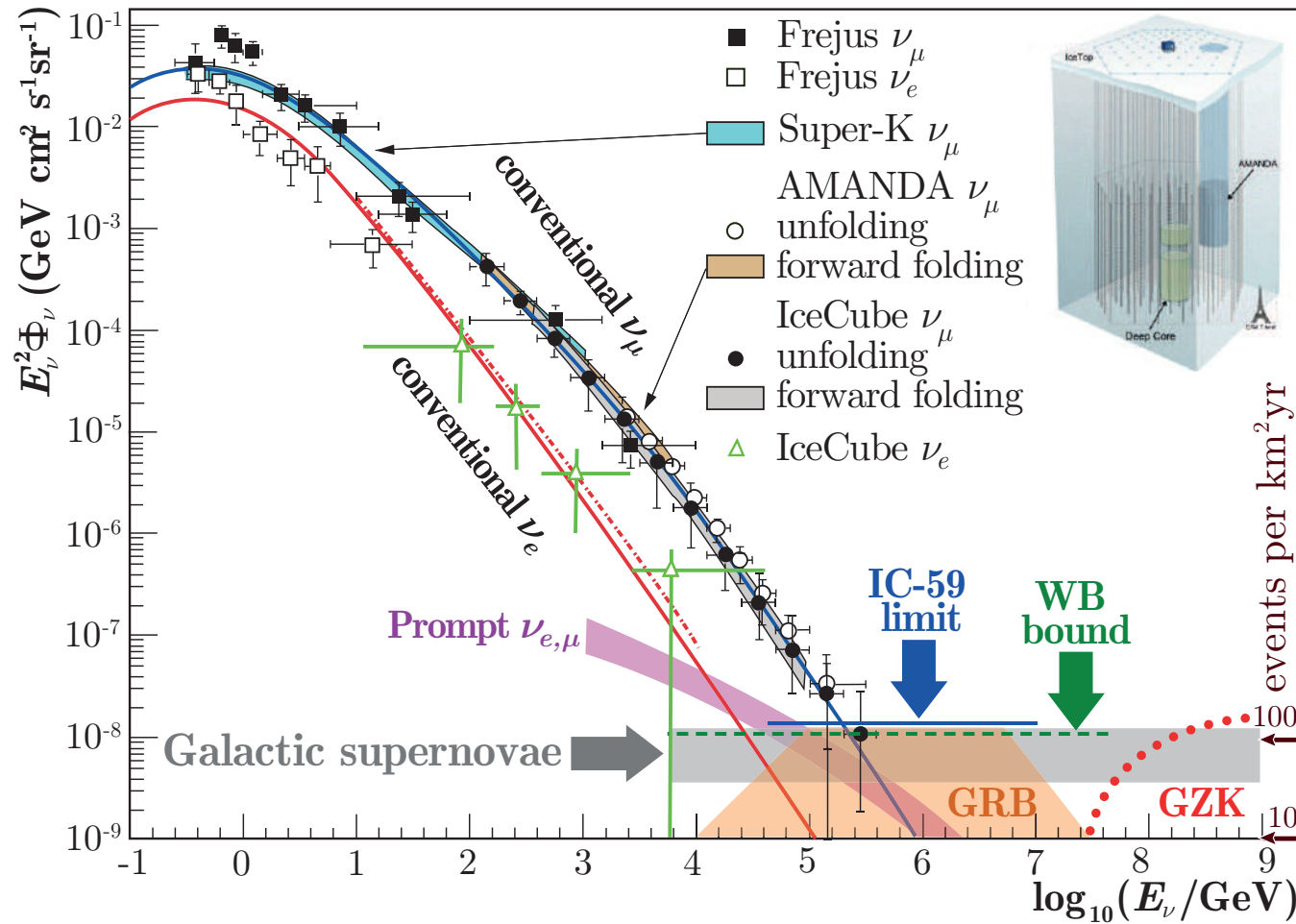
[From M. G. Aartsen *et al.*, "Neutrino oscillation studies with IceCube-DeepCore," Nucl. Phys. B **908** (2016) 161–177.]

AN fluxes at high energies.
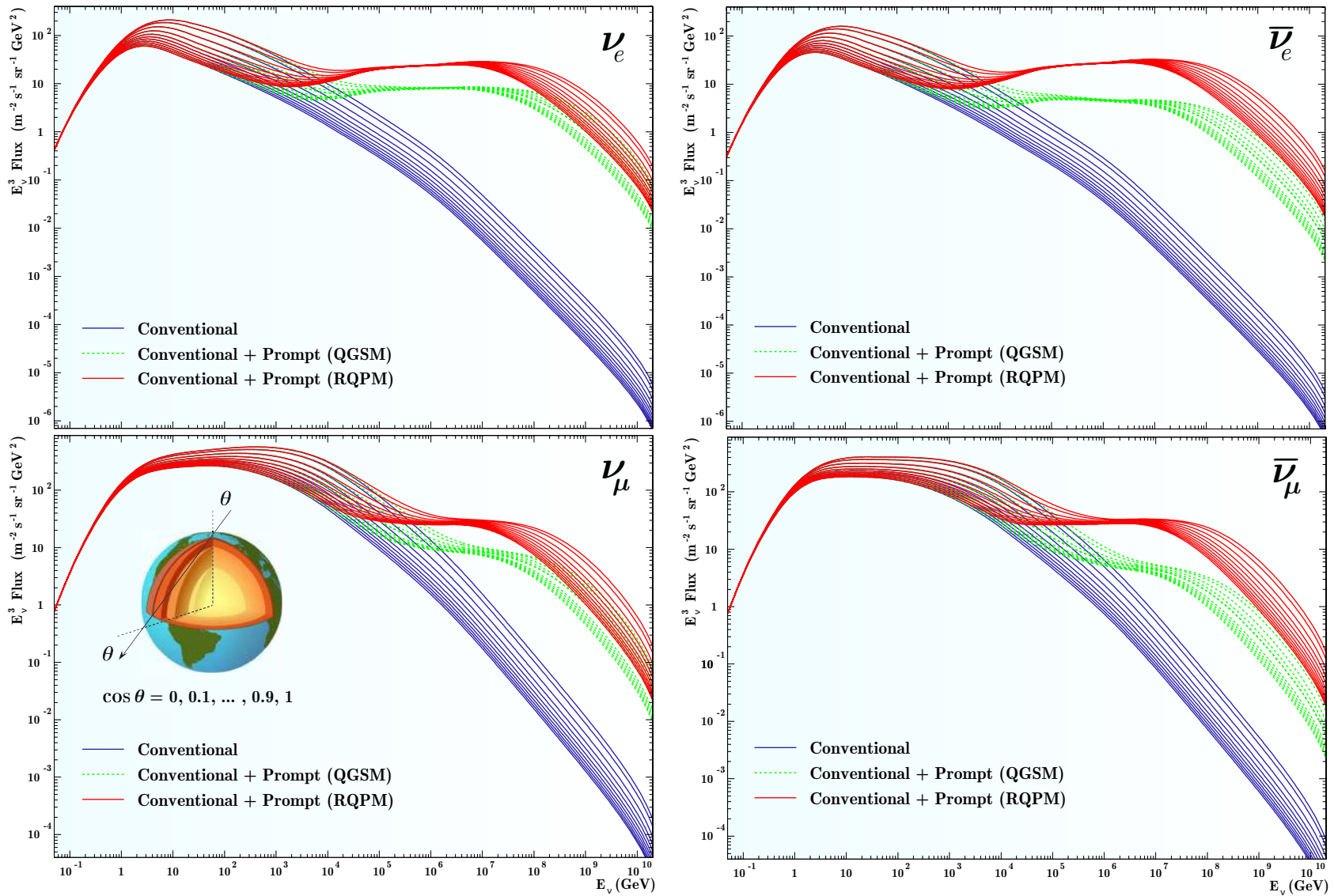
The energy spectra of downward-going ANs for 11 zenith angles with $\cos\theta$ varied from 0 to 1 with an increment of 0.1. The range below several GeVs is for Kamioka site. [See Ref. in p. 61.]
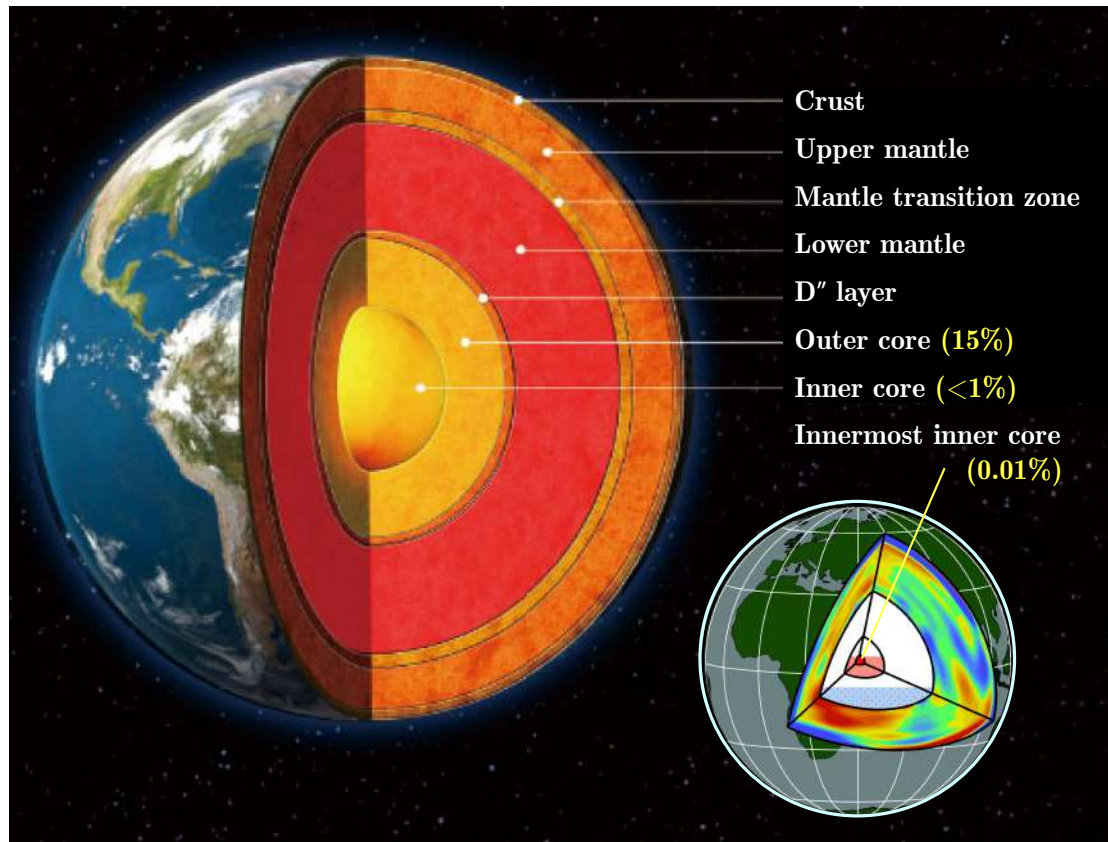
State of the art on September 2013.

Figure legend and axis labels: $E_\nu^2 \Phi_\nu$ (GeV cm^2 s^{-1}sr^{-1}) vs $\log_{10}(E_\nu/\text{GeV})$; events per km^{2}yr. Legend: Frejus ν_μ, Frejus ν_e, Super-K ν_μ, AMANDA ν_μ unfolding, forward folding, IceCube ν_μ unfolding, forward folding, IceCube ν_e. Labels: conventional ν_μ, conventional ν_e, Prompt $\nu_{e,\mu}$, Galactic supernovae, IC-59 limit, WB bound, GRB, GZK.

◁ The atmospheric muon and electron neutrino fluxes as measured by several experiments, together with the theoretical predictions. Also shown is a sample expectation of the cosmic-neutrino fluxes produced by SNRs, GRBs, cosmogenic (GZK) neutrino flux, Waxman-Bahcall (WB) upper bound,

and the IceCube upper limit (IC-59, 59-string configuration) for cosmic muon neutrinos.

[From A. Kappes (for the IceCube Collaboration), "Neutrino astronomy with the IceCube observatory," J. Phys. Conf. Ser. **409** (2013) 012014, arXiv:1209.5855 [astro-ph.HE]; F. Halzen, "The highest energy neutrinos: first evidence for cosmic origin," in Proceedings of the 33rd International Cosmic Ray Conference (Rio de Janeiro, July 2-9, 2013), p. 1289.]

Digression: Interior structure of Earth.

Crust
Upper mantle
Mantle transition zone
Lower mantle
D″ layer
Outer core (15%)
Inner core (<1%)
Innermost inner core (0.01%)

△ A schematic view of Earth's interior.

"Almost everything known or inferred about the inner core, from seismology or indirect inference, is controversial".
D. L. Anderson, "The inner core of Earth," Proc. Natl. Acad. Sci. USA **99** (2002) 13966–13968.

The volumetric relation of the various regions of the core to the whole Earth is shown in the insert: outer core (pale blue) occupies 15%, the inner core (pink) occupies less than 1%, and innermost inner core (red) constitutes only 0.01% of Earth's volume.

The Earth core lies beneath 3,000-km thick, heterogeneous mantle (anomalies with higher than average seismic speed are shown in blue and those with lower than average speed are shown in red) making investigations of core properties challenging.

Preliminary reference Earth model.

For the radial density distribution in the Earth, it is now conventional to use the so-called "Preliminary Reference Earth Model" (PREM).[a]

In PREM, the Earth is divided into 10 concentric layers and the density distribution, $\rho = \rho(R)$, in each layer is approximated by a cubical polynomial:

$$\rho(R) = \sum_{k=0}^{3} a_{nk} \left(R/R_{\oplus} \right)^k,$$
$$R_n \leq R < R_{n+1},$$
$$n = 0, 1, \ldots, 9$$
$$(R_0 = 0, \ R_{10} = R_{\oplus}).$$

The nonzero coefficients a_{nk} [in g/cm^3] are listed in Table.

| n	R_{n+1} (km)	a_{n0}	a_{n1}	a_{n2}	a_{n3}
0	1221.5	13.0885		-8.8381	
1	3480.0	12.5815	-1.2638	-3.6426	-5.5281
2	5701.0	7.9565	-6.4761	5.5283	-3.0807
3	5771.0	5.3197	-1.4836		
4	5971.0	11.2494	-8.0298		
5	6151.0	7.1089	-3.8045		
6	6346.6	2.6910	0.6924		
7	6356.0	2.9000	$\leftarrow$ crust (must be replaced		
8	6368.0	2.6000	with the local values)		
9	6371.0	1.0200	$\leftarrow$ ocean (ditto)		

Coefficients of the polynomials for the PREM.

[a]A. M. Dziewonski and D. L. Anderson, Phys. Earth Planet. Inter. **25** (1981) 297–356; see also A. M. Dziewonski, "Earth structure, global", in Encyclopedia of solid Earth geophysics, edited by D. E. James (Van Nostrand Reinhold, New York, 1989), pp. 331–359.

The figure on the left shows the Earth layers according to PREM. The four outermost and two inner layers are shown as single ones. Radial density distribution in the Earth calculated according to PREM is shown in Figure on the right.
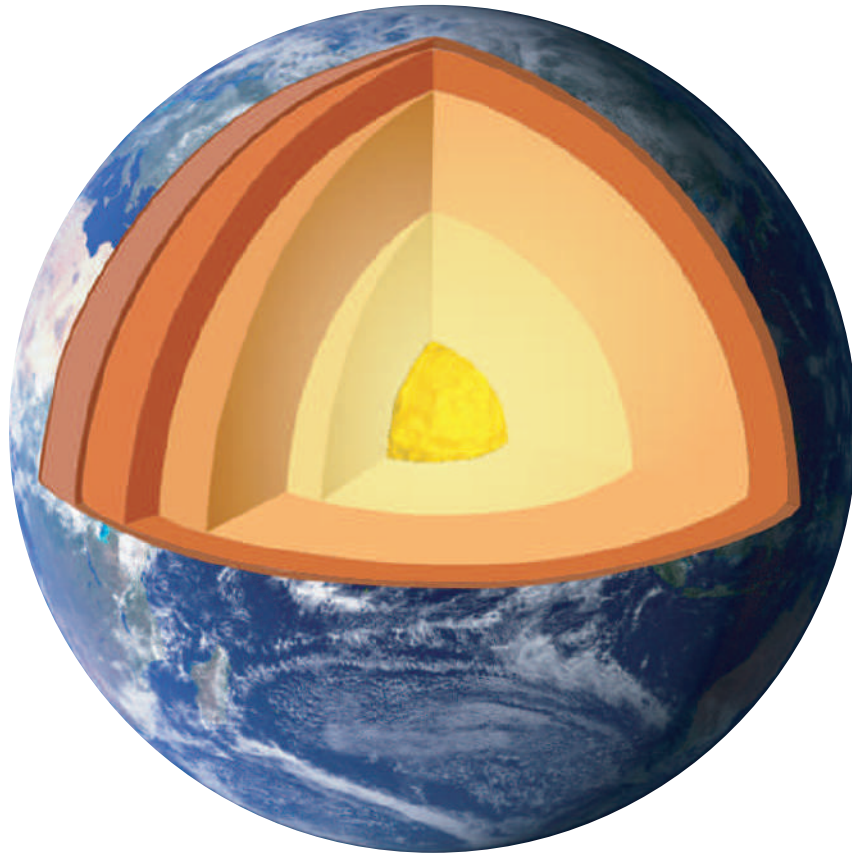
A schematic view of the Earth layers according to PREM.
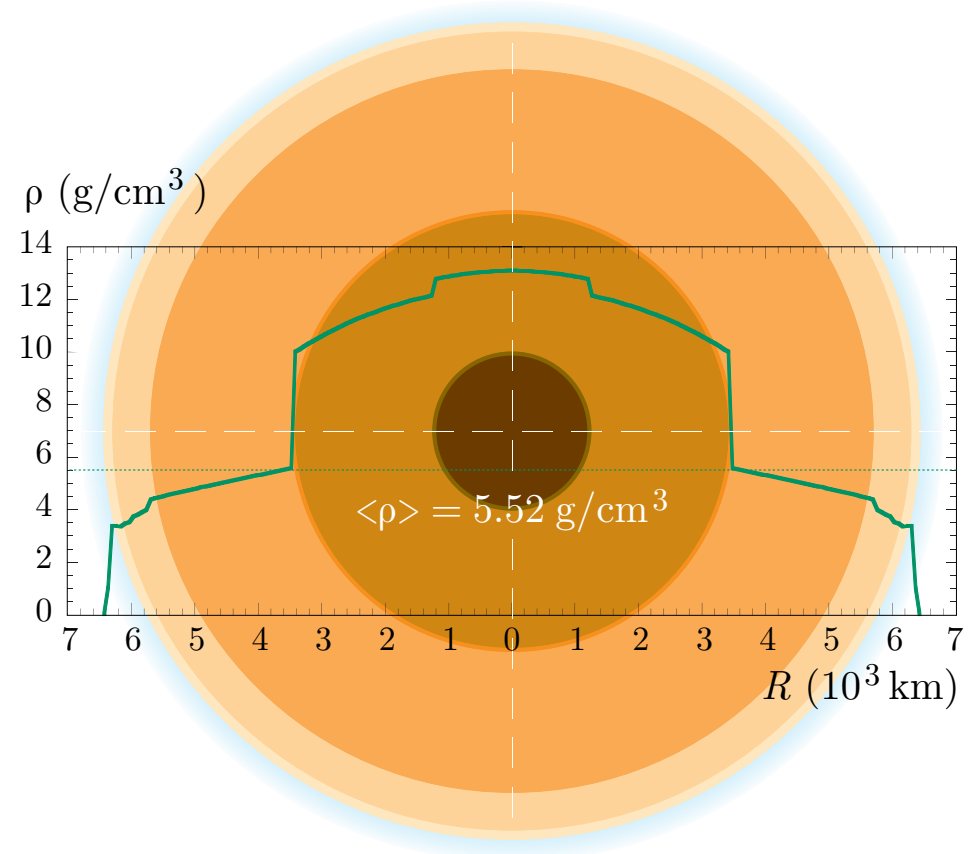
Radial density distribution in the Earth according to PREM.

Chemical composition of the Earth (where the devil dwells in?)

Measurements of the propagation of seismological waves in the Earth and studies of the properties of minerals under high pressure, have been combined to determine the chemical composition of the Earth's interior.

It is dominated by the elements **iron (Fe)**, **oxygen (O)**, **silicon (Si)**, **magnesium (Mg)**, **nickel (Ni)** and **sulfur (S)**. This is because most of the mass of the Earth occurs within the mantle which is composed largely of the ferromagnesium silicate minerals olivine and pyroxenes.

• The **crust** of the Earth mainly comprises the minerals plagioclase, quartz and hornblende and is dominated by the elements **oxygen (O)**, **silicon (Si)**, **aluminium (Al)**, **iron (Fe)**, **calcium (Ca)**, **sodium (Na)** and **potassium (K)**.

• The **core** of the Earth is largely composed of iron-nickel alloy.

Element	1980/82	1993
Magnesium (Mg)	0.0475	0.0389
Silicon (Si)	0.0326	0.0376
Calcium (Ca)	0.0184	0.0178
Sulfur (S)	0.284	0.285
Iron (Fe)	1.45	1.46
Nickel (Ni)	0.0831	0.0871

Masses ($\times 10^{27}$ g) of the six most abundant elements in the whole Earth's core as estimated by Herndon.

[For more details, see J. M. Herndon, Phys. Earth Planet. Inter. **105** (1998) 1 and references therein.]

The overall composition of the Earth is very similar to that of meteorites, and because of this, it is thought that the Earth originally formed from *planetesimals* composed largely of metallic iron and silicates.

Charge-to-mass ratio distribution in Earth.

The mean charge-to-mass ratio, $\langle Z/A \rangle$, has been estimated by Bahcall and Krastev.[a]

Summary:

✦ $\langle Z/A \rangle = 0.468$ for the core
  (83% Fe, 9% Ni and 8% light elements
  with $Z/A = 0.5$),
✦ $\langle Z/A \rangle = 0.497$ for the mantle
  (41.2% SiO_2, 52.7% MgO and 6.1% FeO).

[These data are only in qualitative agreement with those in the Figure.]

The charge composition of the Earth may also be illustrated in terms of the number densities of u and d quarks and electrons.

The composition is almost isoscalar but the deviations are not negligible.
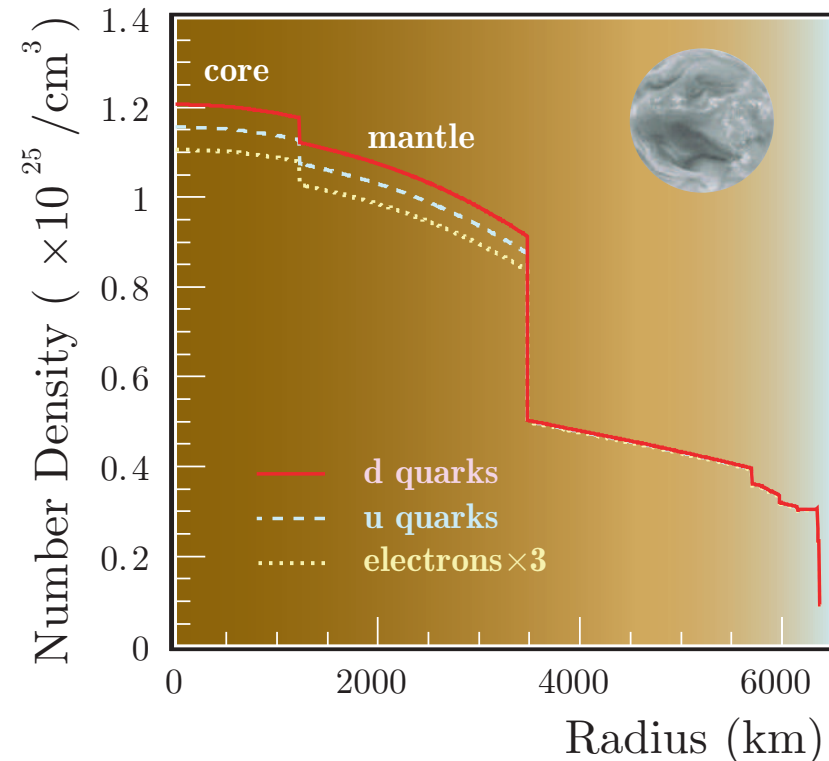
Estimated number densities of quarks and electrons vs distance from the center of the Earth. [From J. Kameda, Ph. D Thesis, University of Tokyo, September, 2002.]

---

[a] J. N. Bahcall and P. I. Krastev, Phys. Rev. C **56** (1997) 2839–2857. The estimations are based on the experimental data from Y. Zhao and D. L. Anderson, Phys. Earth Planet. Inter. **85** (1994) 273–292.

Earth's surface heat flow.
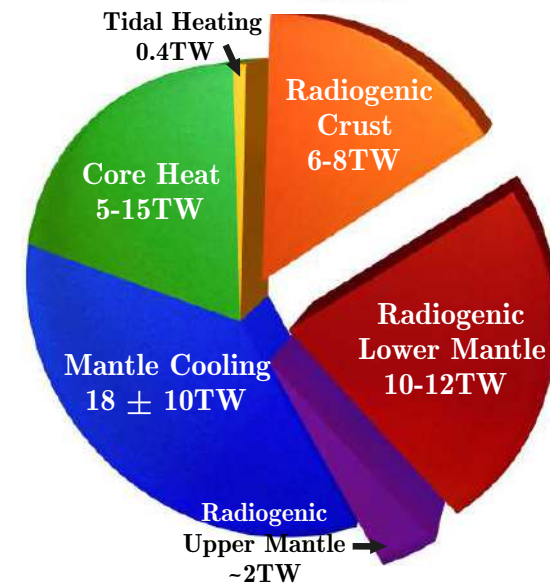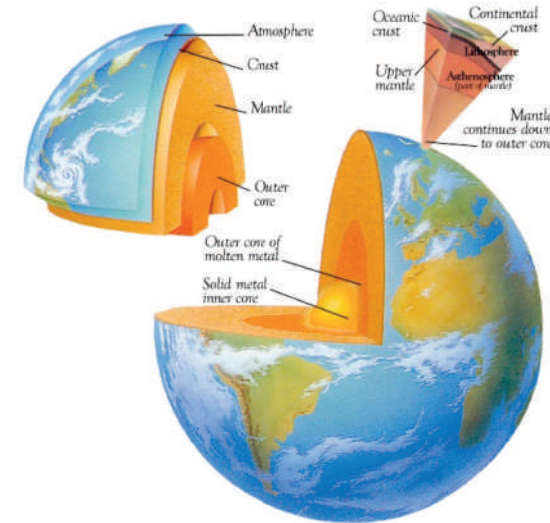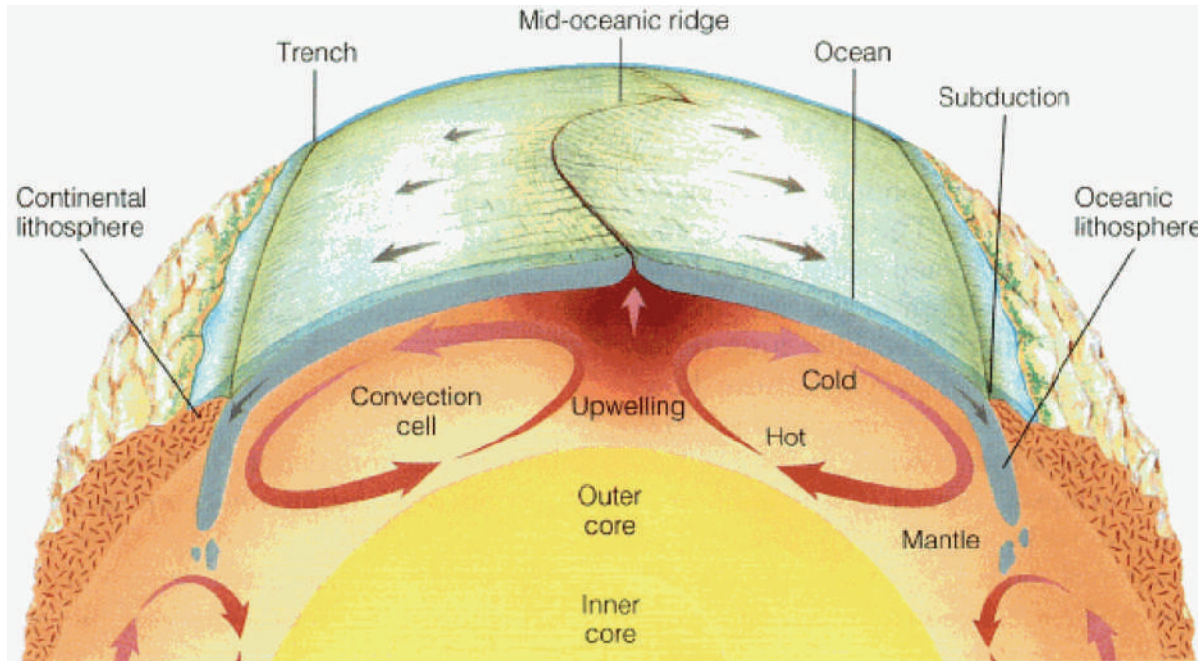
Where does the energy for convections, plate tectonics, etc. come from?

Total heat flow: 46 ± 3 TW (47 ± 2 TW).

$30 - 32$ TW measured (mainly based on bore holes), then extrapolated to account for ocean surface.

Geoneutrinos.

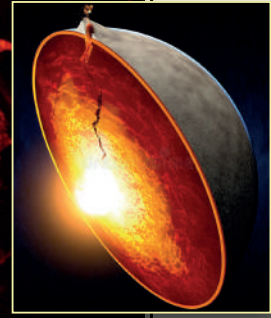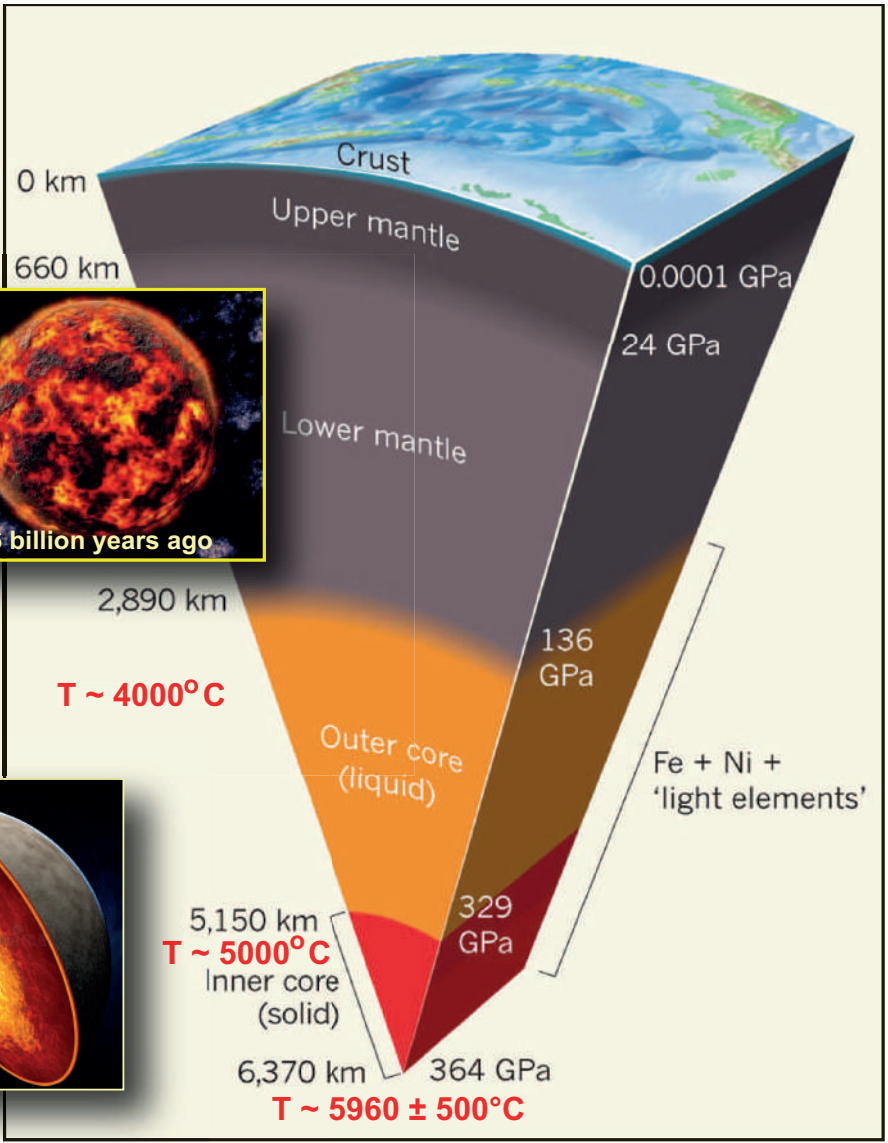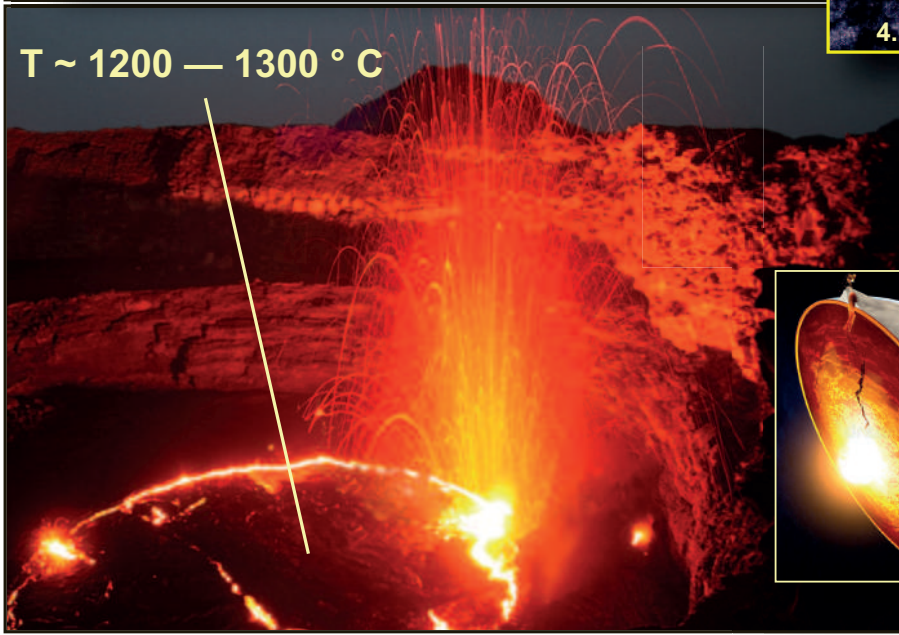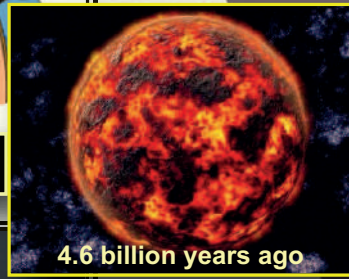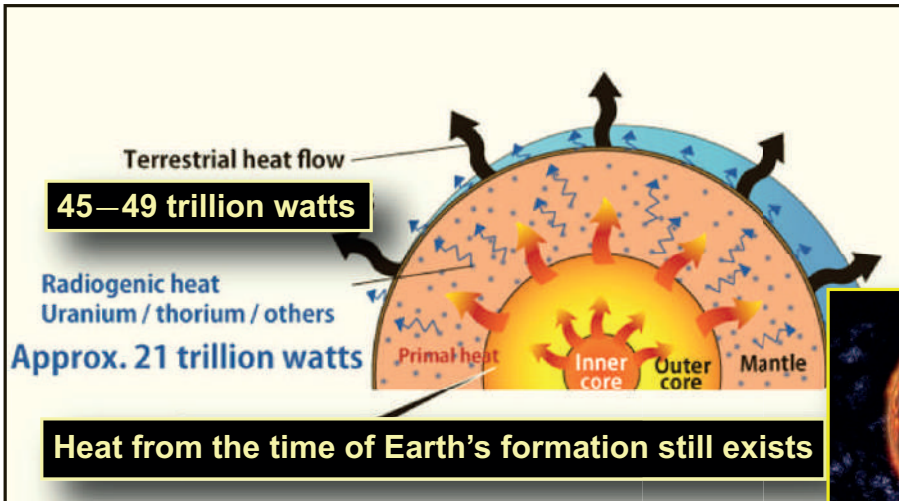The current estimate of radiogenic heat due to U, Th, and K decay is 20 ± 3 TW.

✦ Abundances of elements in extra-terrestrial rocks (namely, in carbonaceous chondritic meteorites) are similar to those in the solar photosphere.

✦ Composition of the Earth should be similar to these chondrites (which are believed to be of the same origin from which the Sun and Earth were formed)[a].

✦ These chondrites contain ^{238}U, ^{232}Th, and ^{40}K. Hence there should be similar concentrations of these isotopes in the Earth.

✦ From these meteorites, it is known that the Th/U mass ratio is about 3.9.

✦ Using these data, a typical "reference" model predicts:

  ○ Uranium and Thorium account for about 8 TW each,
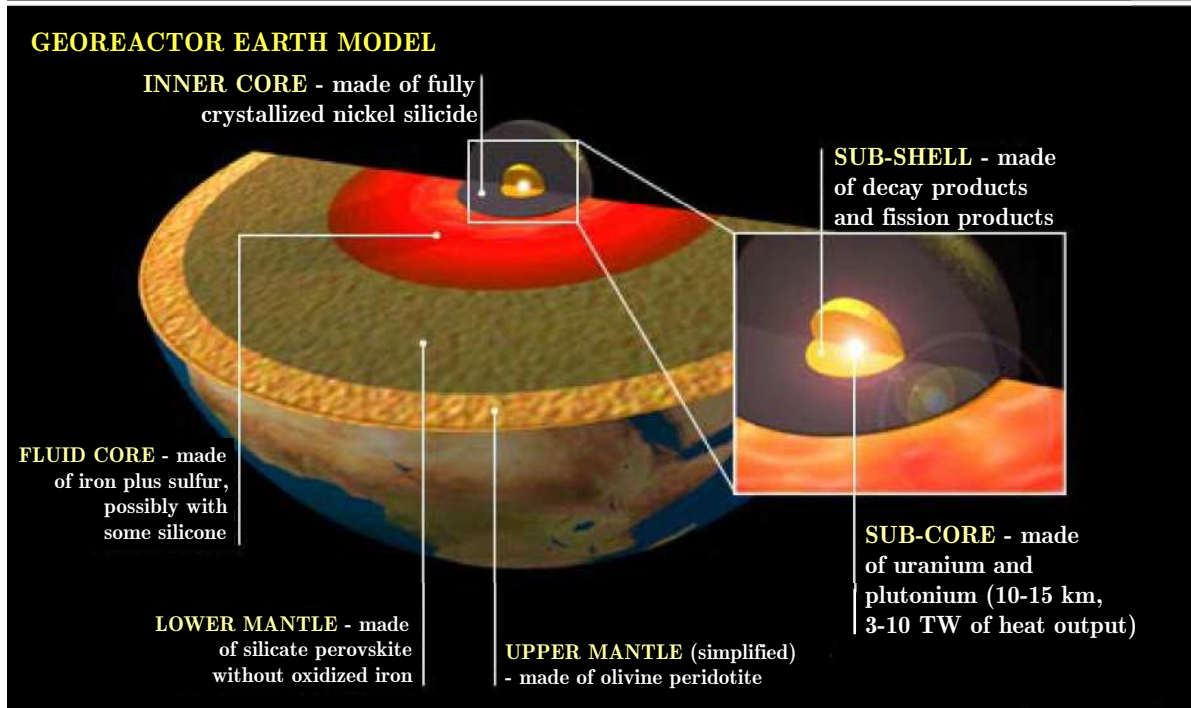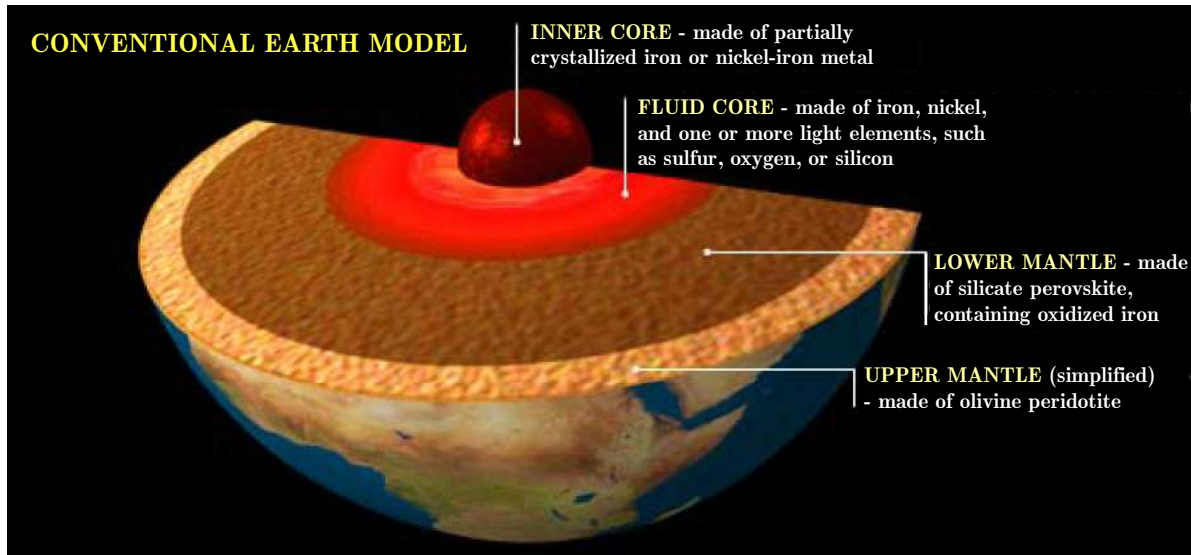 ○ Potassium accounts for 3–4 TW.

$$\Downarrow$$

Total radioactive power is therefore around **20 TW**.

[a] Note that this is a very plausible inference, rather than a well-established fact, see, e.g., I. H. Campbell & H. St. C. O'Neill, "Evidence *against* a chondritic Earth", Nature **483** (2012) 553–558.

Terrestrial heat flow

45—49 trillion watts

Radiogenic heat
Uranium / thorium / others
Approx. 21 trillion watts

Primal heat — Inner core — Outer core — Mantle

Heat from the time of Earth's formation still exists

4.6 billion years ago

T ~ 1200 — 1300 ° C

Crust

0 km

660 km   0.0001 GPa

Upper mantle   24 GPa

Lower mantle

2,890 km   136 GPa

T ~ 4000°C

Outer core (liquid)

Fe + Ni + 'light elements'

5,150 km   329 GPa

T ~ 5000°C
Inner core (solid)

6,370 km   364 GPa

T ~ 5960 ± 500°C

CONVENTIONAL EARTH MODEL

INNER CORE - made of partially crystallized iron or nickel-iron metal

FLUID CORE - made of iron, nickel, and one or more light elements, such as sulfur, oxygen, or silicon

LOWER MANTLE - made of silicate perovskite, containing oxidized iron

UPPER MANTLE (simplified) - made of olivine peridotite

GEOREACTOR EARTH MODEL

INNER CORE - made of fully crystallized nickel silicide

SUB-SHELL - made of decay products and fission products

FLUID CORE - made of iron plus sulfur, possibly with some silicone

SUB-CORE - made of uranium and plutonium (10-15 km, 3-10 TW of heat output)

LOWER MANTLE - made of silicate perovskite without oxidized iron

UPPER MANTLE (simplified) - made of olivine peridotite

Georeactor is not a mainstream model but it is motivated by

✦ the observation that the ^{3}He/^{4}He high at some volcanic eructations,

✦ Oklo natural reactor 2 Gy ago (anomalous ^{235}U/^{238}U, ^{140}Ce/^{142}Ce, ^{147}Sm/^{149}Sm ratios, concentrations of Nd isotopes).

The georeactor in the center of Earth should produce $\overline{\nu}$s according to reactor spectrum.

Decay chain (natural abundance, half-life)	$E_{\max}$ [MeV]	Q [MeV]	Q_{eff} [MeV]	$\varepsilon_{\overline{\nu}}$ [1/(kg s)]	ε_H [W/kg]	$\varepsilon'_{\overline{\nu}}$ [1/(kg s)]	ε'_H [W/kg]
$^{238}\text{U} \rightarrow {}^{206}\text{Pb} + 8\,{}^4\text{He} + 6e + 6\overline{\nu}$	3.26	51.7	47.7	7.46×10^7	9.5×10^{-5}	7.41×10^7	9.4×10^{-5}
(NA = 0.9927, $T_{1/2} = 4.47 \times 10^9$ yr)							
$^{232}\text{Th} \rightarrow {}^{208}\text{Pb} + 6\,{}^4\text{He} + 4e + 4\overline{\nu}$	2.25	42.7	40.4	1.62×10^7	2.7×10^{-5}	1.62×10^7	2.7×10^{-5}
(NA = 1.0000, $T_{1/2} = 1.40 \times 10^{10}$ yr)							
$^{40}\text{K} \rightarrow {}^{40}\text{Ca} + e + \overline{\nu}$ (89%)	1.311	1.311	0.590	2.32×10^8	2.2×10^{-5}	2.71×10^4	2.55×10^{-9}
$^{40}\text{K} + e \rightarrow {}^{40}\text{Ar} + \nu$ (11%)	0.044	1.505	1.461	=	6.5×10^{-6}	=	7.8×10^{-10}
(NA = 1.17×10^{-4}, $T_{1/2} = 1.28 \times 10^9$ yr)							
$^{235}\text{U} \rightarrow {}^{207}\text{Pb} + 7\,{}^4\text{He} + 4e + 4\overline{\nu}$	1.23	46.4	44	3.19×10^8	5.6×10^{-4}	2.30×10^6	4.0×10^{-6}
(NA = 0.0072, $T_{1/2} = 7.04 \times 10^8$ yr)							
$^{87}\text{Rb} \rightarrow {}^{87}\text{Sr} + e + \overline{\nu}$	0.283	0.283	0.122	3.20×10^6	6.1×10^{-8}	8.91×10^5	1.7×10^{-8}
(NA = 0.2783, $T_{1/2} = 4.75 \times 10^{10}$ yr)							

Properties of ^{238}U, ^{232}Th, ^{40}K, ^{235}U, and ^{87}Rb and of their (anti)neutrinos. For each parent nucleus the table presents the natural isotopic mass abundance (NA), half-life ($T_{1/2}$), (anti)neutrino maximal energy ($E_{\max}$), Q value, $Q_{\text{eff}} = Q - \langle E_{(\nu,\overline{\nu})} \rangle$, antineutrino and heat production rates for unit mass of the isotope ($\varepsilon_{\overline{\nu}}$, ε_H), and for unit mass at natural isotopic composition ($\varepsilon'_{\overline{\nu}}$, ε'_H). Note that antineutrinos with energy above threshold for inverse beta decay on free proton ($E_{\text{th}} = 1.806$ MeV) are produced only in the firsts two decay chains.

[From G. Fiorentini *et al.*, "Geo-neutrinos and Earth's interior," Phys. Rept. **453** (2007) 117–172, arXiv:0707.3203 [physics.geo-ph].]

The main sources of geoneutrinos

80
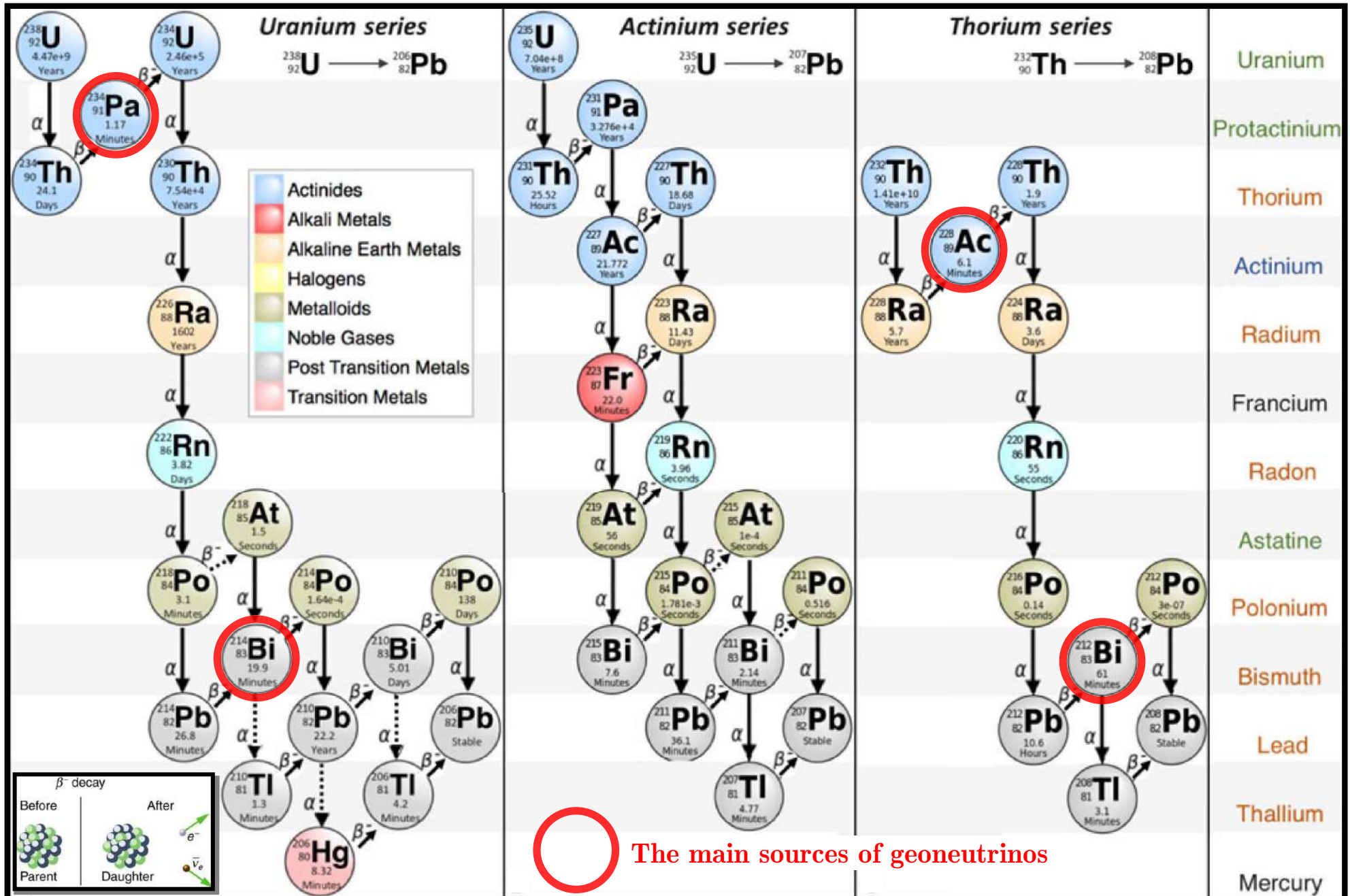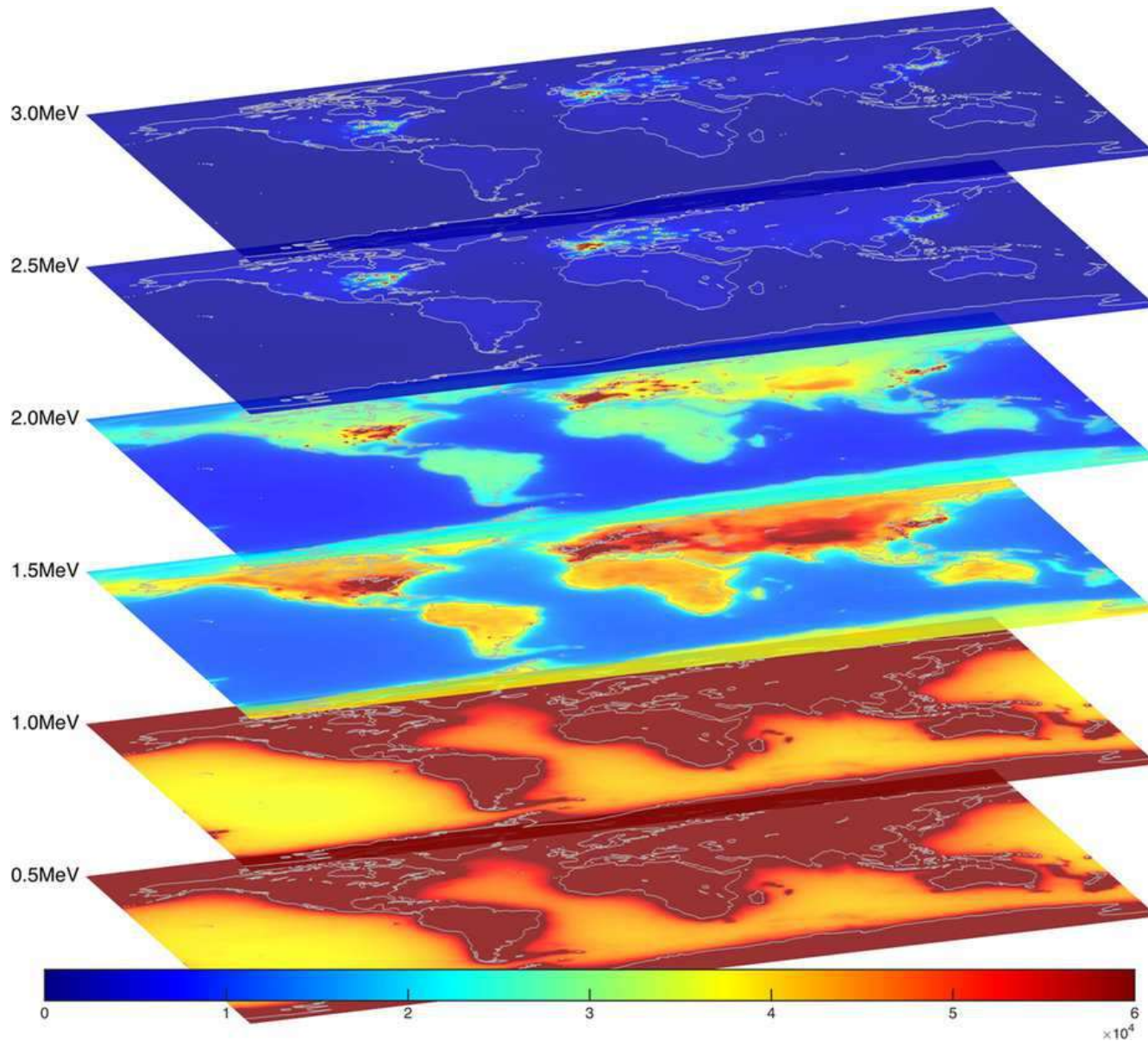
AGM2015 electron antineutrino flux (in units $\overline{\nu}_e/(\mathrm{cm}^2\,\mathrm{s}\,\mathrm{keV})$) displayed at 6 select energy bins out of the 1100 total AGM2015 energy bins, which uniformly span the $0-11$ MeV $\overline{\nu}_e$ energy range. Each energy bin is 10 keV wide. In conjunction with 720 longitude bins and 360 latitude bins, the highest resolution AGM2015 map is a $360 \times 720 \times 1100$ 3D matrix comprising $\sim 3 \times 10^8$ elements total.

[From S. M. Usman *et al.*, "AGM2015: Antineutrino Global Map 2015," Sci. Rep. **5** (2015) 13945, arXiv:1509.03898 [physics.ins-det].]
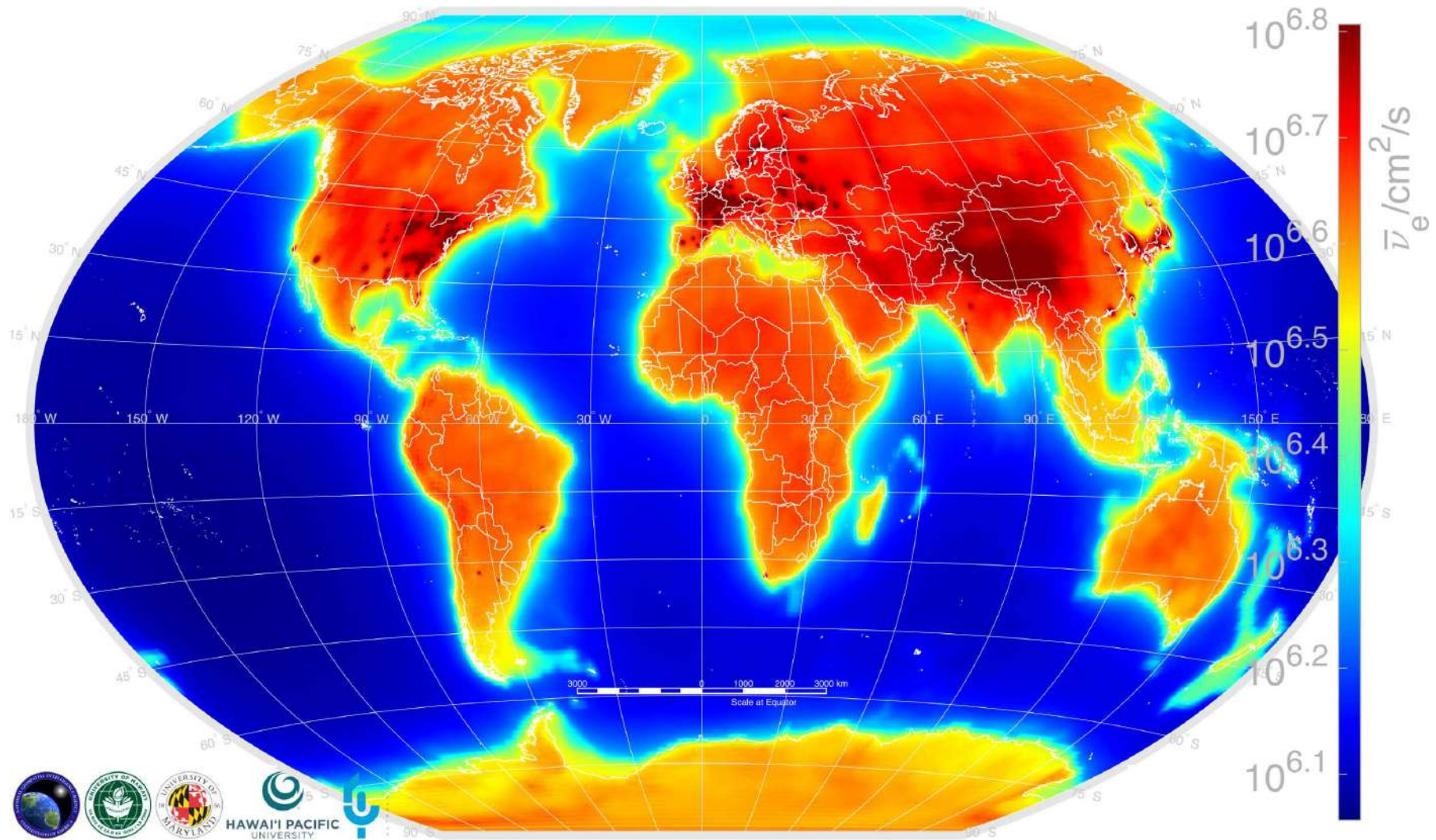
AGM2015: A worldwide $\overline{\nu}_e$ flux map combining geo-$\overline{\nu}_e$s from natural ^{238}U and ^{232}Th decay in the Earth's crust and mantle as well as $\overline{\nu}_e$s emitted by the man-made power reactors worldwide. Flux units are $\overline{\nu}_e/(\text{cm}^2\text{s})$ at the Earth's surface. The map includes $\overline{\nu}_e$s of all energies.
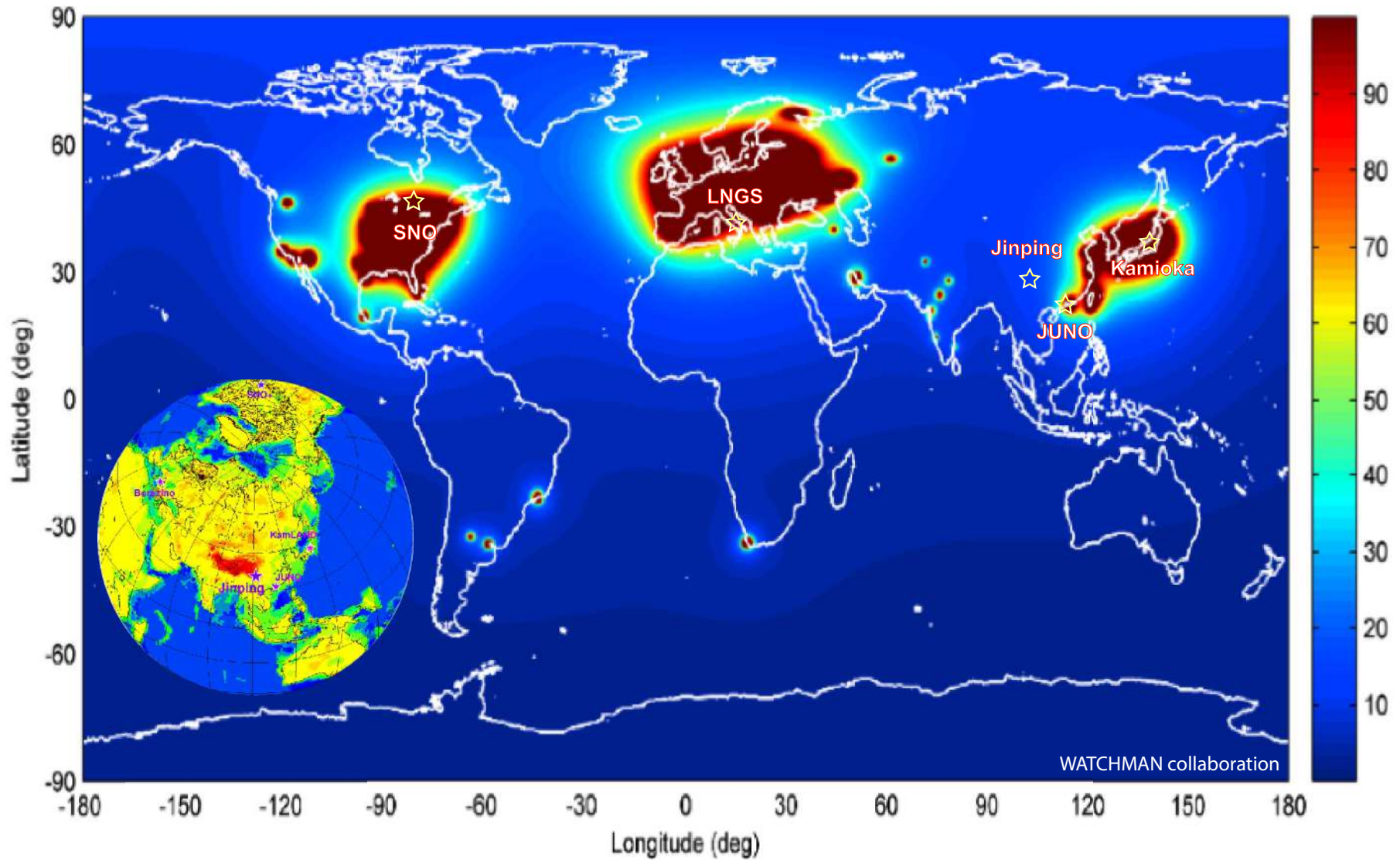
A map of the global nuclear reactor $\overline{\nu}_e$ flux, showing the three important industrialized regions that dominate the worldwide flux (by WATCHMAN simulation package).

[From URL: ⟨ https://ldrd-annual.llnl.gov/ldrd-annual-2015/nuclear/water ⟩.]
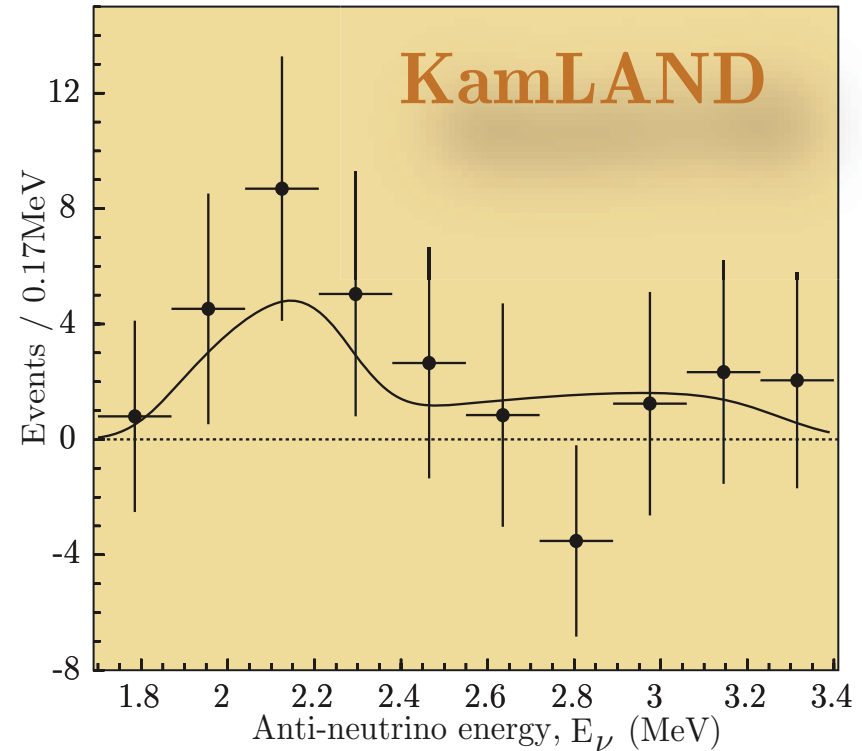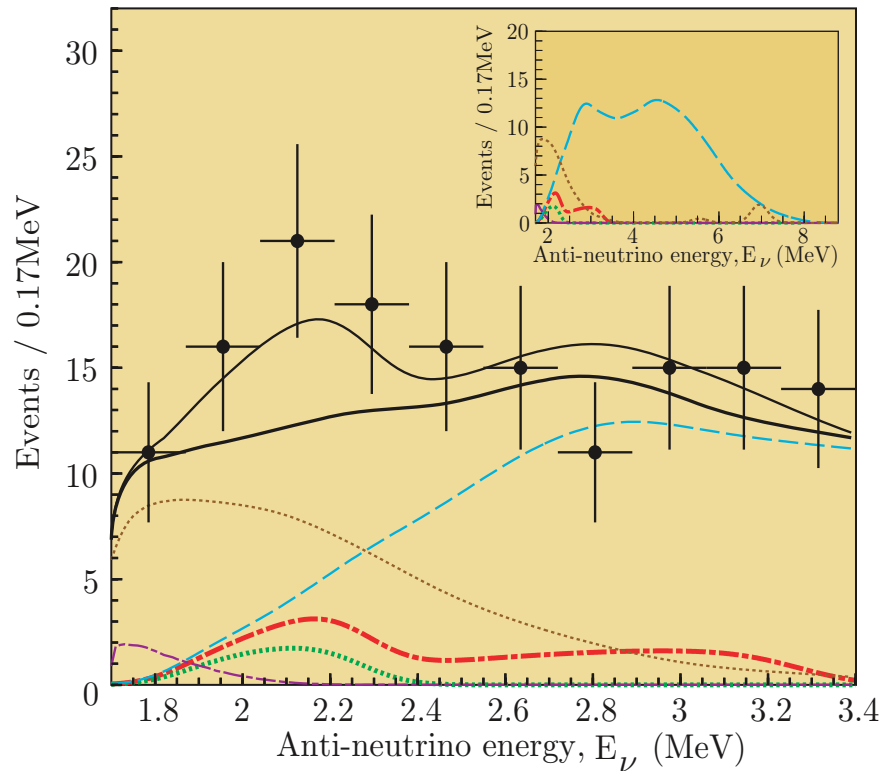
Left panel: $\overline{\nu}_e$ energy spectra of the candidate events (data), the total expectation (thin solid black line), the total background (thick solid black line), the expected ^{238}U (dot-dashed red line, the expected ^{232}Th (dotted green line), and the backgrounds due to reactor $\overline{\nu}_e$ (dash blue line), ^{13}C$(\alpha, n)^{16}$O reactions (dotted brown line) and random coincidences (dot-dashed violet line). The inset shows the expected signal extended to higher energies.

Right panel: $\overline{\nu}_e$ energy spectra of the candidate events substructed by the total backgrounds.

[From A. Suzuki (for the KamLAND Collaboration), "Reactor- and geo-neutrino detections from KamLAND", AIP Conf. Proc. **815** (2006) 19–28.]
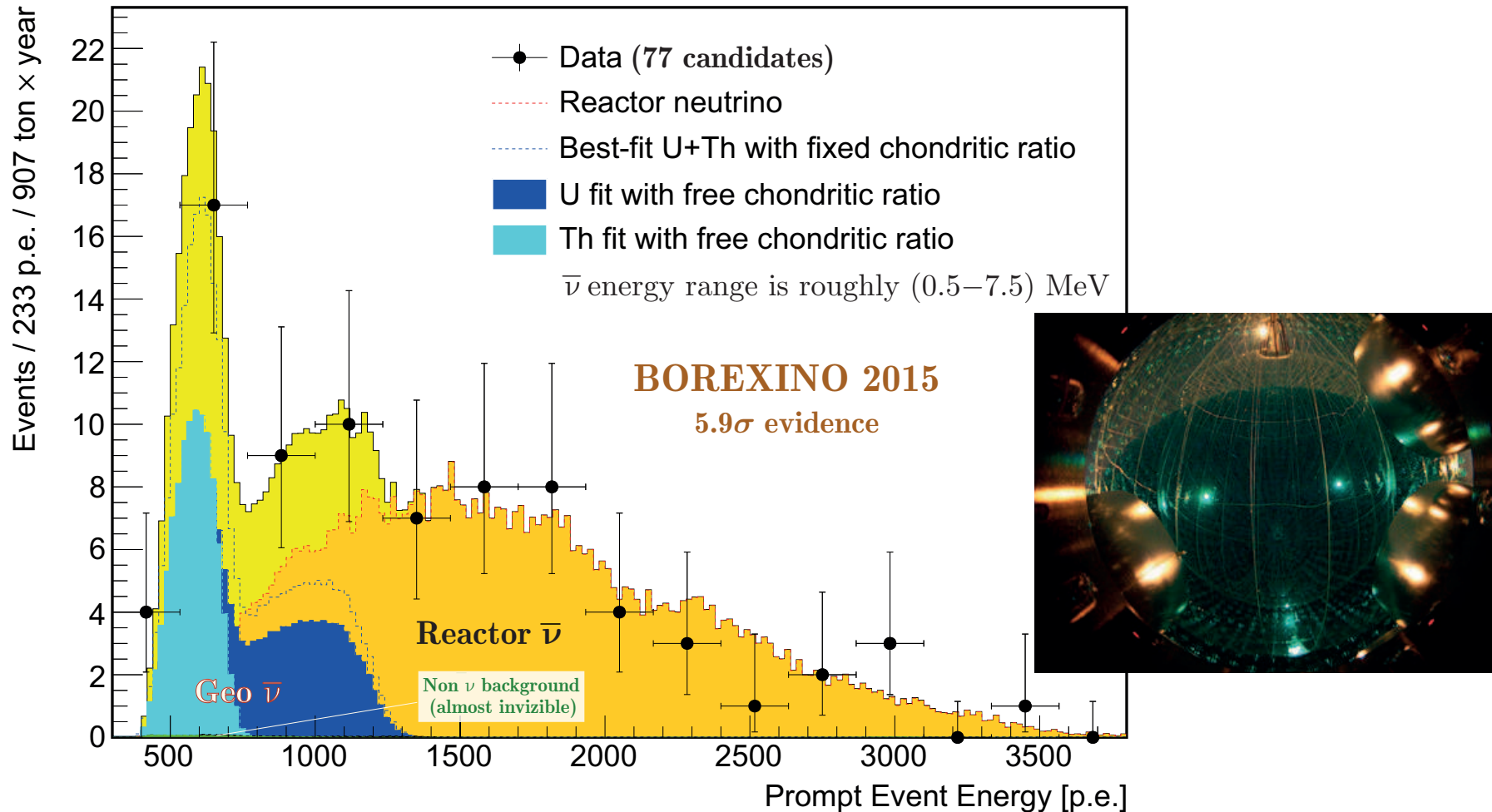
Borexino 2015 result: the prompt light yield spectrum, in units of photoelectrons (p.e.), of geo-$\overline{\nu}_e$ candidates and the best-fit. The best-fit shows the geo- and reactor $\overline{\nu}_e$ spectra (dotted lines) assuming the chondritic ratio. Colored areas show the result of a separate fit with U (blue) and Th (light blue) set as free and independent parameters.

[M. Agostini *et al.* (Borexino Collaboration), "Spectroscopy of geo-neutrinos from 2056 days of Borexino data", Phys. Rev. D **92** (2015) 031101(R), arXiv:1506.04610 [hep-ex].]

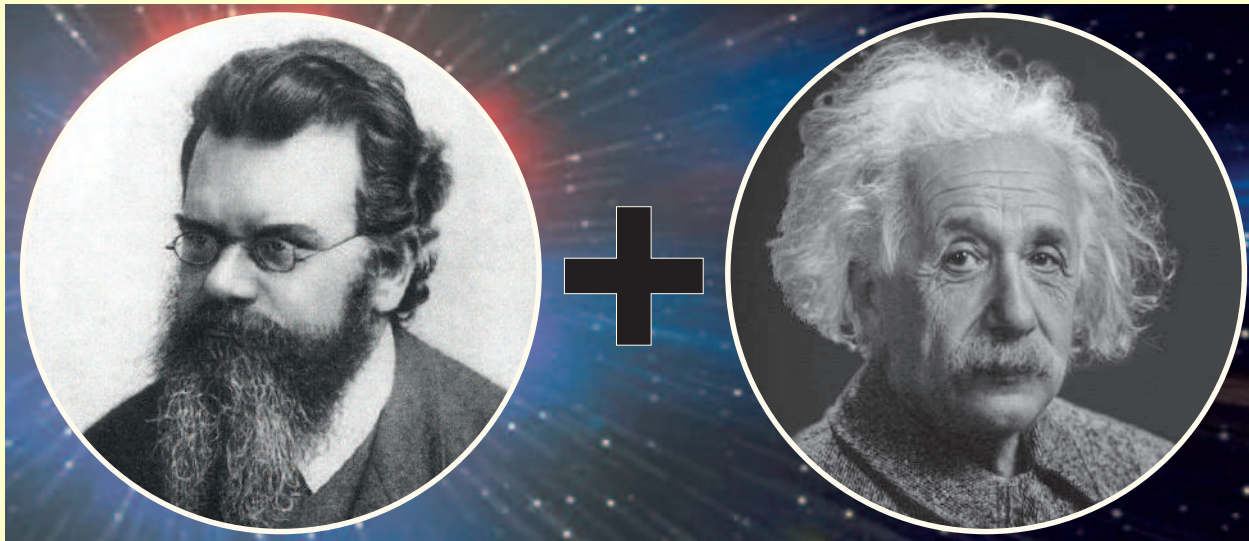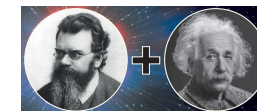A summary of results on the geo-$\overline{\nu}_e$ measurements.
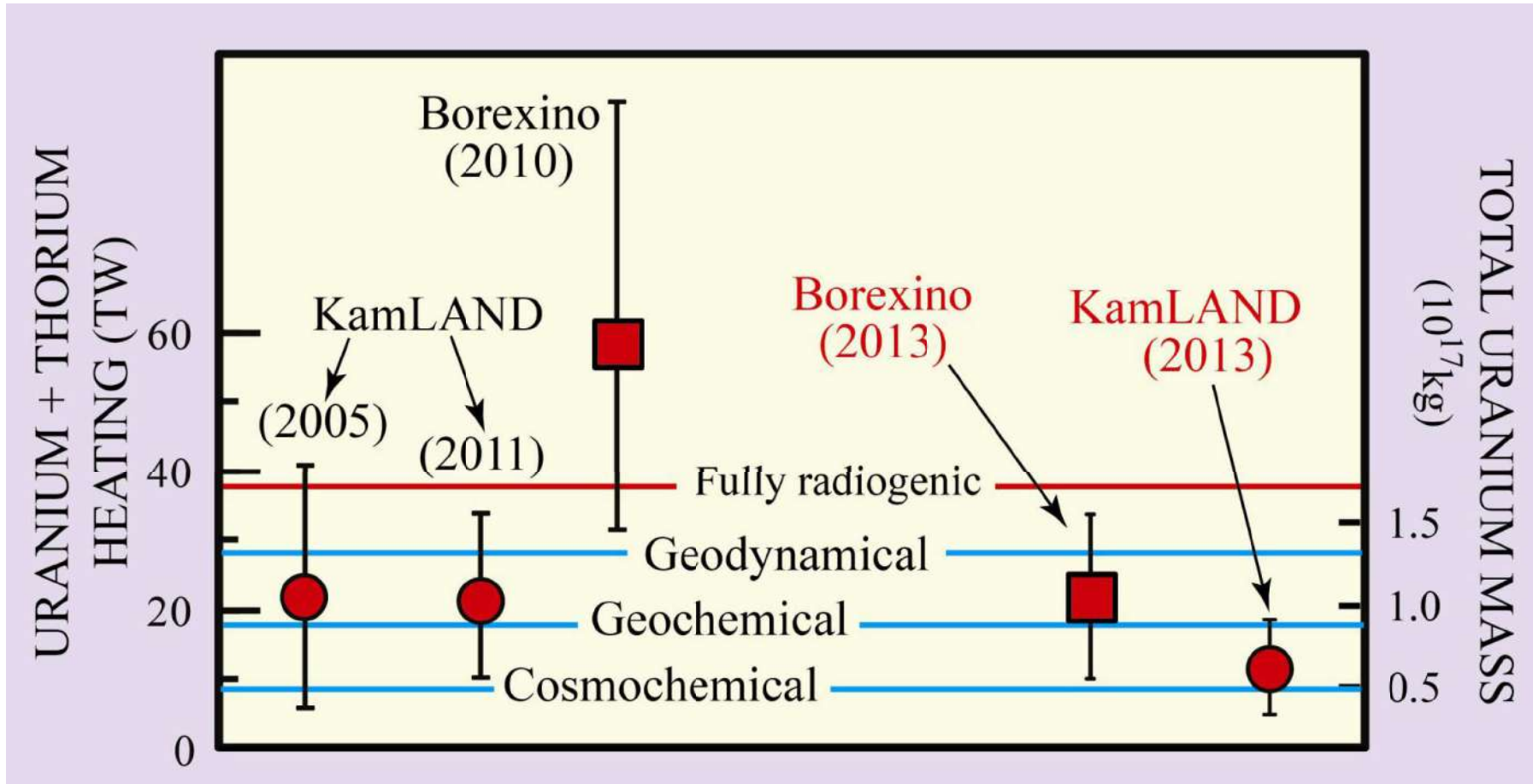
Thanks for your attention!

BACKUP SLIDES

Appendix:

Kinetics of neutrinos in expanding Universe

General-relativistic Boltzmann equation in short.

In the approximation of a weakly interacting gas or plasma, the fundamental equation governing the evolution of particle abundances in the expanding Universe is the general-relativistic Boltzmann equation (BE). [a]

$$\hat{L}f = \sum C[f]. \tag{7}$$

Here $\hat{L}$ is the Liouville operator, $f = f(p, x)$ is distribution function, C is the collision integral (CI) and sum is over all possible interactions. In the general case $\hat{L}$ is defined through Christoffel symbols,

$$\hat{L} = p^{\mu} \frac{\partial}{\partial x_{\mu}} - \Gamma^{\mu}_{\nu\sigma} p^{\nu} p^{\sigma} \frac{\partial}{\partial p_{\mu}}, \quad \Gamma^{\mu}_{\nu\sigma} = \frac{1}{2} g^{\mu\lambda} (g_{\lambda\sigma,\nu} + g_{\nu\lambda,\sigma} - g_{\nu\sigma,\lambda}),$$

but if all distributions are homogeneous and isotropic, that is $f = f(|\mathbf{p}|, t)$, it is drastically simplified:

$$\hat{L} = \frac{\partial}{\partial t} - \frac{\dot{a}}{a} |\mathbf{p}| \frac{\partial}{\partial |\mathbf{p}|}.$$

Here $a = a(t)$ is the cosmic (Robertson-Walker) scale factor – a key parameter of Friedmann's equations (that follow from Einstein equation for perfect fluid and cosmological principle),

$$3 \frac{\dot{a}^2 + k}{a^2} = 8\pi G\rho + \Lambda, \quad \text{(FI)} \quad 3 \frac{\ddot{a}}{a} = -4\pi G(\rho + 3p) + \Lambda, \quad \text{(FII)}$$

G and Λ are the gravitational (Newton) and cosmological constants, $\rho = \rho(t)$ and $p = p(t)$ are the density and pressure, respectively, k is the integer constant $(0, \pm 1)$ throughout a particular solution and defines the shape of the Universe, $\dot{a}/a \equiv H(t)$ is the Hubble parameter; $c = 1$ as usual.

---

[a] See, e.g., J. Bernstein, Kinetic theory in the expanding universe (Cambridge Monographs on Mathematical Physics, Cambridge University Press, New York, New Rochelle, Melbourne, Sydney, 1988).

The CI for fermion 1 participating in a 2-particle process $12 \to 34$ can be written as

$$C[f_1] = \frac{1}{2E_1} \int \left(\prod_{i=2}^{4} \frac{d^3 p_i}{(2\pi)^3 2E_i} \right) [(1 - f_1)(1 - f_2)f_3 f_4 - f_1 f_2(1 - f_3)(1 - f_4)]$$

$$\times \langle |M_{12 \to 34}|^2 \rangle (2\pi)^4 \delta^4(p_1 + p_2 - p_3 - p_4),$$

$\langle \cdots \rangle$ denotes symmetrization (multiplication to $1/2$ for each pair of identical particles in initial or final states) and summation over all spin states but 1. The main reactions are shown in two Tables, where the matrix elements were calculated in the 4-fermion approximation.

Reaction	$\langle |M_{12 \to 34}|^2 \rangle$
$\nu_e \overline{\nu}_e \to \nu_e \overline{\nu}_e$	$128 G_F^2 (p_1 p_4)(p_2 p_3)$
$\nu_e \overline{\nu}_{\mu,\tau} \to \nu_e \overline{\nu}_{\mu,\tau}$	$32 G_F^2 (p_1 p_4)(p_2 p_3)$
$\nu_e \overline{\nu}_e \to \nu_{\mu,\tau} \overline{\nu}_{\mu,\tau}$	$128 G_F^2 (p_1 p_4)(p_2 p_3)$
$\nu_e \nu_{e,\mu,\tau} \to \nu_e \nu_{e,\mu,\tau}$	$32 G_F^2 (p_1 p_2)(p_3 p_4)$
$\nu_e e^- \to \nu_e e^-$	$32 G_F^2 [(C_V + C_A)^2 (p_1 p_2)(p_3 p_4) + (C_V - C_A)^2 (p_1 p_4)(p_2 p_3)$ $-(C_V^2 - C_A^2) m_e^2 (p_1 p_3)]$
$\nu_e e^+ \to \nu_e e^+$	$32 G_F^2 [(C_V + C_A)^2 (p_1 p_4)(p_2 p_3) + (C_V - C_A)^2 (p_1 p_3)(p_2 p_4)$ $-(C_V^2 - C_A^2) m_e^2 (p_1 p_2)]$
$\nu_e \overline{\nu}_e \to e^- e^+$	$32 G_F^2 [(C_V + C_A)^2 (p_1 p_4)(p_2 p_3) + (C_V - C_A)^2 (p_1 p_3)(p_2 p_4)$ $+(C_V^2 - C_A^2) m_e^2 (p_1 p_2)]$

Reaction $(\alpha, \beta = \mu, \tau)$	$\langle |M_{12 \to 34}|^2 \rangle$
$\nu_\alpha \overline{\nu}_\alpha \to \nu_\alpha \overline{\nu}_\alpha$	$128 G_F^2 (p_1 p_4)(p_2 p_3)$
$\nu_\alpha \overline{\nu}_\alpha \to \nu_e \overline{\nu}_e$	$32 G_F^2 (p_1 p_4)(p_2 p_3)$
$\nu_\alpha \overline{\nu}_\beta \to \nu_\alpha \overline{\nu}_\beta \ (\beta \neq \alpha)$	$32 G_F^2 (p_1 p_4)(p_2 p_3)$
$\nu_\alpha \overline{\nu}_\alpha \to \nu_\beta \overline{\nu}_\beta \ (\beta \neq \alpha)$	$32 G_F^2 (p_1 p_4)(p_2 p_3)$
$\nu_\alpha \overline{\nu}_e \to \nu_\alpha \overline{\nu}_e$	$32 G_F^2 (p_1 p_4)(p_2 p_3)$
$\nu_\alpha \nu_{e,\mu,\tau} \to \nu_\alpha \nu_{e,\mu,\tau}$	$32 G_F^2 (p_1 p_2)(p_3 p_4)$
$\nu_\alpha e^- \to \nu_\alpha e^-$	$32 G_F^2 \{ (2 - C_V - C_A)^2 (p_1 p_2)(p_3 p_4) + (C_V - C_A)^2 (p_1 p_4)(p_2 p_3)$ $- [(1 - C_V)^2 - (1 - C_A)^2] m_e^2 (p_1 p_3) \}$
$\nu_\alpha e^+ \to \nu_\alpha e^+$	$32 G_F^2 \{ (2 - C_V - C_A)^2 (p_1 p_4)(p_2 p_3) + (C_V - C_A)^2 (p_1 p_2)(p_3 p_4)$ $- [(1 - C_V)^2 - (1 - C_A)^2] m_e^2 (p_1 p_3) \}$
$\nu_\alpha \overline{\nu}_\alpha \to e^- e^+$	$32 G_F^2 \{ (2 - C_V - C_A)^2 (p_1 p_4)(p_2 p_3) + (C_V - C_A)^2 (p_1 p_3)(p_2 p_4)$ $- [(1 - C_V)^2 - (1 - C_A)^2] m_e^2 (p_1 p_2) \}$

Here and below, $C_V = \frac{1}{2} + 2\sin^2\theta_W$ and $C_A = \frac{1}{2}$, θ_W is the Weinberg angle or weak mixing angle ($\sin^2\theta_W = 1 - m_W^2/m_Z^2 = 0.23153(4)$).

[The data in tables are borrowed from S. Hannestad & J. Madsen, "Neutrino decoupling in the early universe," Phys. Rev. D **52** (1995) 1764–1769, astro-ph/9506015 [astro-ph]. Derivation of the CI can be found in, e.g., К. П. Гуров. «Основания кинетической теории, метод Н. Н. Боголюбова». М. «Наука». 1966.]

There exists a corresponding set of equations for the distribution functions. In absence of an asymmetry it is not needed since antineutrinos follow the same evolution as neutrinos.

As an example, Figure ▷ shows the effective neutrino temperature, defined as

$$T_{\text{eff}} = \frac{p_\nu}{\ln\left[\dfrac{1}{f(p_\nu)} - 1\right]}$$

and evaluated after a numerical solution of the above equations.
[From S. Hannestad & J. Madsen, "Neutrino decoupling in the early universe," Phys. Rev. D **52** (1995) 1764–1769, astro-ph/9506015 [astro-ph].]

Effective neutrino temperature after complete $e^\pm$ annihilation
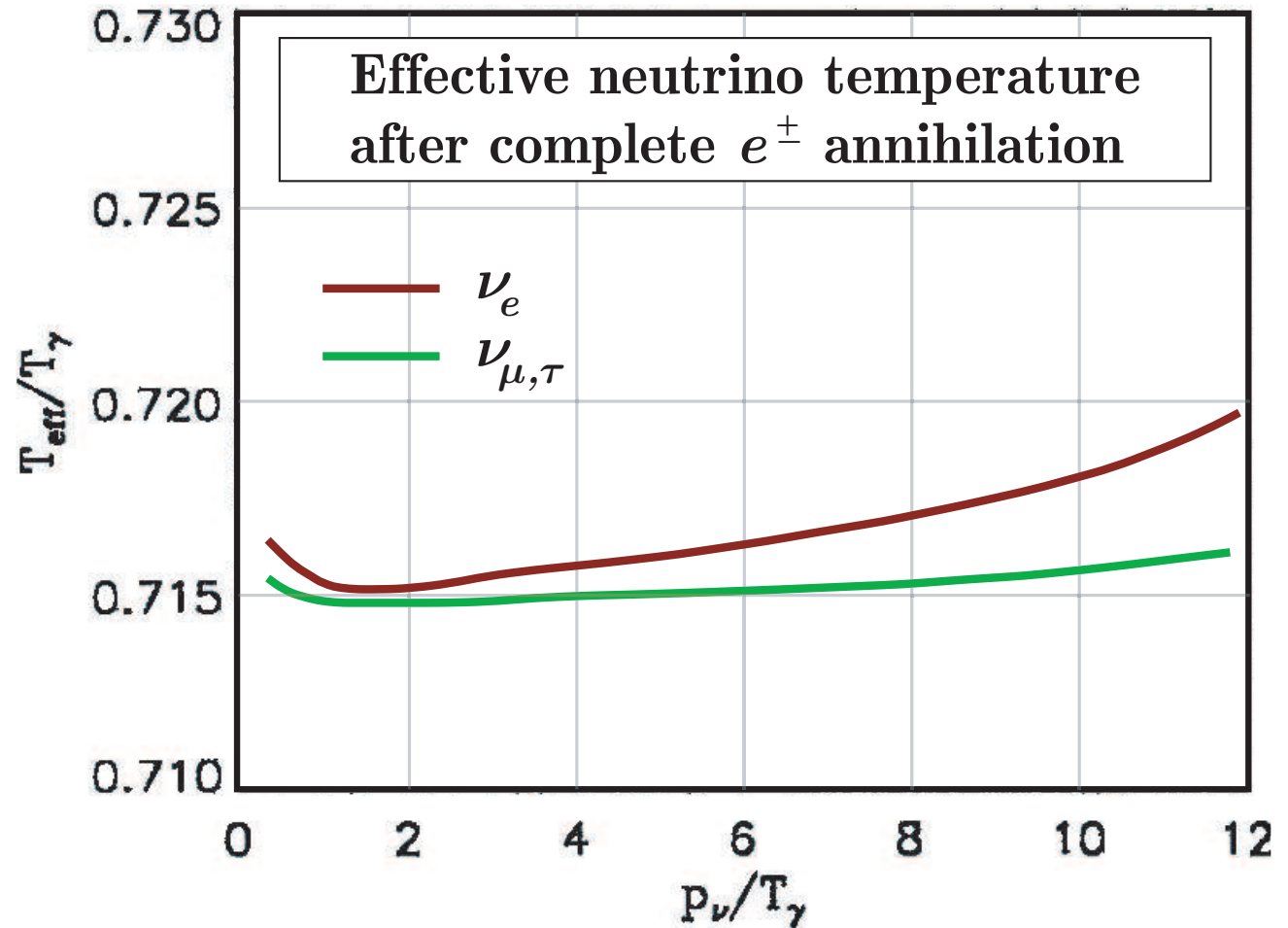
The most serious drawback of the outlined approach is in neglecting the neutrino mixing .

A more general form of the collision integral

The CI for particle a participating in the reactions $a + B \longleftrightarrow C$ (where B and C are generally multiparticle states) is

$$
C[f_a] = \frac{1}{2E_a} \sum_{B,C} \int \left(\prod_{i \in B+C} \frac{d^3 p_i}{(2\pi)^3 2E_i} \right) (2\pi)^4 \delta^4 (p_a + p_B - p_C)
$$

$$
\times \left[\langle |M_{C \to aB}|^2 \rangle \prod_{i \in a+B} (1 - \zeta_i f_i) \prod_{i \in C} f_i - \langle |M_{aB \to C}|^2 \rangle \prod_{i \in C} (1 - \zeta_i f_i) \prod_{i \in a+B} f_i \right],
$$

where $\zeta_i = -1$ for bosons and $+1$ for fermions. In thermal equilibrium $C[f_a] \equiv C_{\text{eq}}[f_a] = 0$ and

$$
f_i^{\text{eq}} = f_i^{\text{eq}}(E_i, \mu_i, T_i) = \frac{1}{\exp\left[(E_i - \mu_i)/T_i \right] + \zeta_i}, \quad i \in a + B + C. \tag{8}
$$

The chemical potential μ_i and temperature T_i are functions of time.

<u>*Problem*</u>: Prove that $C_{\text{eq}}[f_a] = 0$ assuming T invariance and conservation of the chemical potentials.

✦ The chemical potentials conserve only in thermal equilibrium and any system evolves to this state if the reaction rates are sufficiently high.

✦ In elastic scattering, the chemical potential conservation condition is met automatically. Therefore, elastic reactions bring the system to the equilibrium state, forming the canonical energy dependence of the distribution functions (8).

✦ For bosons, the equilibrium solution (8) is not unique (Bose condensate).

✦ The CI reduces to the usual Boltzmann CI for non-identical particles as $\zeta_i = 0$ (low particle density limit).

Let's very schematically explain the origin of the factors f_i and $(1 \pm f_i)$ in the integrand of CI.[a]
The probability of transition $|a + B\rangle \to |C\rangle$ during a (proper) time interval Δt in a volume ΔV is

$$|\langle C|\mathbf{S} - \mathbf{1}|a + B\rangle|^2 \propto \Delta V \Delta t \delta^4(p_a + p_B - p_C)|\langle C|\mathbf{T}|a + B\rangle|^2 \tag{9}$$

in terms of the standard QFT $\mathbf{S}$ and $\mathbf{T}$ matrices. If a_j and $a_j^\dagger$ are the annihilation and creation operators for particle j in a momentum eigenstate, then the operator $\mathbf{T}$ must be proportional to $a_{c_1}^\dagger a_{c_2}^\dagger \ldots a_a a_{b_1} a_{b_2} \ldots$, where $b_1, b_2, \ldots \in B$ and $c_1, c_2, \ldots \in C$ for such a transition.

Let's remind the standard definition for the action of the operators a_j and $a_j^\dagger$ on the Fock state vector of the particle j in the occupation number representation:

Bosons:
$$a_j |n_1, n_2, \ldots, n_j, \ldots\rangle = \begin{cases} \sqrt{n_j} \, |n_1, n_2, \ldots, n_j - 1, \ldots\rangle & \text{if } n_j \geq 1, \\ 0 & \text{if } n_j = 0. \end{cases}$$

$$a_j^\dagger |n_1, n_2, \ldots, n_j, \ldots\rangle = \sqrt{n_j + 1} \, |n_1, n_2, \ldots, n_j + 1, \ldots\rangle.$$

Fermions:
$$a_j |n_1, n_2, \ldots, n_j, \ldots\rangle = \begin{cases} (-1)^{n_1 + n_2 \ldots + n_{j-1}}|n_1, n_2, \ldots, n_{j-1}, 0, \ldots\rangle & \text{if } n_j = 1, \\ 0 & \text{if } n_j = 0; \end{cases}$$

$$a_j^\dagger |n_1, n_2, \ldots, n_j, \ldots\rangle = \begin{cases} (-1)^{n_1 + n_2 \ldots + n_{j-1}}|n_1, n_2, \ldots, n_{j-1}, 1, \ldots\rangle & \text{if } n_j = 0, \\ 0 & \text{if } n_j = 1. \end{cases}$$

The factors $\sqrt{n_j}$ and $\sqrt{n_j + 1}$ appear since each multi-particle bosonic state is properly normalized.

---

[a] Here we partially follow the review by R. V. Wagoner, "The early Universe", in "Physical cosmology" (Les Houches 32, NH, 1979) (Elsevier, 1980), ed. by R. Balian, J. Audouze, and D. N. Schramm, pp. 398–442.

Therefore for both cases we can write (although it is a little bit tricky):

$$a_j \left| n_1, n_2, \ldots, n_j, \ldots \right\rangle = (-1)^{s_j} \sqrt{n_j} \left| n_1, n_2, \ldots, n_j - 1, \ldots \right\rangle,$$

$$a_j^\dagger \left| n_1, n_2, \ldots, n_j, \ldots \right\rangle = (-1)^{s_j} \sqrt{1 - \zeta_j n_j} \left| n_1, n_2, \ldots, n_j + 1, \ldots \right\rangle.$$

Here $\zeta_i = -1(+1)$ for bosons (fermions), the phase integer s_j plays no role, as well as formal definitions of the unphysical "states" with negative occupation numbers or with $n_j = 2$ for fermions.

The average number of transitions $\left| a(p_a) + B\left(p_{b_1}, p_{b_2}, \ldots \right) \right\rangle \to \left| C\left(p_{c_1}, p_{c_2}, \ldots \right) \right\rangle$ from momentum elements[a] $d\Pi_a, d\Pi_{b_1}, d\Pi_{b_2}, \ldots$ to $d\Pi_{c_1}, d\Pi_{c_2}, \ldots$ occurring within the (proper) space-time volume $\Delta V \Delta t$ must be of the form (up to δ-function)

$$\propto \Delta V \Delta t \; d\Pi_a f_a d\Pi_{b_1} f_{b_1} d\Pi_{b_2} f_{b_2} \cdots d\Pi_{c_1} \left[1 - \zeta_{c_1} f_{c_1} \right] d\Pi_{c_2} \left[1 - \zeta_{c_2} f_{c_2} \right] \cdots \; \left| M_{a+B \to C} \right|^2,$$

where now $f_j = \overline{n}_j$ is the distribution function = the number of particles of type j per unit element of (normalized) phase space = the occupation number averaged over "externally statistical conditions".[b]

Similarly, the average number of transitions $\left| C\left(p_{c_1}, p_{c_2}, \ldots \right) \right\rangle \to \left| a(p_a) + B\left(p_{b_1}, p_{b_2}, \ldots \right) \right\rangle$ must be

$$\propto \Delta V \Delta t \; d\Pi_a \left[1 - \zeta_a f_a \right] d\Pi_{b_1} \left[1 - \zeta_{b1} f_{b_1} \right] d\Pi_{b_2} \left[1 - \zeta_{b2} f_{b_2} \right] \cdots d\Pi_{c_1} f_{c_1} d\Pi_{c_2} f_{c_2} \cdots \; \left| M_{C \to a+B} \right|^2.$$

This finally leads to the desired result for CI.

In contrast to classical systems, in quantum systems the probabilities of direct and reverse transitions depend not only on the averaged of the relative occupation numbers of the initial states of the colliding particles, but also on the average relative occupation numbers of final states.

---

[a] $d\Pi_a = \sqrt{-g} d^3 p_a / (2\pi)^3 2 E_{\mathbf{p}_a}$, $g = |g_{\mu\nu}|$ and we assume almost flat space-time $\Longrightarrow g = -1$.

[b] The transition from n_j to f_j is the most difficult step of our intuitive derivation. Full derivation is rather cumbersome; see, e.g., К. П. Гуров. «Основания кинетической теории, метод Н. Н. Боголюбова». М. «Наука». 1966.

Including flavor oscillations (very, very briefly)

To include the neutrino mixing and coherent interactions, the neutrino ensemble is described by generalizing the neutrino density functions (occupation numbers) by the 3×3 density matrix $\boldsymbol{\rho} = ||\rho_{\alpha\beta}(|\mathbf{p}|, t)||$ ($\alpha, \beta = e, \mu, \tau$).[a] The diagonal elements, $\rho_{\alpha\alpha}$, correspond to the usual density functions f_α, while the off-diagonal terms takes into account the neutrino mixing.

The generalized BE for neutrino ν_α is (cf. Eq. (7))

$$\left(\frac{\partial}{\partial t} - H |\mathbf{p}| \frac{\partial}{\partial |\mathbf{p}|} \right) \boldsymbol{\rho} = -i \left[\mathbf{V} \mathbf{H}_0 \mathbf{V}^\dagger + \mathbf{W}, \boldsymbol{\rho} \right] + \mathbf{C}[\boldsymbol{\rho}], \tag{10}$$

where $\mathbf{H}_0 = \mathsf{diag}(m_1^2, m_2^2, m_3^2)/2|\mathbf{p}|$, $\mathbf{V}$ is the vacuum mixing matrix, $\mathbf{W}$ is the matrix responsible for coherent (zero-angle) neutrino-matter interactions,

$$\mathbf{C}[\boldsymbol{\rho}] = ||C[\rho_{\alpha\beta}]||, \quad C[\rho_{\alpha\beta}] = -D\,\rho_{\alpha\beta}, \quad \alpha \neq \beta \quad (D \text{ is a damping function}),$$

$$C[\rho_{\alpha\alpha}] = \frac{1}{2E_1} \sum_{\text{reactions}} \int \left(\prod_{i=2}^{4} \frac{d^3 p_i}{(2\pi)^3 2E_i} \right) [(1 - \rho_{\alpha\alpha})(1 - f_2)f_3 f_4 - \rho_{\alpha\alpha} f_2 (1 - f_3)(1 - f_4)]$$
$$\times \langle |M_{12 \to 34}|^2 \rangle (2\pi)^4 \delta^4 (p_1 + p_2 - p_3 - p_4).$$

Particle 1 is ν_α and $\mathbf{p} = \mathbf{p}_1$; when the particle $i = 2$, 3 or 4 is a neutrino ν_β, you need to replace f_i with the corresponding diagonal term $\rho_{\beta\beta}$.

---

[a] G. Sigl & G. Raffelt, "General kinetic description of relativistic mixed neutrinos," Nucl. Phys. B **406** (1993) 423–451; B. H. McKellar & M. J. Thomson, "Oscillating neutrinos in the early universe," Phys. Rev. D **49** (1994) 2710–2728; G. Mangano *et al.*, "Relic neutrino decoupling including flavour oscillations," Nucl. Phys. B **729** (2005) 221–234. P. F. de Salas & S. Pastor, "Relic neutrino decoupling with flavour oscillations revisited," JCAP07(2016)051, arXiv:1606.06986 [hep-ph].

Appendix: SN1987A, Bert & Ernie
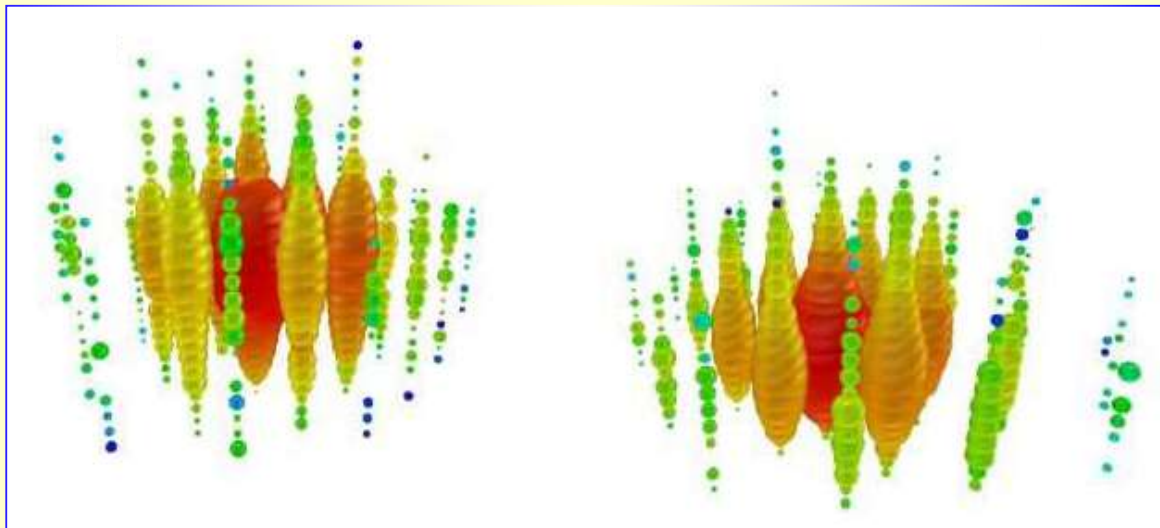
1987 Kamiokande, IMB and Baksan detectors detect burst of antineutrinos from SN 1987A in Large Magellanic Cloud (51.474 kpc), proclaiming the birth of neutrino astronomy, and setting strong limits on neutrino mass and velocity.
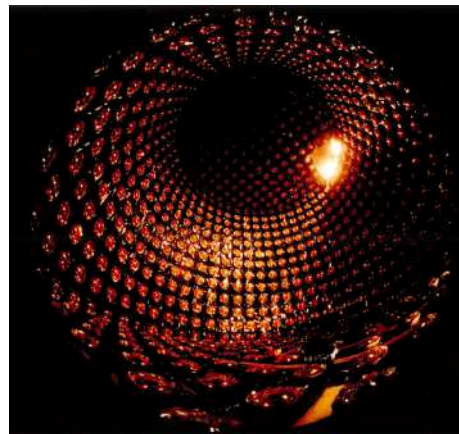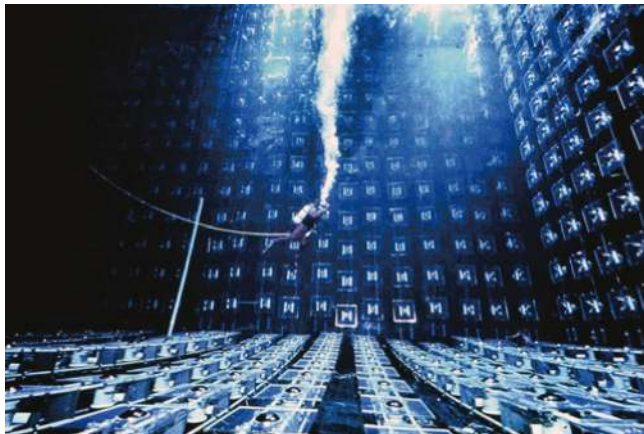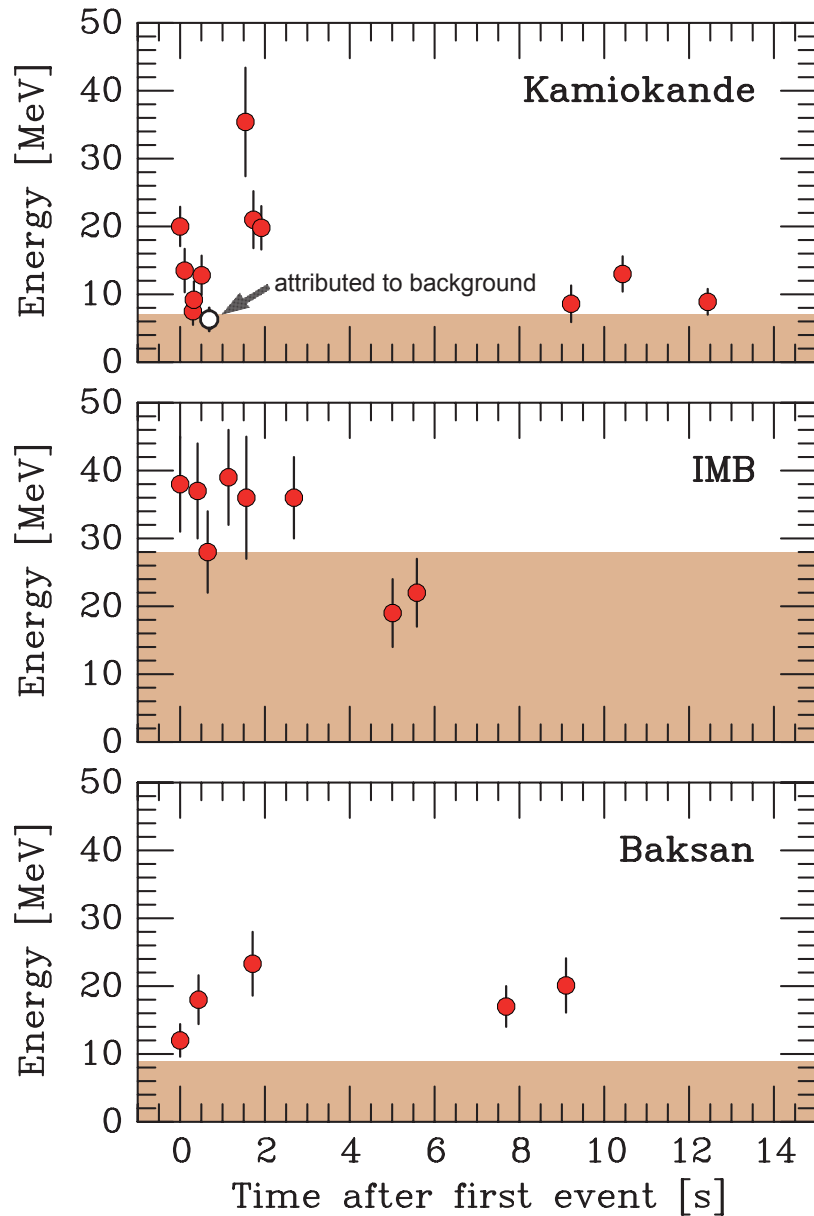
△   SN 1987A antineutrino observations at Kamiokande, IMB and Baksan detectors. The energies refer to the secondary positrons from the reaction $\overline{\nu}_e p \to ne^+$. In the shaded area the trigger efficiency is less than 30%. The clocks have unknown relative offsets; in each case the first event was shifted to $t = 0$.

The signal does show a number of "anomalies".

- The average $\overline{\nu}_e$ energies inferred from the IMB and Kamiokande observations are quite different.
- The large time gap of 7.3 s between the first 8 and the last 3 Kamiokande events looks worrisome.
- The distribution of the positrons should be isotropic, but is found to be significantly peaked away from the direction of the SN.

In the absence of other explanations, these features are blamed on statistical fluctuations in the sparse data.

[From G. G. Raffelt, "Particle physics from stars," Ann. Rev. Nucl. Part. Sci. **49** (1999) 163–216, hep-ph/9903472.]

Kamiokande II result

TABLE I. Measured properties of the twelve electron events detected in the neutrino burst. The electron angle in the last column is relative to the direction of SN1987A. The errors on electron energies and angles are one-standard-deviation Gaussian errors.

Event number	Event time (sec)	Number of PMT's (N_{hit})	Electron energy (MeV)	Electron angle (degrees)
1	0	58	20.0 ± 2.9	18 ± 18
2	0.107	36	13.5 ± 3.2	15 ± 27
3	0.303	25	7.5 ± 2.0	108 ± 32
4	0.324	26	9.2 ± 2.7	70 ± 30
5	0.507	39	12.8 ± 2.9	135 ± 23
6	0.686	16	6.3 ± 1.7	68 ± 77
7	1.541	83	35.4 ± 8.0	32 ± 16
8	1.728	54	21.0 ± 4.2	30 ± 18
9	1.915	51	19.8 ± 3.2	38 ± 22
10	9.219	21	8.6 ± 2.7	122 ± 30
11	10.433	37	13.0 ± 2.6	49 ± 26
12	12.439	24	8.9 ± 1.9	91 ± 39
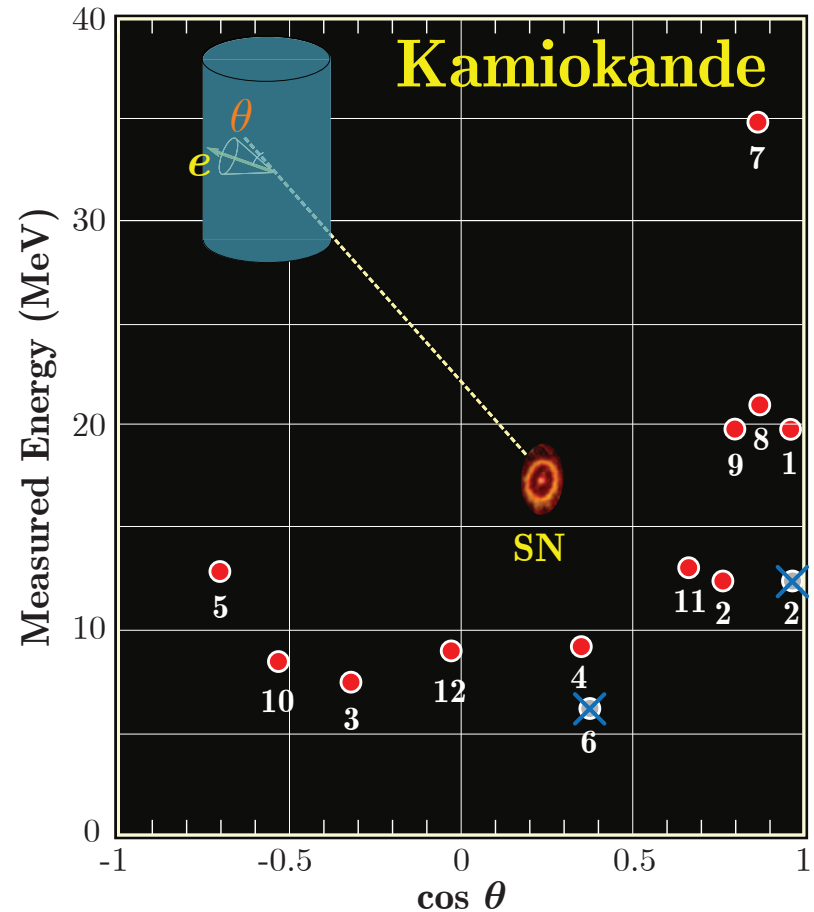
[K. Hirata *et al.* (Kamiokande-II Collaboration) "Observation of a Neutrino Burst from the Supernovae SN 1987A," Phys. Rev. Lett. **58** (1987) 1490–1493; K. Hirata *et al.*, "Observation in the Kamiokande-II Detector of the Neutrino Burst from Supernova SN 1987A," Phys. Rev. D **38** (1988) 448–458.]

IMB result

TABLE III. Characteristics of the contained neutrino events recorded on 23 February.

Event No.[a]	Time (UT)	No. of PMT's	Energy[b] (MeV)	Angular distribution[c] (degrees)
33162	7:35:41.37	47	38	74
33164	7:35:41.79	61	37	52
33167	7:35:42.02	49	40	56
33168	7:35:42.52	60	35	63
33170	7:35:42.94	52	29	40
33173	7:35:44.06	61	37	52
33179	7:35:46.38	44	20	39
33184	7:35:46.96	45	24	102

[a]The event numbers are not sequential. Interspersed with the contained neutrino events are fifteen entering cosmic-ray muons.
[b]Error in energy determination is $\pm 25\%$ (systematic plus statistical).
[c]Individual track reconstruction uncertainty is $15°$. Note that this angular distribution will be systematically biased toward the source because of the location of the inoperative PMT's.

[R. M. Bionta *et al.*, "Observation of a neutrino burst in coincidence with supernova 1987A in the Large Magellanic Cloud," Phys. Rev. Lett. **58** (1987) 1494–1496.]

TABLE I. Energies and angles of the eight events from supernova SN1987A. (a) Absolute UT is accurate to ± 50 ms. Relative times are accurate to the nearest millisecond. (b) Additional systematic error in energy scale estimated to be $\pm 10\%$. (c) Angle with respect to direction away from SN1987A. Angle errors include multiple scattering and event reconstruction. (d) assumes events are due to $\bar{\nu} + p \rightarrow e^+ + n$ on free protons.

Event	(a) Time (UT) 23 Feb. 1987	(b) Measured energy (MeV)	(c) Polar angle (deg)	(d) Antineutrino energy (MeV)
1	7:35:41.374	38±7	80±10	41±7
2	7:35:41.786	37±7	44±15	39±7
3	7:35:42.024	28±6	56±20	30±6
4	7:35:42.515	39±7	65±20	42±7
5	7:35:42.936	36±9	33±15	38±9
6	7:35:44.058	36±6	52±10	38±6
7	7:35:46.384	19±5	42±20	21±5
8	7:35:46.956	22±5	104±20	24±5

[C. B. Bratton *et al.* (IMB Collaboration) "Angular distribution of events from SN 1987A," Phys. Rev. D **37** (1988) 3361–3363.]
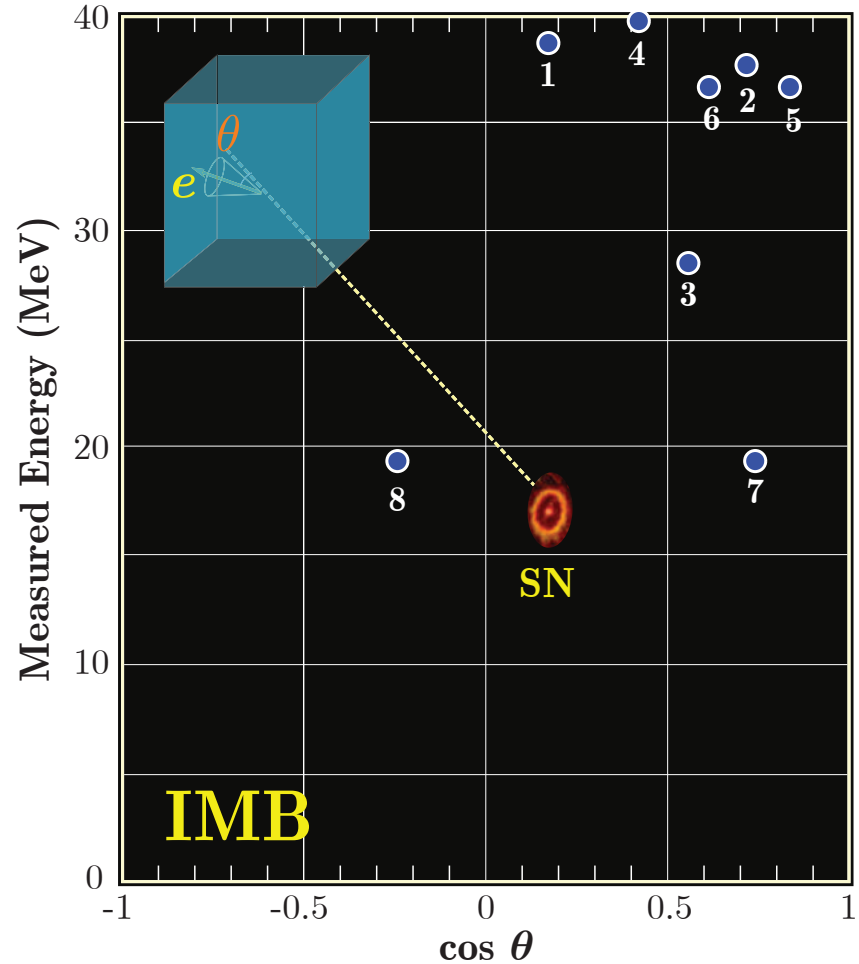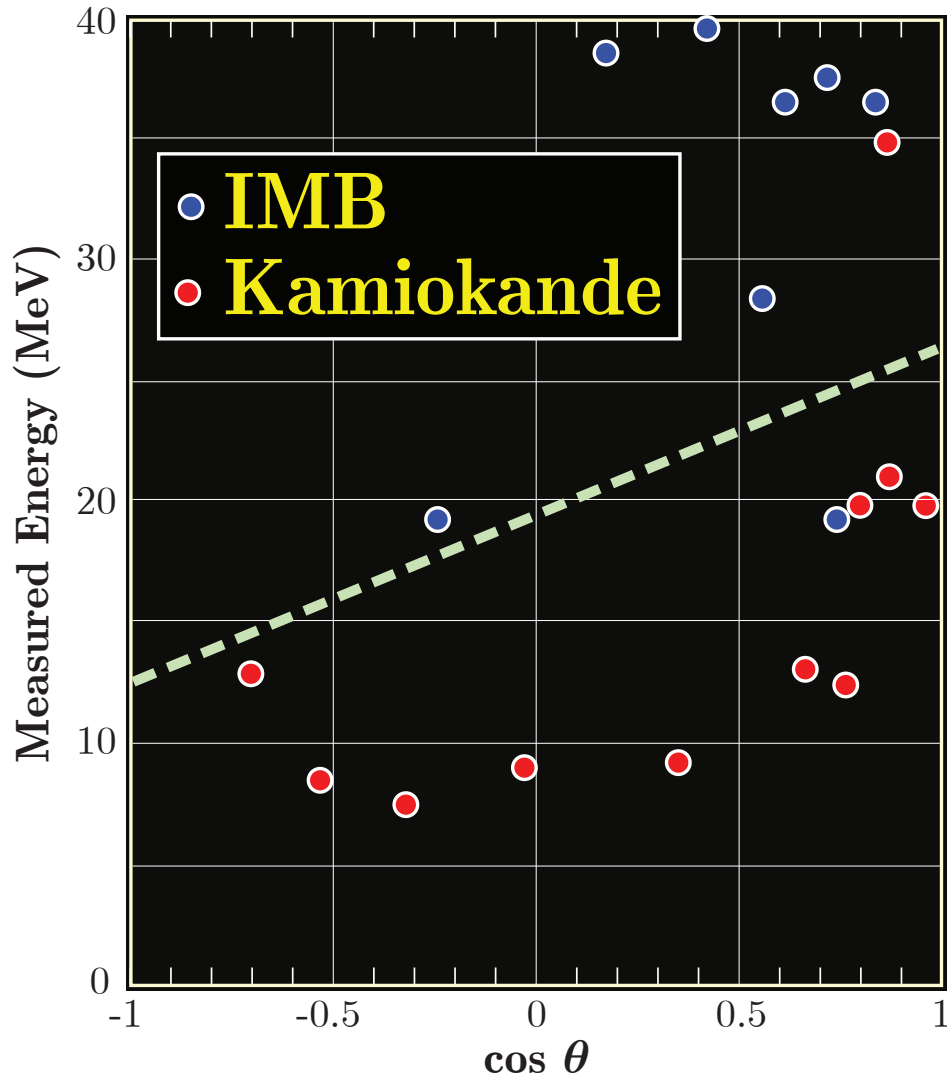
For other interesting facts about SN 1987A, see presentation "Cosmic rays" at ⟨ http://theor.jinr.ru/~vnaumov/Eng/JINR_Lectures/NPA.html ⟩.

We have to remember about the precursor low-energy antineutrino pulse ($E_{\bar{\nu}} = 7 - 11$ MeV) detected by LSD.[a] at 2:52:36 UT that is $4^{\mathrm{h}}44^{\mathrm{m}}$ earlier the second (Kamiokande-II-IMB-BUST) pulse.

The 90 ton Liquid Scintillation Detector in the Mont Blanc Laboratory
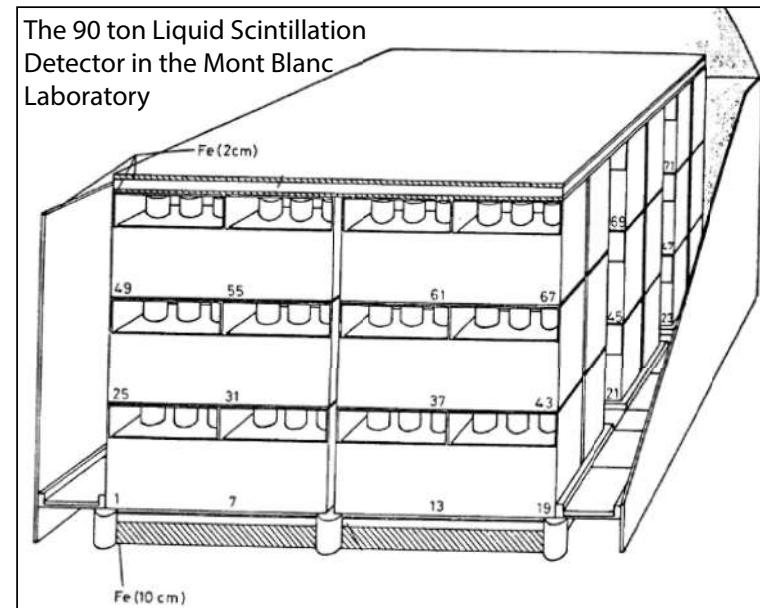
Unfortunately, this fact is often ignored by the community.

---

[a]V. L. Dadykin *et al.*, "Detection of a rare event on 23 February 1987 by the neutrino radiation detector under Mont Blanc," Pisma v Zh. Eksp. Teor. Fiz. **45** (1987) 464–466 [JETP Lett. **45** (1987) 593–595].

Kamiokande-II and IMB
August 11 – October 20, 1987
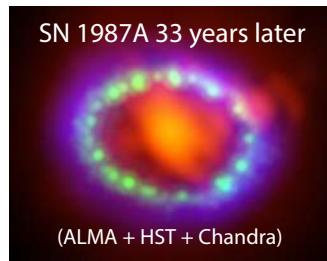
● Kam-II through   10 events
★ Kam-II stopping   2 events
● IMB through   19 events
★ IMB stopping   1 event

R.A.

180° 120° 60° 0° 300° 240° 180°

60°

30°

decl.

0°

-30°

-60°
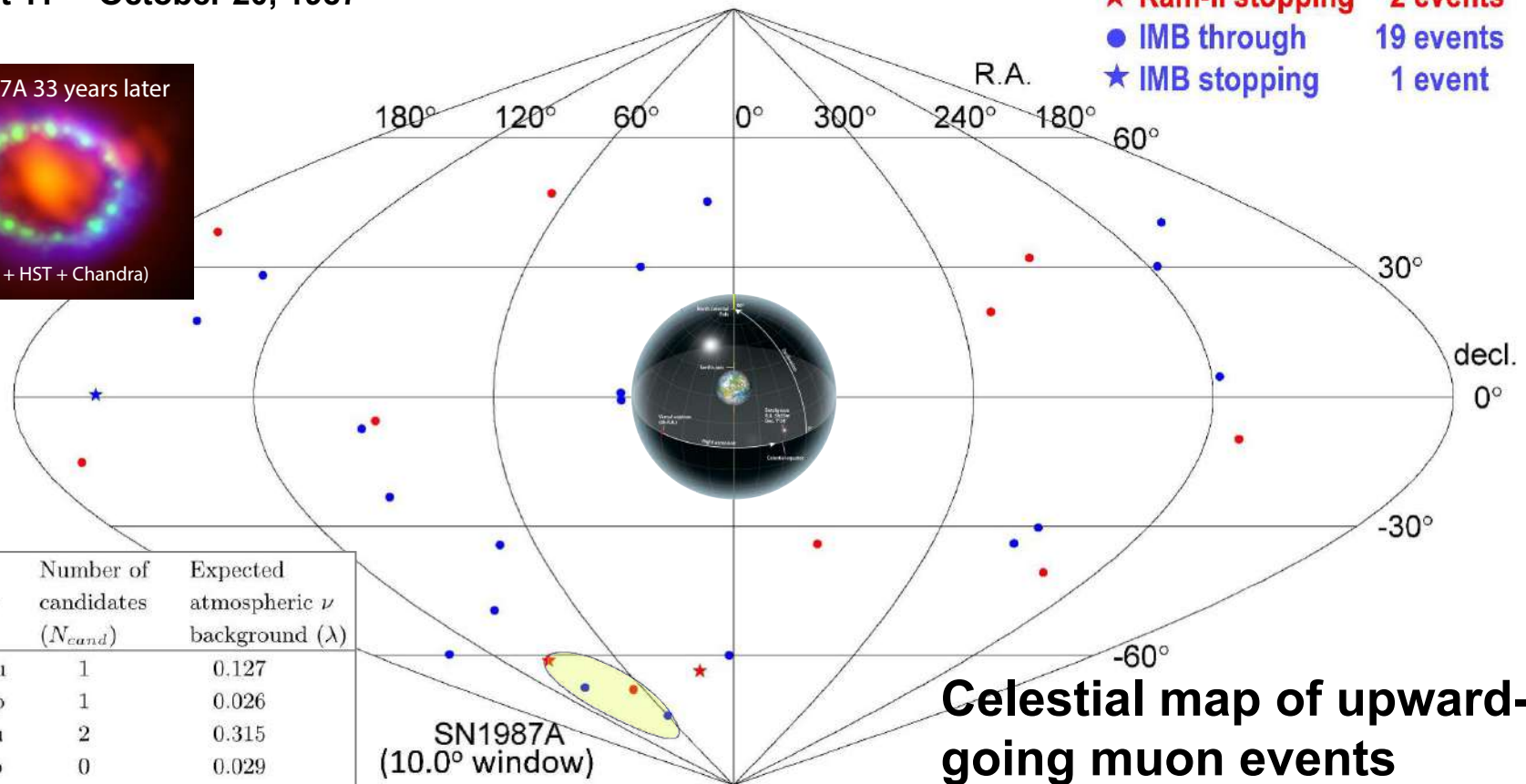
Event Category	Number of candidates (N_{cand})	Expected atmospheric ν background (λ)
Kam-thru	1	0.127
Kam-stop	1	0.026
IMB-thru	2	0.315
IMB-stop	0	0.029

SN1987A
(10.0° window)

Celestial map of upward-going muon events

Four upward-going muons by Kamiokande-II and IMB are observed between Aug. 11 and Oct. 20, 1987 within $10.0°$ angular window around SN 1987A. The probability that these events can be explained by a chance coincidence of atmospheric neutrinos was estimated as 0.27%. These events might be the first (and yet the only) hint of high-energy ($\gtrsim 10$ GeV) νs from a supernova explosion.

[From Y. Oyama, "Evidence of high-energy neutrinos from SN1987A by Kamiokande-II and IMB", arXiv:2108.05347 [hep-ex] (August 15, 2021).]

Neutrino velocity.

The ν burst from SN 1987A (Kamiokande-II, IMB, BUST) [≈ 51 kps, $\langle E_{\bar{\nu}}\rangle \sim 15$ MeV, $E_{\bar{\nu}} \lesssim 40$ MeV] sets the limit:

$$|v_\nu - 1| < 2 \times 10^{-9}.$$

[K. Hirata *et al.* (Kamiokande-II Collaboration), "Observation of a Neutrino Burst from the Supernovae SN1987A," Phys. Rev. Lett. **58** (1987) 1490–1493; R. M. Bionta *et al.*, "Observation of a neutrino burst in coincidence with supernova 1987A in the Large Magellanic Cloud," Phys. Rev. Lett. **58** (1987) 1494–1496 E. N. Alekseev *et al.*, "Possible detection of a neutrino signal on 23 February 1987 at the Baksan underground scintillation telescope of the Institute of Nuclear Research," JETP Lett. **45** (1987) 589–592.]

Arguments: [M. J. Longo, "Test of relativity from SN1987A," Phys. Rev. D **36** (1987) 3276–3277.]

The arrival time of the antineutrinos is known to be within a few seconds of 7:35:40 UT on February 23, 1987. The arrival time of the first light from SN is less well known. The last confirmed evidence of no optical brightening was at approximately 2:20 UT [I. Shelton, IUA Circular No. 4330,1987]. The earliest observations of optical brightening were at 10:38 UT by Garrad and by McNaught [G. Garradd, IUA Circular No. 4316, 1987; R. H. McNaught, *ibid*].

Standard SN theory expects that the neutrinos and antineutrinos are emitted in the first few second of the collapse, while the optical outburst begins ~ 1 h later, when the cooler envelope is blown away. Altogether this leads to an uncertainty of about 3 h: $|v_\nu - 1|_{\max} \sim 3$ h$/(1.6 \times 10^5 \times 365 \times 24h) \approx 2 \times 10^{-9}$. However Longo's limit is generally not robust.
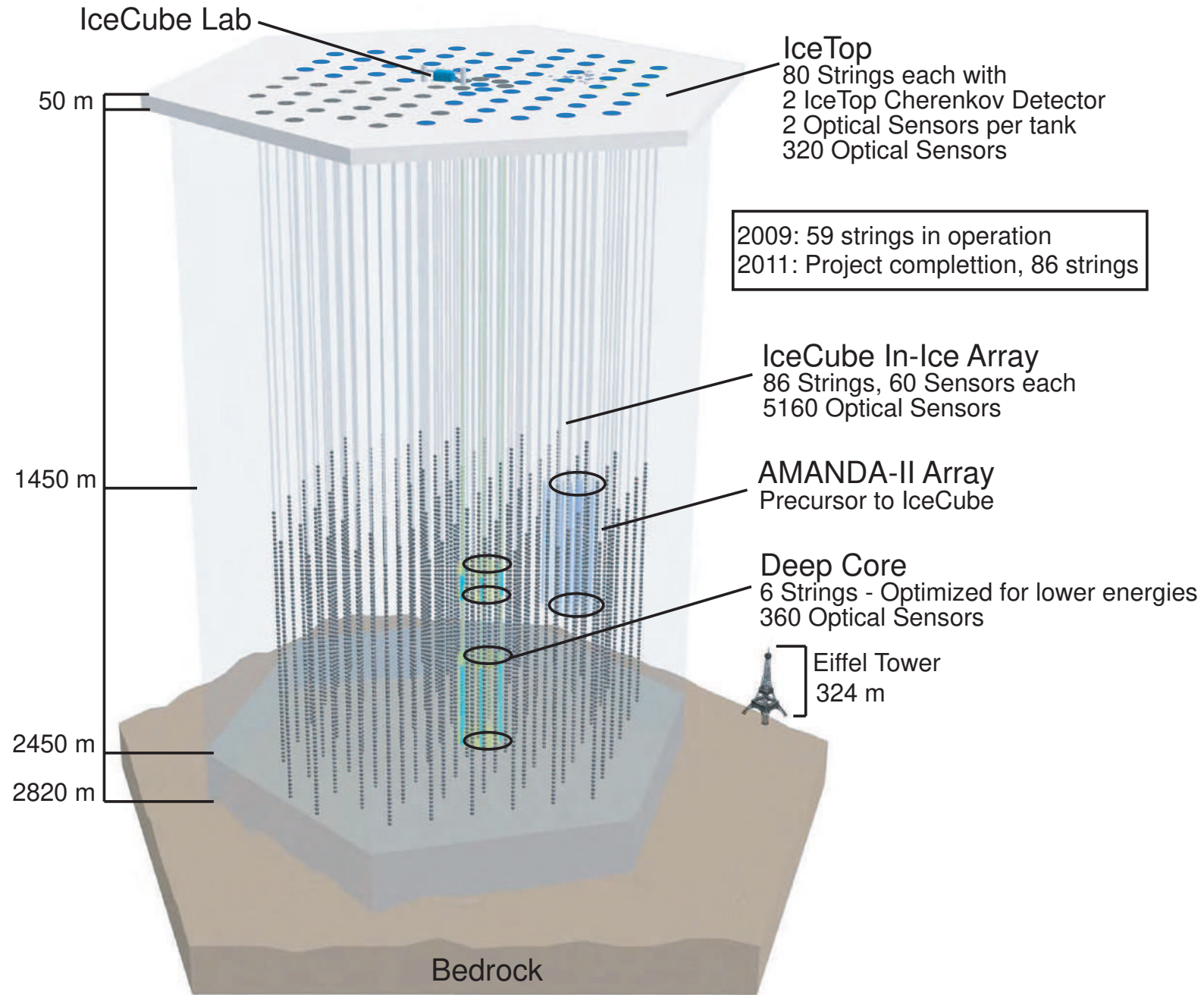
2013 [July 12] The IceCube Collaboration reports observation of two neutrino-induced events which have an estimated deposited energy in the detector of 1.04 ± 0.16 and 1.14 ± 0.17 PeV, respectively, the highest neutrino energies observed so far.
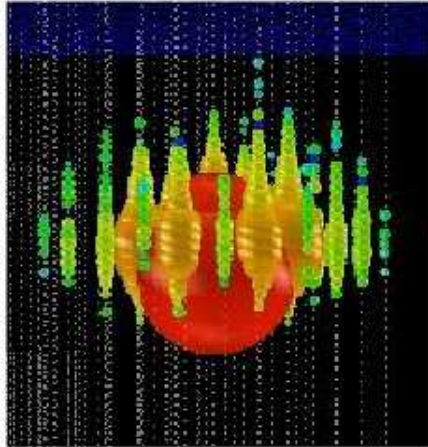

The two events are consistent with fully contained particle showers induced by NC $\nu_{e,\mu,\tau}$ ($\overline{\nu}_{e,\mu,\tau}$) or CC ν_e ($\overline{\nu}_e$) interactions within the detector. The events were discovered in a search for UHE neutrinos using data corresponding to 615.9 days effective live time.

The expected number of AN background is $0.082^{+0.004}_{-0.004}$ (stat) $^{+0.041}_{-0.067}$ (syst). The probability of observing two or more candidate events under the AN background-only hypothesis is 2.9×10^{-3} (2.8σ) taking into account the uncertainty on the expected number of background events. These two events could be a first indication of an astrophysical neutrino flux; the moderate significance, however, does not permit a definitive conclusion.

[From M. G. Aartsen *et al.* (IceCube Collaboration), "First observation of PeV-energy neutrinos with IceCube," Phys. Rev. Lett. **111** (2013) 021103, arXiv:1304.5356v2 [astro-ph.HE].]
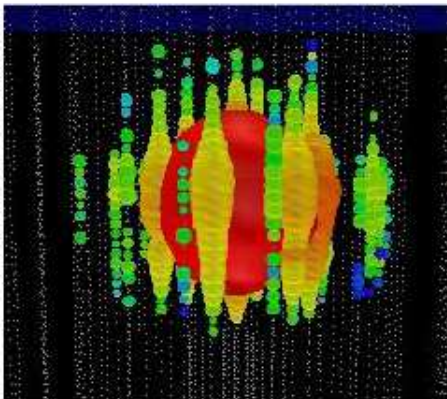
IceCube Lab

IceTop
80 Strings each with
2 IceTop Cherenkov Detector
2 Optical Sensors per tank
320 Optical Sensors

50 m

2009: 59 strings in operation
2011: Project complettion, 86 strings

IceCube In-Ice Array
86 Strings, 60 Sensors each
5160 Optical Sensors

1450 m

AMANDA-II Array
Precursor to IceCube

Deep Core
6 Strings - Optimized for lower energies
360 Optical Sensors

Eiffel Tower
324 m

2450 m
2820 m

Bedrock

January 3, 2012 ("Ernie")

1.14±0.14 PeV
6.09 < log(E/GeV) < 8.65

August 9, 2011 ("Bert")

1.04±0.16 PeV
6.01 < log(E/GeV) < 8.03

IceCube-86 (78+8) intersections (surface) distances and closest string positions for the vertices
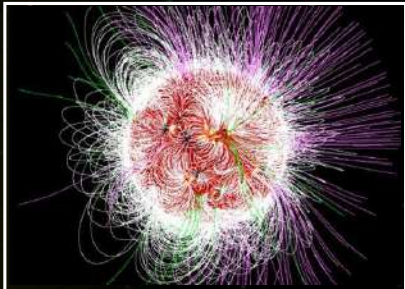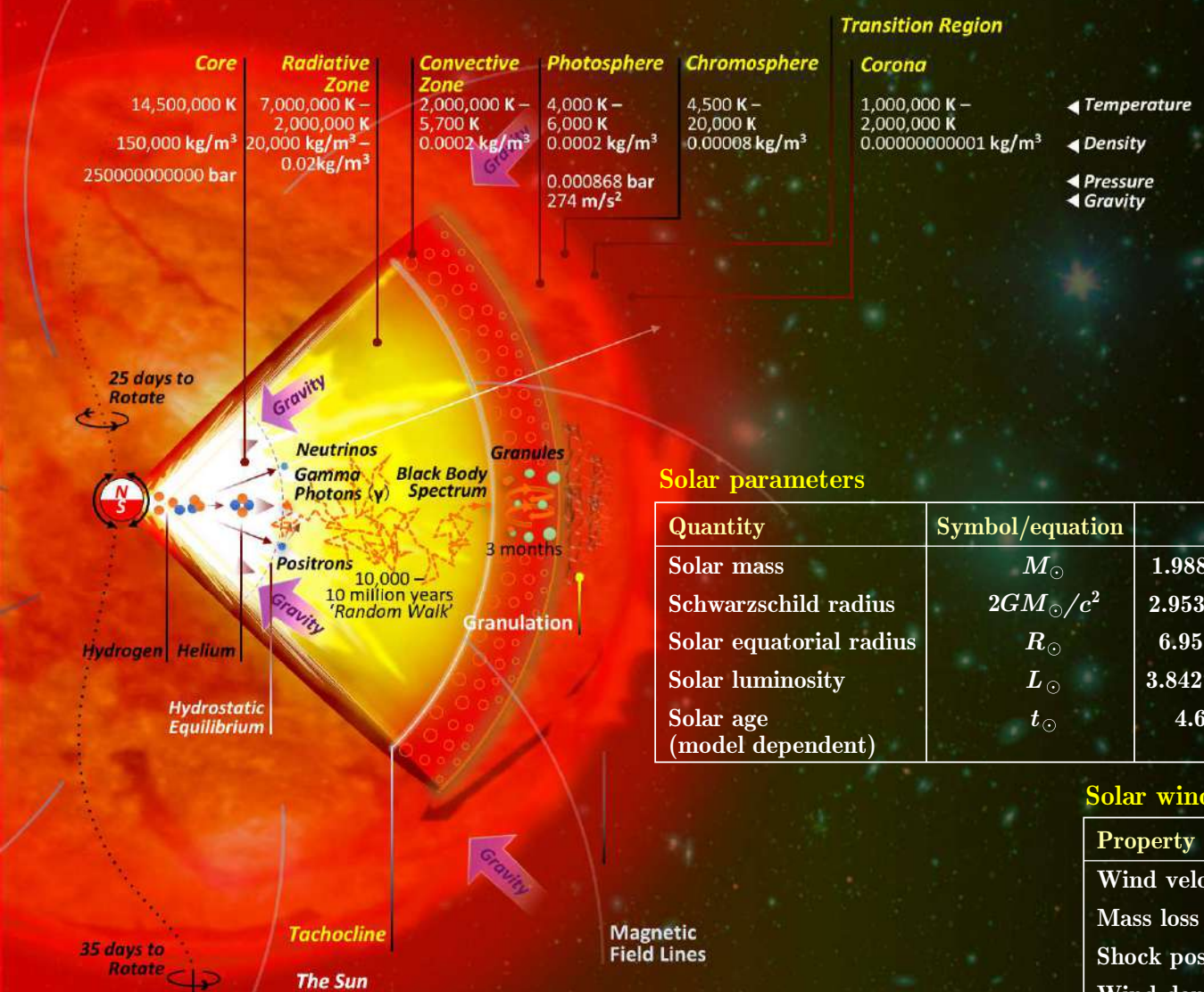
Z = 25 m

Z = 122 m
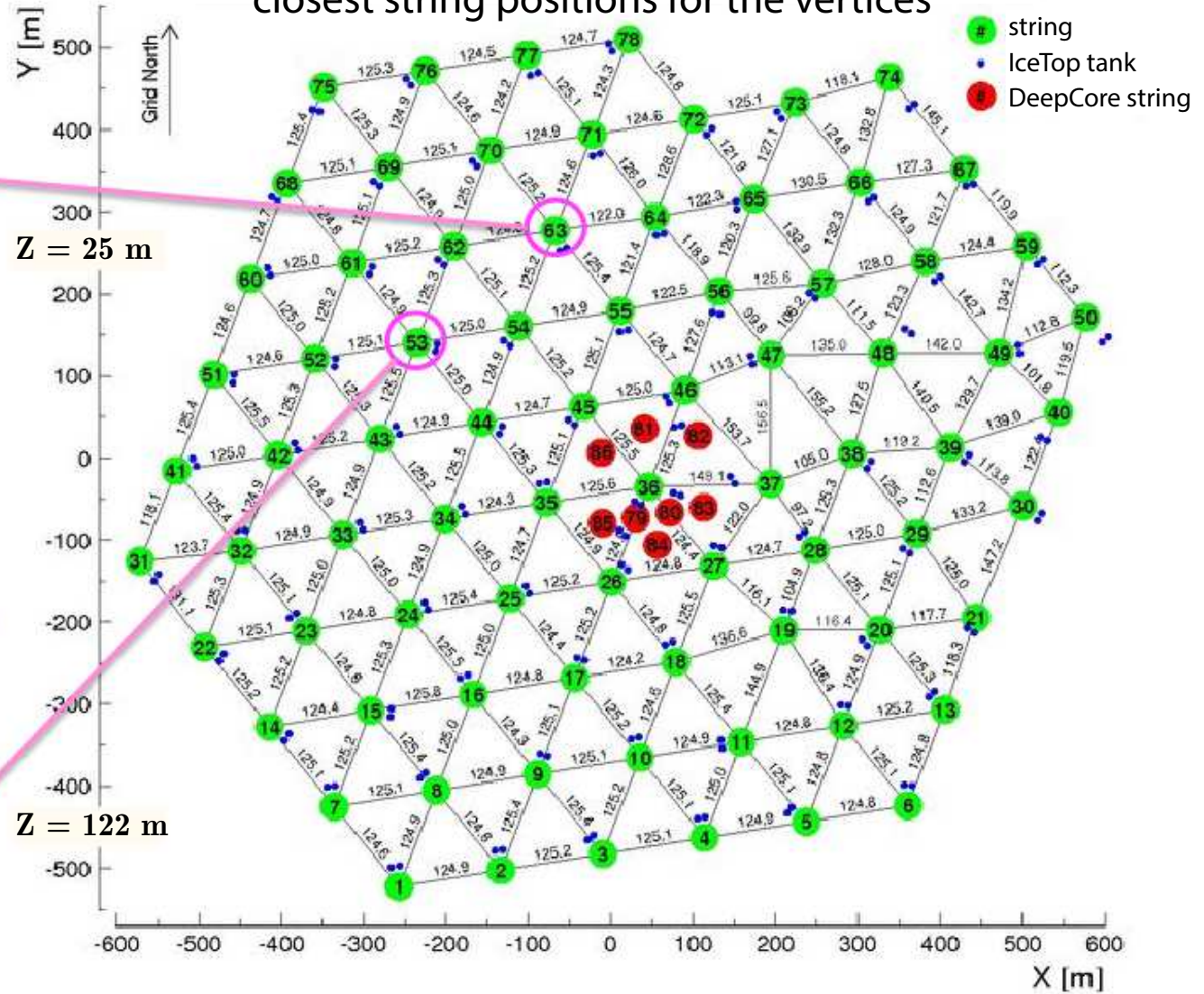
[From K. Mase, "A search for extremely high energy cosmogenic neutrinos with IceCube" (presentation).]

Appendix:
More on solar neutrinos

designContext

Core
14,500,000 K
150,000 kg/m³
250000000000 bar

Radiative Zone
7,000,000 K –
2,000,000 K
20,000 kg/m³ –
0.02kg/m³

Convective Zone
2,000,000 K –
5,700 K
0.0002 kg/m³

Photosphere
4,000 K –
6,000 K
0.0002 kg/m³
0.000868 bar
274 m/s²

Chromosphere
4,500 K –
20,000 K
0.00008 kg/m³

Transition Region

Corona
1,000,000 K –
2,000,000 K
0.00000000001 kg/m³

◀ Temperature
◀ Density
◀ Pressure
◀ Gravity
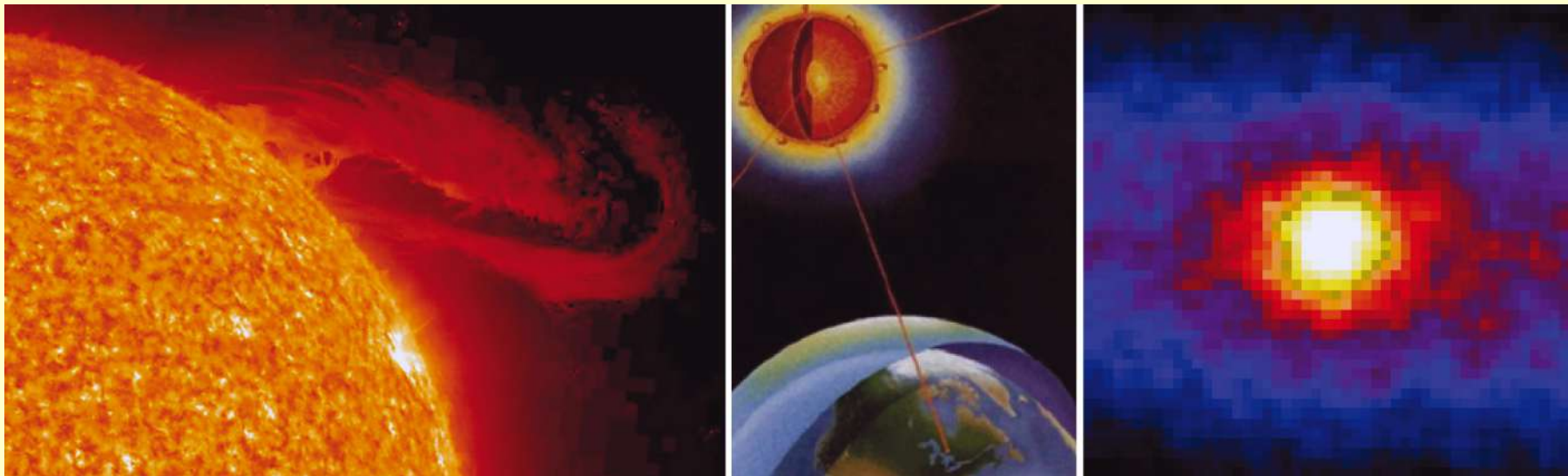
Approximately every 11 years, the magnetic field of the Sun switches its polarity.

25 days to Rotate

Gravity

Neutrinos
Gamma Photons (γ)
Black Body Spectrum
Granules

Positrons
10,000 –
10 million years
'Random Walk'

3 months

Granulation

Hydrogen | Helium

Hydrostatic Equilibrium

35 days to Rotate

Tachocline

The Sun

Magnetic Field Lines

Atmosphere

Solar parameters

Quantity	Symbol/equation	Value	Relative to Earth
Solar mass	$M_\odot$	$1.9884(2) \times 10^{30}$ kg	$3.33 \times 10^5 M_\oplus$
Schwarzschild radius	$2GM_\odot/c^2$	$2.9532500770(2)$ km	$3.33 \times 10^5 R_\oplus^S$
Solar equatorial radius	$R_\odot$	$6.9551(3) \times 10^8$ m	$1.09 \times 10^2 R_\oplus$
Solar luminosity	$L_\odot$	$3.8427(14) \times 10^{26}$ W	–
Solar age (model dependent)	$t_\odot$	$4.6 - 4.7 \times 10^9$ yr	$\gtrsim t_\oplus$

Solar wind parameters

Property	Typical value
Wind velocity (v_{sw})	500 km s^{-1}
Mass loss rate ($\dot{M}_{sw}$)	3×10^{-14} M$_\odot$ yr^{-1}
Shock position (r_{sw}^s)	100 AU
Wind density at r_{sw}^s (ρ_{sw}^s)	10^{-27} g cm^{-3}

1   Basic equations of stellar structure.

$$\text{Continuity equation:} \quad \frac{dm}{dr} = 4\pi r^2 \rho,$$

$$\text{Hydrostatic equation:} \quad \frac{dp}{dr} = -\frac{Gm\rho}{r^2},$$

$$\text{Energy equation:} \quad \frac{dL}{dr} = 4\pi r^2 \left[\epsilon\rho - \rho\frac{d}{dt}\left(\frac{u}{\rho}\right) + \frac{p}{\rho}\frac{d\rho}{dt} \right],$$

$$\text{Energy transfer equation:} \quad \frac{dT}{dr} = \nabla\frac{T}{p}\frac{dp}{dr}.$$

Here
r is distance to the center and t is time [all following variables are functions of r and t],
p is pressure [$p = p_{\text{gas}} + p_{\text{rad}} + B^2/8\pi$],
m is the mass of the sphere interior to r ("shell mass"),
ρ is density,
T is temperature,
L is the flow of energy per unit time through the sphere of radius r,
ϵ is the rate of nuclear energy generation per unit mass and time,
u is the internal energy per unit volume.

Also, the temperature gradient is characterized by $\nabla = d\ln T/d\ln p$ and is determined by the mode of energy transport.

1. Continuity equation

follows from the definition of the shell mass [assuming $\rho(\mathbf{r}) = \rho(r)$]:

$$m = m(r) = \int_{V(r)} \rho(\mathbf{r})d\mathbf{r} = 4\pi \int_0^r \rho(R)R^2 dR,$$

$$\Downarrow$$

$$\frac{dm}{dr} = 4\pi r^2 \rho.$$

2. Hydrostatic equation

follows from the hydrostatic equilibrium between the gravity and pressure gradient. Let $dV = d\sigma\,dr$ be a cylindric volume of the radial extend dr and surface $d\sigma$ with the axis directed to the center. The gravity and pressure forces are, respectively,

$$dF_g = -\frac{Gm}{r^2}\rho dV < 0 \quad \text{and} \quad dF_p = pd\sigma - (p+dp)d\sigma = -dpd\sigma > 0.$$

The equation $dF_g + dF_p = 0$ then yields the hydrostatic equilibrium equation:

$$\frac{dp}{dr} = -\frac{Gm\rho}{r^2}.$$

Derivation of other two equations is not so trivial...

2   Auxiliary equations.

In addition to the basic differential equations, we need auxiliary ones:

$$\text{Equation of state:}\quad \rho = \rho\left(p, T, \{X_i\}\right),$$
$$\text{Equation for opacity:}\quad \kappa = \kappa\left(p, T, \{X_i\}\right),$$
$$\text{Equation for NRR:}\quad \epsilon = \epsilon\left(p, T, \{X_i\}\right).$$

These equations link the thermal quantities and the chemical abundances X_i.

The opacity κ enters the basic equations through the temperature gradient:

$$\nabla = \nabla_{\mathsf{rad}} + \nabla_{\mathsf{conv}},$$

in which

$$\nabla_{\mathsf{rad}} = \frac{3}{16\pi a\tilde{c}G}\, \frac{\kappa p}{T^4}\, \frac{L}{m},$$

$\tilde{c}$ is the speed of light, a is the radiation density constant, and κ is the opacity, defined such that

$$\frac{1}{\kappa r} = \lambda_\gamma = \mathsf{mean\ free\ path\ of\ a\ photon.}$$

In making *"standard"* solar evolutionary models (SSM), the chemical abundance distributions are obtained by the time evolution equations:

$$\frac{\partial X_i}{\partial t} = \left(\frac{\partial X_i}{\partial t}\right)_{\mathsf{nuclear}} + \left(\frac{\partial X_i}{\partial t}\right)_{\mathsf{diffusion}}.$$

Example: Equation of state in SSM

The sophisticated SSM of Bahcall & Pinsonneault[a] uses a quasi-polytropic model with $\gamma = \gamma(r)$. Three regions clearly emerge. In two region the SSM output is approximated by a straight line, indicating polytropic behavior. Of these regions the outermost one ($\gamma \approx 1.667 \approx 5/3$) represents the convective zone where the heat transport is achieved by adiabatic convection. The Sun's inner region constitutes the radiative zone ($\gamma \approx 1.264$) where heat transport is achieved by e/m waves.
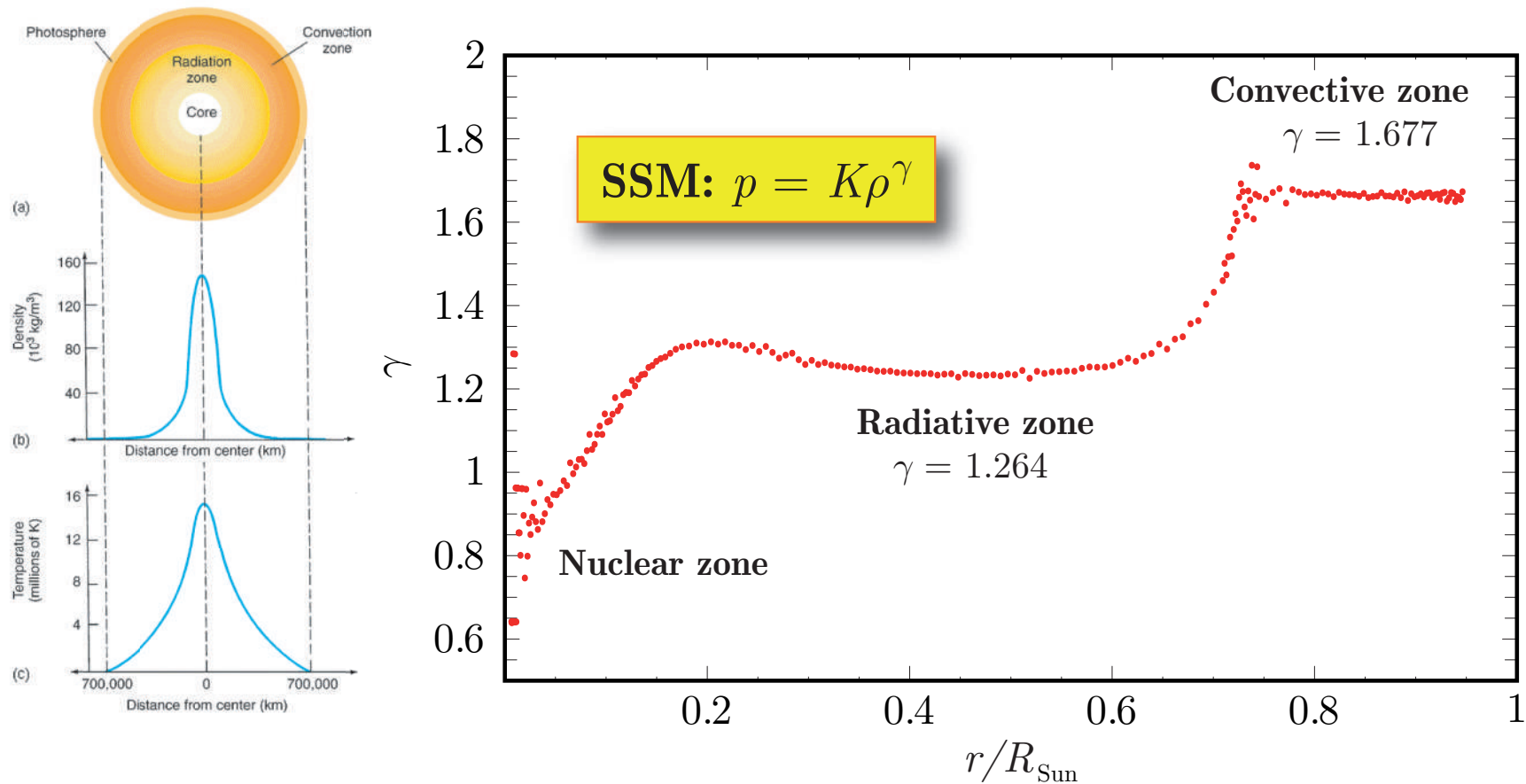
3 Helioseismology in a few images.
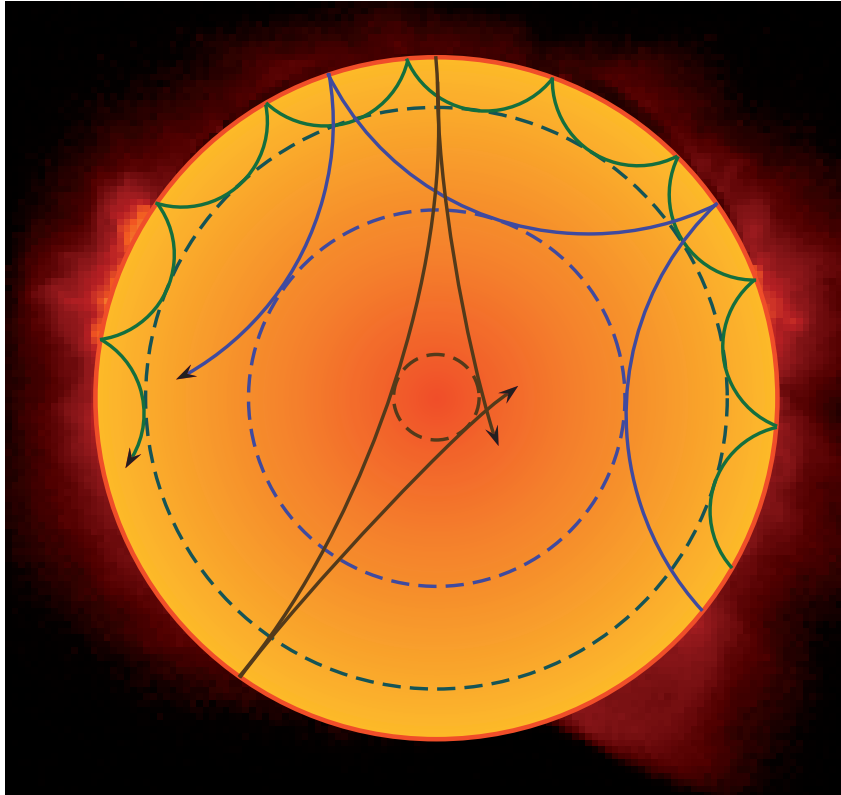
Solar oscillations consist of a reach spectrum of internal acoustic and gravity wave, stochastically exited by turbulent convection.

◁ Propagation of sound rays in a cross section of the solar interior. The ray paths are bent by the increase in sound speed with depth until they reach the inner turning point (indicated by the dotted circles), where they undergo total internal refraction. At the surface the waves are reflected by the rapid decrease in density.

The raw data of helioseismology consist of measurements of the photospheric Doppler velocity and/or (in some cases) intensity in a particular wavelength band taken at a cadence of about one minute and generally collected with as little interruption as possible over periods of months or years.
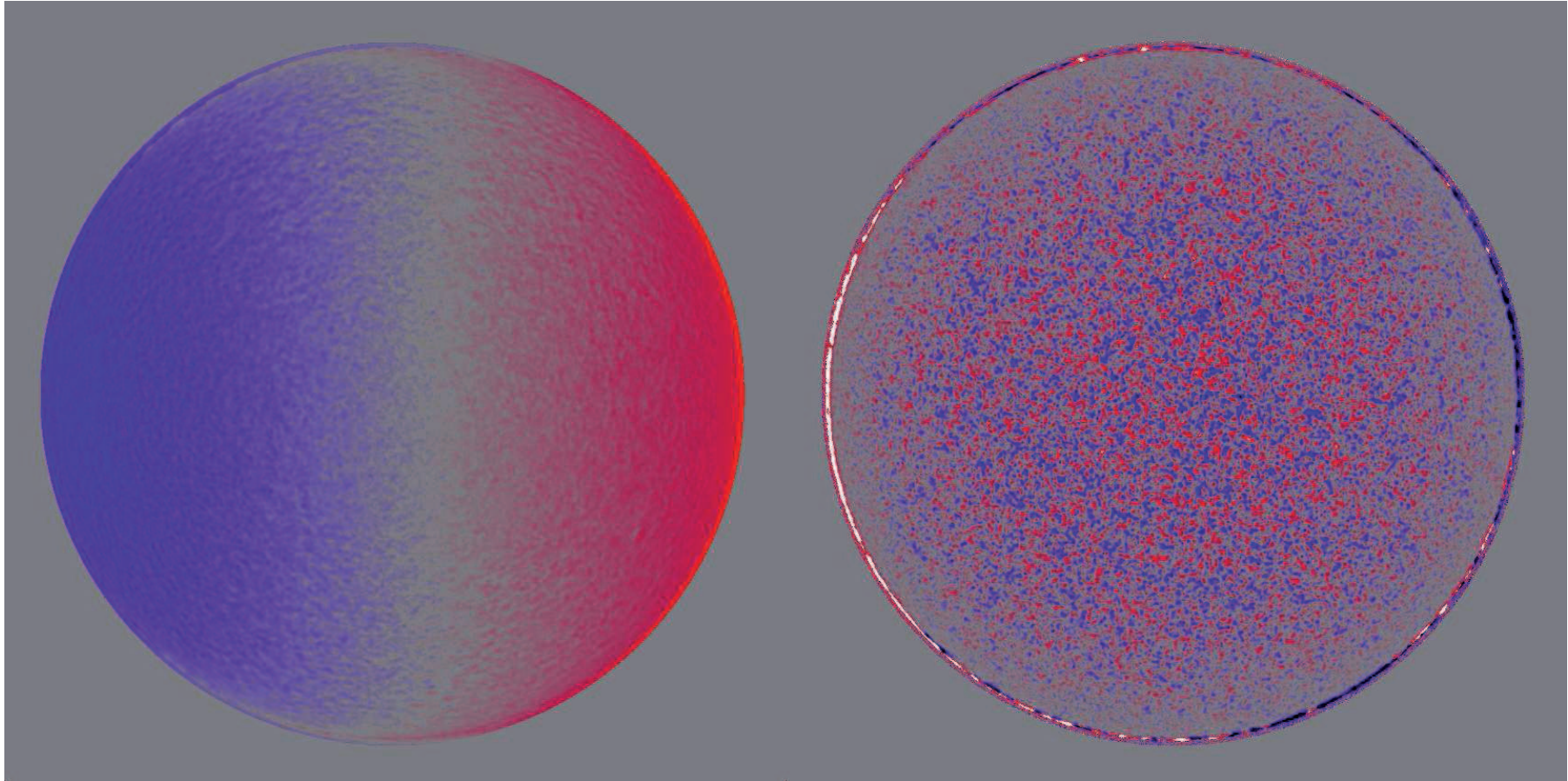
A typical single Doppler velocity image (dopplergram) of the Sun from one GONG (**G**lobal **O**scillation **N**etwork **G**roup] instrument (*left*), and the difference between that image and one taken a minute earlier (*right*), with red corresponding to motion away from, and blue to motion towards, the observer.

The shading across the first image comes from the solar rotation. After removing the rotation, the mottling associated primarily with solar oscillations becomes apparent.

Single Dopplergram
(30-MAR-96 19:54:00)

Single Dopplergram Minus 45 Images Average
(30-MAR-96 19:54:00)

Velocity (m/s)

Velocity (m/s)

SOI / MDI

Stanford Lockheed Institute for Space Research

SOI / MDI

Stanford Lockheed Institute for Space Research

Similar dopplergrams from SOI/MDI.
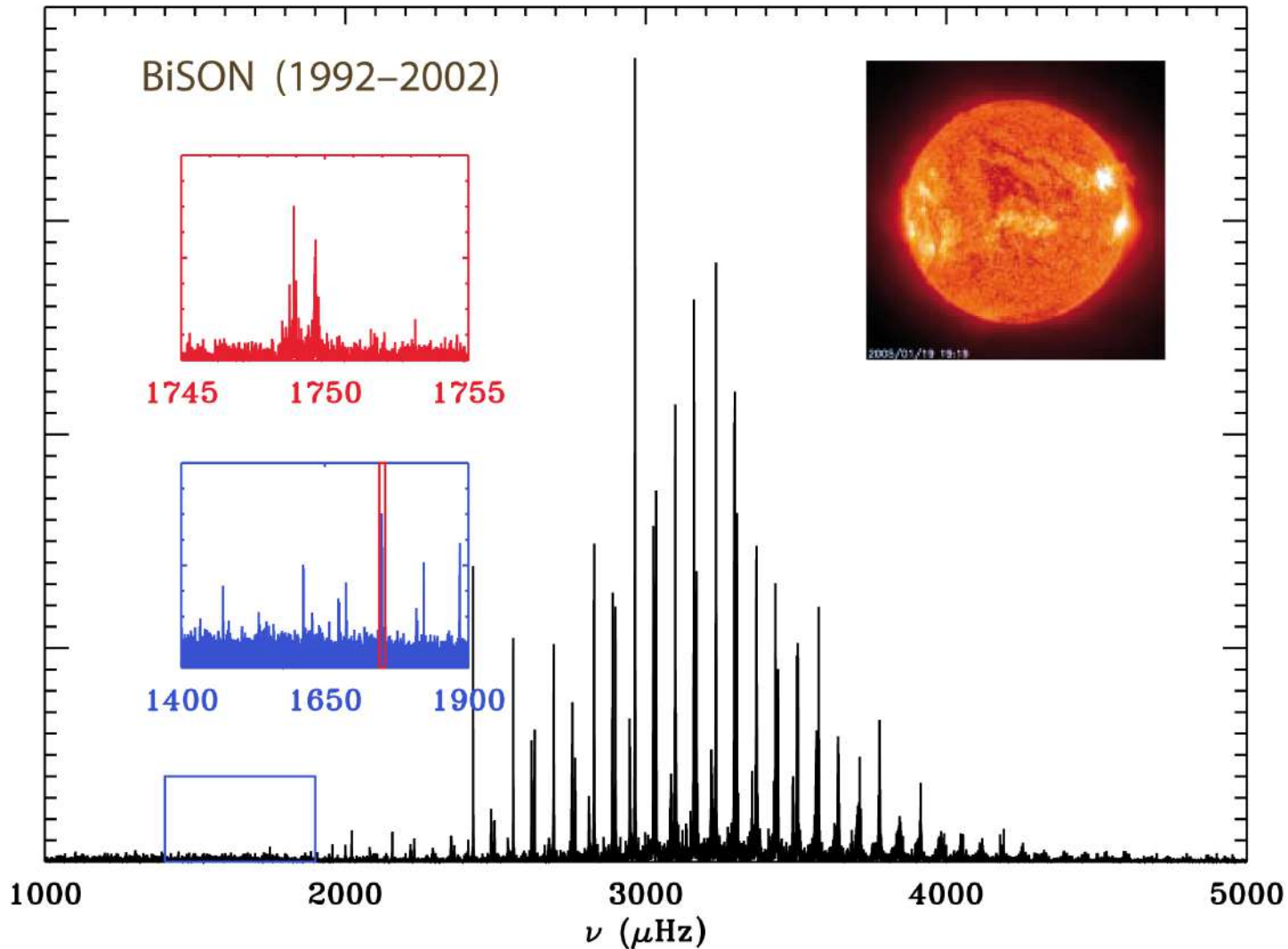
Power spectrum from 10 years of BiSON (**B**irmingham **I**ntegrated **S**olar **N**etwork) data, 1992–2002; the insets show the low-frequency end of the 5-minute band (blue) and a single, rotationally split $l = 1$ peak (red).
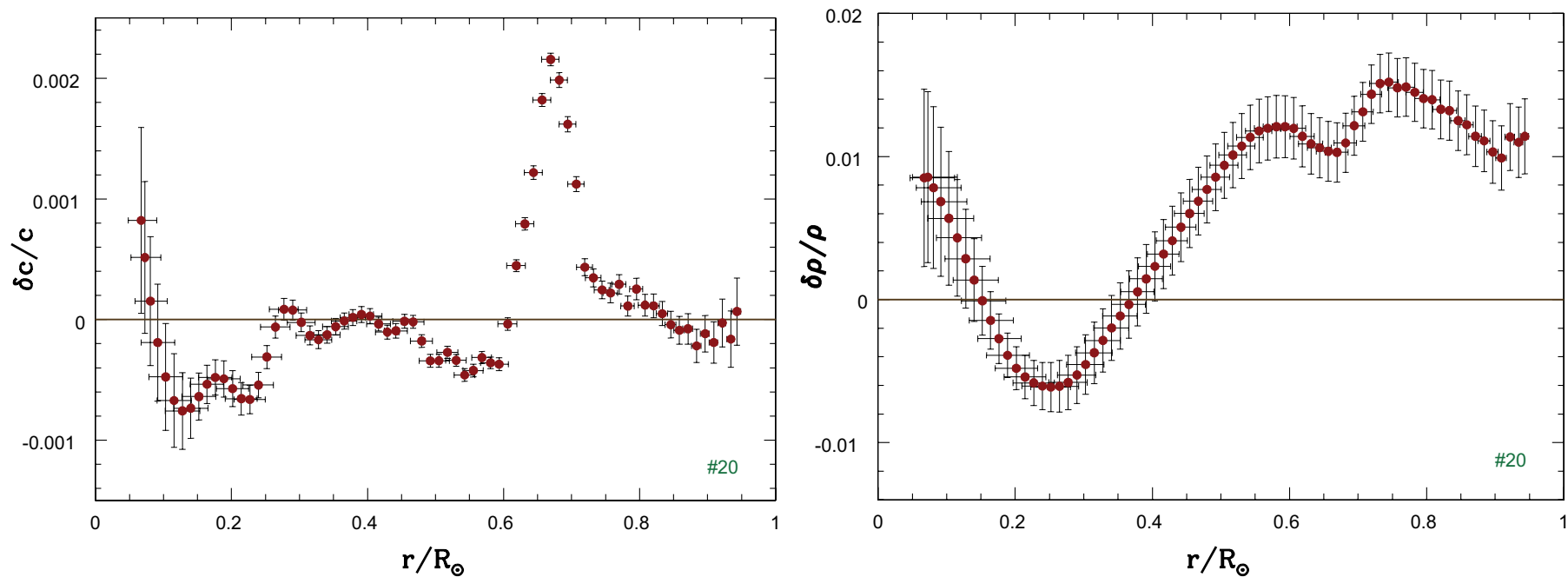
Fractional difference plots [(Sun-SSM)/SSM] for the sound speed (*left panel*) and density (*right panel*) for a SSM.[a] The data were determined by BPB00[b] using the SOHO/MDI (**SO**lar and **H**eliospheric **O**bservatory/**M**ichelson **D**oppler **I**mager) ESA-NASA solar frequency data set.[c] Vertical error bars indicate 1σ errors in the inversion results due to errors in the data. Horizontal error bars are a measure of the resolution of the inversion.

[a] R. A. Winnick *et al.*, "Seismic test of solar models, solar neutrinos, and implications for metal rich accretion," ApJ **576** (2002) 1075–1084, astro-ph/0111096.

[b] S. Basu, M. H. Pinsonneault, and J. N. Bahcall, "How much do helioseismological inferences depend upon the assumed reference model?" ApJ **529** (2000) 1084–1100, astro-ph/9909247.

[c] E. J. Rhodes, Jr. *et al.*, "Measurements of frequencies of solar oscillation for the MDI medium-l program," Solar Phys. **175** (1997) 287–310.
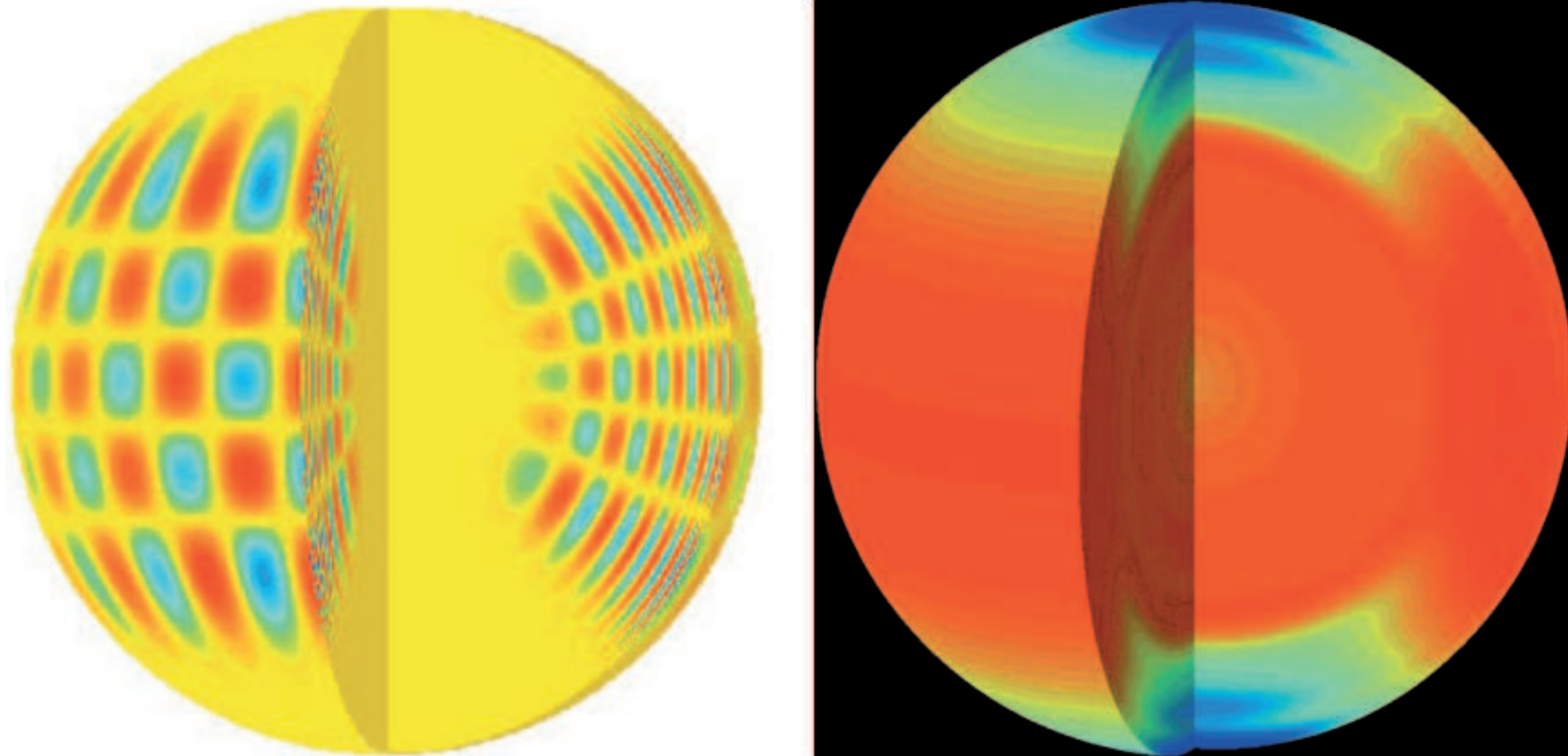
Left: A global acoustic p-mode wave is visualized: The radial order is $n = 14$, the angular degree is $l = 20$, the angular order is $m = 16$, and the frequency is $\nu = 2935.88 \pm 0.1$ μHz with SoHO/MDI (Michelson Doppler Image). The red and blue zones show displacement amplitudes of opposite sign. Right: The internal rotation rate is shown with a color code, measured with SoHO/MDI during May 1996 – April 1997. The red zone shows the fastest rotation rates ($P \approx 25$ days), dark blue the slowest ($P \approx 35$ days). Note that the rotation rate varies in latitude differently in the radiative and convective zones. (Courtesy of SoHO/MDI and NASA.)

4   Solar fusion.

Certain physical investigations in the past year make it probable to my mind that some portion of sub-atomic energy is actually being set free in a star. . . . If five per cent of a star's mass consists initially of hydrogen atoms, which are gradually being combined to form more complex elements, the total heat liberated will more than suffice for our demands, and we need look no further for the source of a star's energy. . .

Sir Arthur Eddington, Nature (1920)
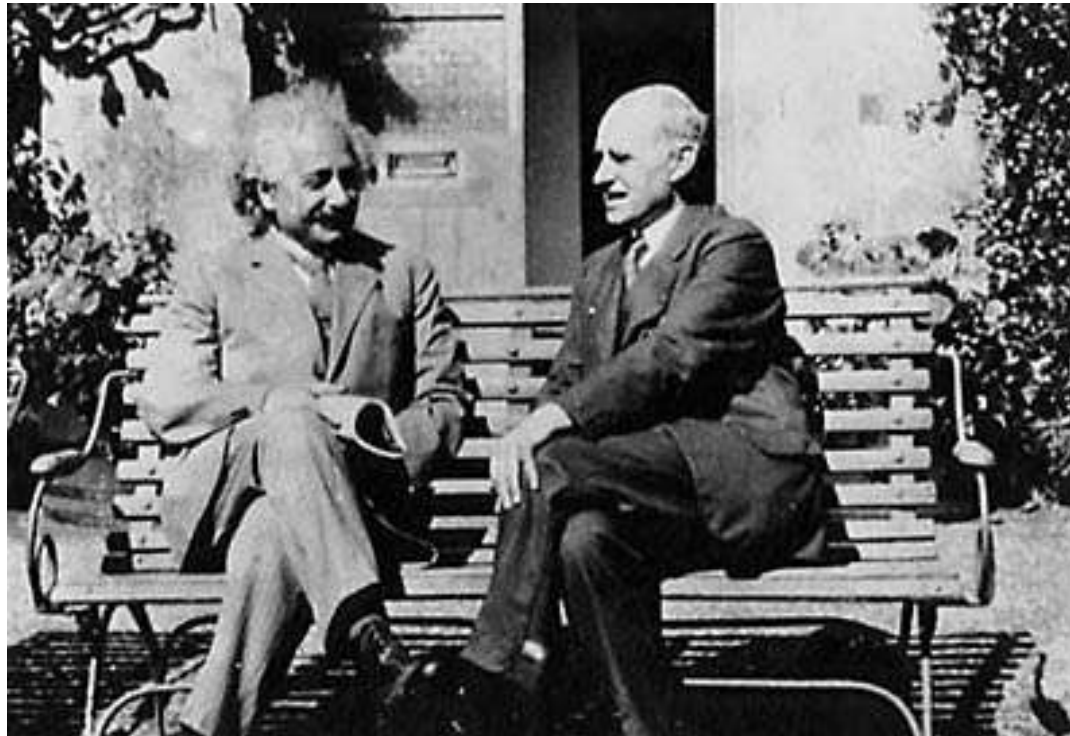
5   The pp fusion step by step.

The evidence is strong that the overall fusion reaction in the Sun is "burning" hydrogen to make helium:

$$4\,^1\mathrm{H} + 2\,e^- \;\rightarrow\; {}^4\mathrm{He} + 2\,\nu_e + 6\,\gamma.$$
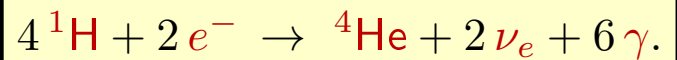
In this reaction, the final particles have less internal energy than the starting particles. Since energy is conserved, the extra energy is released as
  ⋆ energy of motion of the nuclei and electrons in the solar gas,
  ⋆ the production of lots of low energy photons and, finally,
  ⋆ the energy of the neutrinos, which easily shoot out of the Sun.
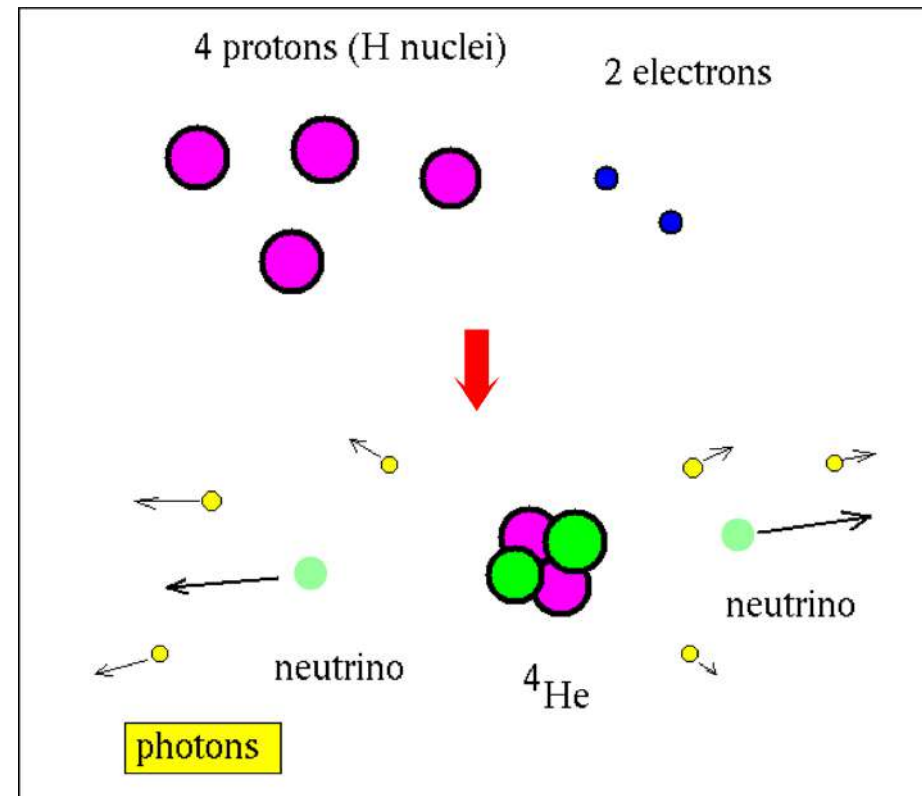
As a result the solar plasma gets hotter and has lots of photons.

The energy release in the reaction $4\,^1\mathrm{H} + 2\,e^- \rightarrow\ ^4\mathrm{He} + 2\,\nu_e + 6\,\gamma$ is

$$Q = (4 \times 1.007825u - 4.002603u) \times 931 \ \mathrm{MeV}/u = 26.732 \ \mathrm{MeV}$$

each time the reaction happens. Here $1.007825u$ is the mass of a hydrogen atom and $4.002603u$ is the mass of a helium atom. Binding energies, neutrinos (small mass), and photons (zero mass) do not enter into the calculation.

The luminosity sum rule:

Thus, the generation of $Q = 26.732$ MeV in the Sun is accompanied by the production of two ν_es. If the Sun is approximately in a steady state with a nuclear energy production rate that equals its luminosity, then the total solar neutrino flux at Earth is (Dar & Nussinov, 1991)

$$\Phi_\nu \approx \frac{2S_\odot}{Q - 2\langle E_\nu \rangle} \approx 6.54 \times 10^{10} \ \mathrm{cm}^{-2}\,\mathrm{s}^{-1},$$

where $S_\odot = L_\odot/4\pi d_\odot^2 = 1.366$ kW m^{-2} is the measured solar constant which yields a solar luminosity $L_\odot = 4\pi d_\odot^2 \approx 3.846 \times 10^{33}$ erg s^{-1} for an average distance $d_\odot \approx 1.496 \times 10^{13}$ cm of the Earth from the Sun, and

$$\langle E_\nu \rangle = \frac{1}{\Phi_\nu} \sum_i E_\nu^{(i)} \Phi_\nu^{(i)}$$

is the mean energy of solar neutrinos which has been approximated by

$$\langle E_\nu^{(pp)} \rangle \approx 0.265 \ \mathrm{MeV},$$

the mean energy of the pp solar neutrinos that dominate the solar neutrino flux.

The fusion reaction as given above is a summary. Really it may only occur in several steps since the temperature in the Sun is too low and, as a result,

---

an inelastic collision of *two* nuclei in the Sun is *nearly impossible.*

The two nuclei have to get within $r_p \sim 10^{-13}$ cm for the strong interactions to hold them together but they repel each other. For example, the potential energy for Coulomb interaction of two protons is

$$U_{\text{Coulomb}} = \frac{e^2}{r_p} \approx 2 \times 10^{-6} \text{ erg} \approx 1.2 \text{ MeV.}$$

Since $T_\odot \lesssim 1.5 \times 10^7$ K (the helioseismology confirms this!)

$$\langle E_p^{\text{kin}} \rangle = \frac{3}{2} k T_\odot \lesssim 2 \text{ keV.}$$

Assuming Maxwellian distribution, the fraction of protons with $E_p^{\text{kin}} > U_{\text{Coulomb}}$ is

$$\exp\left(-E_p^{\text{kin}} / \langle E_p^{\text{kin}} \rangle\right) < e^{-600} \sim 10^{-260}.$$

Considering that the number of protons in the Sun is about 10^{57} we can conclude that

the classical probability of the fusion is ZERO.

Let's estimate the quantum probability.[a] The nucleus wave function can be written

$$\psi \propto \exp\left(i \int p\,dx\right).$$

$$E_p^{\text{kin}} = p^2/2m = E_0 - U, \qquad \Rightarrow \qquad p = \sqrt{2m\,(E_0 - U)}.$$

The repulsion energy of two nuclei with charges $Z_1 e$ and $Z_2 e$ is $U = Z_1 Z_2 e^2/r$ and the classical turning point ($p = 0$) is given by $r_1 = Z_1 Z_2 e^2/E_0$. In quantum theory

$$p = i\sqrt{2m\,(U - E_0)} \quad \text{for} \quad r < r_1$$

and thus the probability of the barrier penetration (tunnel effect) can be estimated as

$$\psi^2(r) \propto \exp\left[-2 \int_r^{r_1} \sqrt{2m\,[U(r') - E_0]}\,dr'\right].$$

where $r \sim r_p$ is the radius of nuclear interaction. Considering that usually $r_p \ll r_1$, for rough estimation we can put $r = 0$.

It is assumed here that one of the nuclei is in rest ($m_2 = \infty$). To take into account its finite mass one have to replace m with the effective dynamic mass of the colliding particles:

$$m \longmapsto M = \frac{m_1 m_2}{m_1 + m_2} = \frac{A_1 A_2}{A_1 + A_2} m_p = A m_p.$$

---

[a]Here we follow the wonderful book by Ya. B. Zeldovich *et al.* [Я. В. Зельдович, С. И.Блинников, Н. И. Шакура, «Физические основы строения и эволюции звезд», Изд. МГУ, Москва, 1981], which is highly recommended to (Russian-speaking) students for further reading.

Than the barrier penetration probability is given by

$$\psi^2(r) \approx \psi^2(0) = e^{-2\pi\eta} \quad \text{(Gamow factor)},$$

where $(\hbar = c = 1 \Longrightarrow e^2/\hbar c = \alpha)$

$$\eta = \frac{r_1}{\pi}\sqrt{2ME_0} \int_0^1 \sqrt{\frac{1}{x} - 1}\, dx = \frac{1}{2\pi}\sqrt{\frac{E_G}{E}} \quad \text{(Sommerfeld parameter)}$$

and

$$E_G = 2\left(\pi Z_1 Z_2 \alpha\right)^2 M \quad \text{(Gamow energy)}.$$

In thermal equilibrium with the temperature T the number of particles with energy E_0 is proportional to $exp\left(-E_0/kT\right)$. Therefore the full probability is proportional to

$$\int e^{-\chi(E_0)}\, dE_0, \quad \text{where} \quad \chi = \sqrt{\frac{E_G}{E_0}} + \frac{E_0}{kT}.$$

The integral can be evaluated by using the saddle-point technique considering that the function χ has a sharp minimum (and thus $e^{-\chi}$ has a sharp maximum, – *Gamow's peak*). The minimum is given by

$$\frac{d\chi}{dE_0} = -\frac{1}{2E_0}\sqrt{\frac{E_G}{E_0}} + \frac{1}{kT} = 0.$$
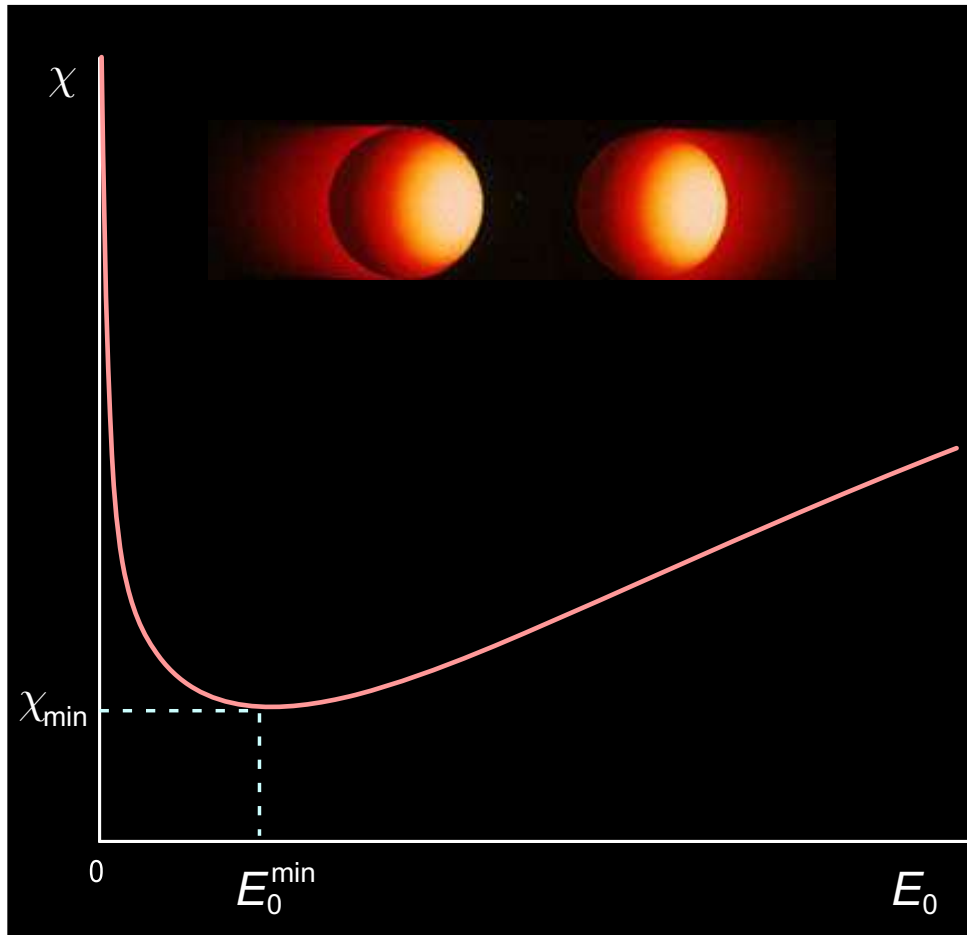
Gamow's peak is given by

$$E_0^{\mathrm{min}} = E_G^{1/3} \left(kT/2\right)^{2/3}$$

$$\simeq 0.122 \left(AZ_1^2 Z_2^2 T_9^2\right)^{1/3} \ \mathrm{MeV},$$

$$\chi_{\mathrm{min}} = 3 \left(\frac{E_G}{4kT}\right)^{1/3}$$

$$\simeq 4.25 \left(\frac{AZ_1^2 Z_2^2}{T_9}\right)^{1/3},$$

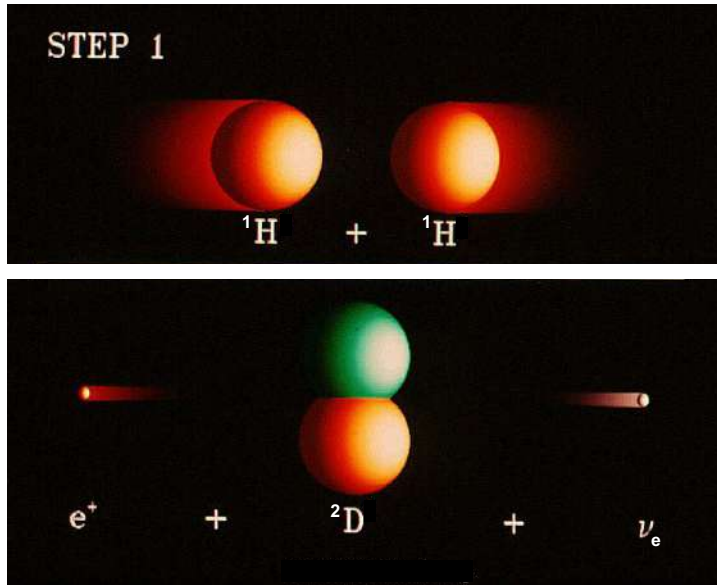where $T_9 = T/(10^9 \ \mathrm{K})$. Now one can approximate $\chi(E_0)$ by

$$\chi(E_0) \simeq \chi_{\mathrm{min}} + \kappa \left(1 - E_0/E_0^{\mathrm{min}}\right)^2,$$

$$\kappa = (3/8) \left(2E_G/kT\right)^{1/3}.$$

Finally, the full probability is estimated by $C(T) \exp\left[-\chi_{\mathrm{min}}(T)\right]$.

Example: for the pp fusion in the center of the Sun ($T_9 \simeq 0.015$)

$$E_0^{\mathrm{min}} \simeq 5.9 \ \mathrm{keV}, \quad \chi_{\mathrm{min}} \simeq 13.7, \quad \exp\left(-\chi_{\mathrm{min}}\right) \simeq 1.15 \times 10^{-6}.$$

The ppI branch.

STEP 1

^{1}H $\quad$ + $\quad$ ^{1}H

e^+ $\quad$ + $\quad$ ^{2}D $\quad$ + $\quad$ ν_e

Note: the secondary positron very quickly encounters a free electron in the Sun and both particles annihilate, their mass energy appearing as two 511 KeV γs:
$e^+e^- \to \gamma\gamma$.

$$\mathbf{p} + \mathbf{p} \to \mathbf{d} + \mathbf{e}^+ + \nu_{\mathbf{e}}$$

The energy liberation in this reaction is $Q = 1.442$ MeV, including in average ~ 0.26 MeV taking away by neutrinos ($E_\nu \le 420$ keV). The number of deuterium nuclei generated in 1 cm^3 per 1 s is

$$\frac{d[\mathrm{D}]}{dt} = C_{11} \frac{n_p^2}{2N_A T_9^{2/3}} \exp\left(-\frac{3.38}{T_9^{1/3}}\right) \left[\mathrm{cm}^{-3}\mathrm{s}^{-1}\right],$$
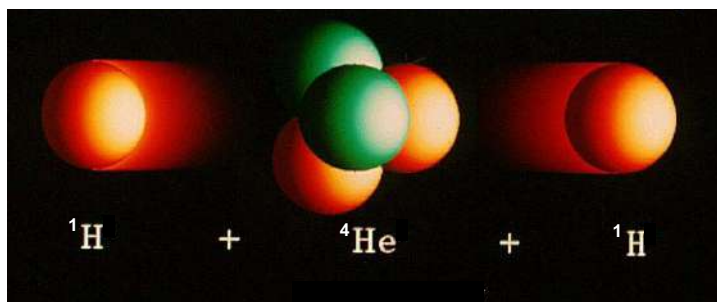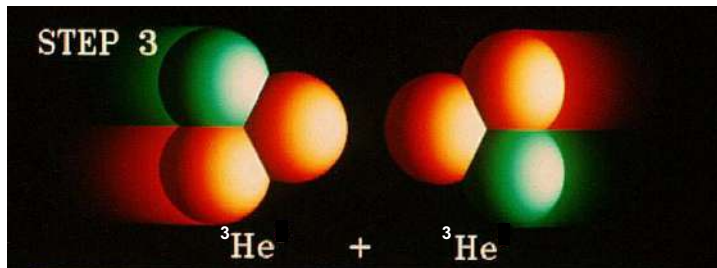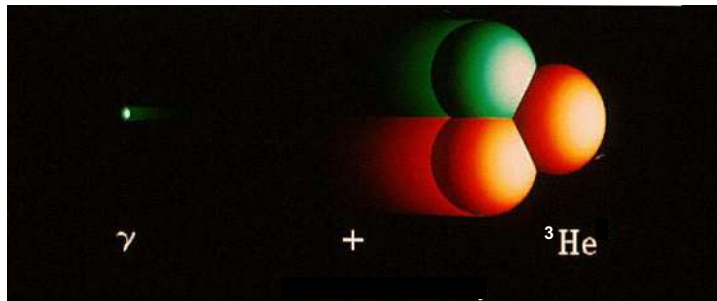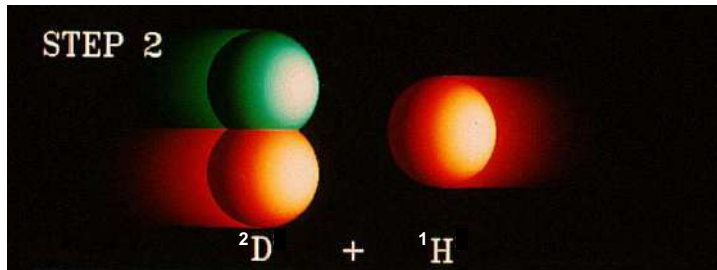
$$C_{11} \approx 4.2 \times 10^{-15}.$$

By introducing the weight concentrations (abundances) for the chemical elements

$$X(i) = \frac{m_{\mathsf{H}} n_i A_i}{\rho} = \frac{n_i A_i}{N_A \rho},$$

we can write the reaction rate:

$$\dot{X}(\mathsf{D}) = C_{11}\rho\left[X(\mathsf{H})\right]^2 T_9^{-2/3} e^{-3.38/T_9^{1/3}} \left[\mathsf{s}^{-1}\right].$$

The characteristic time is $t_{11} \approx 1.3 \times 10^{10}$ yr at $\rho = 100$ g/cm^3 and $T = 1.3 \times 10^7$ K.
The reaction is very rare. That's why the Sun is still burning after $\sim 4.6 \times 10^9$ years!

STEP 2

^{2}D + ^{1}H

γ + ^{3}He

$\mathbf{p} + \mathbf{d} \rightarrow {}^3\mathsf{He} + \gamma$
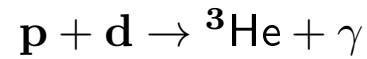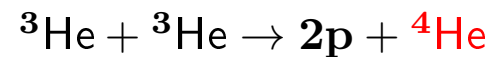
The energy liberation: $Q = 5.494$ MeV; the reaction rate:

$$\dot{X}({}^3\mathsf{He}) = C_{12}\rho X({}^1\mathsf{H})X({}^2\mathsf{D})T_9^{-2/3}e^{-3.72/T_9^{1/3}},$$

$$C_{12} \approx 3.98 \times 10^3 \text{ s}^{-1} \approx 10^{18}C_{11},$$

$$\text{and} \quad t_{12} \approx 6 \text{ s.}$$

STEP 3

^{3}He + ^{3}He

^{1}H + ^{4}He + ^{1}H

$^3\mathsf{He} + {}^3\mathsf{He} \rightarrow \mathbf{2p} + {}^4\mathsf{He}$

The energy liberation: $Q = 12.859$ MeV; the reaction rate:

$$\dot{X}({}^4\mathsf{He}) = C_{33}\rho \left[X({}^3\mathsf{He})\right]^2 T_9^{-2/3}e^{-12.28/T_9^{1/3}},$$

$$C_{33} \approx 1.3 \times 10^{10} \text{ s}^{-1} \approx 3 \times 10^6 C_{12}$$

$$\approx 3 \times 10^{24}C_{11},$$

$$\text{and} \quad t_{33} \approx 10^6 \text{ yr.}$$

● Even at temperatures in the Sun's core, 1.5×10^7 K, the average lifetime of a proton against pp fusion is about $\sim 10^{10}$ yr. It is an extremely slow reaction, and it is this time scale that sets the stellar clock, so to speak, by determining how long the star will remain a stable main sequence object.

● In contrast, the deuteron created will only last about a few seconds before it hits into another proton and fusion creates a ^{3}He nucleus. Therefore it cannot accrue and its stationary concentration is given by $X(\mathrm{D}) = (t_{12}/t_{11})X(\mathrm{H}) \approx 10^{-17}X(\mathrm{H})$.

● The ^{3}He nucleus will last about 250,000 years before it hits another ^{3}He nucleus which has enough energy to penetrate the Coulomb barrier.

The pep fusion.

The deuterium can also be produced in the reaction

$$^1\mathrm{H} +^1 \mathrm{H} + e^- \to {}^2\mathrm{D} + \nu_e \quad (E_\nu = 1.44 \text{ MeV})$$
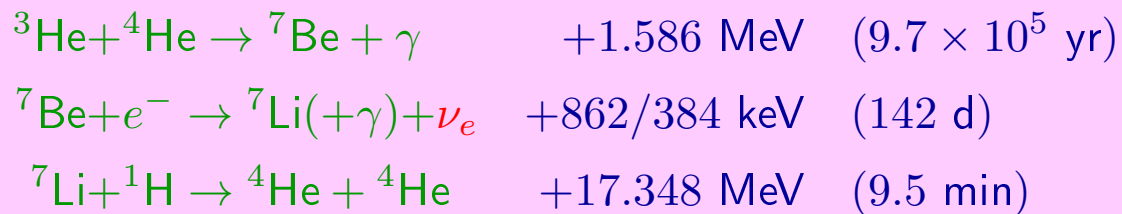
which has a characteristic time scale $\sim 10^{12}$ yr that is rather larger than the age of the Universe at this time. So it is *insignificant* in the Sun as far as energy generation is concerned. Nevertheless, the pep fusion accounts for about 0.25% of the deuterons created in the pp chain.

Enough pep fusions happen to produce a detectable number of neutrinos, so the reaction must be accounted for by those interested in the *solar neutrino problem*.

The pp II branch.

The ^{3}He does not always have to hit another ^{3}He nucleus. It could hit a ^{4}He forming stable ^{7}Be. But ^{7}Be has an affinity for electron capture, and can absorb free electrons. The electron turns one of the Be protons into a neutron, changing the ^{7}Be into ^{7}Li, while tossing out a neutrino. The ^{7}Li will then quickly fuse with a free proton, resulting in unstable ^{8}Be which immediately falls apart into two stable ^{4}He nuclei.

$$^3\text{He} + ^4\text{He} \rightarrow ^7\text{Be} + \gamma \qquad +1.586 \text{ MeV} \quad (9.7 \times 10^5 \text{ yr})$$

$$^7\text{Be} + e^- \rightarrow ^7\text{Li}(+\gamma) + \nu_e \quad +862/384 \text{ keV} \quad (142 \text{ d})$$

$$^7\text{Li} + ^1\text{H} \rightarrow ^4\text{He} + ^4\text{He} \qquad +17.348 \text{ MeV} \quad (9.5 \text{ min})$$

$\sim 14\,\%$ of ^{3}He goes out this way avoiding the pp I chain,

$\sim 99.89\,\%$ of ^{7}Be goes the ^{7}Li route.

$\sim 90\%$ of ^{7}Li nuclei are in the ground state and thus $E_\nu = 862$ keV; the rest lithium is created in an excited state and $E_\nu = 384$ keV.

Note: Fusion with ^{4}He is less likely, because there is more ^{3}He around deep inside the stellar core. But in heavier stars, where the temperatures exceed about 2.4×10^7 K, the pp II chain can rival the pp I chain for energy production inside the star. This is because at higher temperatures the ^{3}He gets used up faster, driving down its abundance compared to ^{4}He.

The pp III branch.

The ^{7}Be has two ways to go – it can either absorb an electron, as in pp II (99.89%), or absorb a proton, as in pp III (0.11%). Absorbing a proton raises the nucleus from beryllium to boron, and the ^{7}Be becomes ^{8}B. But ^{8}B is unstable and takes < 1 s, fairly independent of temperature, to spit out a positron and a neutrino to become beryllium again, only this time it's ^{8}Be. But ^{8}Be falls apart into two ^{4}He nuclei, and once again we have turned hydrogen into helium.

$$^{7}\text{Be}+^{1}\text{H} \rightarrow \, ^{8}\text{B} + \gamma \qquad +135 \text{ keV} \quad (66 \text{ years})$$

$$^{8}\text{B} \rightarrow \, ^{8}\text{Be} + e^{+}+\nu_{e} \qquad 14.02 \text{ MeV} \quad (0.9 \text{ s})$$

$$^{8}\text{Be} \rightarrow \, ^{4}\text{He} + ^{4}\text{He} \qquad +18.074 \text{ MeV} \quad (9.7 \times 10^{-17} \text{ s})$$

$\sim 0.11\,\%$ of ^{7}Be goes this route.

Of course, $e^{+}e^{-} \rightarrow \gamma\gamma$.

Note: In low mass stars the internal temperature is not high enough to finish the pp cycle. They produce the first stage of pp fusion up to ^{3}He, but are unable to force the last stage of ^{3}He fusion, either with another ^{3}He or an ^{4}He. So they fuse hydrogen into ^{3}He instead of ^{4}He. This fact is confirmed by the observation that low mass stars are often anomalously rich in ^{3}He compared to ^{4}He.

The pp IV branch (hep reaction).

The pp chain involves one more process, so-called "hep reaction",

$$^{3}\mathrm{He} + {}^{1}\mathrm{H} \rightarrow {}^{4}\mathrm{Li} \rightarrow {}^{4}\mathrm{He} + e^{+} + \nu_{e}.$$
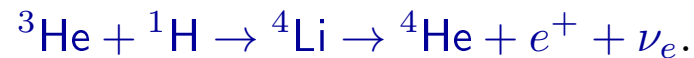
In fact, it is a sub-branch of the pp I chain. The low-energy cross section of this reaction is very uncertain. While the probability of the pp IV branch is estimated to be about $3 \times 10^{-5}\%$, the hep produces highest-energy solar neutrinos,[a]

$$E_{\nu} \leq 18.77 \text{ MeV},$$

which can at some level influence the electron energy spectrum produced by solar neutrino interactions and potentially can be measured in the high-threshold detectors like Super(Hyper)-Kamiokande and SNO+.

---

[a]The maximum neutrino energy is equal to the maximum energy of the $^{4}\mathrm{Li}$ β-decay.

The full pp chain.
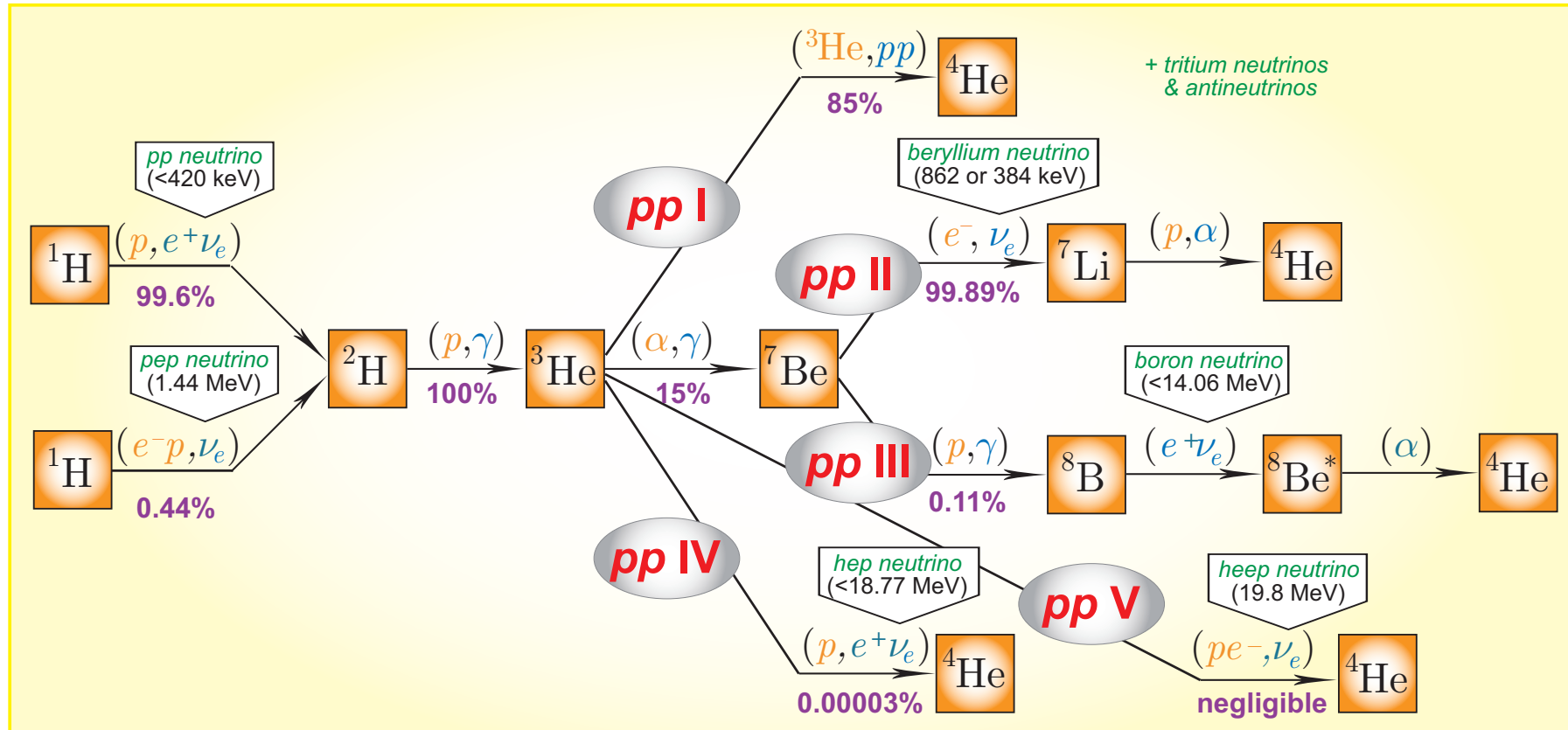
The diagram shows the full pp chain responsible for production of about 98.4% of the solar energy. The neutrinos export 3%, 4%, and 28% of the energy in $pp\,$I, $pp\,$II, $pp\,$III, respectively. Of course, all the chains are active simultaneously in a H-burning star containing significant ^{4}He. The details depend on density, temperature and composition but in the Sun the $pp\,$I strongly dominates.

The pp chain diagram with labeled cycles pp-I, pp-II, pp-III, and pep. Key labels include: ^4He, ^2H, ^3He, ^7Be, ^7Li, ^8B, p, e^-, e^+, ν, γ.

Pie chart: 2% Other, 26% Helium, 72% Hydrogen.

Inset reaction: $4\,^1H \rightarrow 1\,^4He$ + energy

Mass difference in single fusion is $\sim 0.048 \times 10^{-24}$ g. This matter disappears and converts into energy (γs, νs, recoil of nuclei)

https://www.mpi-hd.mpg.de/lin/research_bx.en.html
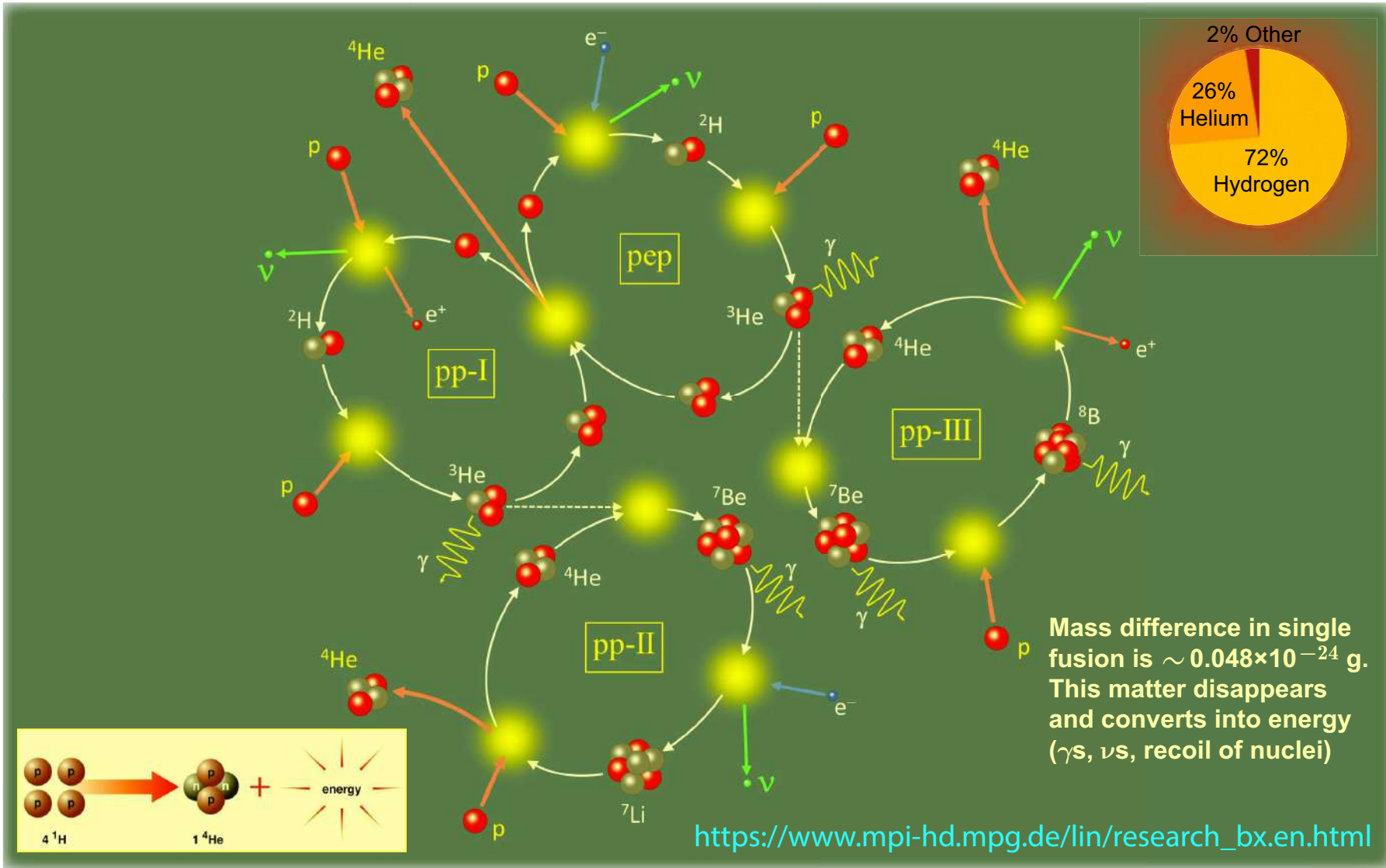
The main part of the pp chain consists of four intertwined loops (loops). But it is a quantum relativistic machine that converts matter into energy. Therefore it is not a Perpetuum Mobile.

Neutrino production profiles.

The rates of the solar neutrino production reactions strongly depend on temperature and thus on distance from the center of the Sun.

Figure shows the normalized flows (i.e. production profiles normalized to unity when integrated over the relative solar radius $R/R_\odot$) of the pp-chain and CNO neutrinos produced within the solar core, calculated within the "BSB(GS98)" model as functions of $R/R_\odot$ (cf. p. 49).

[Figure is taken from J. N. Bahcall, A. M. Serenelli, and S. Basu, "10,000 standard solar models: a Monte Carlo simulation," Astrophys. J. Suppl. Ser. **165** (2006) 400–431, astro-ph/0511337.]
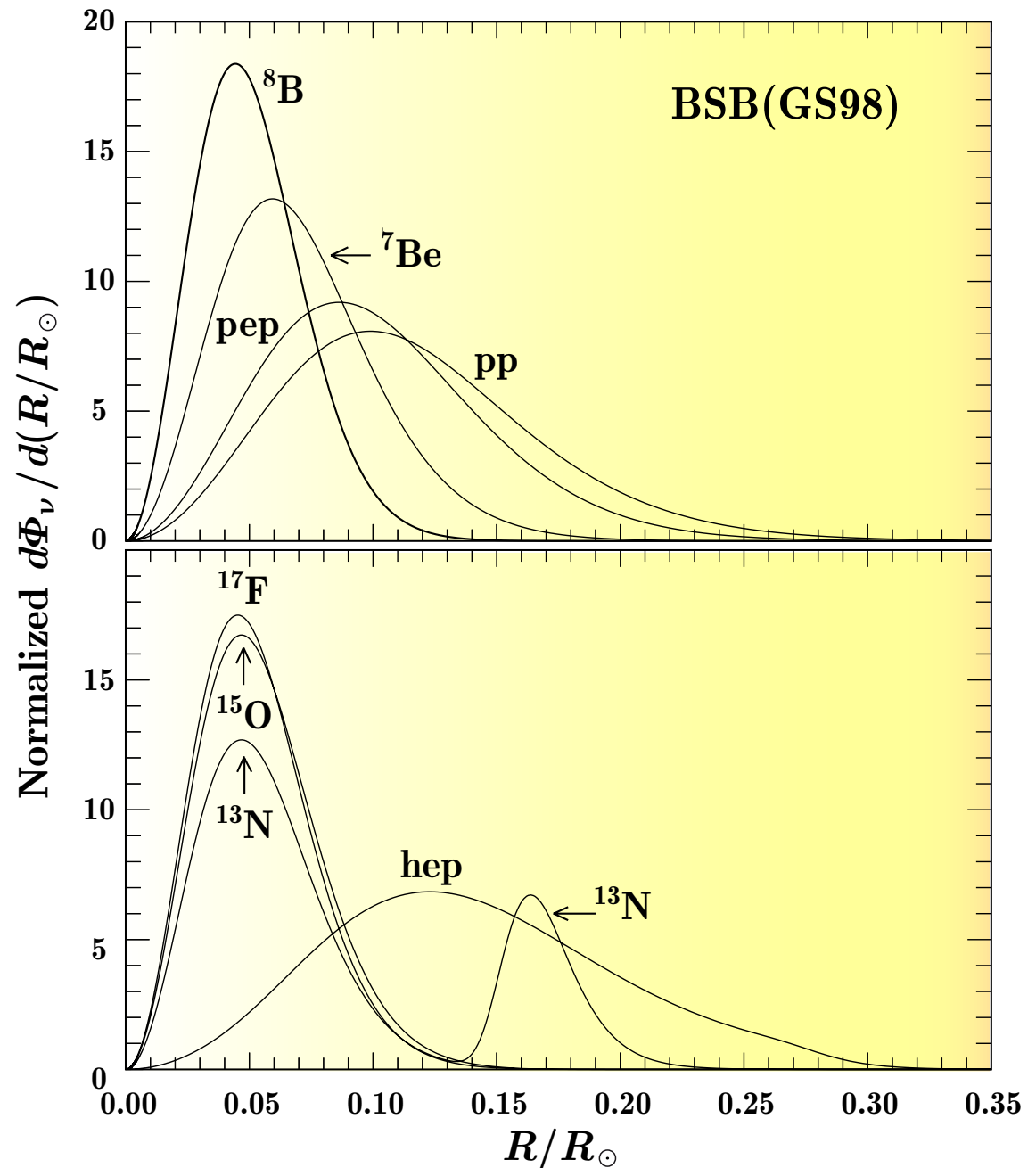
BSB(GS98) is a SSM which uses the same input quantities as the above-mentioned BS05(OP) model, but with improved low-temperature opacities and with the old (high) GS98 metallicities. Very similar results are obtained within solar seismic models (e.g. by Couvidat *et al.*, 2003).

The neutrino flux vanishes at the Sun's center because the neutrino radiation field here is nearly uniform in all directions (neutrino flows crossing a unit area from inside outwards and from outside inwards are the same). With increasing radius, the inward neutrino flux, emerging from the lower-temperature layers, becomes smaller than the outward flux, originating in the high-temperature central regions. The flux from the outer regions of the Sun is obviously zero because the nuclear reactions do not occur below a threshold temperature. Therefore there must be a maximum at some intermediate value of R. This behavior can be seen in the figure on the previous slide.

The ^{8}B, ^{7}Be, ^{15}O, and ^{17}F neutrinos are produced very close to the Sun's center (the inner 10% in radius or 20% in mass) because of the strong temperature dependence of the relevant reaction rates.

The pp, pep, and hep neutrinos appear in broader regions. The ^{13}N neutrino production profile has two peaks. Why? The inner peak at $R \approx 0.047 R_\odot$ corresponds to the region in which the CN reactions operate at quasi-steady state. The outer peak ($R \approx 0.164 R_\odot$) represents the residual burning of ^{12}C by the reaction

$$^{12}\mathrm{C}\,(p,\gamma)\,^{13}\mathrm{N}\,\left(e^+\nu_e\right)\,^{13}\mathrm{C}$$
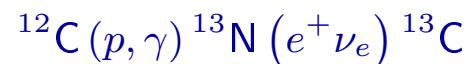
in the (comparatively) low-temperature regions, where the subsequent burning of nitrogen becomes ineffective.

Note that almost half of the solar mass is contained within a radius of $0.25 R_\odot$.
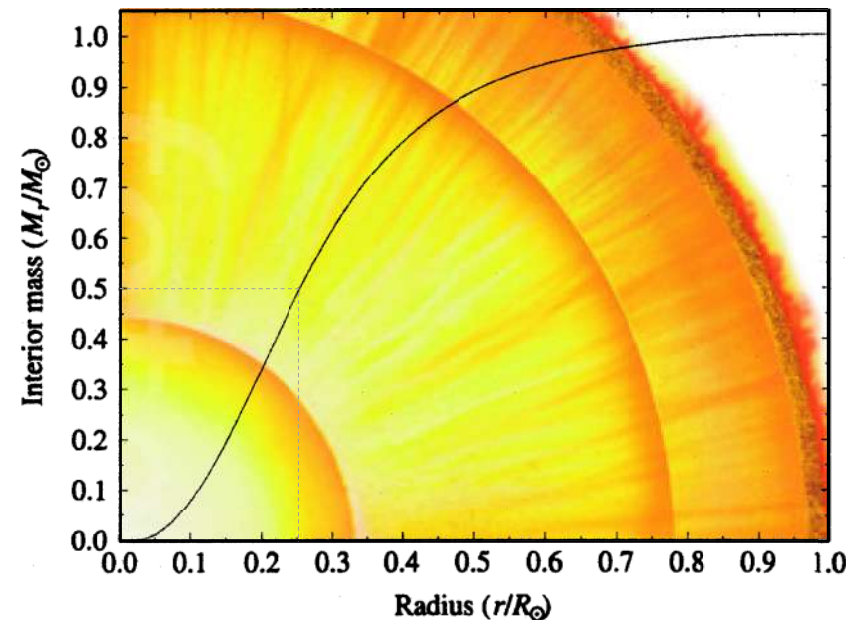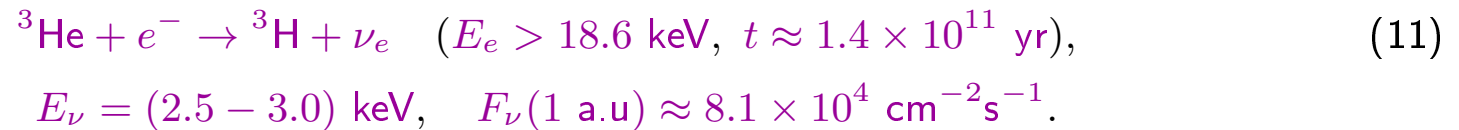
Training.

✦ Estimate the characteristic times t_{11}, t_{12}, etc. for several values of the temperature.

✦ Why $d\,\text{Flux}/d(R/R_\odot) \to 0$ at large $R/R_\odot$?

✦ Why $d\,\text{Flux}/d(R/R_\odot) \to 0$ at $R/R_\odot \to 0$?

✦ Why the fusion $^2\text{H} + {}^2\text{H} \to {}^4\text{He}$ is not effective?

✦ Offer some endothermic reaction(s) in the Sun with ν_e production.

✦ Offer some reaction(s) in the Sun with production of $\overline{\nu}_e$.

✦ Are neutrinos generated in powerful solar flares?
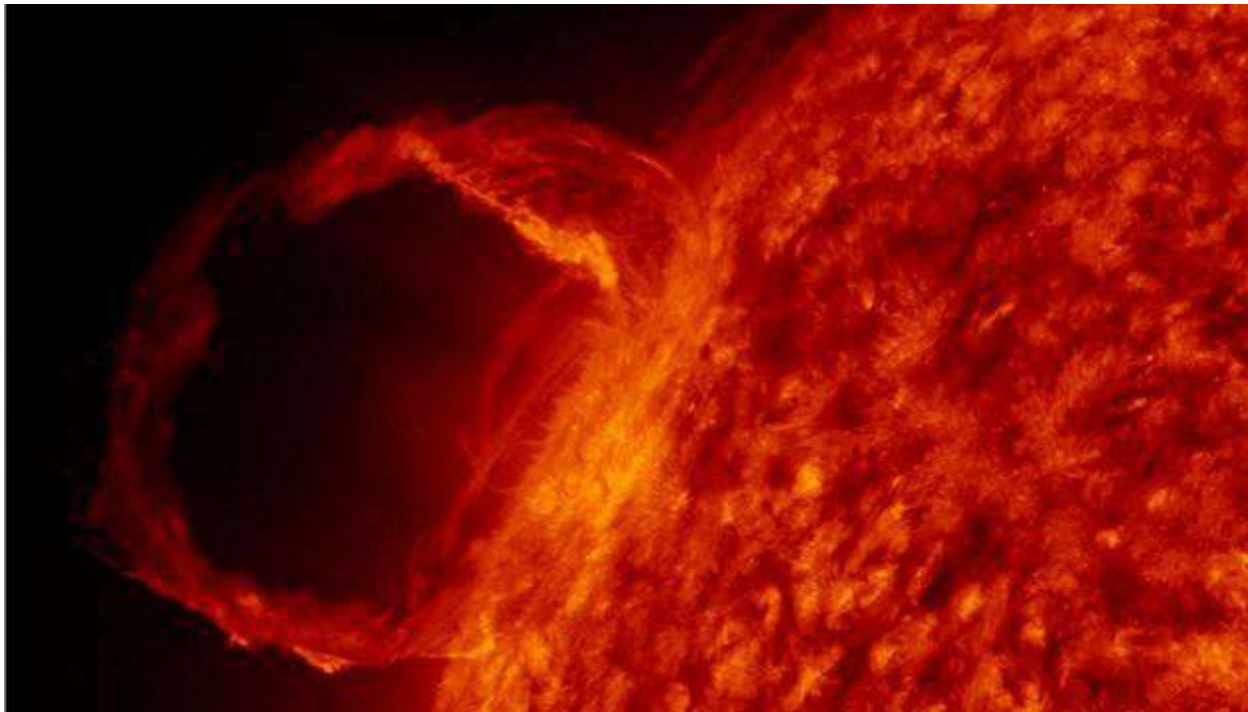
The full pp chain is not full (?)

In fact there must be a lot of other contributions into the pp chain. Let's consider some (*training*) examples.[a]

Tritium neutrinos.

$$^{3}\text{He} + e^{-} \rightarrow {}^{3}\text{H} + \nu_e \quad (E_e > 18.6 \text{ keV}, \; t \approx 1.4 \times 10^{11} \text{ yr}), \tag{11}$$

$$E_\nu = (2.5 - 3.0) \text{ keV}, \quad F_\nu(1 \text{ a.u}) \approx 8.1 \times 10^4 \text{ cm}^{-2}\text{s}^{-1}.$$

This is an example of endothermal reaction. The chain (11) is completed with the fusion reaction

$$^{3}\text{H} + p \rightarrow {}^{4}\text{He} + \gamma \quad (E_\gamma = 19.8 \text{ MeV}).$$

Tritium antineutrinos.

In principle, the capture (11) can be followed by the tritium β-decay with production of *antineutrinos*:

$$E_{\overline{\nu}} < 18.6 \text{ keV}, \quad F_{\overline{\nu}}(1 \text{ a.u.}) \approx 10^3 \text{ cm}^{-2}\text{yr}^{-1}.$$

Alas! Both the energy and flux are very small. This does not allow detecting the solar antineutrinos in the current experimental setups.

---

[a] B. I. Goryachev, "The extreme energies lines in the solar neutrino spectrum," arXiv:1005.3458 [astro-ph.SR].

The pp V branch (heep reaction).

It is believed that neutrinos with maximum energy are produced in the hep-reaction $E_\nu^{\max} \approx 18.8$ MeV. But, in fact, the most energetic solar neutrinos are produced in the reaction

$$^{3}\mathrm{He} + e^{-} + p \to {}^{4}\mathrm{He} + \nu_e \quad E_\nu = 19.8 \text{ MeV}. \tag{12}$$

Estimated flux is $F_\nu(1 \text{ a.u.}) \approx 2.5 \times 10^{-4} \text{ cm}^{-2}\text{s}^{-1}$.

K-shell electron screening.

All our estimations implicitly assume that all the nuclei in the solar core are "bare". But even a comparatively small fraction of ions in the solar plasma affects the ν flux.

Example: Screening in $^{7}\mathrm{Be} + {}^{1}\mathrm{H} \to {}^{8}\mathrm{B} + \gamma$.[a]

Figure shows the predicted enhancement factor

$$\gamma(E) = \sigma_{\mathsf{screened}}(E)/\sigma_{\mathsf{bare}}(E)$$

(vs. the center-of-mass energy) due to K-shell electron.

---

[a] V. B. Belyaev, D. E. Monakhov, D. V. Naumov, and F. M. Penkov, "Electron screening in the $^{7}\mathrm{Be} + p \to {}^{8}\mathrm{B} + \gamma$," Phys. Lett. A **247** (1998) 241–245, astro-ph/9803003.
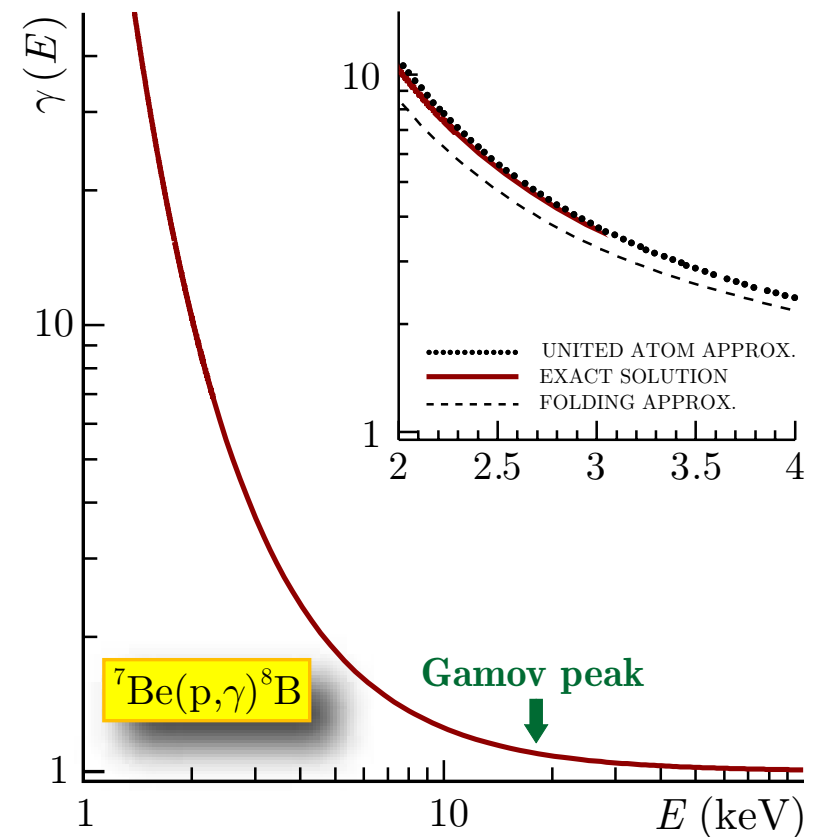
6   An excursus: chemical composition of the Sun.

The matter that formed the Sun had already been cycled through one or more generations of stars. We can see elements up to and beyond ^{56}Fe in the photosphere.
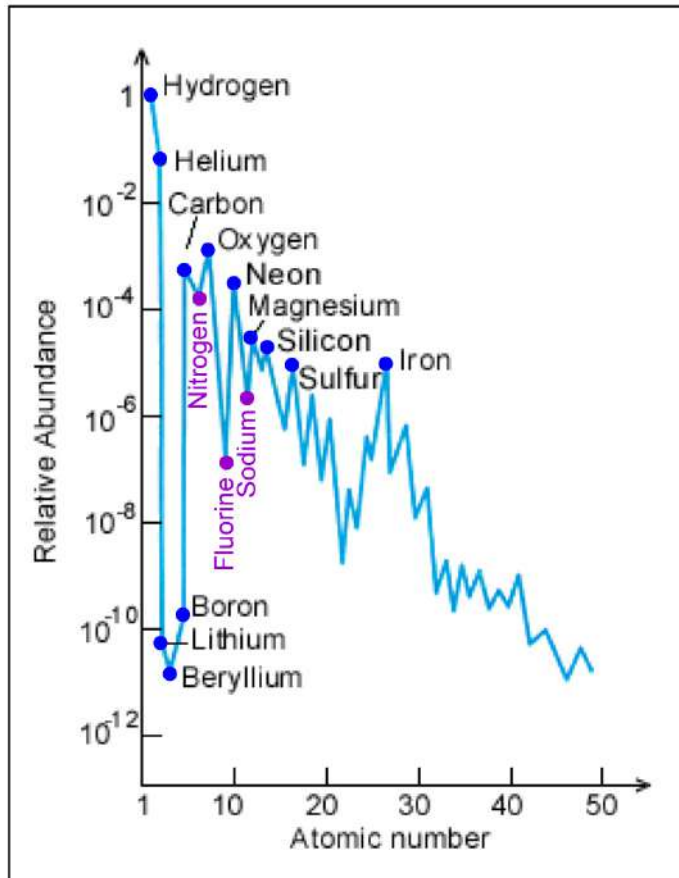
ELEMENTAL ABUNDANCE IN THE SUN

Element	% by mass	% by number
Hydrogen	73.4	92.0
Helium	25.0	7.8
Oxygen	0.80	0.06
Carbon	0.20	0.02
Neon	0.16	0.01
Iron	0.14	0.003
Nitrogen	0.09	0.008
Silicon	0.09	0.004
Magnesium	0.06	0.003
Sulfur	0.05	0.002

Present-day solar abundance curve is shown in the figure (the ordinate compares all elements to Hydrogen) and the relative abundances (by mass and by number) are shown in the table.
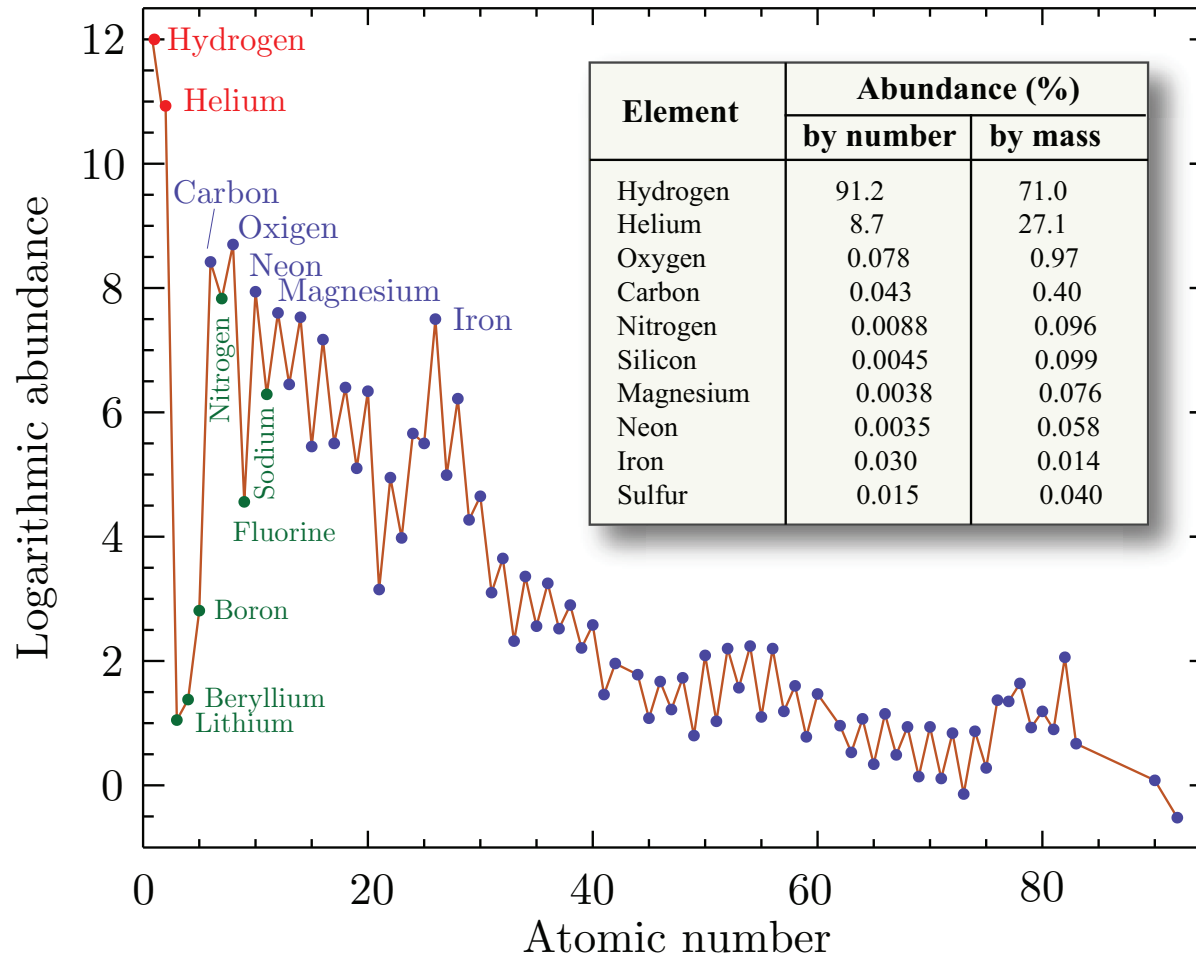
[Upadated] present-day solar photospheric elemental abundances vs. Z according to M. Asplund *et al.*, arXiv:0909.0948 [astro-ph.SR]. The logarithmic abundance ϵ_H of hydrogen is defined to be $\log \epsilon_H = 12$ that is $\log \epsilon_X = \log(n_X/n_H) + 12$, where n_X and n_H are the number densities of elements X and H, respectively. The insert shows the relative abundances of the ten most prevalent elements. Find ten differences with the previous slide.

Comments:

✦ The general trend is towards ever decreasing abundances as the atomic number increases.

✦ There is a distinct zig-zag (up-down) pattern to the whole curve. For example,
 – between Carbon and Oxygen there is a decrease (the element is Nitrogen);
 – between Neon and Magnesium the decrease element is Sodium;
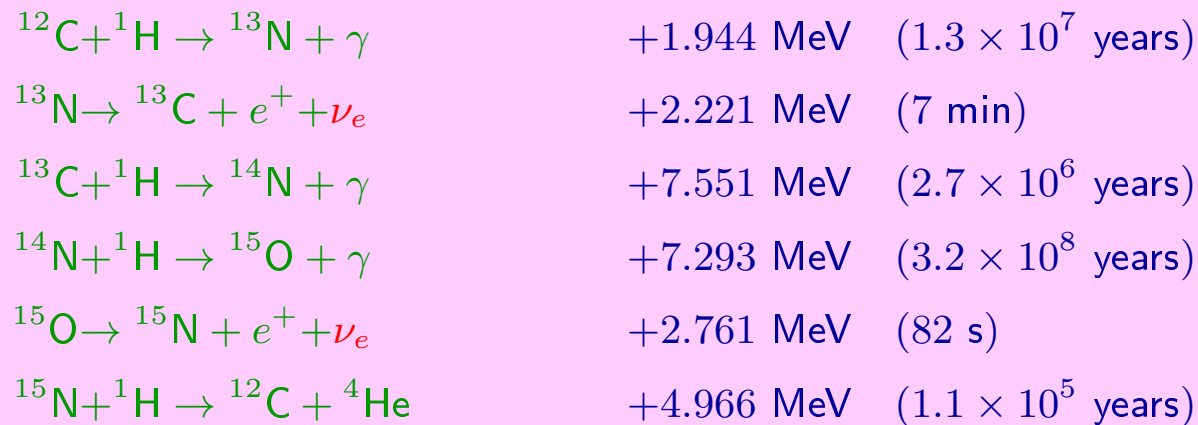 – the largest drop is between Oxygen and Neon, the element that thus decreases notably is Fluorine.
 The reason for this fluctuating pattern is just this: elements with *odd* numbers of nucleons are less stable, resulting in one unpaired (odd) proton or neutron – those that pair these particles result in offsetting spins in opposite directions that enhance stability.
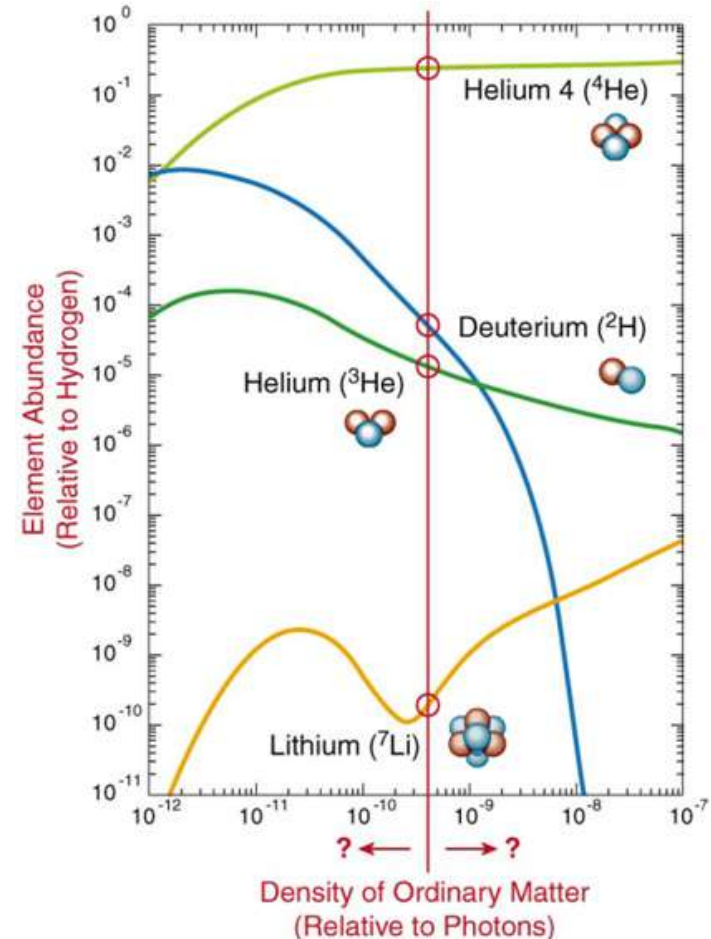
✦ There is a huge drop in abundance for the Lithium-Beryllium-Boron triplet. This results from two factors:
 – at the Big Bang, nuclear processes that could fuse the proper H or He isotopes into Li and/or the other two were statistically very rare and hence inefficient, and
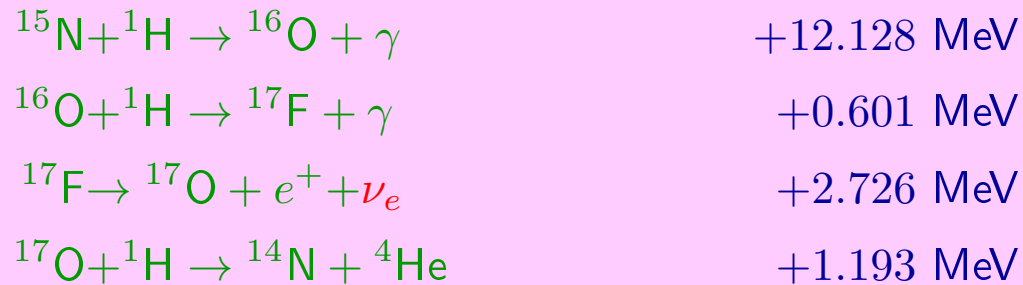 – some of the Li-Be-B that formed and survived may be destroyed in processes with stars.

7 The CNO cycle.

The presence of the "impurities" in the solar core opens the door to another fusion reaction. The most important (after the pp) is the CNO bi-cycle, which is responsible for as much as 1.6% of the Sun's total output. The main CNO reactions ("cycle I") are

$$^{12}\text{C} + {}^{1}\text{H} \rightarrow {}^{13}\text{N} + \gamma \qquad +1.944 \text{ MeV} \quad (1.3 \times 10^{7} \text{ years})$$

$$^{13}\text{N} \rightarrow {}^{13}\text{C} + e^{+} + \nu_{e} \qquad +2.221 \text{ MeV} \quad (7 \text{ min})$$

$$^{13}\text{C} + {}^{1}\text{H} \rightarrow {}^{14}\text{N} + \gamma \qquad +7.551 \text{ MeV} \quad (2.7 \times 10^{6} \text{ years})$$

$$^{14}\text{N} + {}^{1}\text{H} \rightarrow {}^{15}\text{O} + \gamma \qquad +7.293 \text{ MeV} \quad (3.2 \times 10^{8} \text{ years})$$

$$^{15}\text{O} \rightarrow {}^{15}\text{N} + e^{+} + \nu_{e} \qquad +2.761 \text{ MeV} \quad (82 \text{ s})$$

$$^{15}\text{N} + {}^{1}\text{H} \rightarrow {}^{12}\text{C} + {}^{4}\text{He} \qquad +4.966 \text{ MeV} \quad (1.1 \times 10^{5} \text{ years})$$

- The cycle uses carbon, nitrogen, and oxygen as catalysts to suck up four protons and build a ^{4}He nucleus out of them. The relative abundances of C, N, and O do not change.

- The cycle does not start until the pp fusion has begun, and provides the energy necessary to allow a low level of proton fusions onto the heavier nuclei.

- The cycle timescale is determined by the slowest reaction ($^{14}\text{N} + {}^{1}\text{H}$) while the approach to equilibrium is determined by the second slowest reaction ($^{12}\text{C} + {}^{1}\text{H}$).

The second minor branch ("cycle II") is a similar type of cycle, and it joins onto the first. Starting with ^{14}N, the process steps through two of the last-three reactions given above until ^{15}N is produced. It then proceeds as follows to convert ^{15}N back into ^{14}N, with the production of ^{17}F (fluorine-17) occurring in one of the steps:

$$^{15}\text{N}+^{1}\text{H} \rightarrow\ ^{16}\text{O} + \gamma \qquad\qquad +12.128 \text{ MeV}$$

$$^{16}\text{O}+^{1}\text{H} \rightarrow\ ^{17}\text{F} + \gamma \qquad\qquad +0.601 \text{ MeV}$$

$$^{17}\text{F} \rightarrow\ ^{17}\text{O} + e^{+} + \nu_e \qquad\qquad +2.726 \text{ MeV}$$

$$^{17}\text{O}+^{1}\text{H} \rightarrow\ ^{14}\text{N} + ^{4}\text{He} \qquad\qquad +1.193 \text{ MeV}$$

The latter cycle is much less frequent, with the first reaction having a probability of about 4×10^{-4} relative to the last reaction of the cycle I.

The fractions of the nuclear energy loss from the core through neutrino emission in the first and second branches of the CNO process are 6% and 4%, respectively.

Note: The CNO cycle lacks significance at the low temperatures in the Sun. For abundances characteristic of the Sun, the CNO process becomes important for core temperatures of roughly 1.5×10^7 K (1.3 keV), and it provides virtually all of the conversion of hydrogen into helium in the later stages of the solar lifetime when the temperature exceed 2.5×10^7 K (2.2 keV).

CNO neutrinos are finally discovered by Borexino!
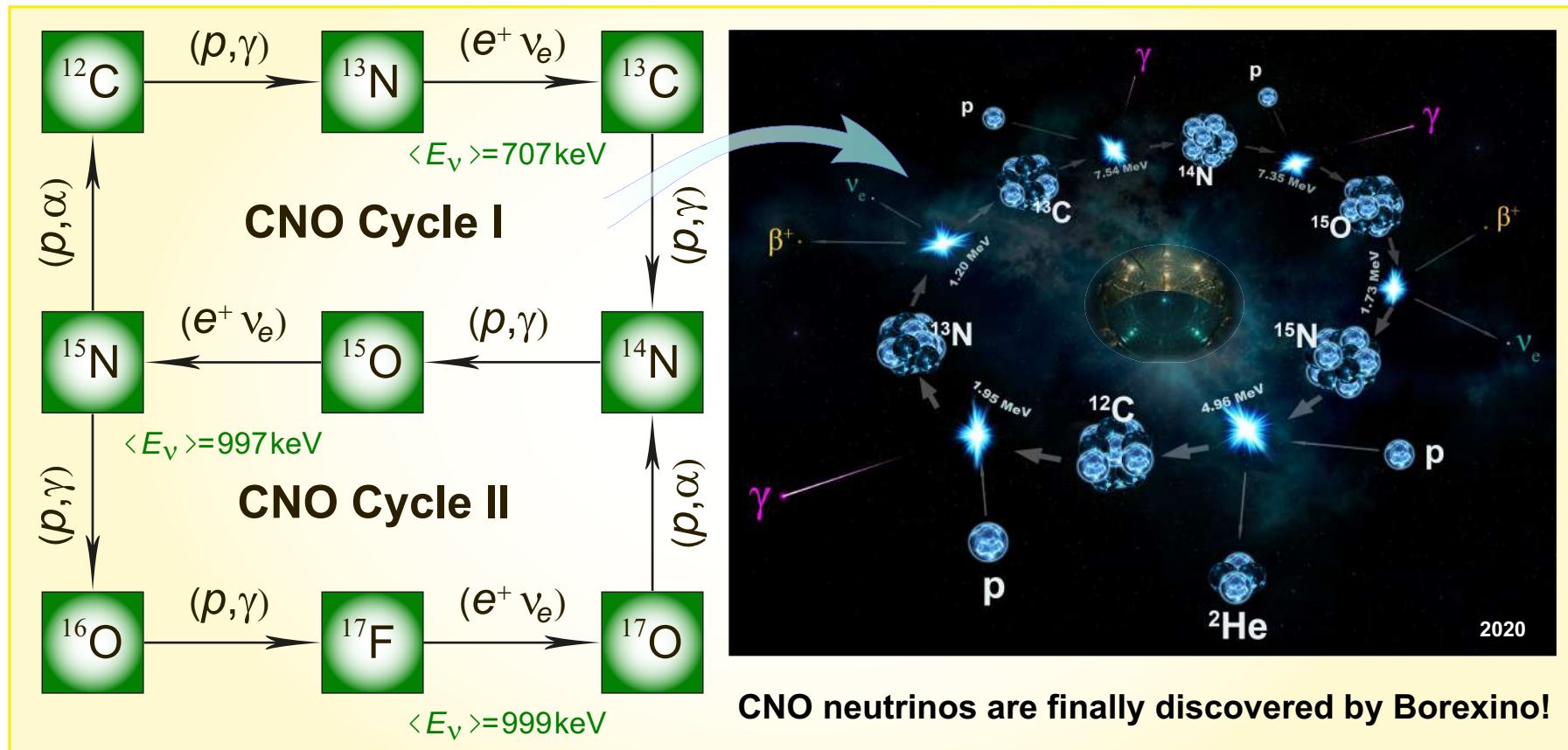
The full CNO bi-cycle (Carl von Weizsacker, Hans Bethe) responsible for production of about 1.5–1.6% of the solar energy. The cycle I fully dominates (cycle II occurs 0.04% of the time).

- The CNO cycles III and IV are only essential for the hydrogen burning in massive stars. The full net includes ^{18}F, ^{18}O, and ^{19}F (see next slide).
- Recently, there has been strong experimental evidence for the presence of the CNO neutrinos.[a]

[a] N. Agostini *et al.* (The Borexino Collaboration) "Experimental evidence of neutrinos produced in the CNO fusion cycle in the Sun," Nature **587** (2020) 577–582, arXiv:2006.15115 [hep-ex].

The full CNO poly-cycle.
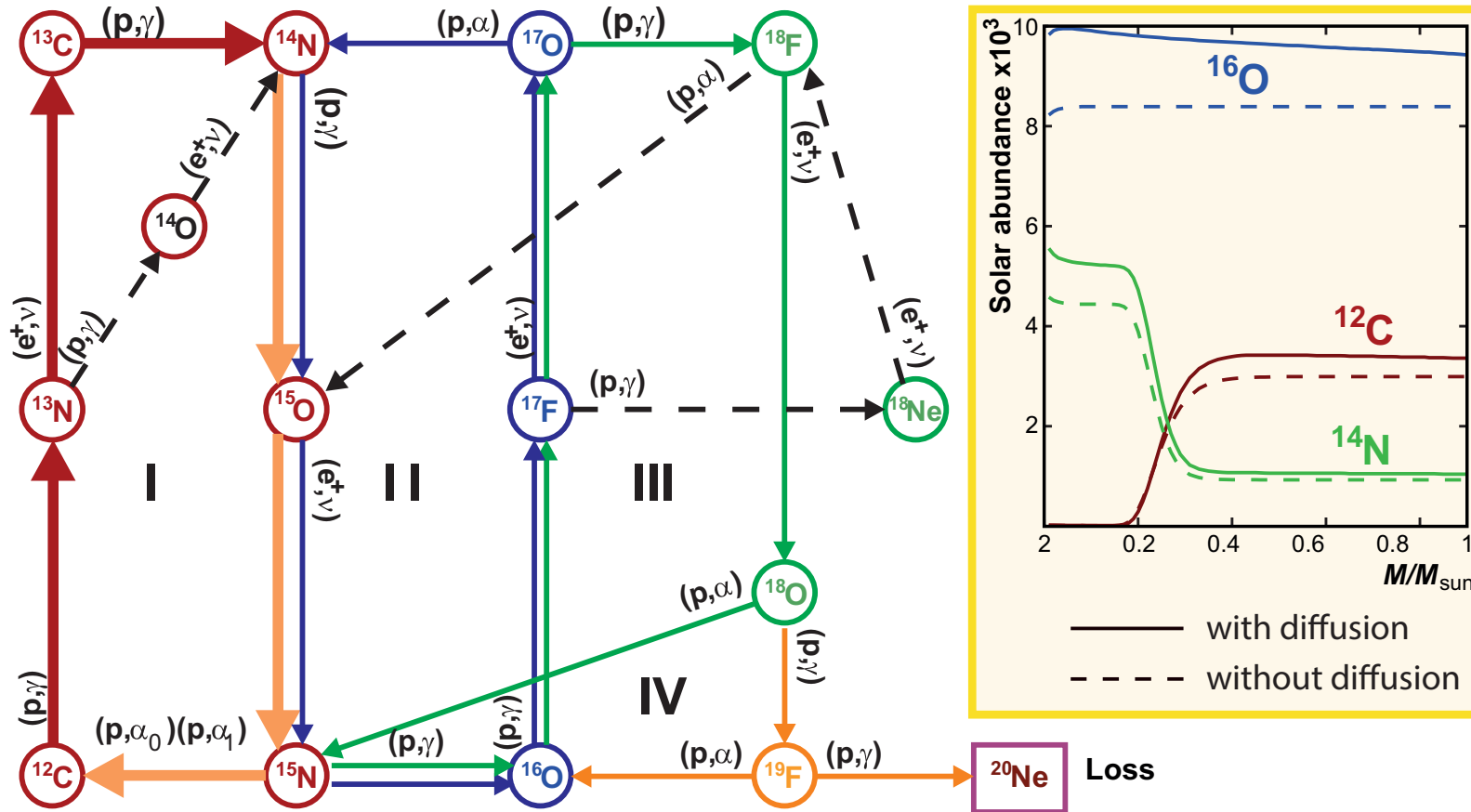
The full CNO poly-cycle. The widths of the arrows illustrate the significance of the reactions in determining the nuclear fusion rates in the poly-cycle. Certain "Hot CNO" processes are indicated by dashed lines. The insert shows the abundances of ^{12}C, ^{14}N, and ^{16}O, in the interior of the sun.

CNO electron capture.

An additional (minor) contribution to the CNO neutrino flux usually not included into the solar models is electron capture (EC) on those isotopes.[a] The relevant reactions are

$$^{13}\text{N} + e^- \to {}^{13}\text{C} + \nu_e, \quad {}^{15}\text{O} + e^- \to {}^{15}\text{N} + \nu_e, \quad {}^{17}\text{F} + e^- \to {}^{17}\text{O} + \nu_e.$$

At solar temperatures and densities one must take into account the contribution from both bound (mainly K-shell) and continuum electrons.

Таблица 1: Neutrino fluxes and energies from the CNO β^+ decays and electron capture.

	Mean β^+ decay flux $(\text{cm}^{-2}\text{s}^{-1})$	$\langle E_\nu \rangle$ (MeV)	EC flux $(\text{cm}^{-2}\text{s}^{-1})$	E_ν (MeV)	$(\text{EC}/\beta^+ \text{ decay})_{\text{lab}}$
^{13}N	5.48×10^8 $(^{+0.21\%}_{-0.17\%})$	0.707	4.33×10^5	2.220	1.96×10^{-3}
^{15}O	4.80×10^8 $(^{+0.25\%}_{-0.19\%})$	0.997	1.90×10^5	2.754	9.94×10^{-4}
^{17}F	5.63×10^6 $(^{+0.25\%}_{-0.25\%})$	0.999	3.32×10^5	2.761	1.45×10^{-3}

The flux of the CNO EC neutrinos is of the same order as the boron neutrino flux, though at lower energies. So the rate of these neutrinos on current detectors is small but not fully negligible.

---

[a] J. N. Bahcall, "Line versus continuum solar neutrinos," Phys. Rev. D **41** (1990) 2964–2966; L. C. Stonehill, J. A. Formaggio, & R. G. H. Robertson, "Solar neutrinos from CNO electron capture," Phys. Rev. C **69** (2004) 015801, hep-ph/0309266.

8 Solar neutrino spectrum.
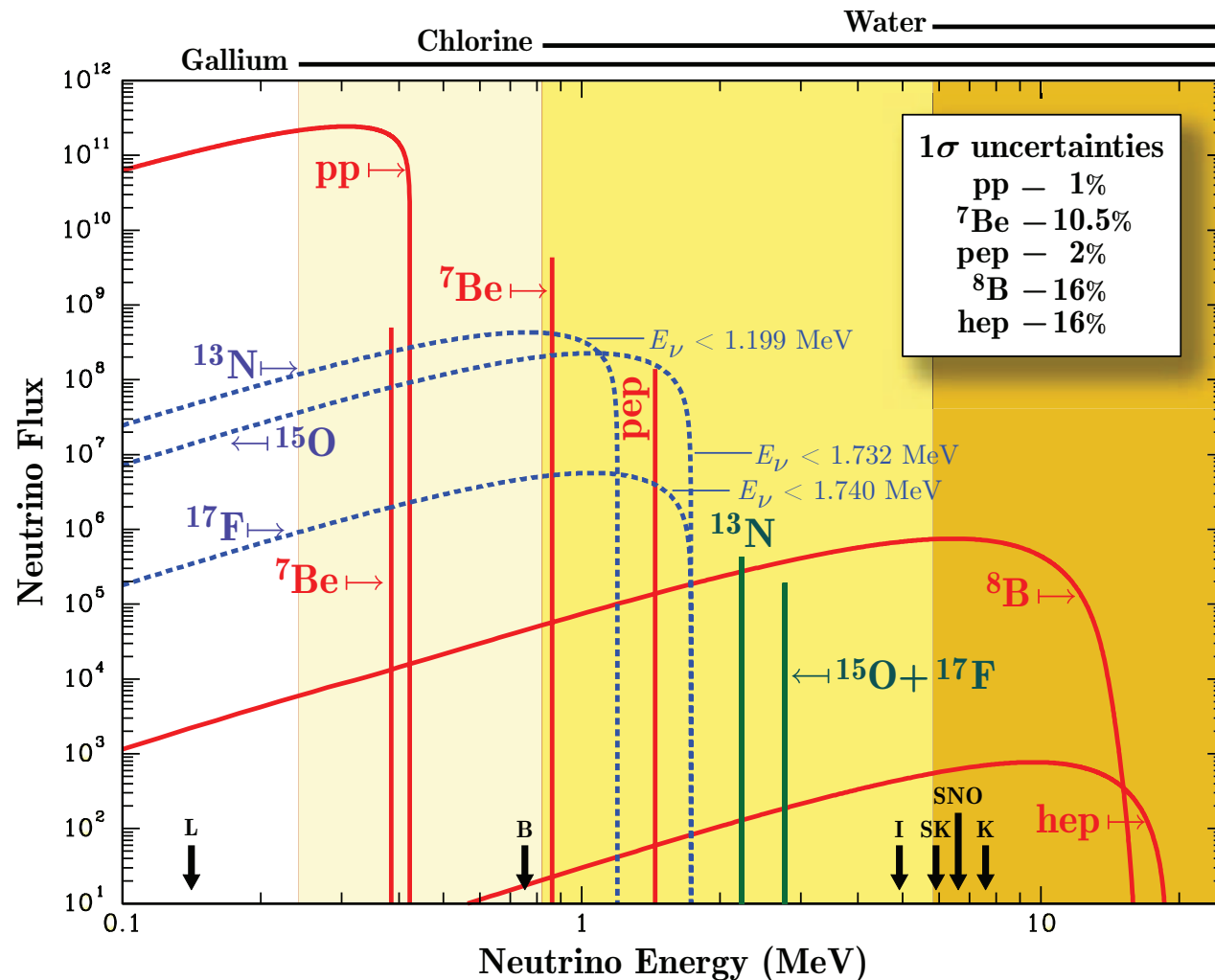
The predicted electron neutrino energy spectrum at 1 a.u. from the pp chain and CNO bi-cycle reactions. Line fluxes are in $cm^{-2}s^{-1}MeV^{-1}$ and spectral fluxes are in $cm^{-2}s^{-1}$. Also shown the uncertainties of the pp cycle neutrino flux calculation (on 1σ level) and the threshold neutrino energies for several detectors.

[The combined data are from J. N. Bahcall, A. M. Serenelli, and S. Basu, "New solar opacities, abundances, helioseismology, and neutrino fluxes," ApJ **621** (2005) L85–L88 and L. C. Stonehill, J. A. Formaggio, and R. G. H. Robertson, "Solar neutrinos from CNO electron capture," Phys. Rev. C **69** (2004) 015801.]

Comparison between the "Standard Solar Models" of Bahcall & Pinsonneault (1995) [BP95] and of Dar & Shaviv (1996) [DS96].[a]

Parameter/Effect	BSP98	DS96
$M_\odot$	1.9899×10^{33} g	1.9899×10^{33} g
$L_\odot$	3.844×10^{33} erg s^{-1}	3.844×10^{33} erg s^{-1}
$R_\odot$	6.9599×10^{10} cm	6.9599×10^{10} cm
$t_\odot$	4.566×10^{9} y	4.57×10^{9} y
Rotation	Not Included	Not Included
Magnetic Field	Not Included	Not Included
Mass Loss	Not Included	Not Included
Angular Momentum Loss	Not Included	Not Included
Premain Sequence Evolution	Not Included	Included
Initial Abundances :		
^{4}He	Adjusted	Adjusted
C, N, O, Ne	Adjusted	Adjusted
All Other Elements	Adjusted	Meteoritic

---

[a] From A. Dar and G. Shaviv, "The solar neutrino problem: An update," Phys. Rept. **311** (1999) 115–141, astro-ph/9808098.

Continued

Parameter/Effect	BSP98	DS96
Photospheric Abundances :		
^{4}He	Predicted	Predicted
C, N, O, Ne	Photospheric	Photospheric
All Other Elements	Meteoritic	Predicted
Radiative Opacities	OPAL 1996	OPAL 1996
Equation of State	Straniero 1996?	Dar − Shaviv 1996
Partial Ionization Effects	Not Included	Included
Diffusion of Elements :		
H, ^{4}He	Included	Included
Heavier Elements	Approximated by Fe	All Included
Partial Ionization Effects	Not Included	Included
Nuclear Reaction Rates :		
$S_{11}(0)$ eV $\cdot$ b	4.00×10^{-19}	4.07×10^{-19}
$S_{33}(0)$ MeV $\cdot$ b	5.3	5.6
$S_{34}(0)$ keV $\cdot$ b	0.53	0.45
$S_{17}(0)$ eV $\cdot$ b	19	17
Screening Effects	Included	Included
Nuclear Equilibrium	Imposed	Not Assumed

The table in next slide summarizes the predicted capture rates for the chlorine and gallium detectors published during 20 years (till 2010).[a] The list is certainly incomplete, but rather representative. The quoted errors are combinations of (usually 3σ) uncertainties from all known sources added quadratically. he recent SSM calculations by Bahcall *et al.* (2006) and Peña-Garay & Serenelli (2008) use the two solar abundances determinations with high and low metallicity, labelled as CS98 and AGS05, respectively. The SSM and seismic model (SeSM) by Turck-Chièze & Couvidat (2010) use the most recent AGSS09 abundances model.

It is seen that the predictions of different models for the gallium target are more robust than those for the chlorine one: the former vary from model to model within 22% (9% for the most recent models that is within the quoted model uncertainties), while the disagreement between the chlorine predictions is as large as 78% (29% for the recent models). Essentially all these models are based on the same physical principles and the disagreement between the output values is mainly due to the input nuclear-physics and astrophysical parameters. The most non-traditional approach has been adopted by Dar and Shaviv (1994, 1996) whose model predicted the lowest solar neutrino flux. The authors have demonstrated that it is possible to "tweak" the standard solar model enough to significantly reduce the high-energy neutrino flux without any major disruption of our understanding of how the Sun shines and how neutrinos behave. However the model of Dar and Shaviv was met with a hostile reception from the solar neutrino community (headed by Bahcall). The main source of uncertainties in the modern solar models is the choice of the input chemical composition of the Sun. The consistency between the different chlorine predictions is much less satisfactory. The "terms-of-trade" between the low (AGS05), high (GS98), or medium (AGSS09, L10) metallicities (LZ, HZ, MZ) is not a matter of majority vote and in any case, today, there is no generally accepted criterion of the optimal model choice.

---

[a] V. A. Naumov, "Solar neutrinos. Astrophysical aspects." Phys. Part. Nucl. Lett. **8** (2011) 683–703.

Predicted capture rates for chlorine and gallium targets.

Year	Authors	^{37}Cl (SNU)	^{71}Ga (SNU)	
1990	Sackmann et al.	7.68	125.0	
1992	Bahcall & Pinsonneault	8.0 ± 3.0	131.5^{+21}_{-17}	
1993	Turck-Chièze & Lopes	6.4 ± 1.4	122.5 ± 7	
1993	Schramm & Shi	4.7	117	a
1994	Shi et al.	7.3	129	
1994	Castellani et al.	7.8	130	
1994	Dar & Shaviv	4.2 ± 1.2	116 ± 6	
1995	Bahcall & Pinsonneault	$9.3^{+1.2}_{-1.4}$	137^{+7}_{-8}	
1996	Dar & Shaviv	4.1 ± 1.2	115 ± 6	
1996	Christensen-Dalsgaard et al.	8.2	132	
1997	Morel et al.	8.93	144	b
1998	Bahcall et al.	$7.7^{+1.2}_{-1.0}$	129^{+8}_{-6}	
1998	Brun et al.	7.18	127.2	
1999	Brunet et al.	7.25 ± 0.94	127.1 ± 8.9	c
2001	Bahcall et al.	$8.0^{+1.4}_{-1.1}$	128^{+9}_{-7}	
2001	Turck-Chièze et al.	7.44 ± 0.96	127.8 ± 8.6	
2003	Couvidat et al.	6.90 ± 0.90	126.8 ± 8.9	d
2004	Bahcall & Peña-Garay	8.5 ± 1.8	131^{+12}_{-10}	e
2004	Turck-Chièze et al.	7.60 ± 1.10	123.4 ± 8.2	
2006	Bahcall et al. (GS98)	8.12	126.08	
2006	Bahcall et al. (AGS05)	6.58	118.88	
2008	Peña-Garay & Serenelli (GS98)	$8.46^{+0.87}_{-0.88}$	$127.9^{+8.1}_{-8.2}$	
2008	Peña-Garay & Serenelli (AGS05)	$6.86^{+0.69}_{-0.70}$	$120.5^{+6.9}_{-7.1}$	
2010	Turck-Chièze & Couvidat (SSM)	6.315	120.9	
2010	Turck-Chièze & Couvidat (SeSM)	7.67 ± 1.1	123.4 ± 8.2	

Footnotes to Table in p. 153:

  [a] The quoted numbers are corrected according to Shi *et al.* (1994).
  [b] Several models; the quoted numbers are for the model "D11" preferred by the authors.
  [c] Several models; the quoted numbers are for the reference model "BTZ" as cited by Couvidat *et al.* (2003).
  [d] Several models; the quoted numbers are for the model "Seismic$_2$" provided minimal predicted rate.
  [e] Several models; the quoted numbers are for the model "BP04" preferred by the authors.

SSM neutrino fluxes from the GS98-SFII (HZ) and AGSS09-SFII (MZ) SSMs, with associated uncertainties (averaging over asymmetric uncertainties).[a] The solar values come from a luminosity constrained analysis of the Borexino data (before 2012). [See p. 204 for the newer Borexino results.]

Reaction	E_ν^{max} (MeV)	GS98-SFII	AGSS09-SFII	Solar	Units
$p + p \rightarrow {}^2\mathrm{H} + e^+ + \nu$	0.42	$5.98(1 \pm 0.006)$	$6.03(1 \pm 0.006)$	$6.05(1^{+0.003}_{-0.011})$	$10^{10}/\mathrm{cm}^2\mathrm{s}$
$p + e^- + p \rightarrow {}^2\mathrm{H} + \nu$	1.44	$1.44(1 \pm 0.012)$	$1.47(1 \pm 0.012)$	$1.46(1^{+0.010}_{-0.014})$	$10^8/\mathrm{cm}^2\mathrm{s}$
${}^7\mathrm{Be} + e^- \rightarrow {}^7\mathrm{Li} + \nu$	0.86 (90%)/0.38 (10%)	$5.00(1 \pm 0.07)$	$4.56(1 \pm 0.07)$	$4.82(1^{+0.05}_{-0.04})$	$10^9/\mathrm{cm}^2\mathrm{s}$
${}^8\mathrm{B} \rightarrow {}^8\mathrm{Be} + e^+ + \nu$	~ 15	$5.58(1 \pm 0.14)$	$4.59(1 \pm 0.14)$	$5.00(1 \pm 0.03)$	$10^6/\mathrm{cm}^2\mathrm{s}$
${}^3\mathrm{He} + p \rightarrow {}^4\mathrm{He} + e^+ + \nu$	18.77	$8.04(1 \pm 0.30)$	$8.31(1 \pm 0.30)$	—	$10^3/\mathrm{cm}^2\mathrm{s}$
${}^{13}\mathrm{N} \rightarrow {}^{13}\mathrm{C} + e^+ + \nu$	1.20	$2.96(1 \pm 0.14)$	$2.17(1 \pm 0.14)$	≤ 6.7	$10^8/\mathrm{cm}^2\mathrm{s}$
${}^{15}\mathrm{O} \rightarrow {}^{15}\mathrm{N} + e^+ + \nu$	1.73	$2.23(1 \pm 0.15)$	$1.56(1 \pm 0.15)$	≤ 3.2	$10^8/\mathrm{cm}^2\mathrm{s}$
${}^{17}\mathrm{F} \rightarrow {}^{17}\mathrm{0} + e^+ + \nu$	1.74	$5.52(1 \pm 0.17)$	$3.40(1 \pm 0.16)$	≤ 59.0	$10^6/\mathrm{cm}^2\mathrm{s}$
χ^2/P^{agr}		3.5/90%	3.4/90%		

  [a] W. C. Haxton, R. G. Hamish Robertson, and A. M. Serenelli, "Solar Neutrinos: Status and Prospects," Ann. Rev. Astron. Astrophys. **51** (2013) 21–61, arXiv:1208.5723 [astro-ph.SR].

Appendix:
Solar neutrino experiments

9 Current (2018) status of the solar neutrino problem.

< http://theor.jinr.ru/~neutrino15/talks/Smirnov.pdf >
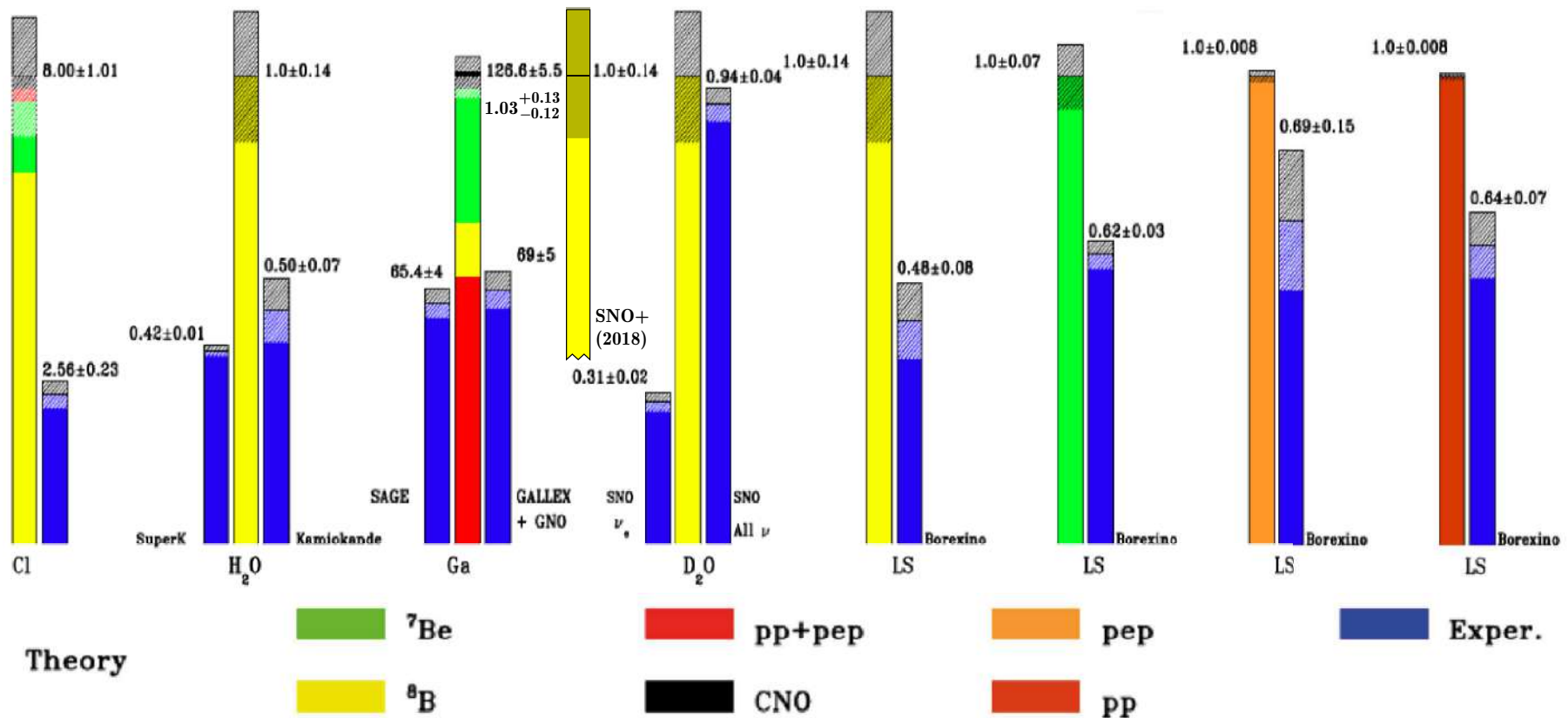
[From O. Smirnov, "Solar- and geo-neutrinos," lecture on the VIth International Pontecorvo Neutrino Physics School, August 27 – September 4, 2015, Horný Smokovec. The SNO+ data are from M. Anderson *et al.* (SNO+ Collaboration), "Measurement of the ^{8}B solar neutrino flux in SNO+ with very low backgrounds," arXiv:1812.03355 [hep-ex].]

Main news come from SNO (Sect. 14, p. 197) and Borexino (Sect. 15, p. 200). Some progress in theory is mostly due to the refinement of the input data.

Experiment	Measured flux (SNU / 10^{10} count/m^{2}s)	Ratio experiment/theory	Threshold energy	Years of running
Homestake	$2.56 \pm 0.16 \pm 0.16$	$0.33 \pm 0.03 \pm 0.05$	814 keV	1970-1995
Kamiokande	$2.80 \pm 0.19 \pm 0.33$	$0.54 \pm 0.08^{+0.10}_{-0.07}$	7.5 MeV	1986-1995
SAGE	$75 \pm 7 \pm 3$	$0.58 \pm 0.06 \pm 0.03$	233 keV	1990-2006
GALLEX	$78 \pm 6 \pm 5$	$0.60 \pm 0.06 \pm 0.04$	233 keV	1991-1996
Super-K	$2.35 \pm 0.02 \pm 0.08$	$0.465 \pm 0.005^{+0.016}_{-0.015}$	5.5 (6.5) MeV	from 1996
GNO	$66 \pm 10 \pm 3$	$0.51 \pm 0.08 \pm 0.03$	233 keV	from 1998
SNO (CC)	$1.68 \pm 0.06^{+0.08}_{-0.09}$		1.44 MeV	
SNO (ES)	$2.35 \pm 0.22 \pm 0.15$		6.75 MeV	from 1999
SNO (NC)	$4.94 \pm 0.21^{+0.38}_{-0.34}$		2.22 MeV	
SNO+ (ES)	$2.53^{+0.31}_{-0.28}{}^{+0.13}_{-0.10}$		6 MeV	69.2kt-days exp.

○ The values are given in SNU (defined as 10^{-36} capture per second per target atom) for the radiochemical experiments and in units of 10^{10} counts/m^{2}s for the water-Cherenkov experiments.

○ The first and errors for the relative values correspond to experimental and theoretical errors, respectively, with the statistical and systematic errors added quadratically. The models by Bahcall and Pinsonneault BP98 and BP00 were used in the calculations.

[The data (partially obsolete!) are borrowed from the *Ultimate Neutrino Page* maintained by Juha Peltoniemi and Juho Sarkamo, of Oulu University, URL: ⟨http://cupp.oulu.fi/neutrino/⟩ (last modified 10.4.2005) and from eprint arXiv:1812.03355 (cited in p. 156). For the most recent data see arXiv:1812.03355 [hep-ex] and references therein.]

10 Cl-Ar experiment at Homestake.

<http://www.bnl.gov/bnlweb/raydavis/research.htm>
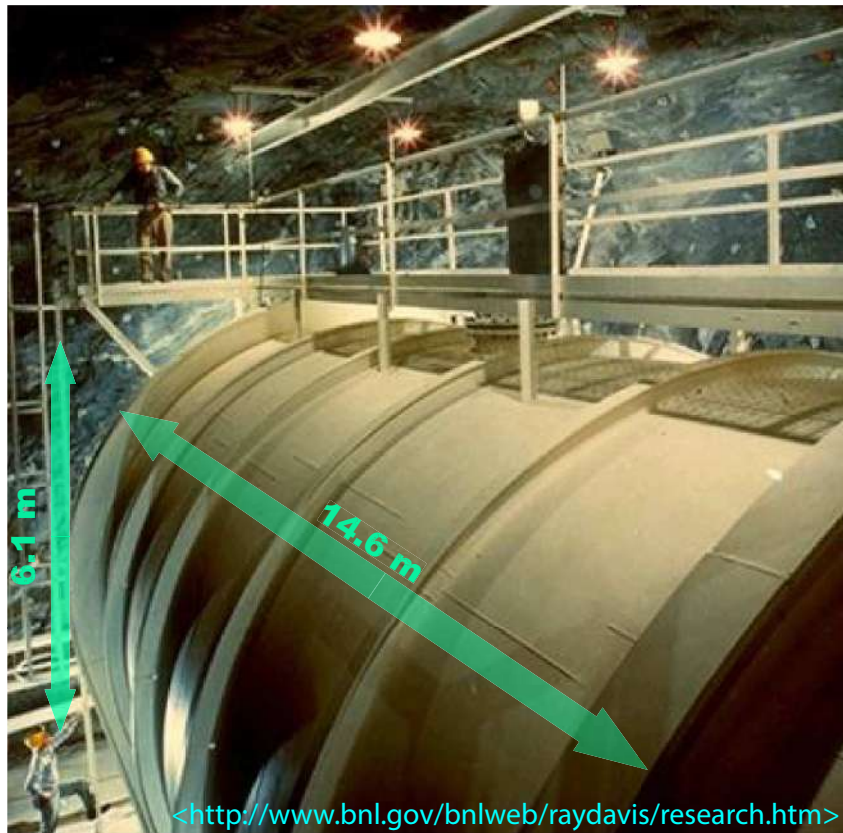
The Homestake Neutrino Trap is a tank 20 feet (6.1 m) in diameter and 48 feet (14.6 m) long filled with 100,000 gallons (378,520 liters) of a common cleaning fluid, tetrachloroethylene (C_2Cl_4). On the average each molecule of C_2Cl_4 contains one atom of the desired isotope, $^{37}_{17}Cl$. The other three chlorine atoms $^{35}_{17}Cl$ contain two less neutrons.

When a neutrino of the right energy reacts with an atom of $^{37}_{17}Cl$, it produces an atom of $^{37}_{18}Ar$ and an electron (B. Pontecorvo, 1946, L.V. Alvarez, 1949):

$$\nu_e + {}^{37}_{17}Cl \rightarrow {}^{37}_{18}Ar + e^- \quad (E_\nu^{th} \approx 814 \text{ keV}).$$
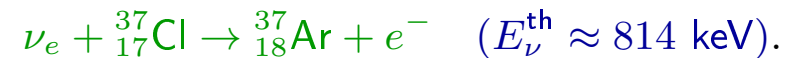
Then the radioactive argon decays back to chlorine:

$$e^- + {}^{37}_{18}Ar \rightarrow {}^{37}_{17}Cl + \nu_e + \gamma \quad (T_{1/2} \approx 35 \text{ days}).$$

The idea is to tell that the reaction happened by seeing the positron. The argon-37 is allowed to build up for several months, then is removed by purging the tank with helium gas. The argon is adsorbed in a cold trap and assayed for radioactivity.

The chlorine-argon experiment has been run by Raymond Davis, Jr., Kenneth C. Hoffman and Don S. Harmer of Brookhaven National Laboratory. The detector is located nearly a mile underground, in a rock cavity at the 4,850 foot level (1.48 km) below the surface in the Homestake Gold Mine in the town of Lead, South Dakota.

Suggested in 1964 by John Bahcall and Raymond Davis, the experiment was begun on 1967 and continued to measure the solar neutrino flux until the late 1990s, when the Homestake Mine ceased operating.

The first results of the experiment showed that the Sun's output of neutrinos from the isotope boron-8 was less than expected.
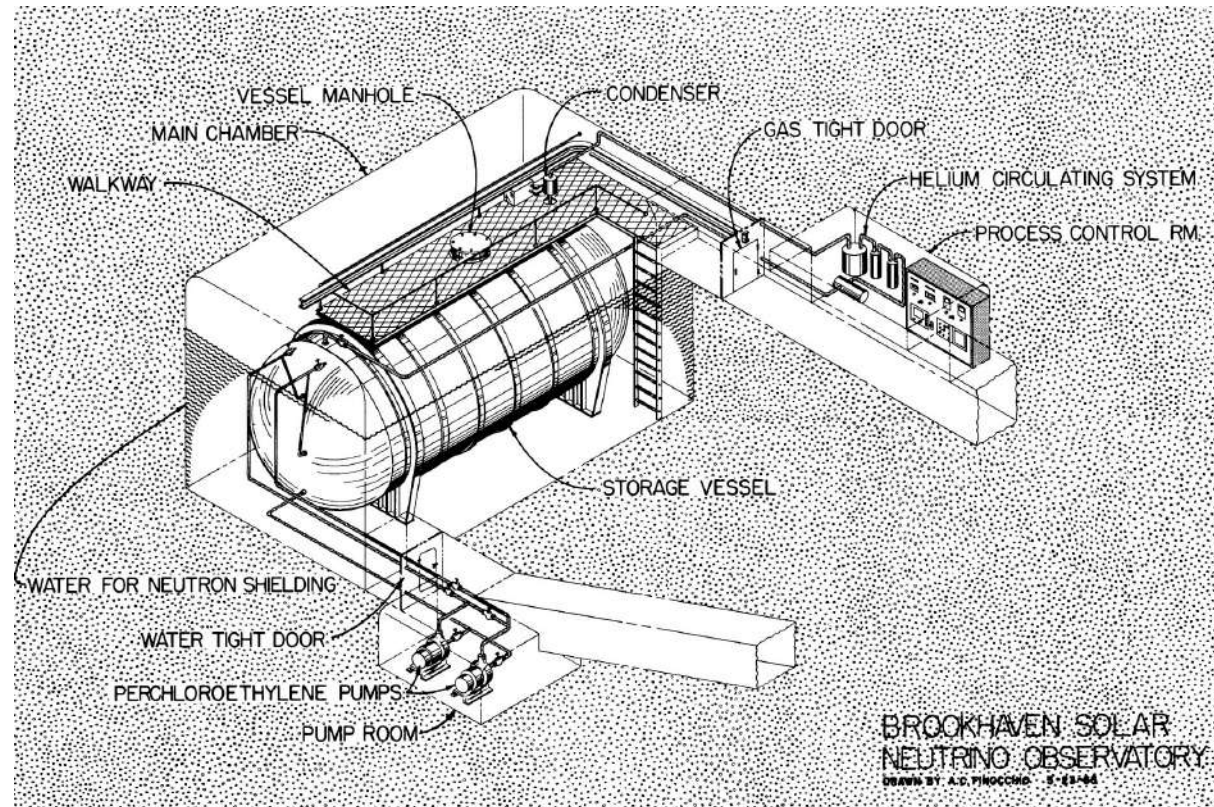
[From J. N. Bahcall, "Neutrinos from the Sun," Sci. Am. **221** (1969) 28–37.]

Figure on the right shows the argon extraction system which is deep underground next to the 100,000-gallon neutrino trap. Helium is circulated through the tank to sweep up any atoms of ^{37}Ar that have been formed from ^{37}Cl.

The efficiency of the extraction is determined by previously inserting in the tank a small amount of ^{36}Ar, a rare, nonradioactive isotope of argon. The helium and argon pass through the apparatus at left, where the argon condenses in a charcoal trap cooled by liquid nitrogen.
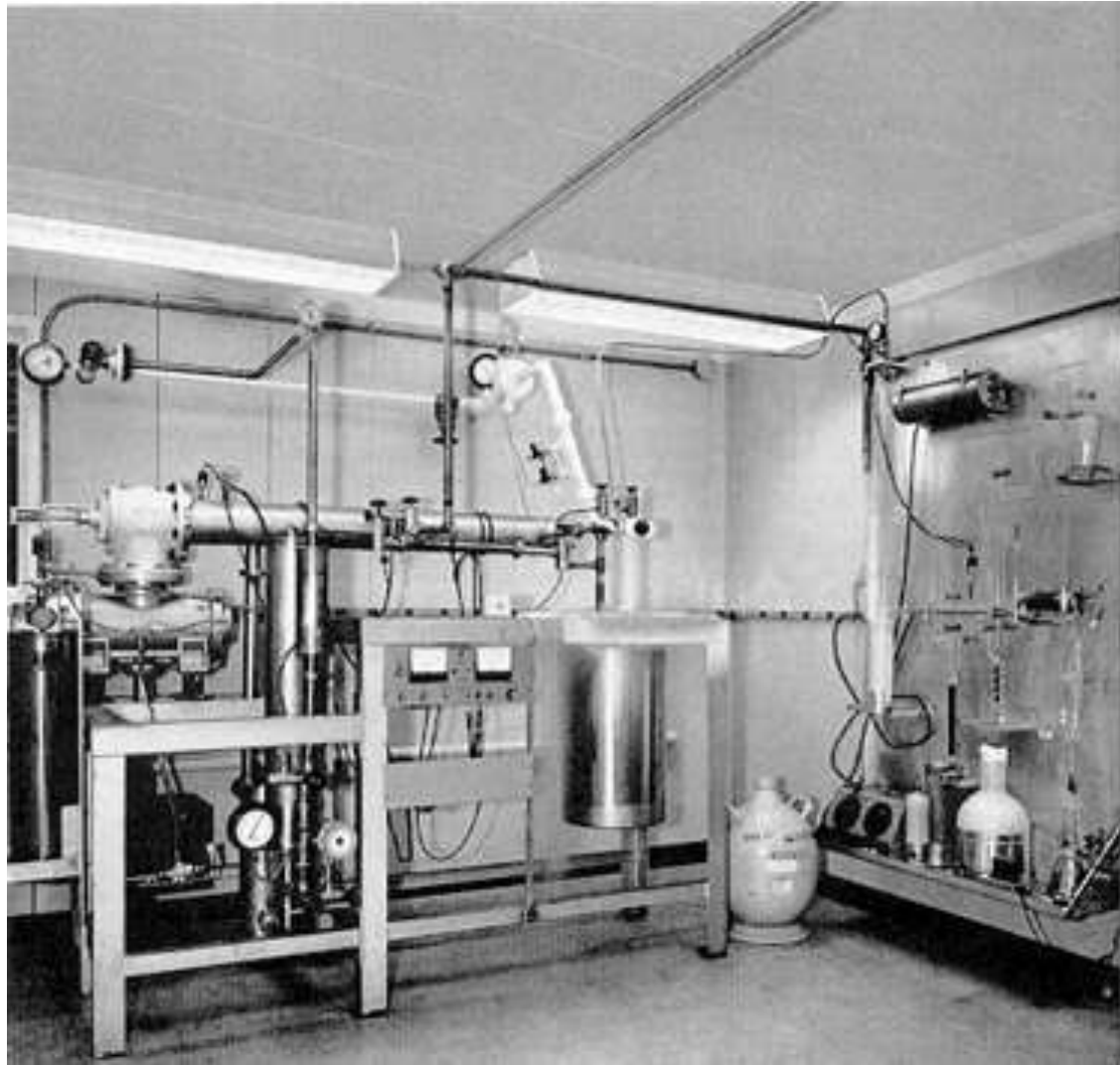
This argon fraction is purified in the apparatus at the right. The purified sample is then shipped to Brookhaven, where the content of ^{37}Ar is determined in shielded counters.

[From J. N. Bahcall, "Neutrinos from the Sun," Sci. Am. **221** (1969) 28–37.]

Deep-mine location shields the solar-neutrino detector from the intense flux of cosmic-ray (atmospheric) muons. Being very penetrating, the muons can knock protons out of atomic nuclei well below the earth's surface.

If a muon-induced proton entered the neutrino detector, it could mimic the entry of a solar neutrino by converting an atom of ^{37}Cl into an atom of radioactive ^{37}Ar.

Figure on the right shows the ^{37}Ar production rate in 3.8×10^5 liters of perchloroethylene as a function of the depth below the surface. The corresponding background effect is about 0.2 atoms per day in 10^5 gal. Other sources of the background are estimated to be on the same level or less, in particular,

○ fast neutrons from (α, n) reactions and spontaneous fission of U in the rock wall: 0.1–0.3;
○ internal contamination (U, Th, Ca): $\lesssim 0.1$;
○ atmospheric neutrino interactions: $\lesssim 0.01$.

[From R. Davis, Jr. and D. S. Harmer, "Solar neutrino detection by the $^{37}Cl - ^{37}Ar$ method," in Proc. of the Informal Conference on Experimental Neutrino Physics (CERN, January 20–22, 1965), CERN 65-32, pp. 201–212.]

161
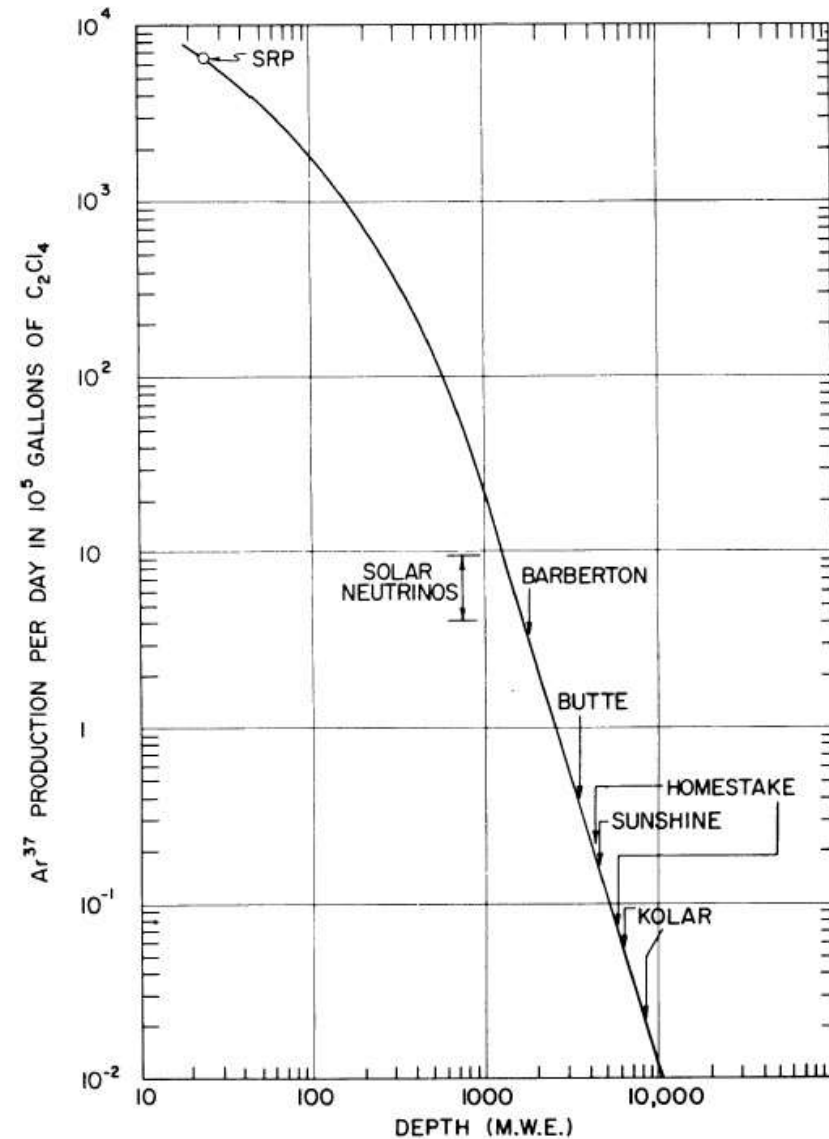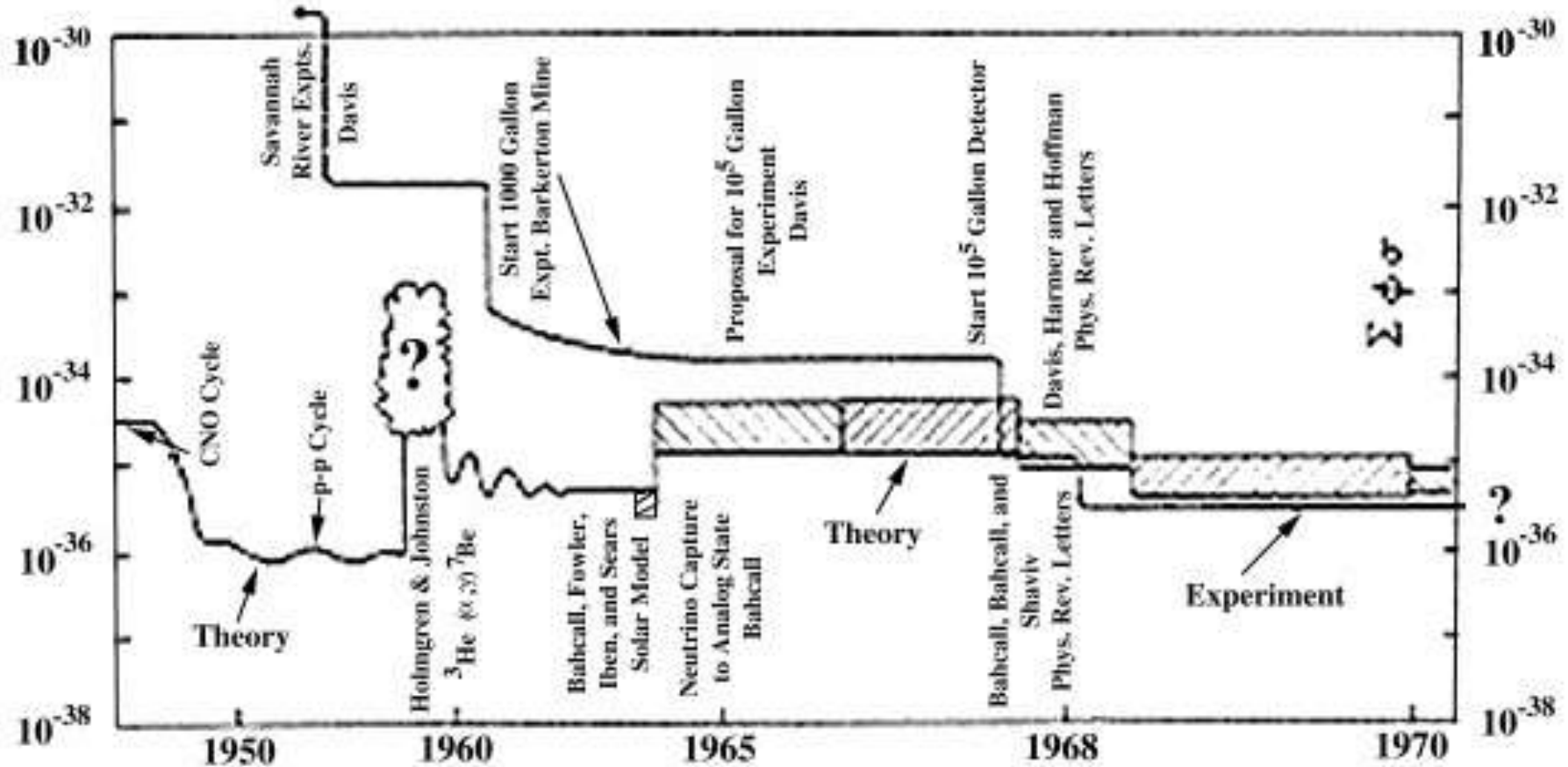
This figure is an overall pictorial history of the subject as it looked in 1970. It shows some of the principal events in the development of the solar neutrino problem. The experimental upper limit is indicated by the thin curve and the range of theoretical values (after 1964) by the cross-hatched region. The units are captures per target atom per second (10^{-36} captures/atom/s $\equiv 1$ SNU). A few of the major events are indicated on the figure at the period corresponding to the time they occurred.

Figure shows the observed (Davis & coauthors) and predicted (Bahcall & co-authors) neutrino capture rates published within the period from 1964 to 1980. The earliest observational upper limits of 4000 and 160 SNU (obtained in 1955 and 1964, respectively) are not shown since these would not fit conveniently in the plot [see previous slide].

The theoretical uncertainties are more "experimental" than "theoretical" since the basic theory has not changed since 1964. What have changed are the best estimates for many different input parameters. The error bars shown for the theoretical points represent the range of capture rates that were obtained from standard solar models when the various nuclear and atomic parameters were allowed to vary over the range conventionally regarded as acceptable at the time the calculations were made.
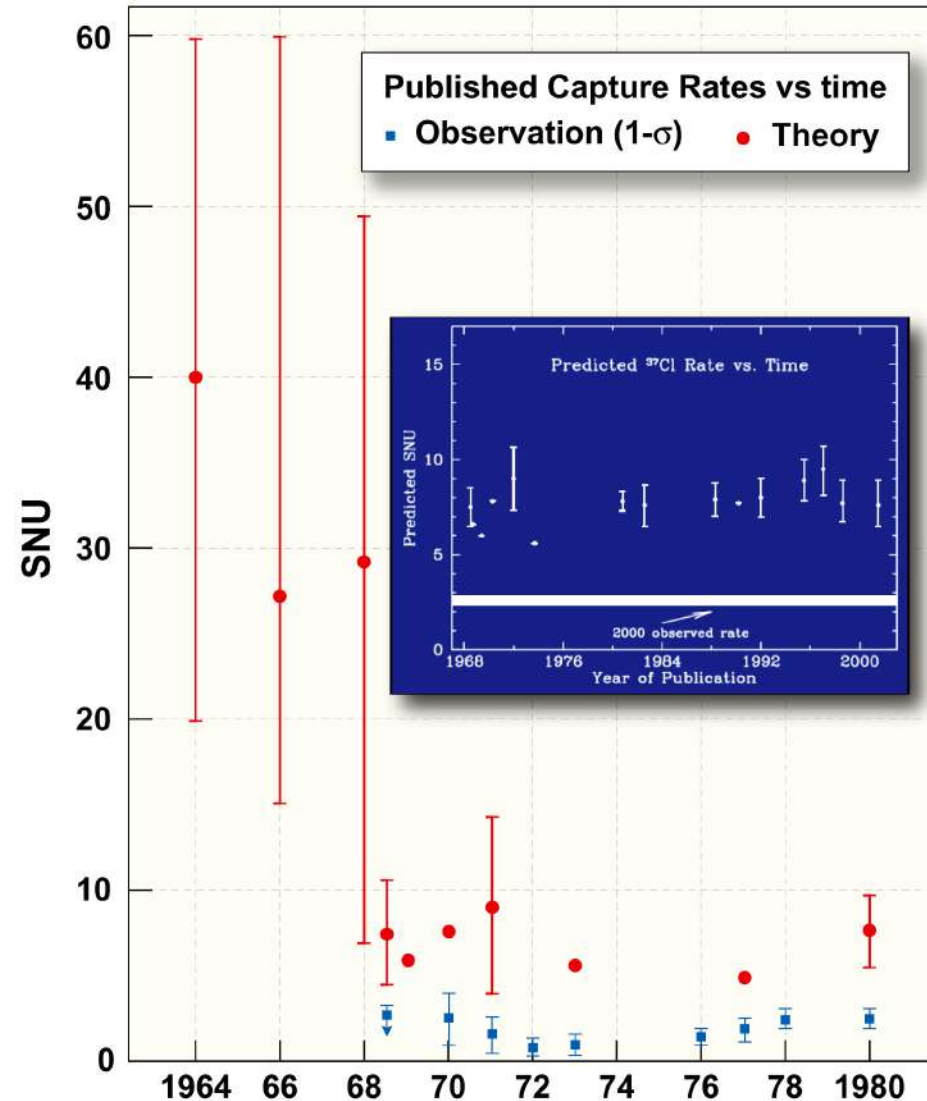
[From J. N. Bahcall and R. Davis, Jr., "An account of the development of the solar neutrino problem," in Essays in Nuclear Astrophysics, edited by C. A. Barnes, D. D. Clayton, and D. Schramm (Cambridge University Press, 1982), pp. 243–285.]
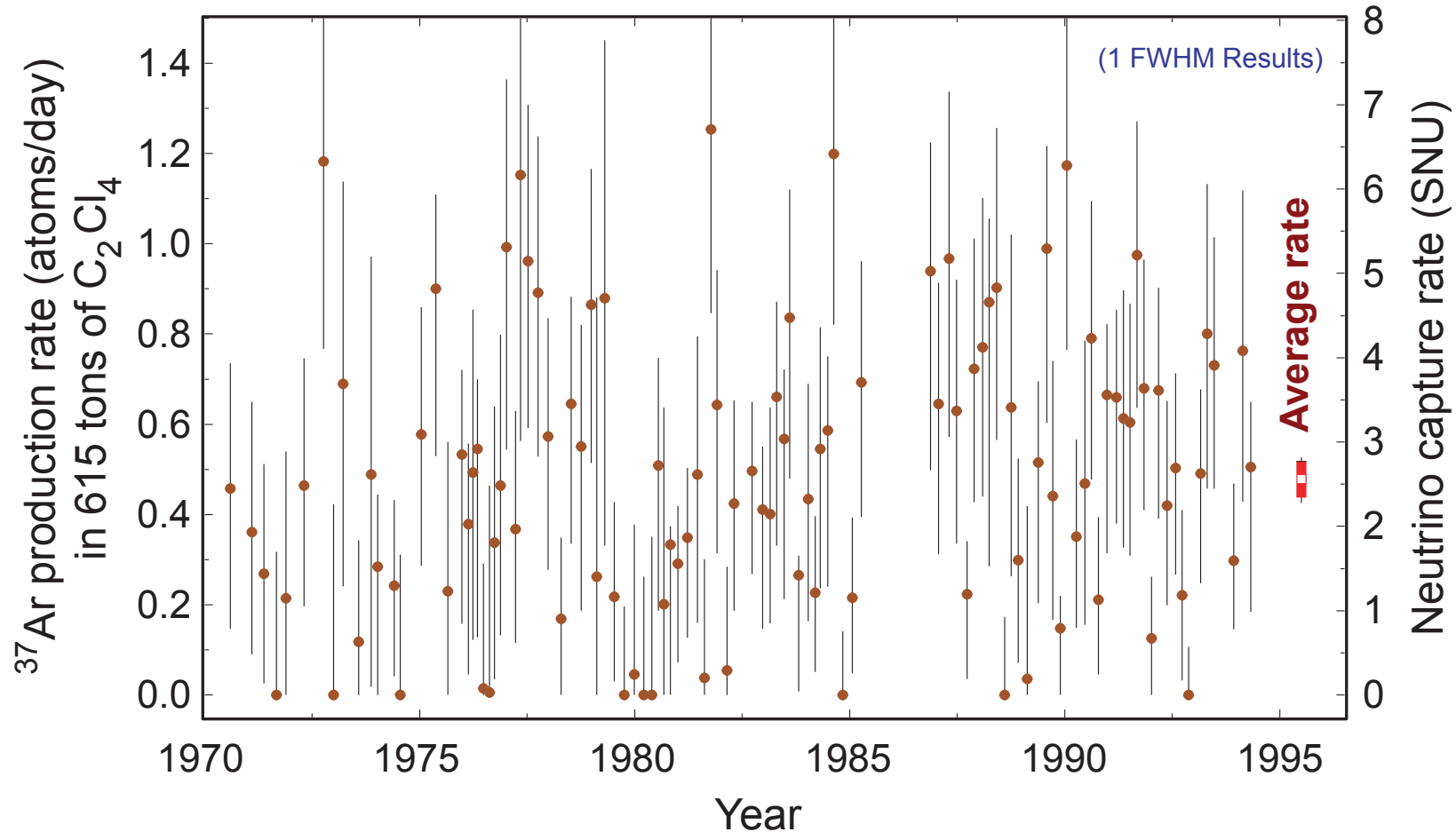
The final Homestake chlorine experiment one-FWHM (full width at half maximum) results for 108 individual solar neutrino observations (no. 18 to 133). All known sources of nonsolar ^{37}Ar production are subtracted. The errors of individual measurements are statistical errors only and are significantly non-Gaussian for near zero rates. The error of the cumulative result is the combination of the statistical and systematic errors in quadrature. [From B. T. Cleveland *et al.*, "Measurement of the solar electron neutrino flux with the Homestake chlorine detector," ApJ **496** (1998) 505–526. (2133 citations in InSPIRE!)]

Solar neutrino puzzle # I.

The average over 1970-1995 runs solar ν induced ^{37}Ar production rate in the Homestake detector is $0.478 \pm 0.030_{\text{stat}} \pm 0.029_{\text{syst}}$ day^{-1}. Since the detector contains 2.16×10^{30} ^{37}Cl atoms, this gives a neutrino capture rate of

$$\langle \sigma \Phi_{\nu_e} \rangle = 2.56 \pm 0.16_{\text{stat}} \pm 0.16_{\text{syst}} \text{ SNU}.$$

This measurement has to be compared with the SSM predictions for the chlorine detector:

$$\langle \sigma \Phi_{\nu_e} \rangle_{\text{theor}} = \begin{cases} 7.63 \text{ SNU} & \text{(Sackman, Boothroyd \& Fowler, 1990)} \\ 6.36 \text{ SNU} & \text{(Turck-Chièze \& Lopes, 1993)} \\ (4.2 \pm 1.2) \text{ SNU} & \text{(Dar \& Shaviv, 1994)} \\ (9.3 \pm 1.3) \text{ SNU} & \text{(Bahcall \& Pinsonneault, 1995)} \\ (4.1 \pm 1.2) \text{ SNU} & \text{(Dar \& Shaviv, 1996)} \\ (7.7 \pm 1.2) \text{ SNU} & \text{(Bahcall, Basu \& Pinsonneault, 1998)} \\ (8.1 \pm 1.2) \text{ SNU} & \text{(Bahcall \& Serenelli, 2005),} \\ 6.315 \text{ SNU} & \text{(Turck-Chièze \& Couvidat, 2010) [SSM],} \\ (7.67 \pm 1.1) \text{ SNU} & \text{(Turck-Chièze \& Couvidat, 2010) [SeSM].} \end{cases}$$

The observed flux is much lower than that predicted (except for the Dar & Shaviv results). This discrepancy between observation and prediction has existed since the early 1970s when the observations of the Homestake detector were first reported.

This is "The Solar Neutrino Puzzle, Number I".

Solar neutrino puzzle # II.
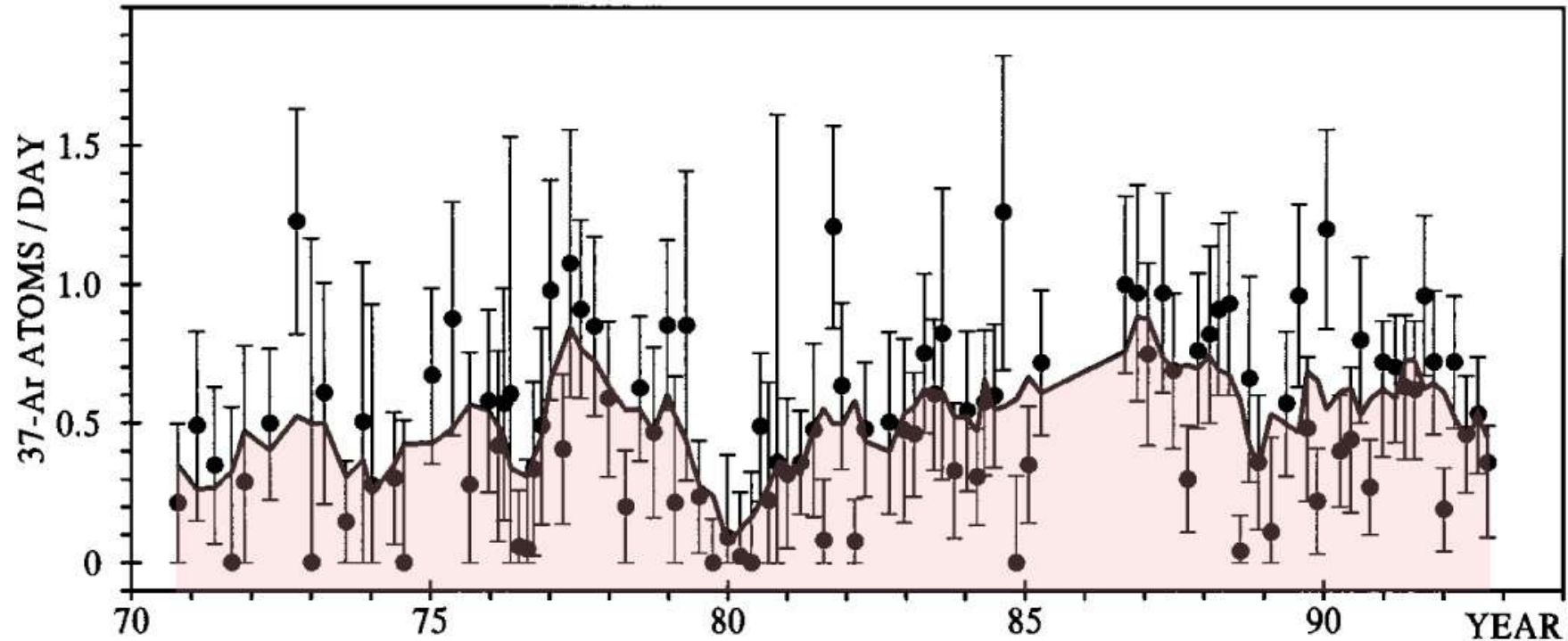
Homestake neutrino data with error bars and 5-point running-averaged values (solid line) from runs No. 18 to No. 126. The 5-point running-average values (Q5) are used to illustrate better the long-term behaviour considering that the original neutrino data are very scattered. Other choices for the smoothing, for instance 3- or 7-point running averages, do not alter qualitatively the results.

[This and next figures are borrowed from S. Massetti, M. Storini, and N. Iucci, "Correlative analyses for Homestake neutrino data," Nuovo Cim. **20 C** (1997) 1021–1026.]
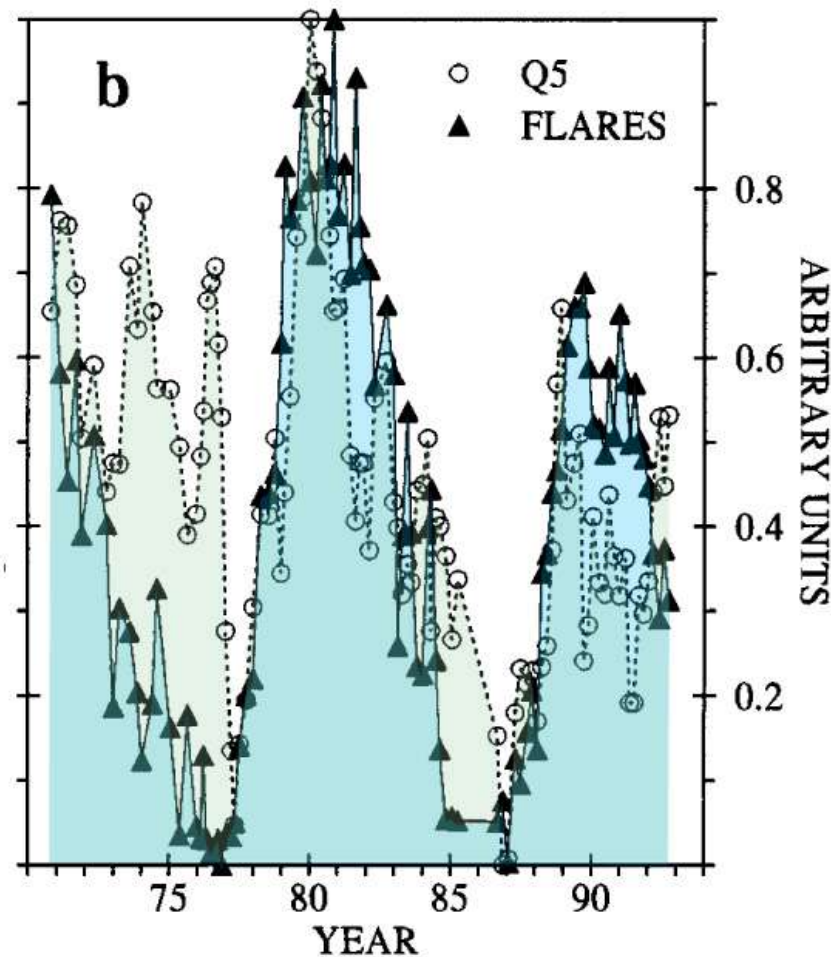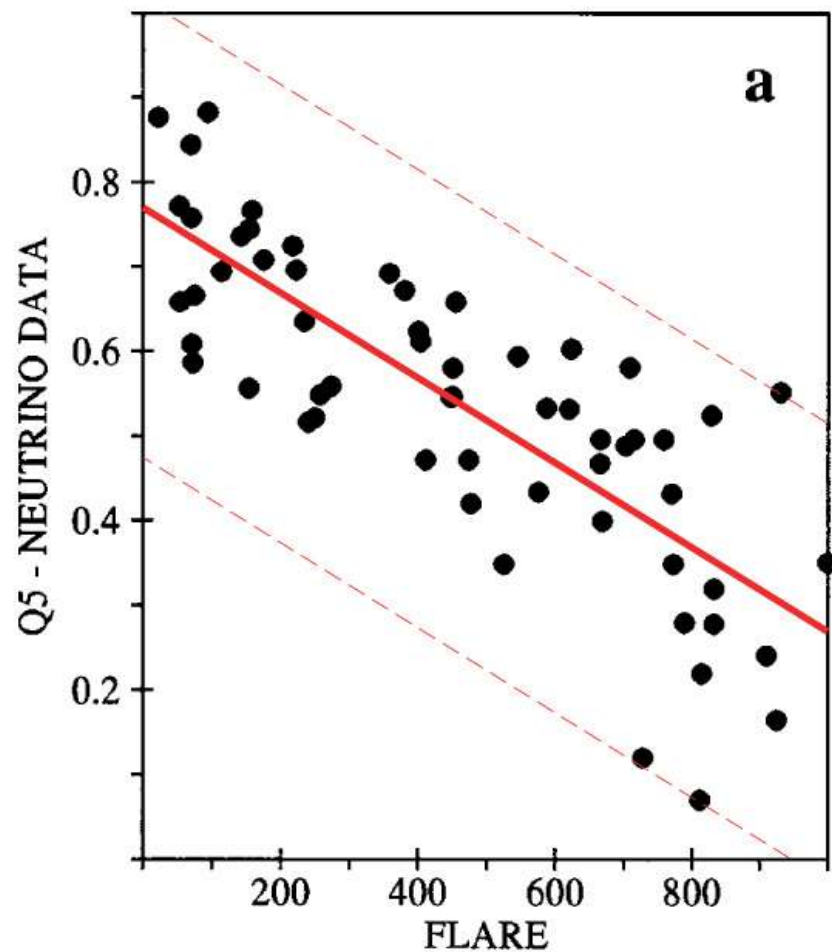
Scatter plot of solar flares counts vs. 5-point running averages of Homestake neutrino values in the period 1977 to 1989 (a) and the above data sets plotted as a function of time in the period 1970 to 1992 (b); the neutrino data in (b) are reported with an inverted scale and both data sets are normalized in a way that minimum = 0 and maximum = 1.
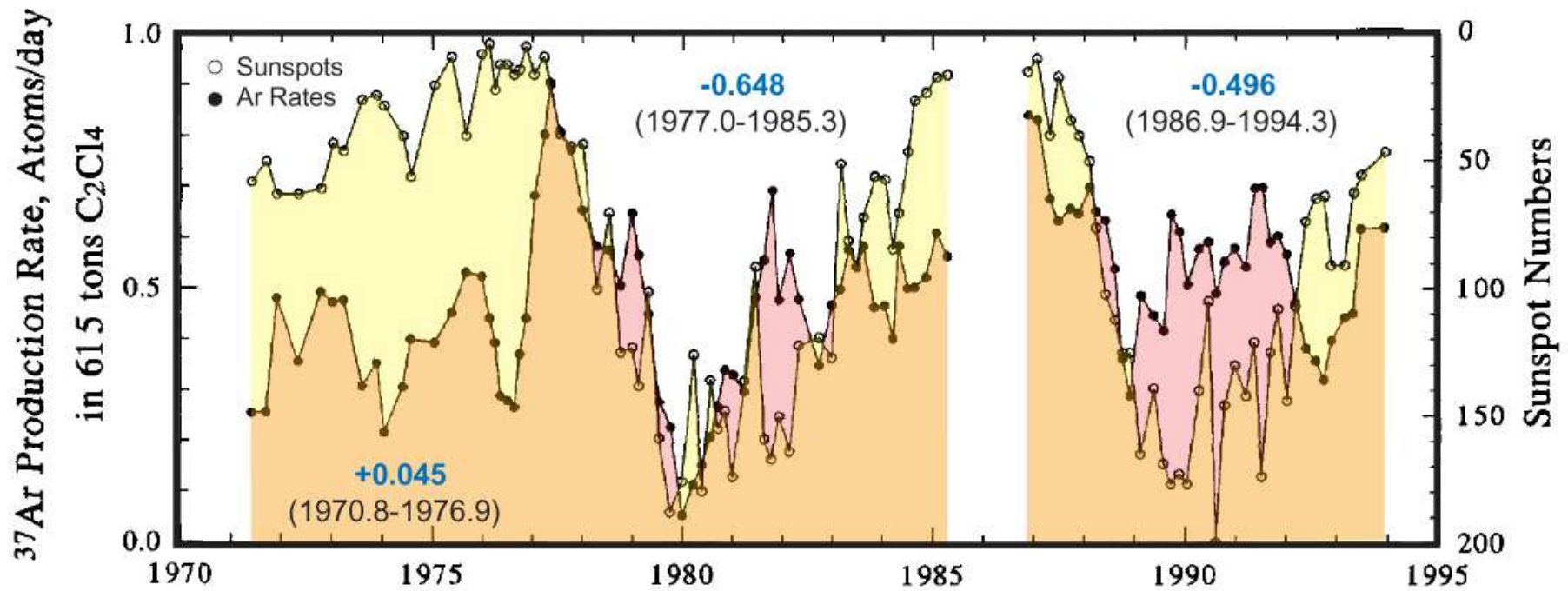
The plot shows the 5-point running averages of the Homestake data compared to sunspot numbers; the sunspots are plotted on an inverted scale.

[R. Davis Jr., "A review of measurements of the solar neutrino flux and their variation," Nucl. Phys. B (Proc. Suppl.) **48** (1996) 284–298.]

Some of the conclusions of the authors are:

The Homestake data:

i) Exhibit a clear modulation of the neutrino signal, almost on the long term.

ii) Are badly correlated with geomagnetic indices, supporting the hypothesis that the source of the modulation is on the Sun.

iii) Are correlated with cosmic-rays intensity only in the period 1970-1982, whereas over the total period the correlation is near zero.

iv) Are better correlated with flare counts than with sunspot numbers. Note that flare phenomena are intimately related to the toroidal component of the heliomagnetic field. The best correlated period (1977–1989) corresponds to that characterized by a reinforcement of the interplanetary magnetic-field intensity, suggesting again an enhancement of the global heliomagnetic field.

More or less similar conclusions were found in the regression analyses reported by many authors. These results suggest a pulsating character of the Homestake data and their anticorrelation with the solar magnetic activity (sunspot or flare numbers).

<p style="text-align:center; color:red;">This is "The Solar Neutrino Puzzle, Number II".</p>

A veritable host of new ideas was brought forth to resolve the solar neutrino puzzles. Let's consider a (very incomplete) list of these solutions.

Solutions.

Astrophysics and/or Nuclear Physics.

- Models with convective mixing of the solar core [*Ezer & Cameron, 1968; Shaviv & Salpeter, 1968; Bahcall, Bahcall & Ulrich, 1968*].
- Models with turbulent diffusion of ^{3}He [*Schatzman, 1969*].
- A secular instability such that the presently observed solar luminosity does not equal the current energy-generation rate [*Fowler, 1968, 1972; Sheldon, 1969*].
- An overabundance of ^{3}He in the present-day Sun [*Kocharov & Starbumov, 1970*].
- Models with the strong central magnetic field (the energy density of the Sun's central magnetic field $|\mathbf{B}|^2/8\pi$ is a few percent of the gas pressure) [*Abraham & Iben, 1971; Bahcall & Ulrich, 1971; Bartenwerfer, 1973; Parker, 1974; Ulrich, 1974*].
- Models with low heavy elements ("low Z") abundances in the solar interior [*Bahcall & Ulrich, 1971; Schatzman, 1981; Maeder, 1990*].
- An instability of the Sun that makes now a special time [*Fowler, 1972; Dilke & Gough, 1972*].
- A low-energy resonance in the ^{3}He$+^3$He $\rightarrow$ ^{4}He$+2^1$H reaction [*Fowler, 1972; Fetisov & Kopysov 1972*].

- Helium core (the Sun is assumed to be in a later stage of stellar evolution, such that hydrogen is burned-out and the core is made of helium) [*Prentice, 1973*].
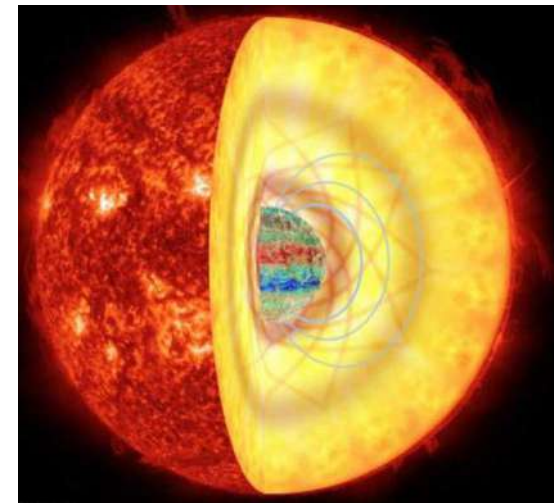
- Models with a rapidly rotating solar interior (the rotation is lowering the central pressure and temperature) [*Demarque, Mengel & Sweigert, 1973; Roxburgh, 1974; Rood & Ulrich 1974*].
- Rotation plus magnetic fields [*Snell, Wheeler & Wilson, 1976*].
- A half-solar mass core of large heavy element abundance that survived the big bang and subsequently accreted another half solar mass at the time of the formation of the solar system [*Hoyle, 1975*].
- A departure from the Maxwellian distribution [*Clayton et al., 1975*].
- A fractionation of the primordial hydrogen and helium [*Wheeler & Cameron, 1975*].
- Mixing of ^{3}He due to rapid filamental flow downward [*Cummings & Haxton, 1996*].
- Temporal and spatial variations in temperature [*Dar & Shaviv, 1998*].
- Collective plasma processes [*Salpeter & Van Horne, 1969; ...; Tsytovich et al., 1995, Dar & Shaviv, 1998*].
- A new solar model in which the Sun is formed by accretion of fresh SN debris on the collapsed core of a supernova; neutron emission from the SN remnant at the solar core; neutron decay major elements are iron, nickel, oxygen, silicon [*Manuel, Miller & Katragada, 2003*].
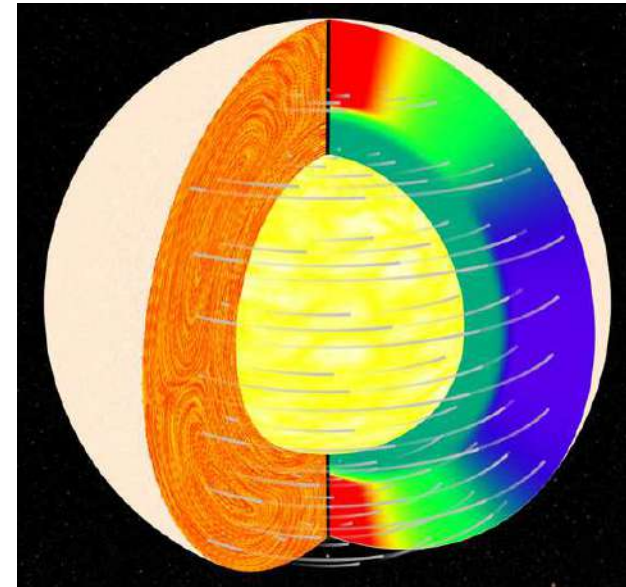
Nonstandard Neutrino Properties.

- Vacuum neutrino oscillations [*Gribov & Pontecorvo, 1969, Bilenky & Pontecorvo, 1977,...*].
- An appreciable (anomalous) magnetic moment for the neutrino [*Cisneros 1971; Okun, Voloshin & Vysotsky, 1986*].
- Neutrino instability [*Bahcall, Cabibbo & Yahil, 1972*].
- Goldstone neutrinos resulting from a spontaneous breakdown of supersymmetry [*Das, 1984*].
- **Matter enhanced neutrino oscillations [*Wolfenstein 1978; ...; Mikheev & Smirnov, 1985.*]**
- Matter-induced neutrino decay $\nu \to \overline{\nu} + $ Majoron [*Berezhiani & Vysotsky, 1987*].
- Resonant neutrino spin–flavor precession in the solar magnetic field [*Akhmedov, 1987; Lim & Marciano, 1988*].
- Nonstandard (in particular, flavor-changing) neutrino interactions with matter [*Roulet, 1991; Guzzo, Masiero & Petcov, 1991; Barger, Phillips & Whisnant, 1991*].
- A nonstandard (strong enough) $\nu_e \gamma$ interaction that would cause the neutrinos to disappear before they leave the Sun or make them lose energy towards detection thresholds [*Dixmier, 1994*]

Exotics and Science Fiction.

- Quark catalysis [*Libby & Thomas, 1969; Salpeter, 1970*].
- Accretion onto a central black hole (the model assumes that the Sun's energy did not come from fusion, rather from release of energy from accretion onto a black hole at the center of the Sun) [*Clayton, Newman & Talbot, 1975*].
- Multiplicative mass creation [*Maeder, 1977*].
- WIMPs as a source of solar energy [*Faulkner & Gilliland, 1985; Spergel & Press, 1985; Press & Spergel, 1985; Faulkner, Gough & Vahia, 1986; Gilliland et al., 1986*].
- Violation of equivalence principle (gravitational forces may induce neutrino mixing and flavor oscillations if the equivalence principle is not true) [*Gasperini, 1988, 1989; Halprin & Leung, 1991; ...; Gago, Nunokawa & Zukanovich, 2000; Pantaleone, Kuo & Mansour, 2000*].
- Daemon[a] catalysis (it is assumed that daemons are capable of catalyzing proton-fusion reactions, which may account for the observed solar neutrino deficiency) [*Drobyshevski, 1996, 2002*].

---
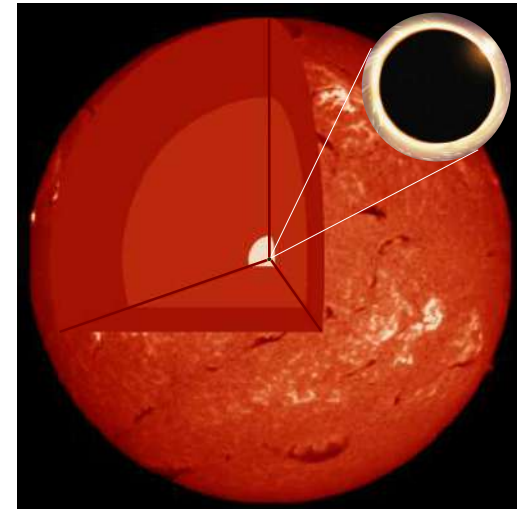
[a]**Daemon** = **Da**rk **E**lectric **M**atter **O**bject, a hypothetical Planckian particle carrying a negative electric charge of up to $Z = 10$ (something like a negatively charged Planckian black hole). [Etymology: "Dæmon" is the Latin version of the Greek "$\delta\alpha\iota\mu\omega\nu$" ("godlike power", "fate", "god" in classical mythology).]

11   Ga-Ge detector SAGE.

These solar neutrino experiments are based on the reaction (originally proposed by V. A. Kuzmin in 1965)

$$\nu_e + {}^{71}_{31}\text{Ga} \rightarrow {}^{71}_{32}\text{Ge} + e^- \quad (E^{\text{th}}_\nu \approx 232.696 \pm 0.15 \text{ keV}).^{\text{a}}$$

Then the radioactive germanium decays back to gallium:

$$ {}^{71}_{32}\text{Ge} \rightarrow {}^{71}_{31}\text{Ga} + e^+ + \nu_e \quad (T_{1/2} \approx 11.4 \text{ days}).$$

Backgrounds for the gallium experiments are caused by ^{71}Ge production through non-neutrino mechanisms

$$ p + {}^{71}_{31}\text{Ga} \rightarrow {}^{71}_{32}\text{Ge} + n \quad (E^{\text{th}}_p \approx 1.02 \text{ MeV}).$$
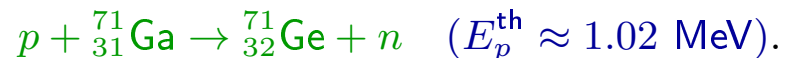
Like in the chlorine experiment, the protons may be produced by cosmic muon interactions, fast neutrons or residual radioactivity. Radon gas and its daughter products are also a large cause of background; the radon half-life is about 3.8 days.

In the SAGE (Soviet–American Gallium solar neutrino Experiment), the ^{71}Ge atoms are chemically extracted from a 50-metric ton target of gallium metal and concentrated in a sample of germane gas (GeH_4 – the germanium analogue of methane) mixed with xenon. The ^{71}Ge atoms are then individually counted by observing their decay back to ^{71}Ga in a small proportional counter.

The SAGE group regularly performs solar neutrino extractions, every four weeks, reducing the statistical error, and explores further possibilities for reducing the systematic uncertainties.

---

[a]This is the weighted average of all the available measurements for the neutrino energy threshold of this reaction computed (including estimates of systematic errors) by G. Audi and A. H. Wapstra.

B-
Gallium-Germanium
Neutrino Telescope

206 м

Global Intensity
$(3,0\pm0,15)\cdot10^{-9} \mathcal{M}\, cm^{-2}\cdot s^{-1}$
~ 4800 m.w.e.

INR RAS
Baksan Neutrino Observatory

Mountain Andyrchi

A - Scintillator Telescope

C - Solar Neutrino Detectors
(projects)

D - Low Background Chambers

Muon Flux (cm^{-2} s^{-1})

Meters over sea level

Baksan

Meters from entrance
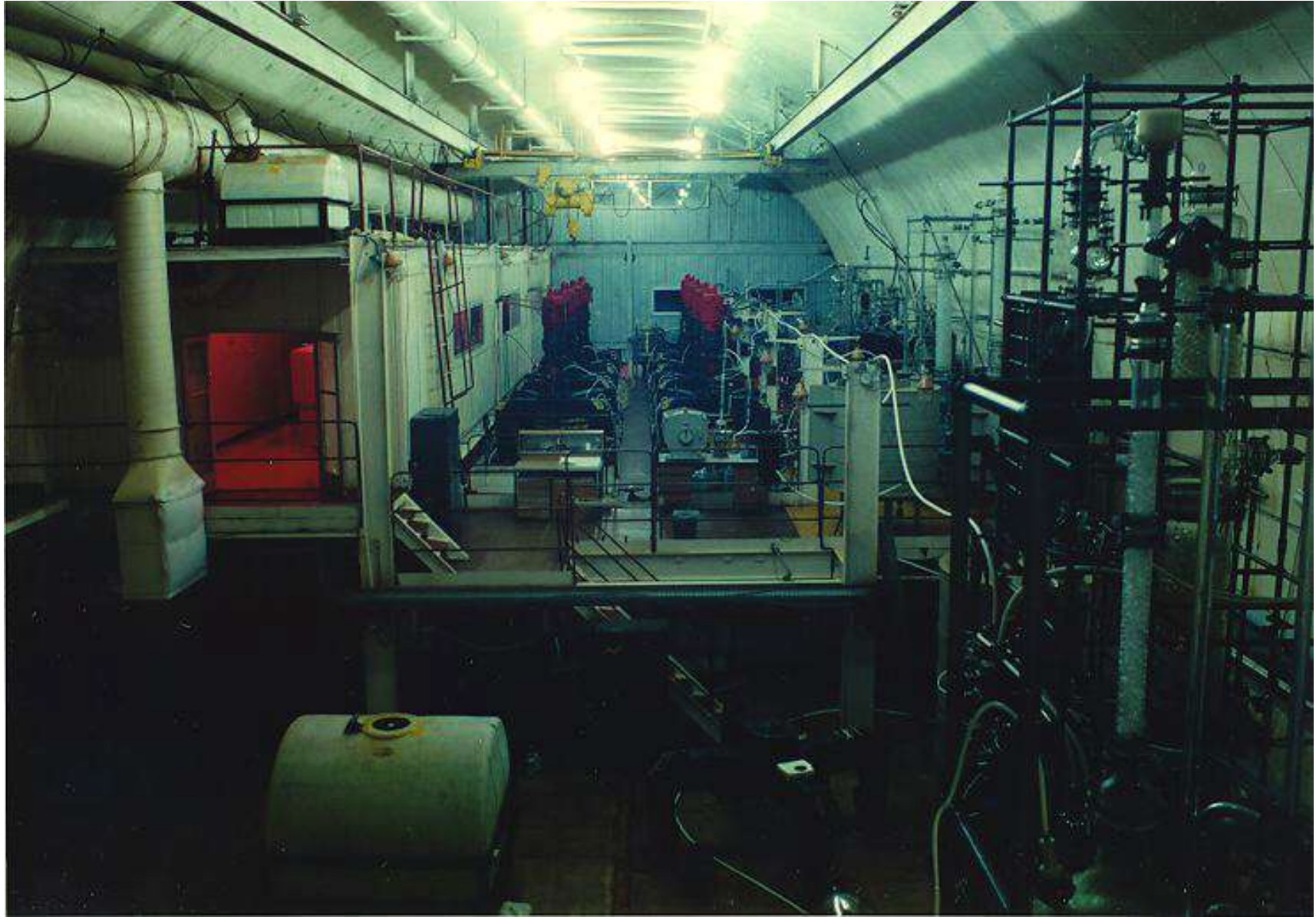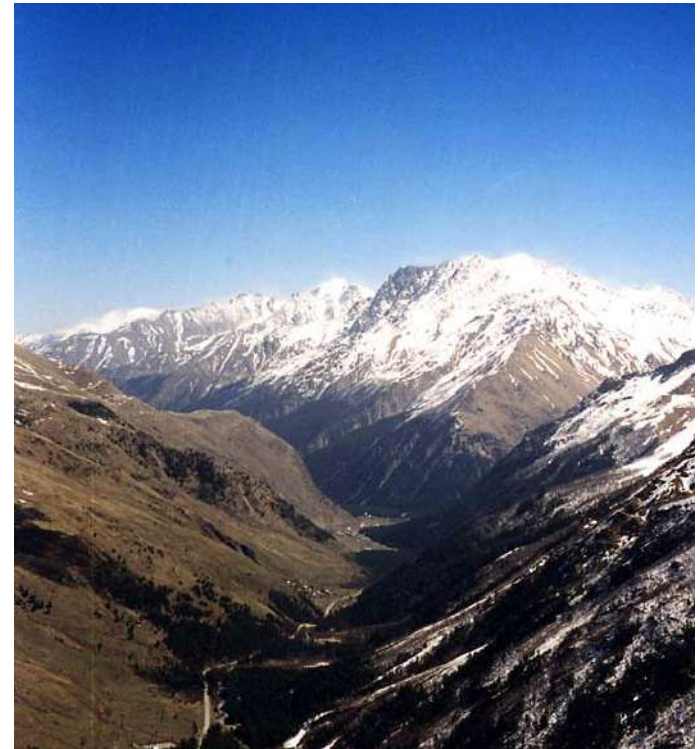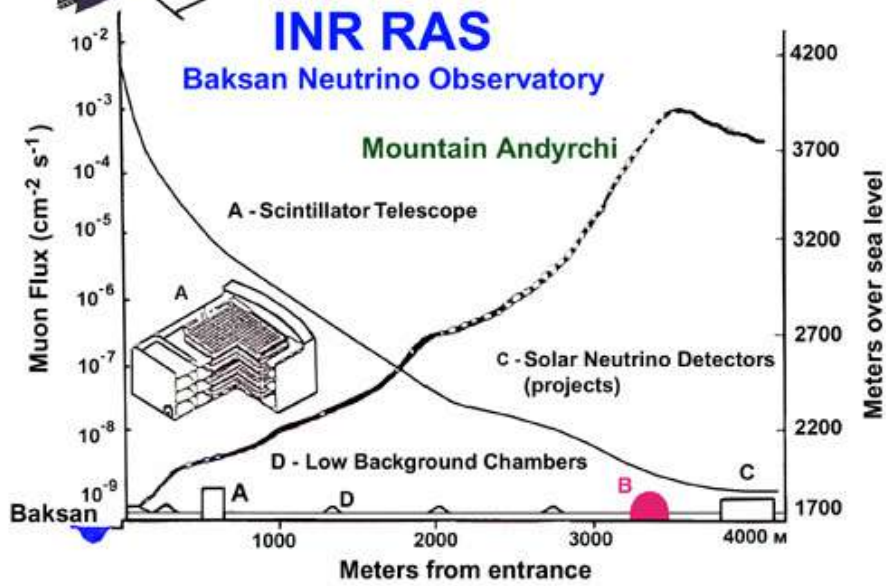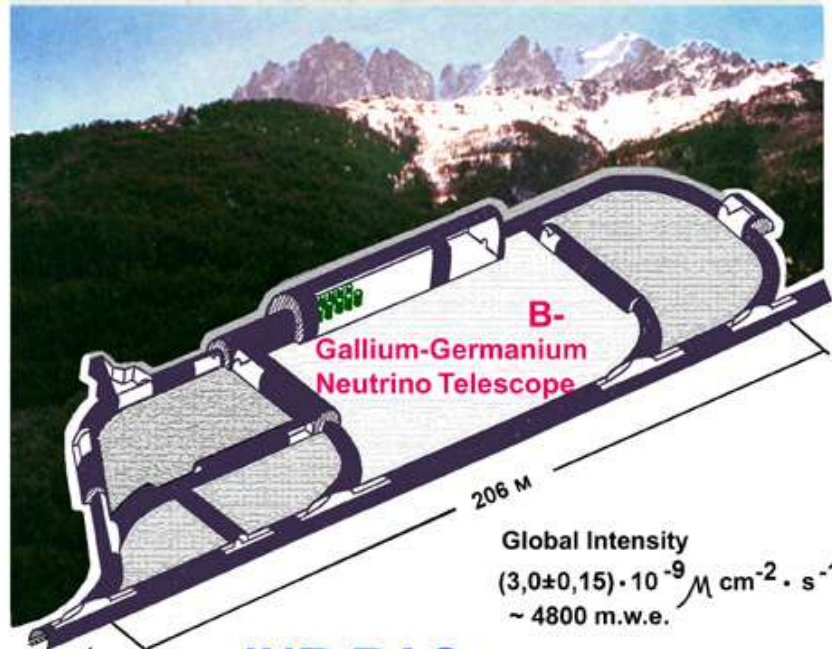
To check the response of the SAGE experiment to low-energy neutrinos, a source of ^{51}Cr was produced by irradiating 512.7 g of 92.4%-enriched ^{50}Cr in a high-flux fast neutron reactor. This source, which mainly emits monoenergetic 747-keV neutrinos, was placed at the center of a 13.1 ton target of liquid gallium and the cross section for the production of ^{71}Ge by the inverse beta decay reaction ^{71}Ga$(\nu_e, e^-)^{71}$Ga was measured to be

$$(5.55 \pm 0.60_{\mathrm{stat}} \pm 0.32_{\mathrm{stat}}) \times 10^{-45} \ \mathrm{cm}^2.$$

Decay scheme of ^{51}Cr to ^{51}V through electron capture

^{51}Cr (27.7 days)

427 keV ν (9.0%)
432 keV ν (0.9%)

747 keV ν (81.6%)
752 keV ν (8.5%)

320 keV γ

^{51}V
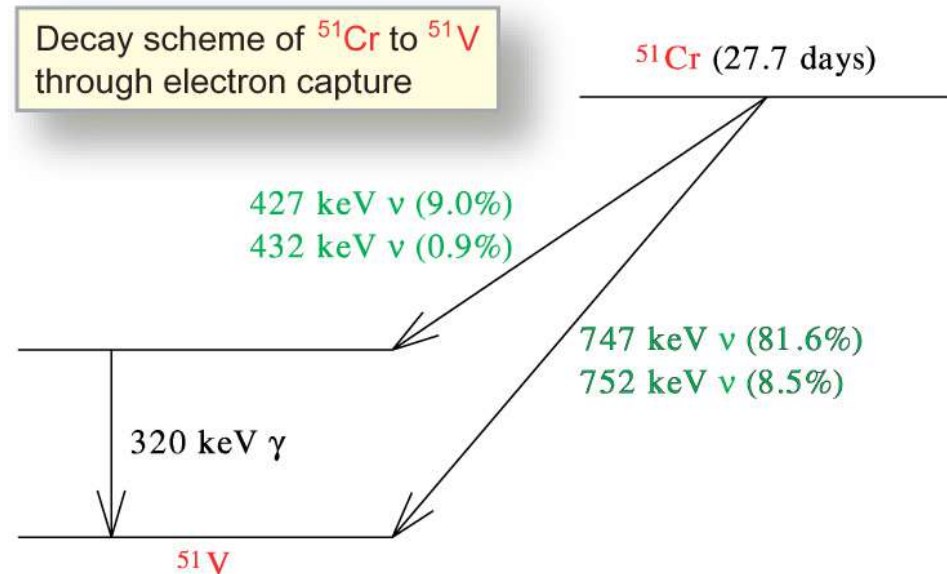
[From J. N. Abdurashitov *et al.*, "Measurement of the response of a gallium metal solar neutrino experiment to neutrinos from a ^{51}Cr source," Phys. Rev. C **59** (1999) 2246–2263.]

The ratio of this result to the theoretical cross section of Bahcall and of Haxton are

$$0.95 \pm 0.12 \, (\mathrm{exp}) \, {}^{+0.035}_{-0.027} \, (\mathrm{theor}) \quad \text{and} \quad 0.87 \pm 0.11 \, (\mathrm{exp}) \pm 0.09 \, (\mathrm{theor}),$$

respectively. This good agreement between prediction and observation implies that the overall experimental efficiency is correctly determined and provides considerable evidence for the reliability of the solar neutrino measurement.

BUT! The remaining small discrepancy might be a hint to something interesting...
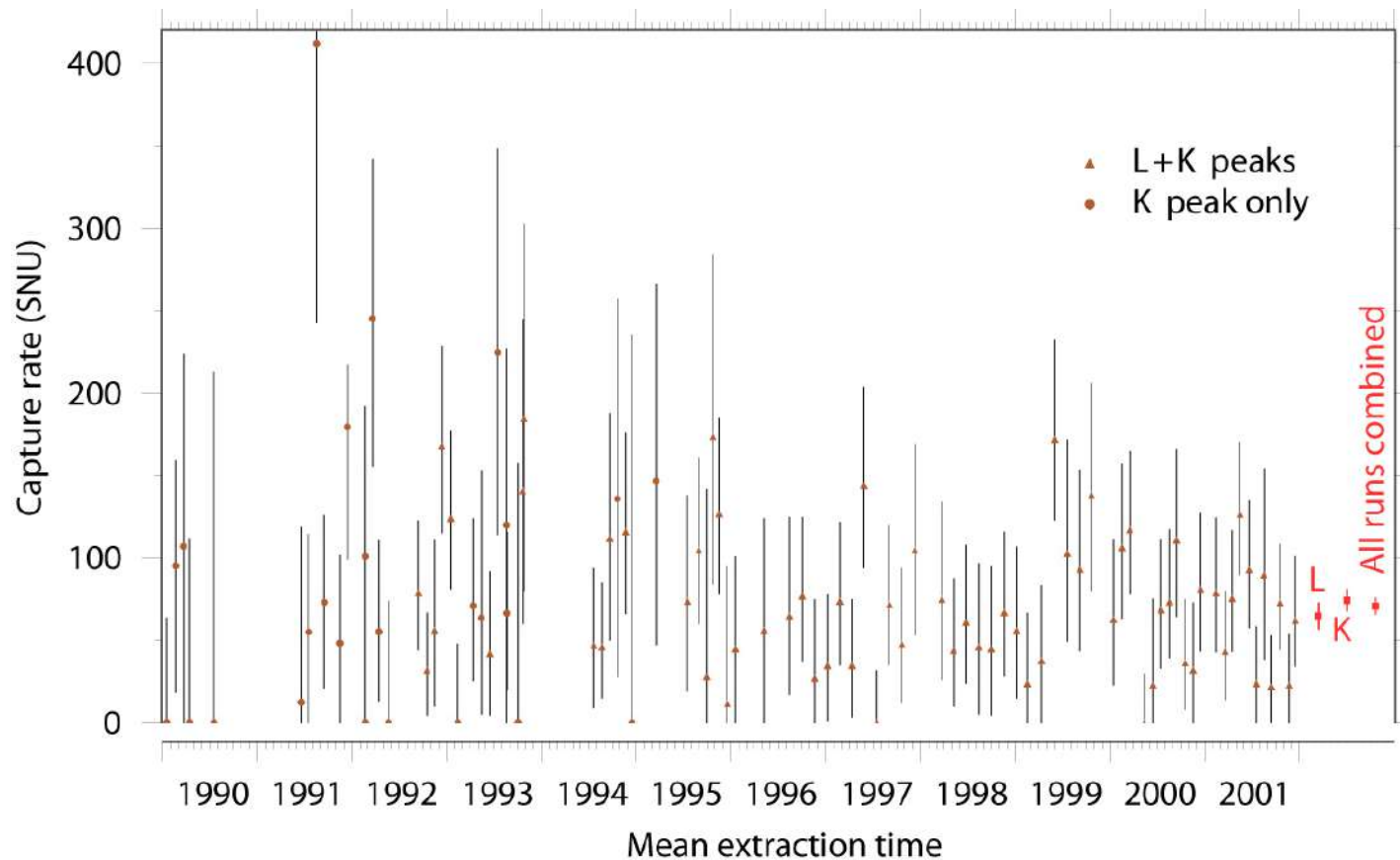
The capture rate from all SAGE extractions versus time: the triangles are for the L and K peaks and the circles are for the K peak alone; the vertical bars near each point correspond to a statistical error of 68%. The average rates for the L, K, and $L + K$ peaks are also shown.
[This and next figures are borrowed from J. N. Abdurashitov *et al.*, "Solar neutrino flux measurements by the Soviet-American Gallium Experiment (SAGE) for half the 22-Year Solar Cycle," Zh. Eksp. Teor. Fiz. **122** (2002) 211–226 [JETP **95** (2002) 181–193], astro-ph/0204245.]
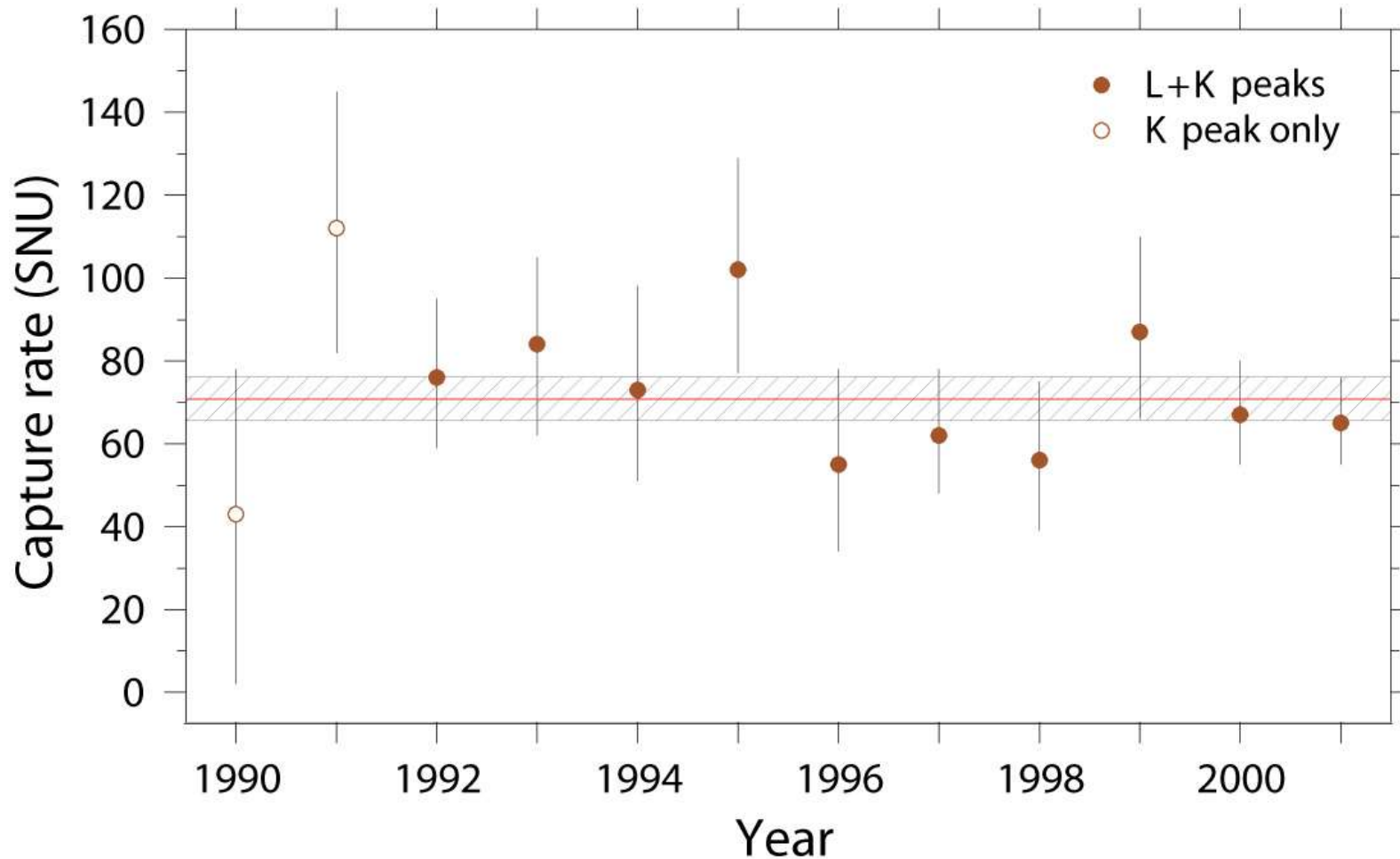
Results of the measurements combined by years; open and filled symbols refer to K and $K + L$ peaks, respectively; the hatched region corresponds to the SAGE result of $70.8^{+5.3}_{-5.2}$ (stat) $^{+3.7}_{-3.2}$ (syst) SNU. The data shown have a statistical error of 68%. The neutrino capture rate was constant during the entire data acquisition period with a 83% probability.

12 Ga-Ge detectors GALLEX and GNO.

Gran Sasso lab, ground level

Gran Sasso lab, underground
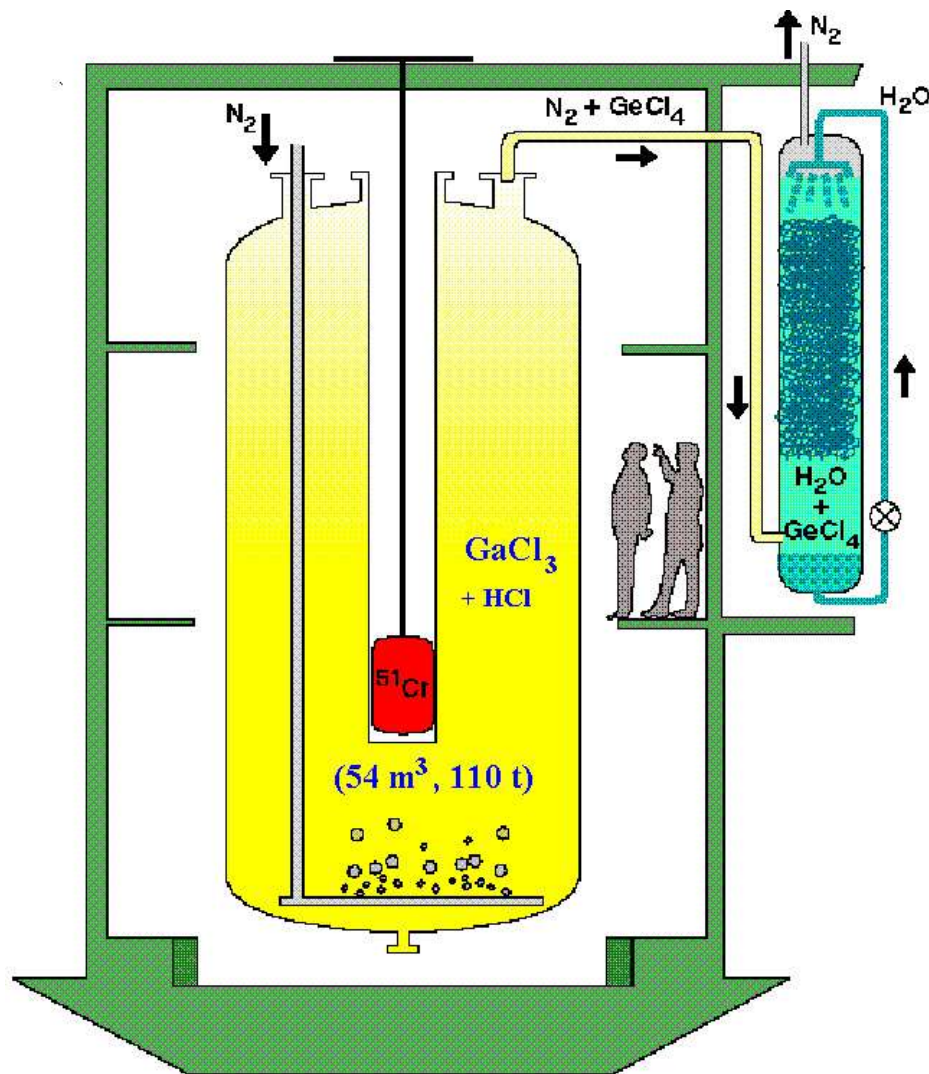
Figure on the left shows a scheme of the GALLEX detector tank with the absorber system and the Chromium source inserted inside the thimble.

The experimental procedure for GALLEX is as follows: 30.3 tons of gallium in form of a concentrated $GaCl_3$-HCl solution are exposed to solar neutrinos. In $GaCl_3$-HCl solution, the neutrino induced ^{71}Ge atoms (as well as the inactive Ge carrier atoms added to the solution at the beginning of a run) form the volatile compound $GeCl_4$, which at the end of an exposure is swept out of the solution by means of a gas stream (nitrogen). The nitrogen is then passed through a gas scrubber where the $GeCl_4$ is absorbed in water.

The $GeCl_4$ is finally converted to GeH_4, which together with xenon is introduced into a proportional counter in order to determine the number of ^{71}Ge atoms by observing their radioactive decay.

[From URL: ⟨http://www.mpi-hd.mpg.de/nuastro/gallex/detector.htm⟩.]

181
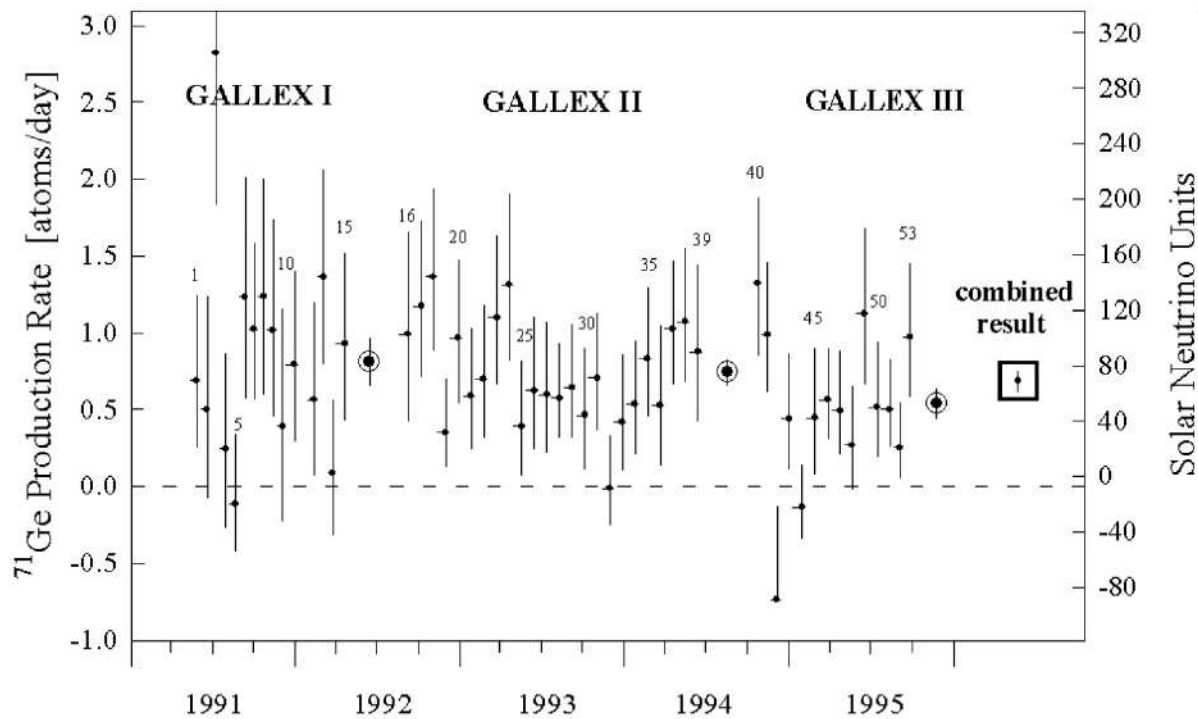
GALLEX I, II, and III single run overview.

Results for the 14 solar neutrino runs of GALLEX III (labels 40-53), shown together with the earlier results from GALLEX I (labels 1-15) and from GALLEX II (labels 16-39).

The left-hand scale is the measured ^{71}Ge production rate; the right hand scale, the net solar neutrino production rate (SNU) after subtraction of side reaction contributions.

Error bars are $\pm 1\sigma$, statistical only. The label "combined" applies to the mean global value for the total of all 53 runs. The visibility is enhanced by a square box, but its error is the small bar inside the box. Horizontal bars represent run duration; their asymmetry reflects the "mean age" of the ^{71}Ge produced.
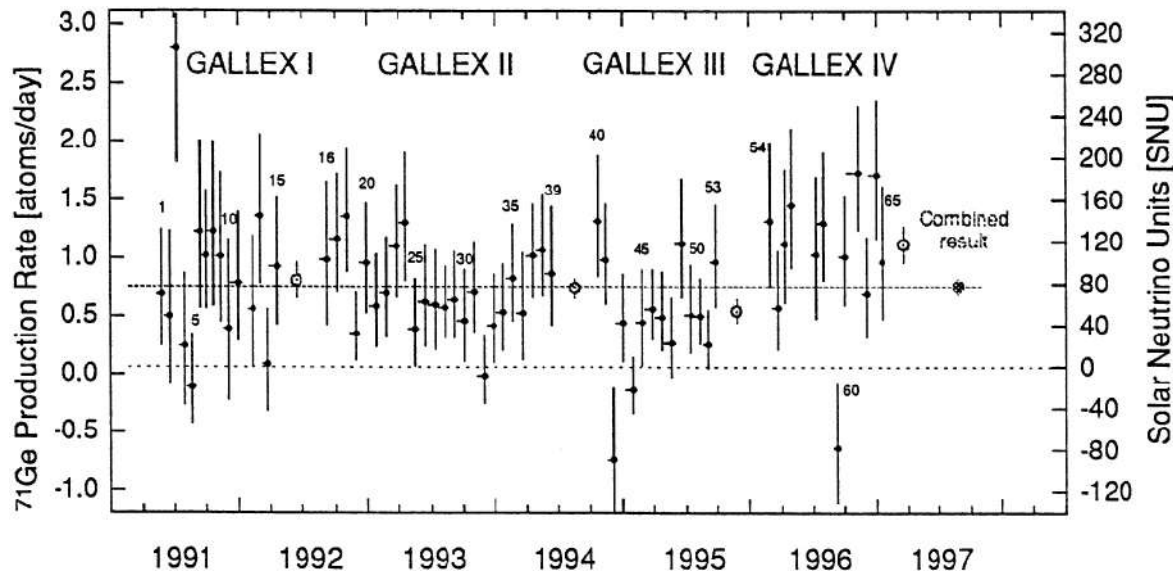
Summary of the results of GALLEX individual solar runs closed points. The left hand scale is the measured ^{71}Ge production rate; the right hand scale, the net solar neutrino production rate SNU after subtraction of side reaction contributions.

Error bars are $\pm 1\sigma$ statistical only. Open circles are the combined results for each of the measuring periods, GALLEX I, II, III and IV. The label "combined" applies to the mean global value for the total of all 65 runs. Horizontal bars represent run duration; their asymmetry reflects the "mean age" of the ^{71}Ge produced. The combined result which comprises 65 solar runs, is $77.5 \pm 6.2^{+4.3}_{-4.7} (1\sigma)$ SNU. The GALLEX experimental program to register solar neutrinos has now been completed.

In April 1998, GALLEX was succeeded by a new project, the Gallium Neutrino Observatory (GNO), with newly defined motives and goals.
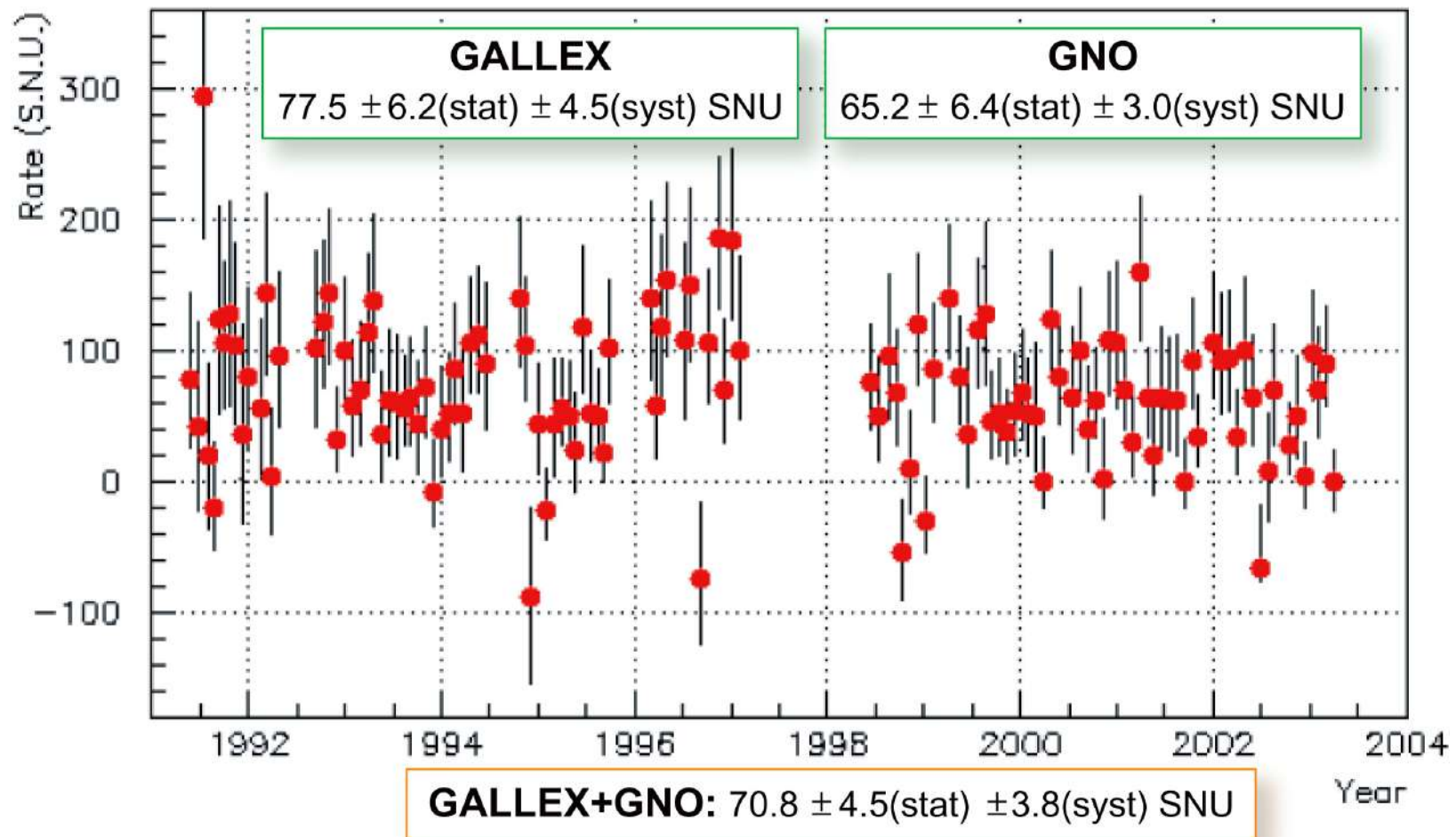
Single run results for GNO and GALLEX during a full solar cycle. Plotted is the net solar neutrino production rate in SNU after subtraction of side reaction contributions. Error bars are $\pm 1\sigma$, statistical only. [From M. Altmann *et al.* (GNO Collaboration), "Complete results for five years of GNO solar neutrino observations," Phys. Lett. B **616** (2005) 174–190, hep-ex/0504037.]

13 Water-Cherenkov neutrino detectors (Kamiokande and Super-Kamiokande).

Super-Kamiokande (SK), as well as its precursor Kamiokande (K), is an underground ring-imaging water-Cherenkov neutrino detector located in the Kamioka mine, Japan ($137.32°$ E longitude, $36.43°$ N latitude). SK is a cylindrical tank (41.4 m in height, 39.3 m in diameter) filled with 50 kton of ultra-pure water, and situated under about 1 km of rock (2700 m.w.e.). The rock provides a shield against the cosmic-ray muons: the muon count rate in the detector is reduced to 2.2. Hz.
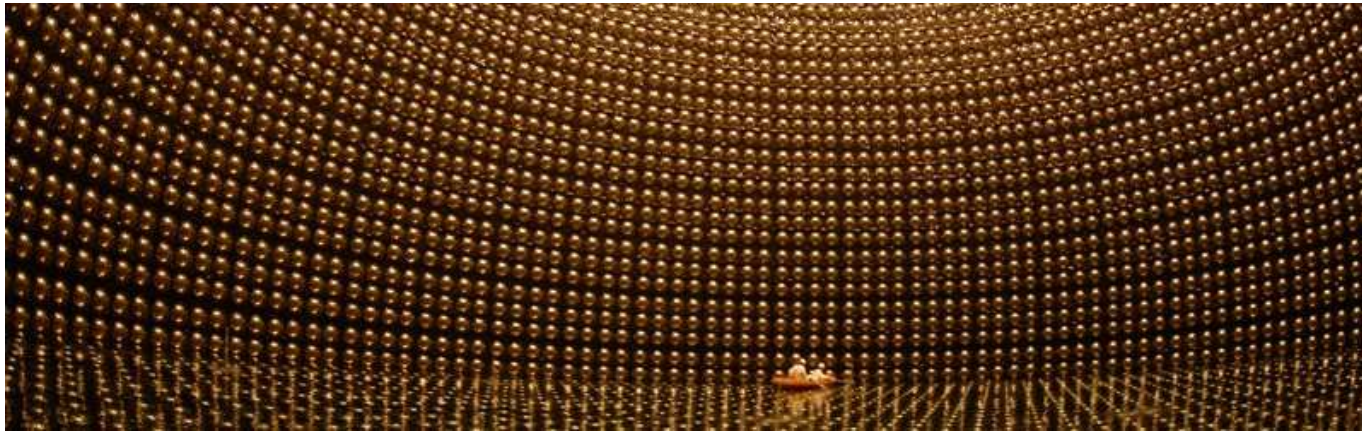
The outer walls of the tank are constructed from 5 cm thick stainless steel sheets, which are attached to the rock cavity and backed by concrete. About 2 m in from the walls is a 1 m wide structure of stainless beams that provide the backbone for the mounting PMTs. The structure divides the whole detector tank into an inner detector (ID) and outer detector (OD).

The 11,146 inward-facing ID PMTs that are used in event detection are mounted on the inside of the steel beam structure and are surrounded with black polyethylene sheets to minimize light reflection within the ID region. They provide a photo-coverage of 40%.

Electronics Huts

LINAC

Control Room

Inner Detector

Outer Detector

Water System

Mt. Ikeno
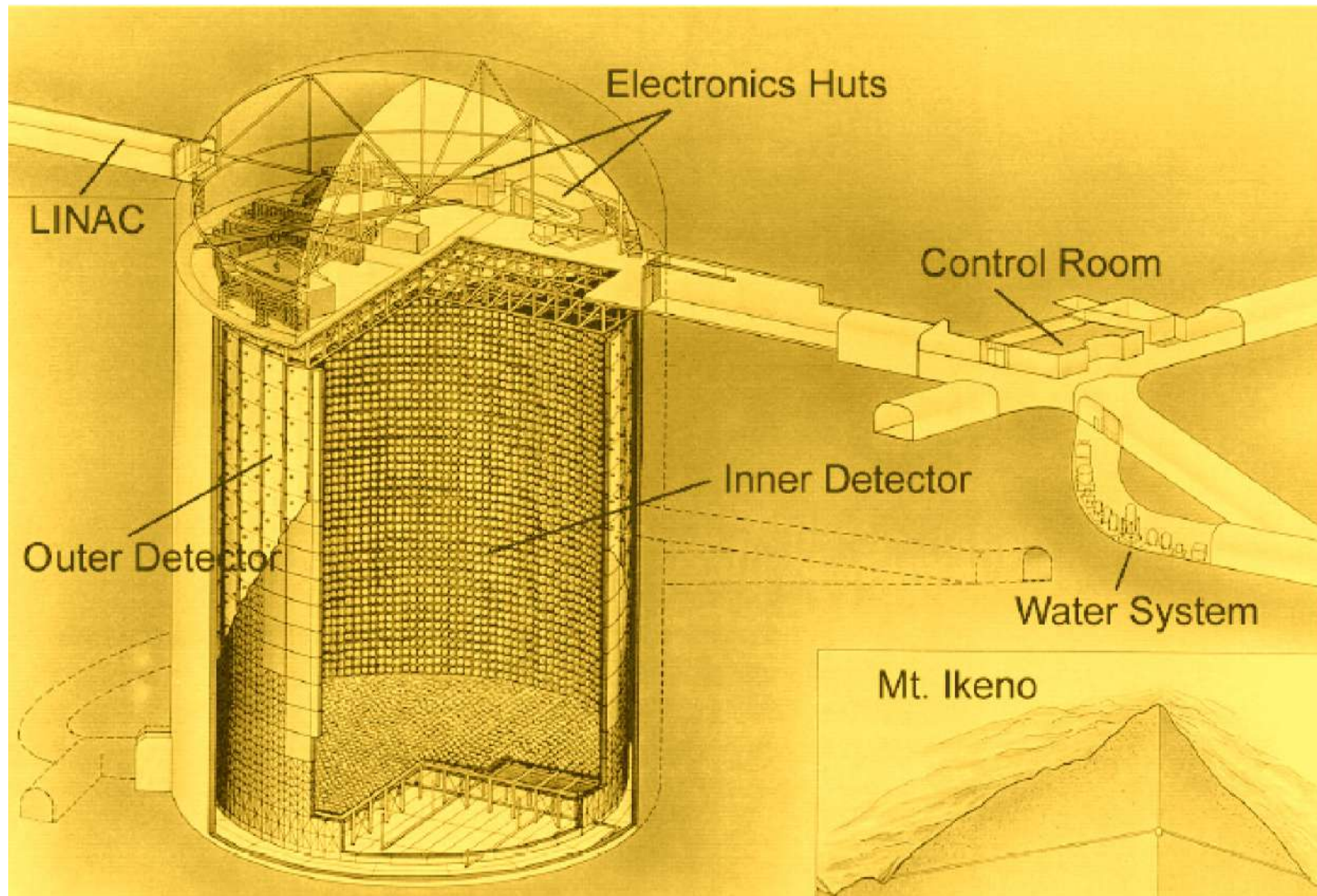
[This and next figures are borrowed from D. Turčan, "Solar neutrino at Super-Kamiokande solving the solar neutrino puzzle via neutrino flavor oscillations", Ph. D. Thesis, Faculty of the Graduate School, Maryland University, 2003.]
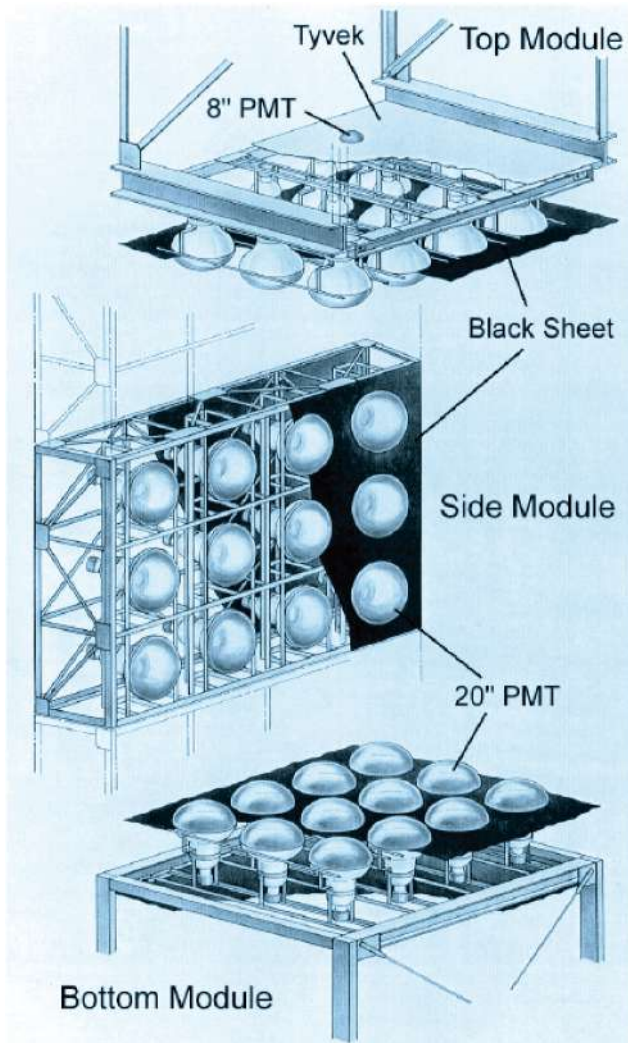
The entire ID region is a volume of 32.5 kt while the region actually used in the analysis is 2 m inside the PMT structure and represents a fiducial volume of 22.5 kt. There are at the least two reasons for excluding the 10 kt volume:

1) It is necessary to reduce the background from radioactive decays of radon which is particularly prominent near the PMTs and beams. The radon is still the main source of background in the fiducial volume, but the 2 m reduction brings the background to a manageable level.

2) There is a need for multiple PMT hits: if an event happens very near a PMT, all the light will be collected by that same PMT, and there will not be sufficient information for reconstructing that event. The PMTs used in SK's ID are 50 cm in diameter; they are largest PMTs in the world, designed and constructed especially for the SK experiment.

The OD, which surrounds the steel structure, has 1885 outward-facing 20 cm PMTs.

The top of the tank is a flat sheet that covers the entire are of the detector. It is under a dome, which lined with a polyurethane material ("Mineguard"), to reduce the radon emanation and erosion from the rock walls.

Cherenkov method of particle detection.

In a transparent medium with an index of refraction $n > 1$ the light velocity is $v_c = c/n < c$. When a charged particle traverses the medium with velocity $v > v_c$, the Cherenkov light is emitted in a cone of half angle $\theta_C = \arccos(c/nv)$ from the direction of the particle's track.
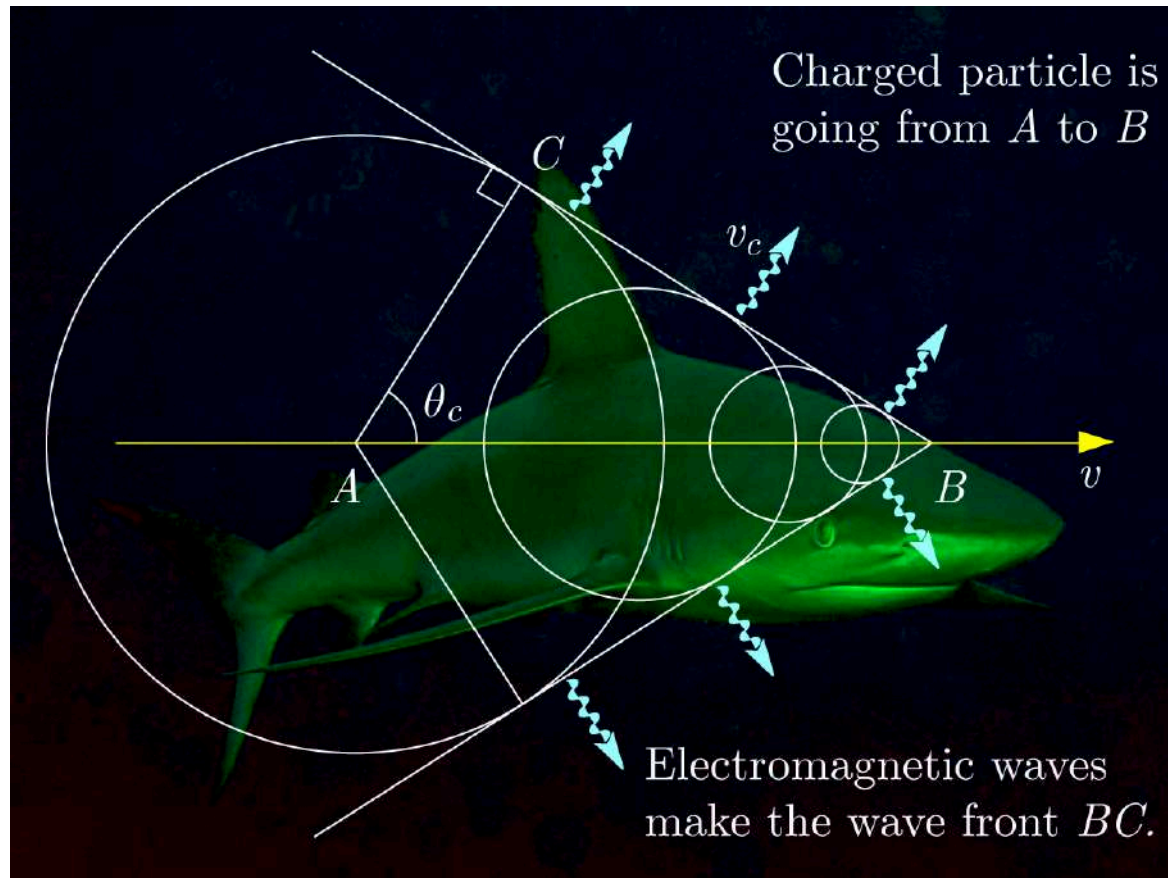
This may easily be understood from Huygens' principle:

$$AB/v = AC/v_c$$

$$\Downarrow$$

$$\cos\theta_C = AC/AB = v_c/v.$$

The refractive index of pure water is about 4/3 for a wavelength region 300 to 700 nm (where the PMTs are sensitive). Therefore the Cherenkov light is emitted by ultrarelativistic particles under about $42°$.

Charged particle is going from A to B

Electromagnetic waves make the wave front BC.

The number of photons produced along a flight path dx in a wave length bin $d\lambda$ for a particle carrying charge ze is

$$\frac{d^2 N_\gamma}{d\lambda dx} = \frac{2\pi\alpha z^2 \sin^2\theta_C}{\lambda^2},$$

where $\alpha \approx 1/137$ is the fine structure constant. The number of Cherenkov photons emitted per unit path length with wavelength between λ_1 and λ_2 is

$$\frac{dN_\gamma}{dx} = 2\pi\alpha z^2 \int_{\lambda_1}^{\lambda_2} \left[\frac{d^2 N_\gamma}{d\lambda dx}\right] \frac{d\lambda}{\lambda^2} \approx 2\pi\alpha z^2 \sin^2\theta_C \left(\frac{1}{\lambda_1} - \frac{1}{\lambda_2}\right)$$

(neglecting the dispersion of the medium). In particular, for the optical range (400–700 nm)

$$\frac{dN_\gamma}{dx} = \frac{491.3\, z^2 \sin^2\theta_C}{1\text{ cm}}.$$

A single charged particle emits about 214 (380) photons per 1 cm of the path length in water within the optical range (the PMT sensitive range).

For $v \approx c$ the Cherenkov light yield is independent of the energy of the charged particle. This means the light output of a single particle does not allow its energy to be measured.
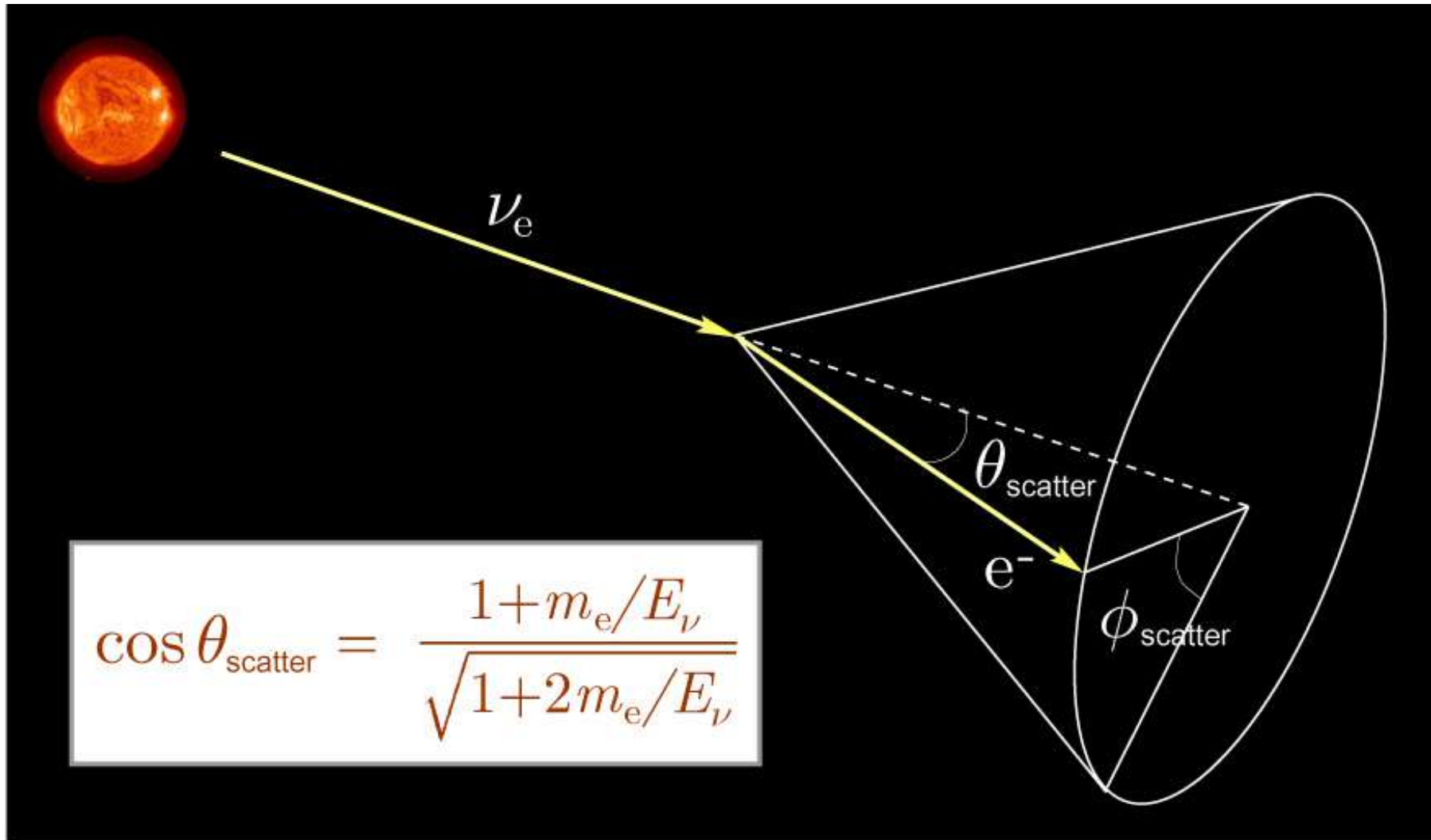
The energies E_C and momenta p_C of some particles with $v = v_c$ in water (Cherenkov thresholds) are shown in Table assuming $n(H_2O) = 1.33$).
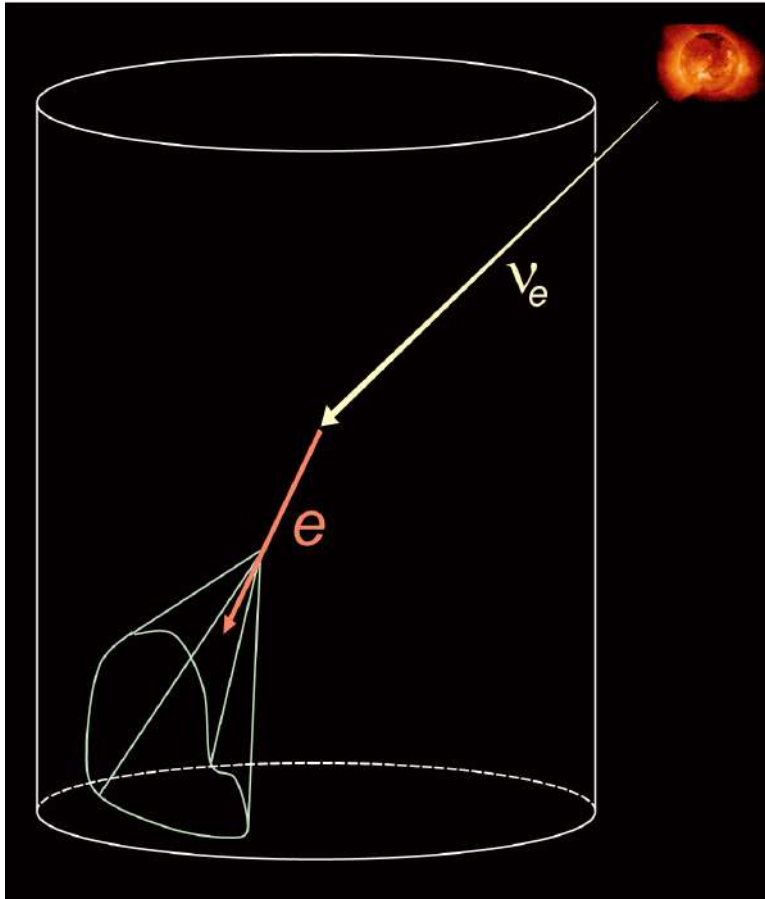
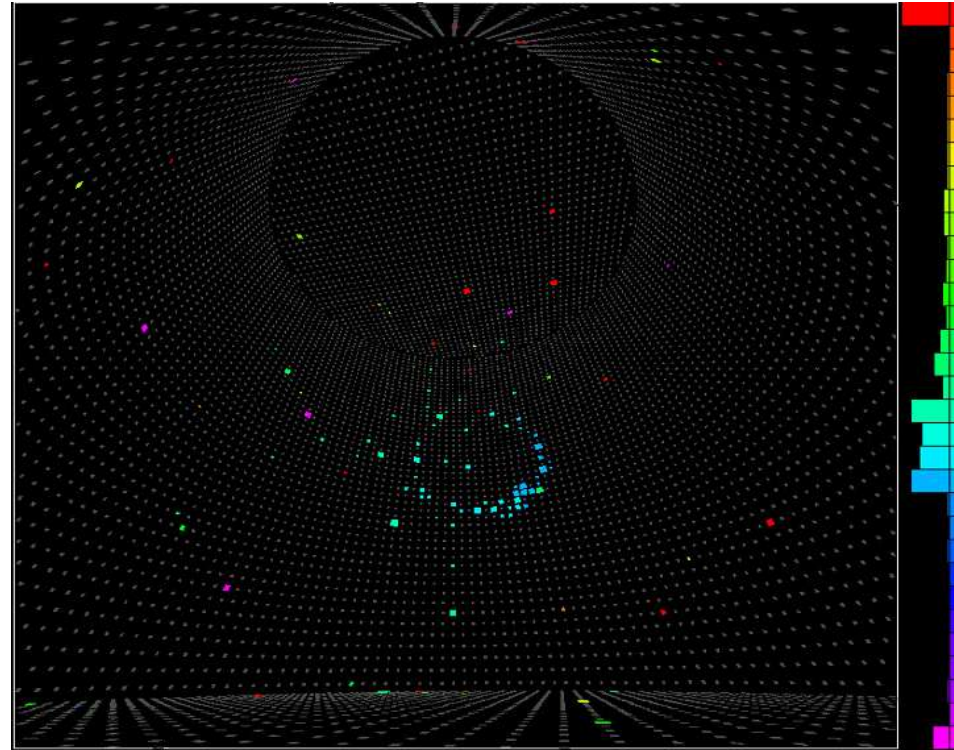| Particle	E_C (MeV)	p_C (MeV/c)
$e^\pm$	0.775	0.583
$\mu^\pm$	160.3	120.5
$\pi^\pm$	211.7	159.2
p	1423	1070
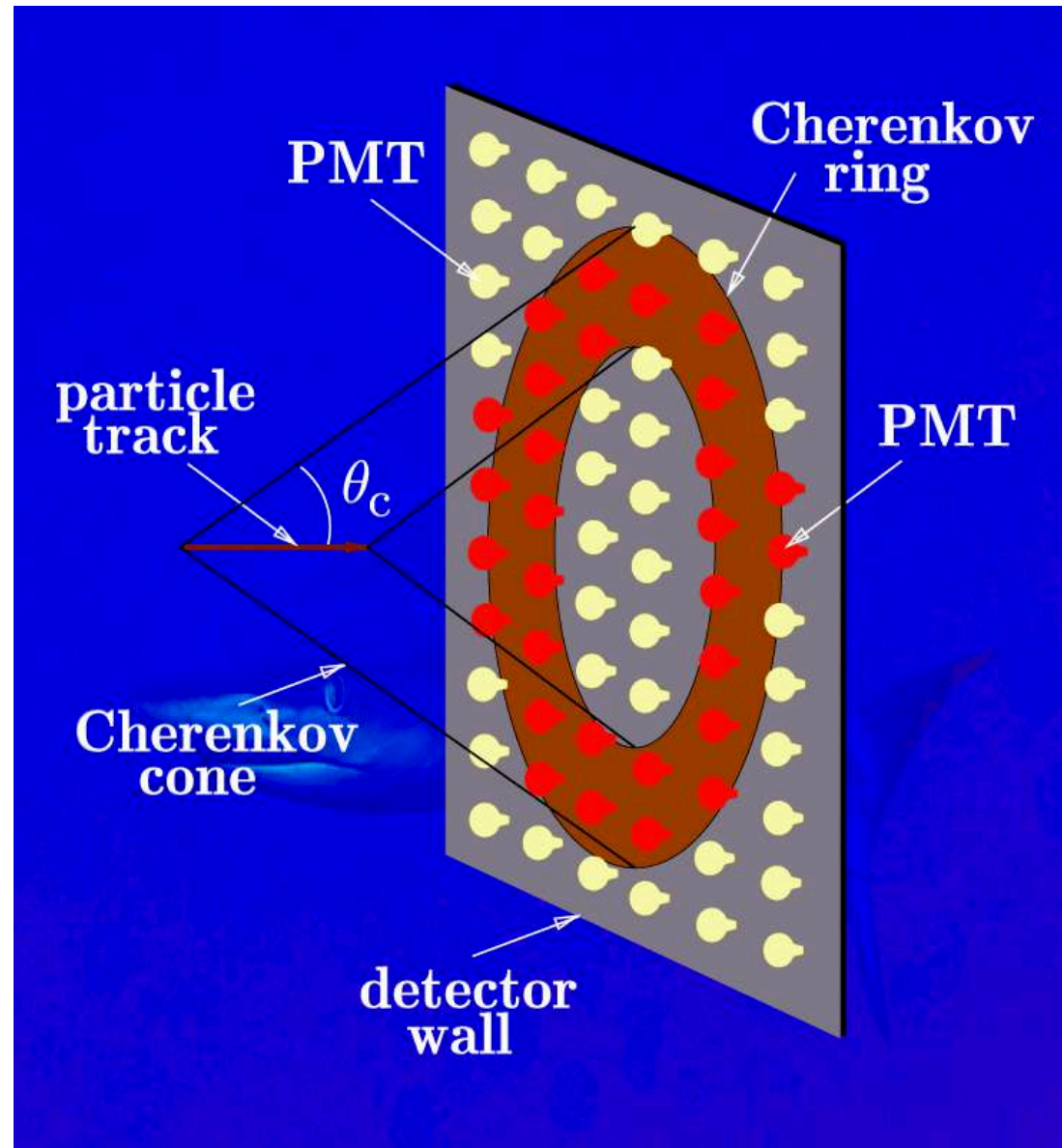
Cherenkov ring.

Solar event reconstruction method.

Super-Kamiokande uses elastic scattering of neutrinos from electrons. Cherenkov radiation emitted by the electron is detected by phototubes. The image looks like a diffuse ring on the detector walls.

A real event recorded in the Super-Kamiokande detector on 1998-03-12 14:08:40. It is about 12.5 MeV and has an unusually nice, well-defined ring. The color scale is time. This event was found by Mark Vagins.

[From I. Semeniuk, "Feature – Astronomy and the New Neutrino," Sky & Telescope, September 2004, pp. 42–48; see also Tomasz Barszczak, URL: ⟨http://www.ps.uci.edu/~tomba/sk/tscan/pictures.html⟩.]

Angular distribution of solar neutrino event candidates in Super-Kamiokande-I. ▷

The angular deviation between the true solar and reconstructed direction of events with total energies ranging between 5 and 20 MeV is shown. From the strong forward peak due to elastic scattering of solar ^8B neutrinos off
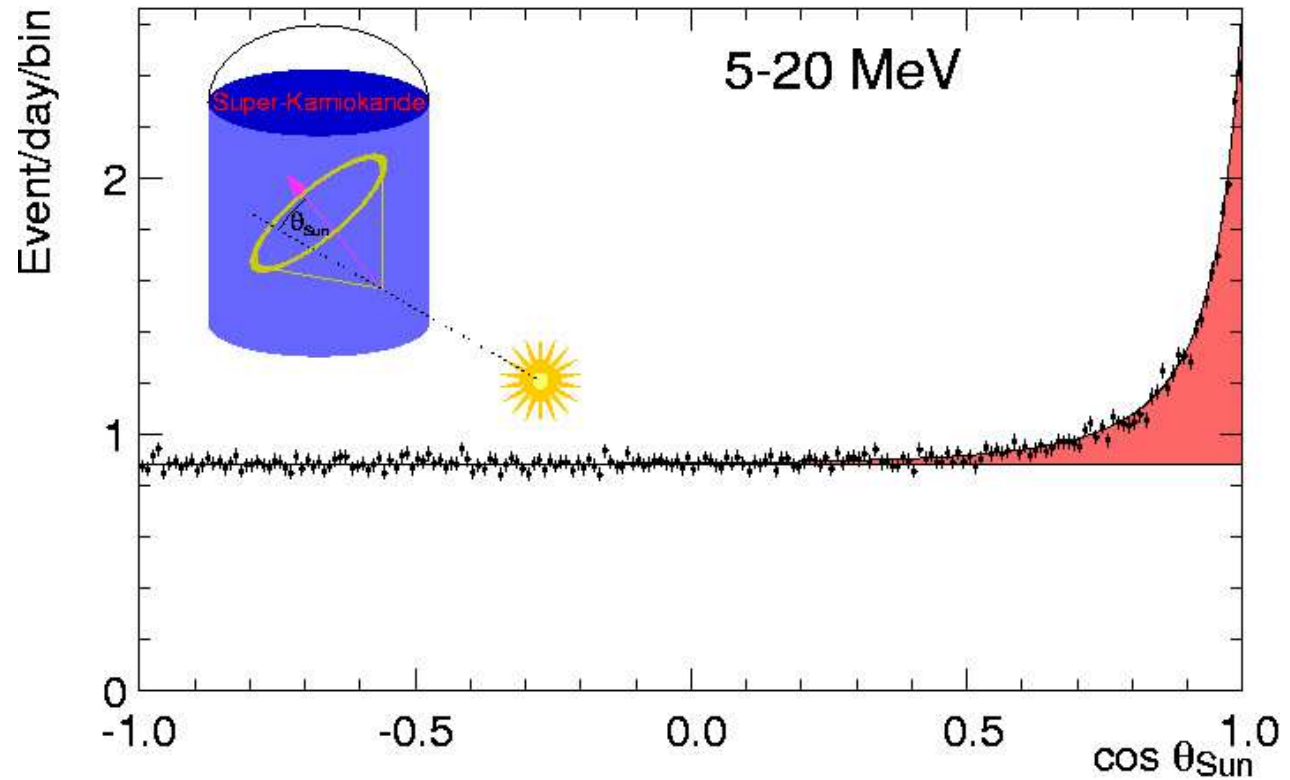
electrons $22,400 \pm 200_{\text{stat}}$ neutrino interactions were observed in 22,500 metric tons of water of the SK tank during 1496 live days. The observed solar neutrino interaction rate is $0.465 \pm 0.005^{+0.016}_{-0.015}$ of the rate expected by the standard solar model (SSM). Assuming only solar ν_e the observed rate corresponds to a ^{8}B flux of

$$\Phi\left(^8\text{B}\right) = (2.35 \pm 0.02_{\text{stat}} \pm 0.08_{\text{syst}}) \times 10^6 \text{ cm}^{-2}\text{s}^{-1}.$$

All uncertainties given for the time variation data are only statistical and based on an asymmetric Gaussian approximation of the underlying likelihood functions obtained by an unbinned maximum likelihood fit to the $\cos\left(\theta_{\text{Sun}}\right)$ distributions.

Seasonal variation of the solar neutrino flux.

Time variation of the SN flux scaled by the SSM prediction.

▷

The curves represent the expected flux modulation due to the eccentricity of the Earth's orbit. The SK data are as of December 2002. The top two panels show the Super-Kamiokande-I rate as a function of time. The topmost panel uses bins of 10 days width, the middle panel displays 45 day bins. The lower left panel combines the 10-day bins into 12 bins to show the yearly cycle assuming asymmetric Gaussians for the probability density functions.
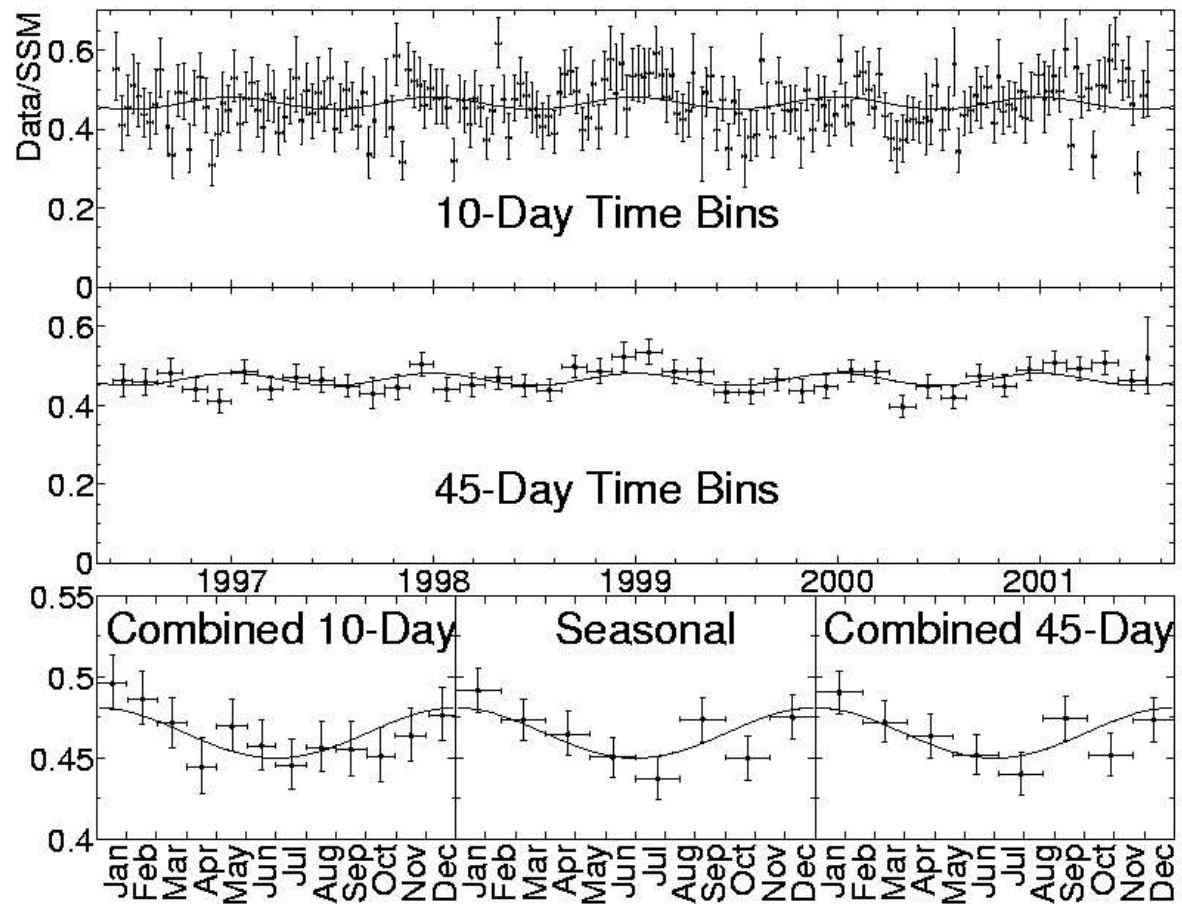
The lower right panel shows the yearly variation data in 8 bins obtained from a similar combination of the 45-day data bins. The middle right panel is the yearly variation data in those same 8 bins, but resulting directly from a maximum likelihood fit to the $\cos(\theta_{Sun})$ distribution.

Possible signatures of the solar neutrino oscillations.

1. Reduction of the event rate.

Because of the oscillation, the number of ν_e reduces while the number of ν_μ and ν_τ increases.
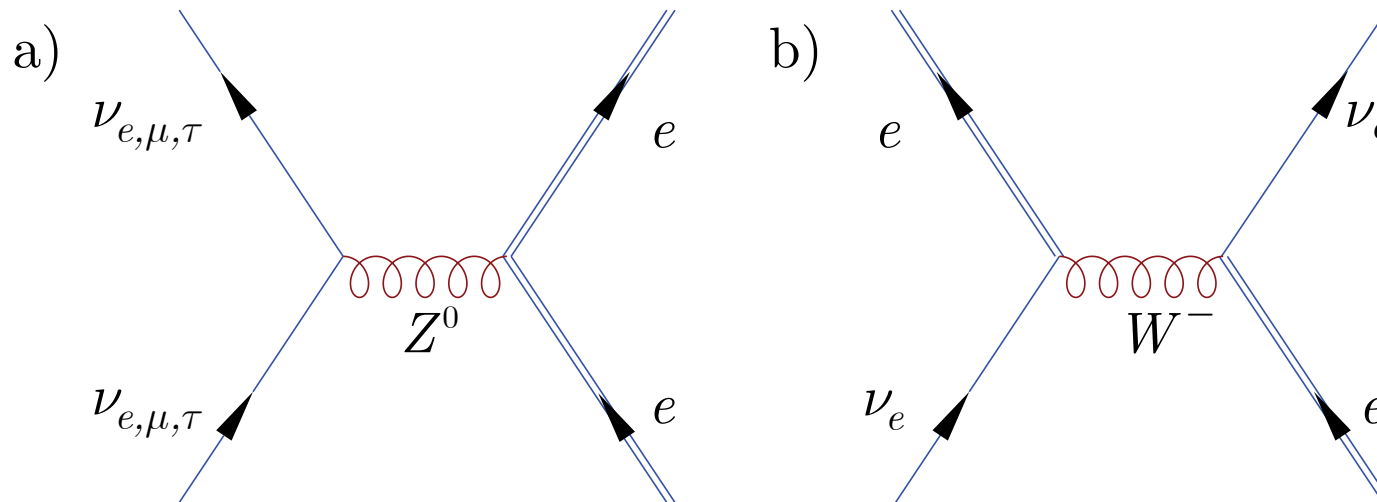
Interaction cross sections at $E_\nu = 10$ MeV are

$$\sigma\left(\nu_e + e^- \to \nu_e + e^-\right) \approx 9.5 \times 10^{-44} \text{ cm}^2,$$

$$\sigma\left(\nu_{\mu,\tau} + e^- \to \nu_{\mu,\tau} + e^-\right) \approx 1.6 \times 10^{-44} \text{ cm}^2,$$

Due to the difference of the cross sections, the observed number of events is reduced.

2. Day/Night event rate difference.

When the neutrino goes through the Earth, the oscillation probability is affected by the MSW effect.
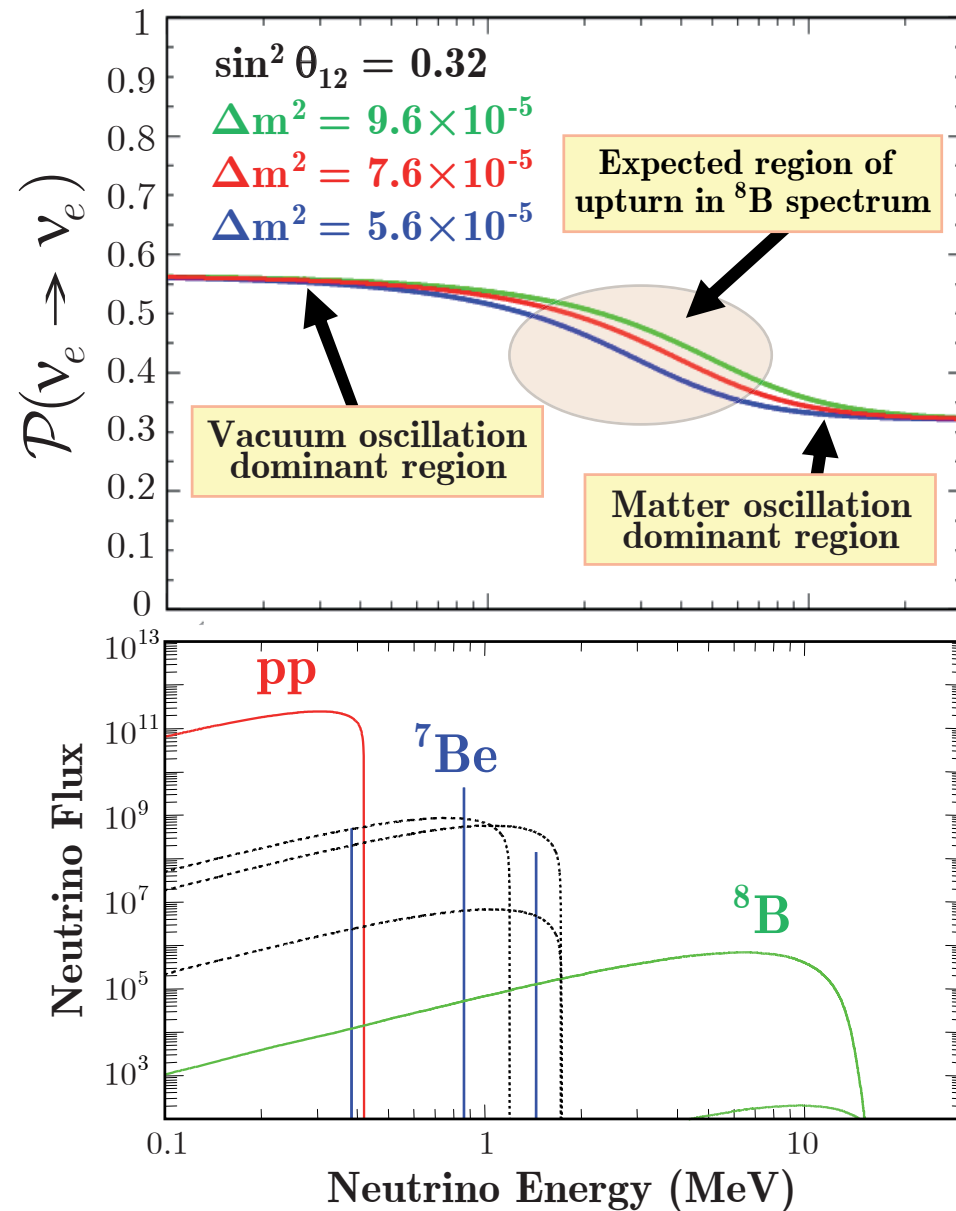
3. Gradual change of the oscillation effect.

Transition from the matter effect dominant region to the vacuum oscillation dominant region could be observed by lowering the energy threshold. It would be a crucial test for the MSW effect.

SK4 needs to reduce background events and systematic uncertainties. Study is going on and collecting data with the SK4 detector.

The Figure on the right is from Yoshinari Hayato's report.

The issue was resolved in the Borexino experiment in 2018,

$\sin^2 \theta_{12} = 0.32$
$\Delta m^2 = 9.6 \times 10^{-5}$
$\Delta m^2 = 7.6 \times 10^{-5}$
$\Delta m^2 = 5.6 \times 10^{-5}$

Expected region of upturn in ^{8}B spectrum

Vacuum oscillation dominant region

Matter oscillation dominant region

$\mathcal{P}(\nu_e \to \nu_e)$

pp

^{7}Be

^{8}B

Neutrino Flux

Neutrino Energy (MeV)

196

14 D_2O detector SNO.

SNO is a 1 ktonne water Cherenkov detector, located at a depth of 2092 m (6010 m of water equivalent) in the INCO Ltd. Creighton mine near Sudbury, Ontario in Canada.

The detector consists of a 5.5 cm thick, 12 m diameter acrylic vessel (AV), holding the 1000 t ultra-pure D_2O target, surrounded by 7 kt of ultra-pure H_2O shielding.

The AV is surrounded by a 17.8 m diameter geodesic sphere, holding 9456 inward-looking and 91 outward-looking 20 cm photomultiplier tubes (PMTs).

Figure shows a view of the SNO detector after installation of the bottom PMT panels, but before cabling (photo by Ernest Orlando, Lawrence Berkeley National Laboratory).
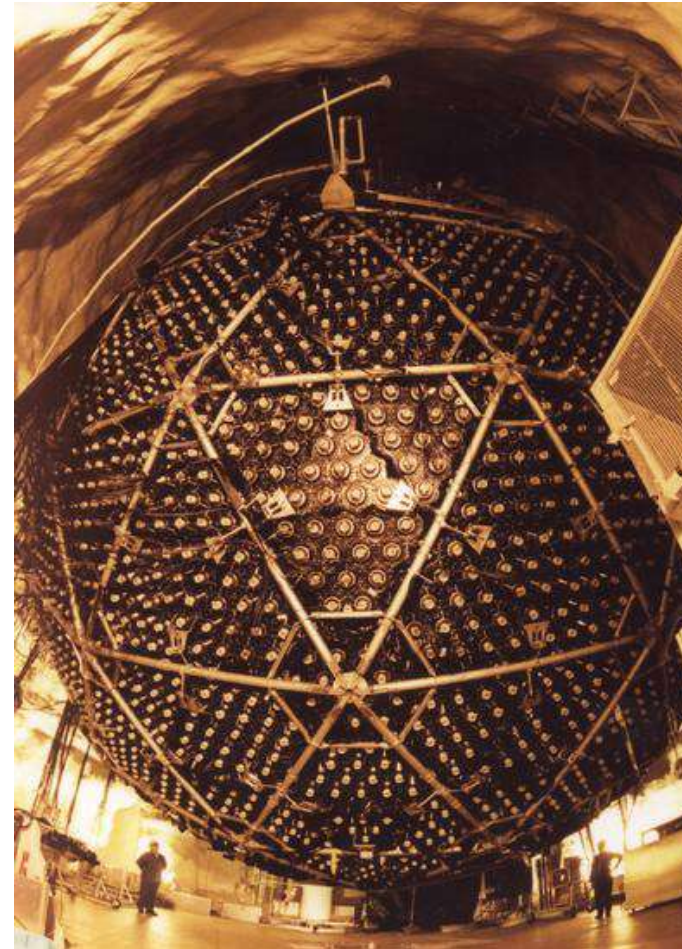
[From The Sudbury Neutrino Observatory webpage, $\langle$ http://www.sno.phy.queensu.ca/sno/ $\rangle$.]

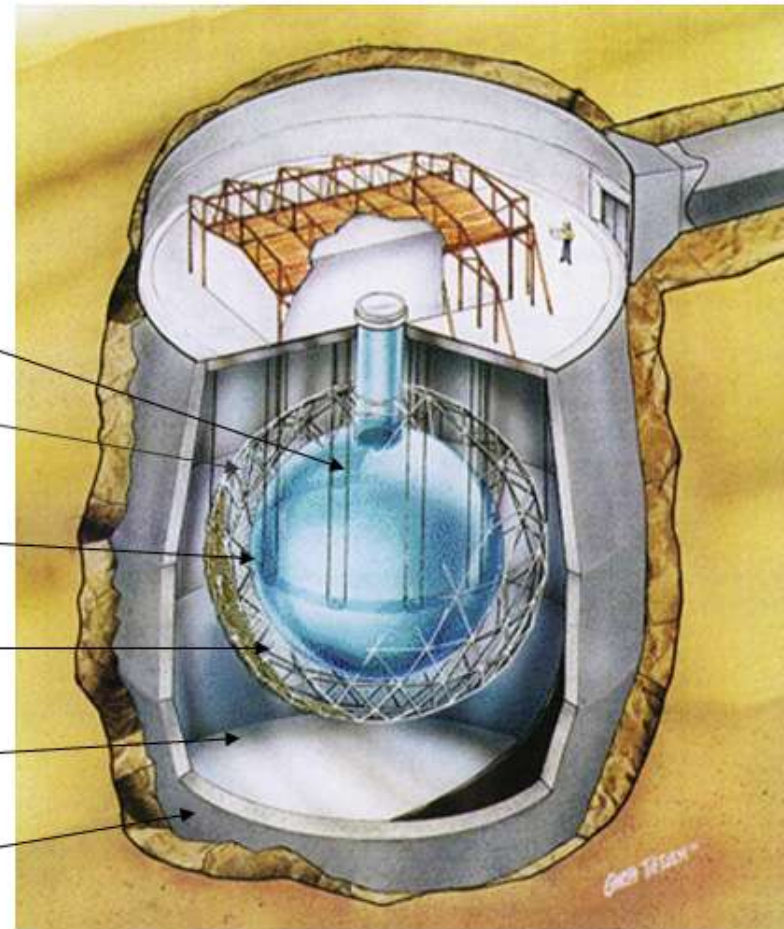# Sudbury Neutrino Observatory
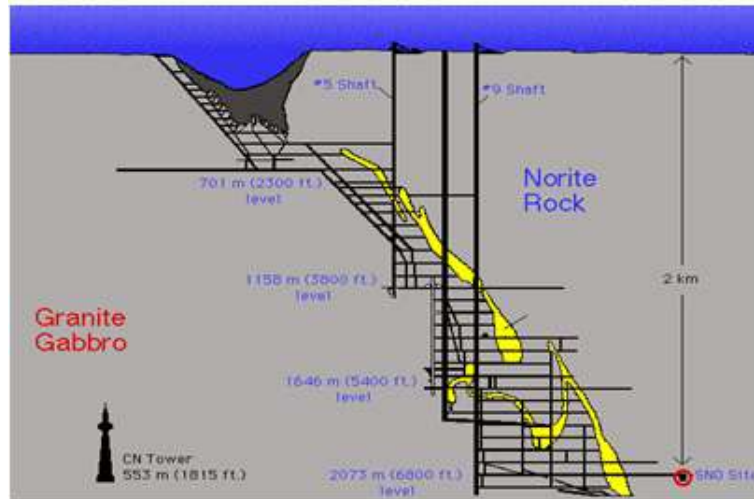
1000 tonnes D_2O

Support Structure for 9500 PMTs, 60% coverage
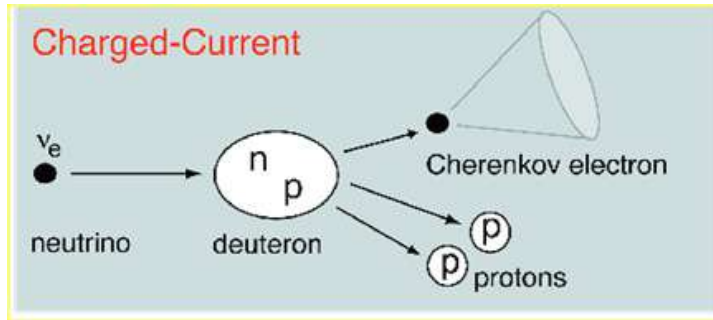
12 m Diameter Acrylic Vessel

1700 tonnes Inner Shielding H_2O

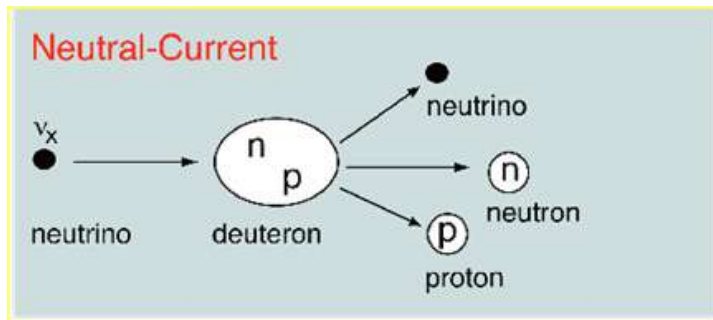5300 tonnes Outer Shield H_2O

Urylon Liner and Radon Seal

198

Unique signatures in SNO
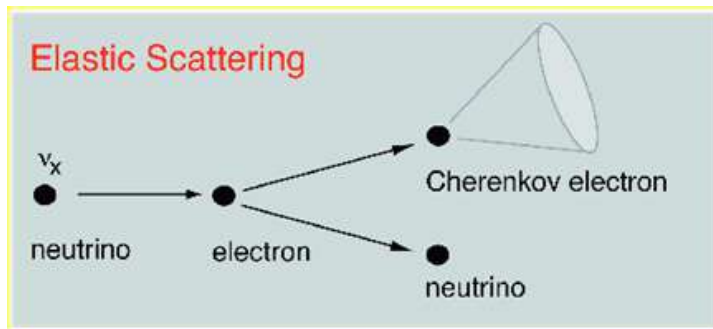

Charged Current (CC) interaction:

$$\nu_e + d \to e^- + p + p$$

$E_\nu^{\text{th}} = 1.44$ MeV. Allows detecting of ν_e only.

Neutral Current (NC) interaction:

$$\nu_\alpha + d \to \nu_\alpha + n + p$$

$E_\nu^{\text{th}} = 2.22$ MeV. Equally sensitive to all neutrinos.

Elastic Scattering (ES):

$$\nu_\alpha + e^- \to \nu_\alpha + e^-$$

$E_\nu^{\text{th}} = 6.75$ MeV. Sensitive to all active neutrinos but enhanced for ν_e.
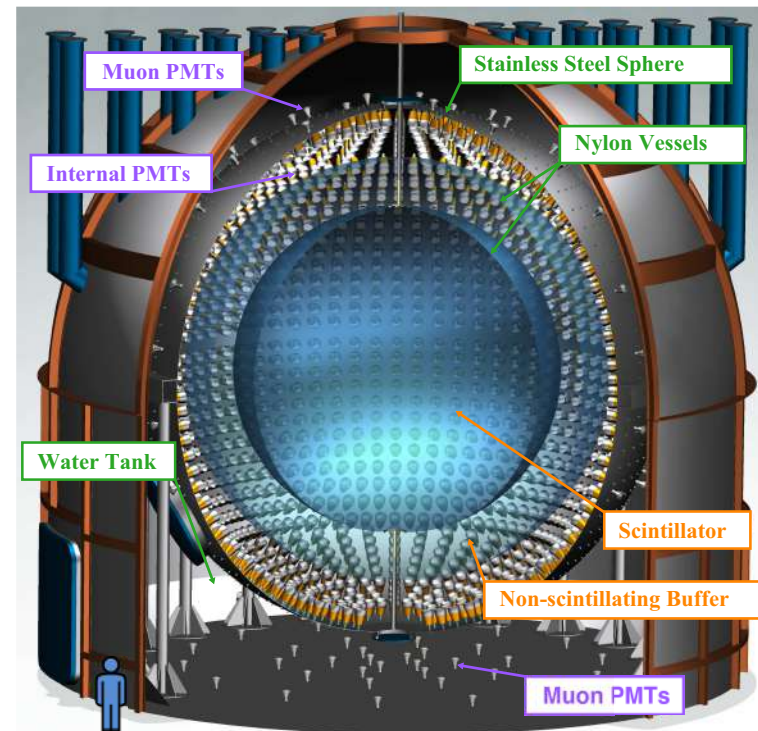
15   BOREXINO.

Borexino (the small Boron Experiment) is a part of the *Laboratori Nazionali del Gran Sasso* (LNGS), inside the Gran Sasso mountain, Abruzzo, Italy. The mountain shields the LNGS experiments from outside radiation, allowing to study rare interactions involving neutrinos and other particles. The experiment uses boron-loaded scintillators to measure the flux of solar neutrinos due to ^{7}Be electron captures. It is a multipurpose experiment performed by an international collaboration. Its physics program is centered on solar neutrino physics, but also includes other relevant topics in low-background neutrino detection and underground physics.

The Borexino detector is a real time detector for low energy (sub-MeV) solar neutrinos, with the specific goal of measuring the ^{7}Be neutrino flux from the Sun. The very low energy experimental threshold (250 keV) requires extreme radiopurity of the detector.

A Borexino prototype, called Counting Test Facility (CTF) was built and operated in LNGS Hall C. CTF demonstrated the achievement of ultralow count rates (radiopurities of $\sim 10^{-16}$ gr/gr of ^{238}U equivalent) on the several-ton scale. The Borexino detector was built on the CTF experience. The first data acquisition (DAQ) run with the full detector was started on May 16, 2007. By now (2021), Borexino has completed its main tasks and solved many other burning problems in neutrino physics.
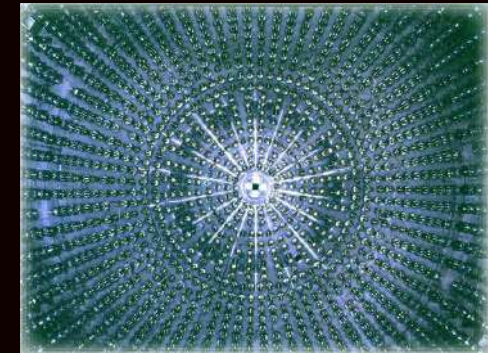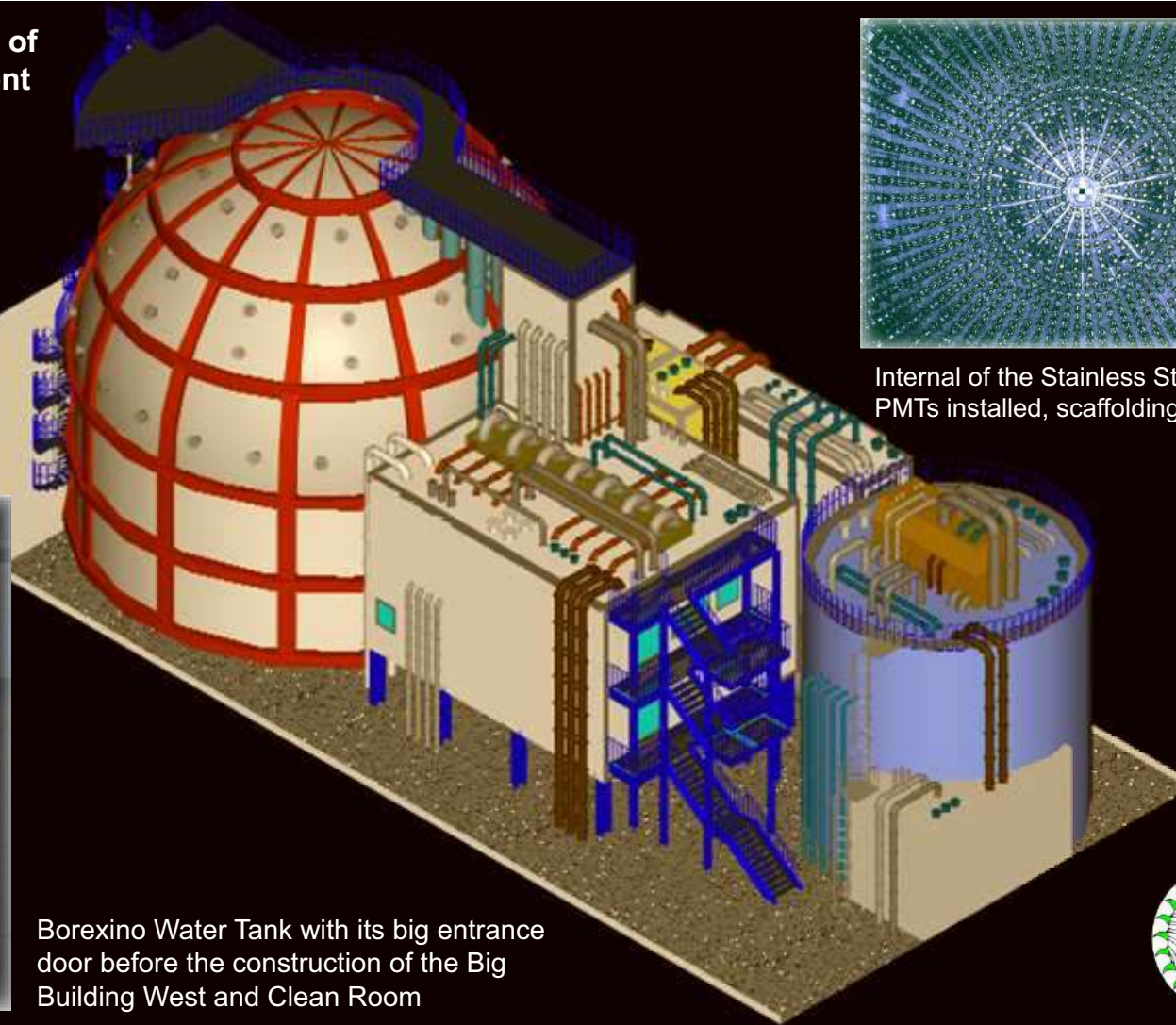
[For more detail, see M. Agostini *et al*. (Borexino Collaboration). "Comprehensive measurement of pp-chain solar neutrinos," Nature **562** (2018) 505–510 and references therein.]

The major components of the Borexino experiment in Hall C, earlier stage

Internal of the Stainless Steel Sfere. PMTs installed, scaffoldings removed

Borexino Water Tank with its big entrance door before the construction of the Big Building West and Clean Room

From left to right: the Borexino water tank; the "Big Building" (East and West) which house the control room, DAQ, and portions of the purification system; the purification skids; the CTF detector.
[From Ch. Ghiano, "Measurement of the neutrino charged current interaction rate on ^{13}C in Borexino," (Ph.D. Thesis, Thesis, Universitá degli Studi dell'Aquila, 2011).]

Modern view of the Borexino complex at Hall C.

The Borexino experiment in LNGS detects light produced when solar νs scatter off electrons in a large vat of liquid scintillator — a medium that produces light in response to the passage of charged particles. The detector is wrapped in thermal insulation to control its temperature variations.

Modern view of the Borexino neutrino detector.

[From G. D. Orebi Gann, "Neutrino detection gets to the core of the Sun," Nature **587** (2020) 550–551.]

Results of the Borexino Phase-I–III solar neutrino analyses.

The rates and fluxes are integral values without any threshold; the first error is statistical, the second systematic. The rate-to-flux conversion uses the global-fit oscillation parameters by Capozzi *et al.* (2018). The last two columns show the fluxes as predicted by the HZ- and LZ-SSM. The fluxes of *pp*, ^{7}Be, *pep*, CNO, ^{8}B, and *hep* νs are normalized to 10^{10}, 10^9, 10^8, 10^8, 10^6, and 10^3, respectively.[a]

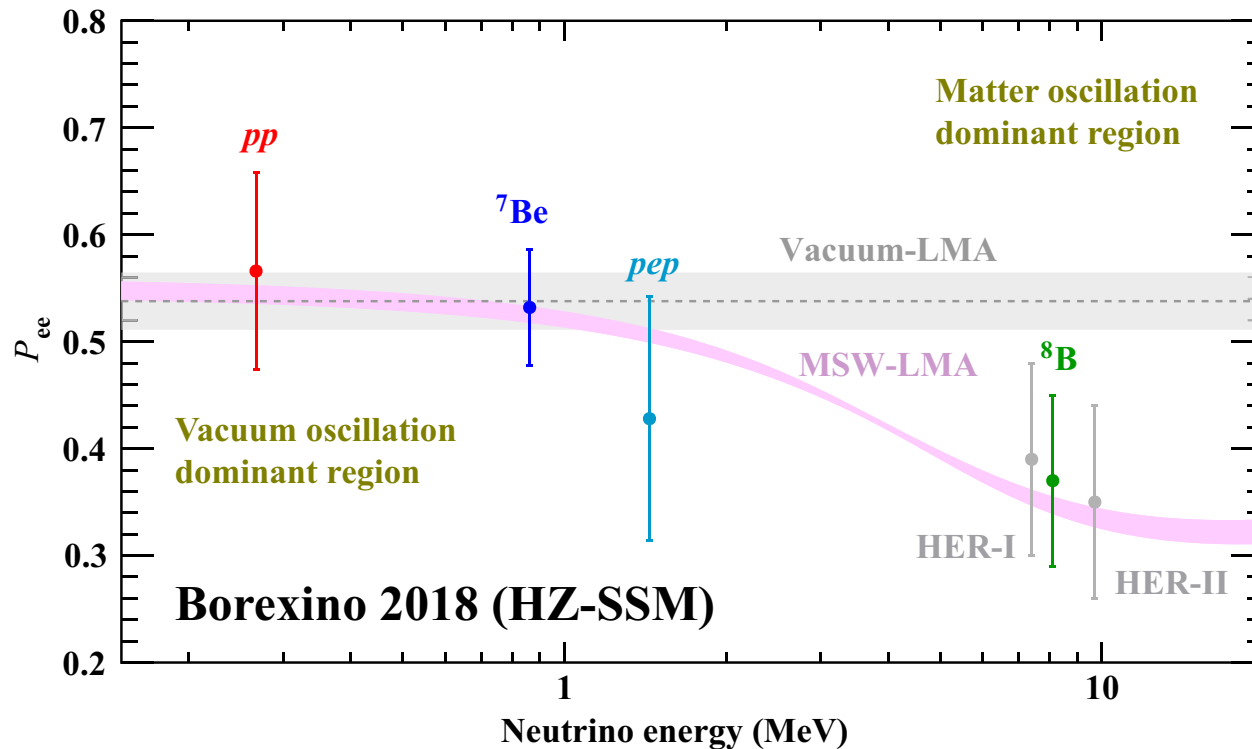| Solar neutrinos	Rate	Flux	HZ-SSM Flux	LZ-SSM Flux
	(cpd/100 ton)	(cm^{-2}s^{-1})	(cm^{-2}s^{-1})	(cm^{-2}s^{-1})
Phase-II (12/2011 − 05/2016)				
pp	$134 \pm 10^{+6}_{-10}$	$(6.1 \pm 0.5^{+0.3}_{-0.5})$	$5.98(1.0 \pm 0.006)$	$6.03(1.0 \pm 0.006)$
^{7}Be	$48.3 \pm 1.1^{+0.4}_{-0.7}$	$(4.99 \pm 0.11^{+0.06}_{-0.08})$	$4.93(1.0 \pm 0.06)$	$4.50(1.0 \pm 0.06)$
pep (HZ)	$2.43 \pm 0.36^{+0.15}_{-0.22}$	$(1.27 \pm 0.19^{+0.08}_{-0.12})$	$1.44(1.0 \pm 0.01)$	$1.46(1.0 \pm 0.009)$
pep (LZ)	$2.65 \pm 0.36^{+0.15}_{-0.24}$	$(1.39 \pm 0.19^{+0.08}_{-0.13})$	$1.44(1.0 \pm 0.01)$	$1.46(1.0 \pm 0.009)$
CNO	<8.1 (95% C.L.)	<7.9 (95% C.L.)	$4.88(1.0 \pm 0.11)$	$3.51(1.0 \pm 0.10)$
Phase-I + II (01/2008 − 12/2016)				
^{8}B$_{\text{HER-I}}$	$0.136^{+0.013+0.003}_{-0.013-0.013}$	$(5.77^{+0.56+0.15}_{-0.56-0.15})$	$5.46(1.0 \pm 0.12)$	$4.50(1.0 \pm 0.12)$
^{8}B$_{\text{HER-II}}$	$0.087^{+0.080+0.005}_{-0.010-0.005}$	$(5.56^{+0.52+0.33}_{-0.64-0.33})$	$5.46(1.0 \pm 0.12)$	$4.50(1.0 \pm 0.12)$
^{8}B$_{\text{HER}}$	$0.223^{+0.015+0.006}_{-0.016-0.006}$	$(5.68^{+0.39+0.03}_{-0.41-0.03})$	$5.46(1.0 \pm 0.12)$	$4.50(1.0 \pm 0.12)$
Phase-I (part) + II + III (part) (11/2009 − 10/2017)				
hep	<0.002 (90% C.L.)	<180 (90% C.L.)	$7.98(1.0 \pm 0.30)$	$8.25(1.0 \pm 0.12)$
Phase-III (07/2016 − 02/2020)				
CNO	$7.2^{+3.0}_{-1.7}$	$(7.0^{+3.0}_{-2.0})$	$4.88(1.0 \pm 0.11)$	$3.51(1.0 \pm 0.10)$

[a] Borrowed from S. Kumaran, L. Ludhova, Ö. Penek, and G. Settanta, "Borexino results on neutrinos from the Sun and Earth," Universe **7** (2021) 231, arXiv:2105.13858 [hep-ex]. Abbreviations, used here and below: HZ = High Metallicity, LZ = Low Metallicity, cpd = counts per day, HER = High Energy Range.
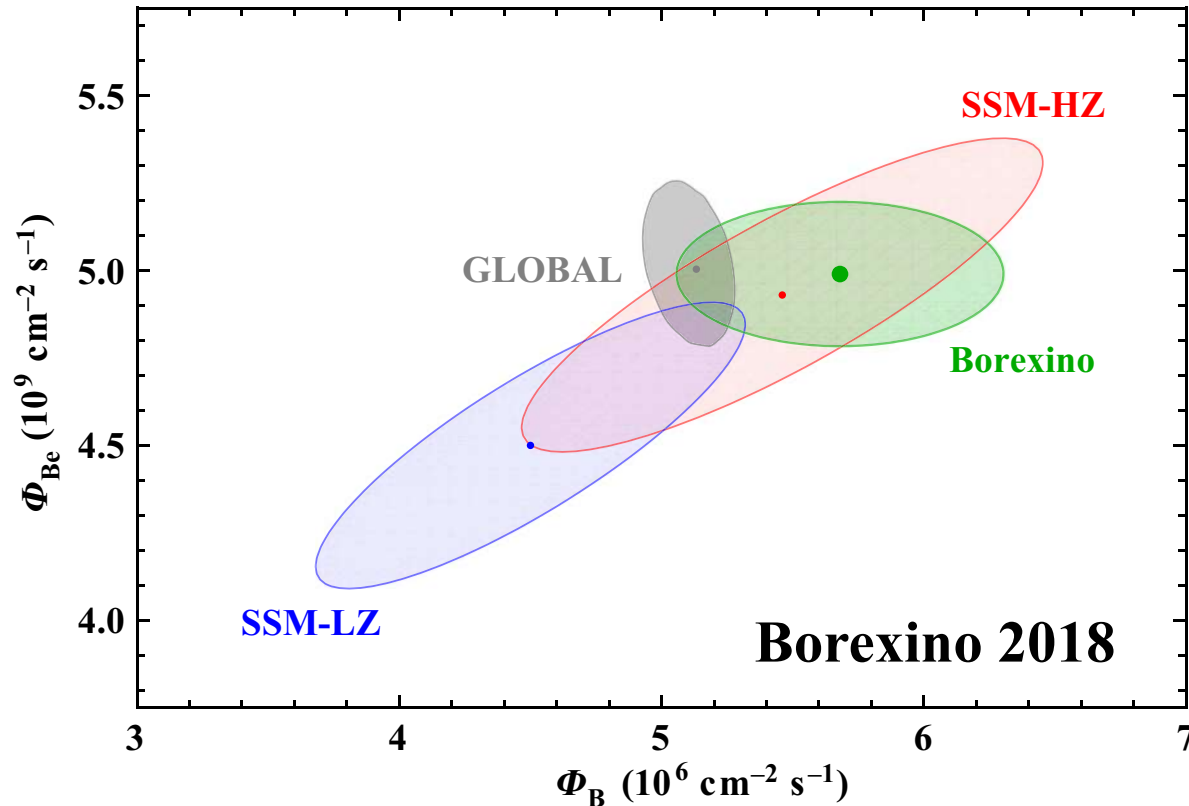
The Borexino results are compatible with the temperature profiles predicted by both HZ- and LZ-SSMs. However, the ^{7}Be and ^{8}B solar ν_e fluxes measured by Borexino provide an interesting hint in favor of the HZ-SSM prediction. However, this hint weakens when the Borexino data are combined with data of all other solar ν_e experiments + KamLAND reactor $\overline{\nu}_e$ data.

Borexino results and analysis in the $\Phi_{^7\mathrm{Be}} - \Phi_{^8\mathrm{B}}$ space. Borexino results for ^{7}Be and ^{8}B neutrino fluxes (green point and shaded area). Allowed contours in the $\Phi_{^7\mathrm{Be}} - \Phi_{^8\mathrm{B}}$ space are obtained by combining these new results with all solar and KamLAND data in a global analysis, and leaving free the oscillation parameters θ_{12} and Δm_{12}^2 (grey ellipse, marked as GLOBAL). The theoretical predictions for the low-metallicity (LZ) (blue) and the high-metallicity (HZ) (red) SSMs are also shown. The fit returns the following oscillation parameters: $\tan^2 \theta_{12} = 0.47 \pm 0.03$ and $\Delta m_{12}^2 = (7.5 \pm 10^5) \pm 0.03$. All contours correspond to $68.27\,\%$ C.L.

[From M. Agostini *et al.* (Borexino Collaboration). "Comprehensive measurement of pp-chain solar neutrinos," Nature **562** (2018) 505–510; see also reference in footnote of p. 204.]

Matter oscillation dominant region

Vacuum-LMA

MSW-LMA

Vacuum oscillation dominant region

Borexino 2018 (HZ-SSM)

HER-I

HER-II

pp

^{7}Be

pep

^{8}B

P_{ee}

Neutrino energy (MeV)

Measured ν_e survival probabilities are

$P_{ee}\,(pp,\,0.267\,\mathrm{MeV})\;=\;0.57\pm0.09,$

$P_{ee}\left(^7\mathrm{Be},\,0.862\,\mathrm{MeV}\right)\;=\;0.53\pm0.05,$

$P_{ee}\,(pep,\,1.44\,\mathrm{MeV})\;=\;0.43\pm0.11,$

$P_{ee}\left(^8\mathrm{B_{HER\text{-}I}},\,7.4\,\mathrm{MeV}\right)\;=\;0.39\pm0.09,$

$P_{ee}\left(^8\mathrm{B_{HER}},\,8.1\,\mathrm{MeV}\right)\;=\;0.37\pm0.08,$

$P_{ee}\left(^8\mathrm{B_{HER\text{-}II}},\,9.7\,\mathrm{MeV}\right)\;=\;0.35\pm0.09.$

Electron neutrino survival probability $P_{ee} \equiv \mathcal{P}\left(\nu_e \to \nu_e\right)$ as a function of neutrino energy. The pink band is the $\pm1\sigma$ prediction of MSW-LMA while the grey band represents the vacuum-LMA solution. Data points show the Borexino 2018 results for pp, ^{7}Be, pep, and ^{8}B (green for the HER range, and grey for the separate HER-I and HER-II sub-ranges), assuming HZ-SSM. The ^{8}B and pp data points are set at the mean energy of neutrinos that produce scattered electrons above the detection threshold. The quoted error bars include experimental and theoretical uncertainties.

Borexino data disfavors the vacuum-LMA hypothesis at 98.2 % C.L. and are in excellent agreement with the expectations from the MSW-LMA paradigm.

[From M. Agostini *et al.* (Borexino Collaboration). "Comprehensive measurement of pp-chain solar neutrinos," Nature **562** (2018) 505–510; see also reference in footnote of p. 204.]

Borexino 2017

$$R(t) = R_0 + \overline{R}\left[1 + \epsilon \cos \frac{2\pi}{T}(t - \phi)\right]^2$$
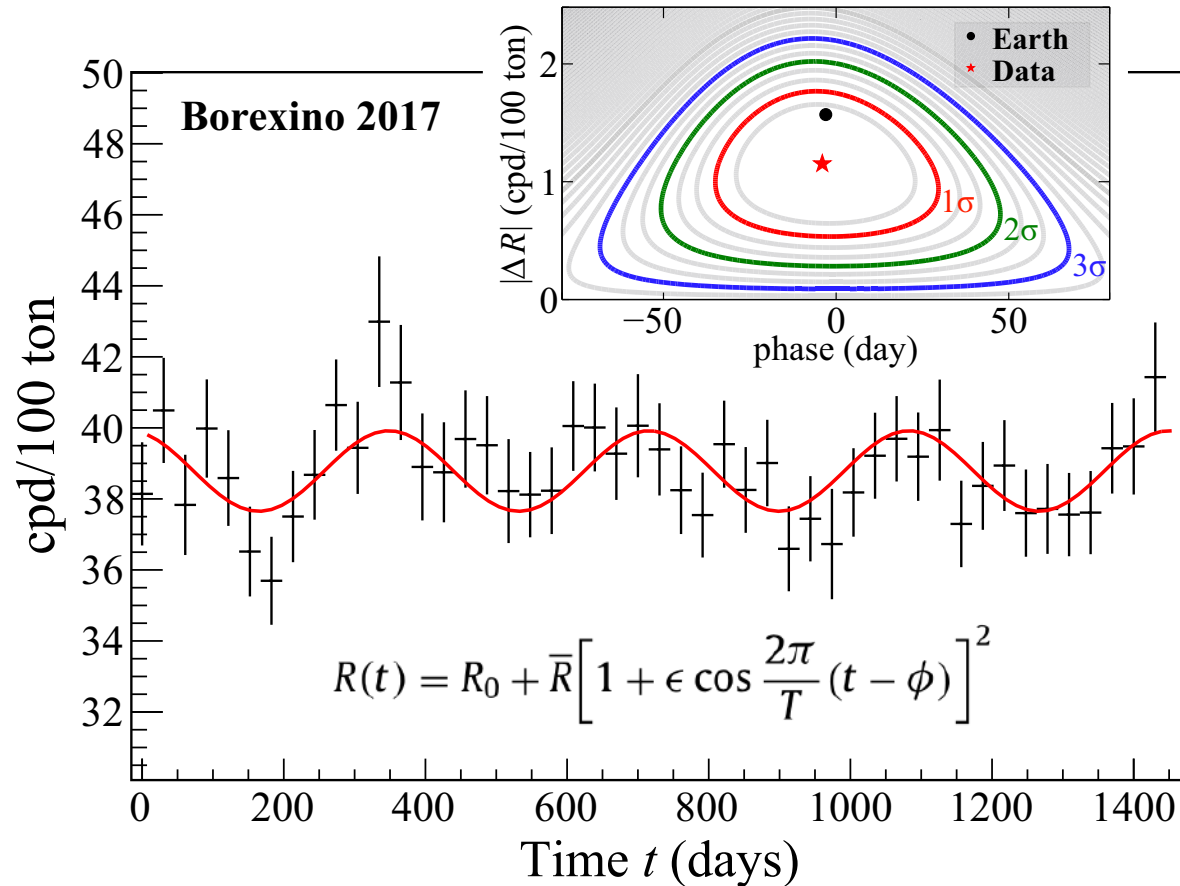
Borexino was able to measure the annual modulation of solar neutrinos with high significance, confirming the solar origin of the measured ^{7}Be signal. The fit values for the modulation periodicity and its amplitude obtained with three different analytical approaches are well consistent with each other and with the expectations.

Borexino rejected the hypothesis of no modulation with a confidence level of 99.99%.

Borexino Phase-II rate of β-like events passing selection cuts in 30.43-days long bins starting from Dec. 11, 2011. The red line is resulting function from the fit with the equation shown in the figure, where $\epsilon = 0.0167$ is the Earth orbital eccentricity, $T = 1$ year is the period, ϕ is the phase relative to the perihelion, $\overline{R}$ is the average neutrino interaction rate, and R_0 is the time-independent background rate. Insert shows the amplitude and phase. The red star indicates the best-fit results, while the black point the expected values. Confidence contours of 1, 2, and 3σ are indicated with colored solid lines.

[From M. Agostini *et al.* (Borexino Collaboration), "Seasonal modulation of the ^{7}Be solar neutrino rate in Borexino," Astropart. Phys. **92** (2017) 21–29; 1701.07970 [hep-ex]; see also reference in footnote of p. 204.]